Semiconductors, Vol. 39, No. 11, 2005, pp. 1235–1266. Translated from Fizika i Tekhnika Poluprovodnikov, Vol. 39, No. 11, 2005, pp. 1281–1311.

REVIEW

Light-Emitting Diodes Based on GaSb Alloys for the 1.6–4.4 μm Mid-Infrared Spectral Range

T. N. Danilova, B. E. Zhurtanov, A. N. Imenkov, and Yu. P. Yakovlev^

Ioffe Physicotechnical Institute, Russian Academy of Sciences, Politekhnicheskaya ul. 26, St. Petersburg, 194021 Russia

^e-mail: yak@ioptI.ioffe.rssi.ru

Submitted July 14, 2004; accepted for publication December 17, 2004

Abstract—The available publications concerned with fabrication and study of light-emitting diodes (LEDs) intended for operation in the 1.6–4.4 μm spectral range; based on GaSb substrates; and grown by liquid-phase epitaxy, which makes it possible to form fairly thick layers lattice-matched to GaSb, are reviewed. In these studies, the active region consists of the GaInAsSb compound in LEDs for the spectral ranges 1.8–2.4 and 3.4–4.4 μm and the AlGaAsSb compound for the spectral region 1.6–1.8 μm. The wide-gap AlGaAsSb confining layers contain up to 64% of Al, which is an unprecedentedly high content for liquid-phase epitaxy. Asymmetric (GaSb/GaInAsSb/AlGaAsSb) and symmetric (AlGaAsSb/GaInAsSb/AlGaAsSb) heterostructures have been fabricated and studied. Various types of designs that make it possible to improve the yield of radiation generated in the active region have been developed. The measured external quantum yield of emission is as high as 6.0% at 300 K for the LEDs operating at the wavelengths 1.9–2.2 μm. A pulsed optical-radiation power of 7 mW at a current of 300 mA with a duty factor of 0.5 and 190 mW at a current of 1.4 A with a duty factor of 0.005 have been obtained. The external quantum emission yield of ~1% has been obtained for LEDs that emit in the spectral range 3.4–4.4 μm; this yield exceeds that obtained for the known InAsSb/InAsSbP heterostructure grown on an InAs substrate by a factor of 3. The measured lifetime of minority charge carriers (5–50 ns) is close to the theoretical lifetime if only the radiative recombination and impact CHCC bulk recombination are taken into account. The impact recombination is prevalent at temperatures higher than 200 K for LEDs operating in the spectral range 3.4–4.4 μm and at temperatures higher than 300 K for LEDs operating in the spectral range 1.6–2.4 μm. © *2005 Pleiades Publishing, Inc.*

1. INTRODUCTION

Light-emitting diodes (LEDs) occupy a prominent place in optoelectronics. They are simpler and more reliable than lasers and operate at much lower current densities. In the case where a high resolution is not required, LEDs are more attractive than lasers, since the latter are more expensive devices; in addition, the need to bring the narrow emission line of a gas into coincidence with its absorption line complicates the experimental setup owing to the requirement for precision heating. Compared to thermal radiation sources, LEDs offer an advantage, since they emit a fairly narrow spectral line (therefore, there is no need for optical filters) and, in addition, admit a high-rate of electrical modulation, meaning that there is no need to use mechanical choppers.

LEDs based on GaSb and its GaInAsSb and AlGaAsSb solid solutions are sources of spontaneous radiation in the 1.6–2.5 μm spectral range, within which there are absorption lines of water vapors, CO_2, nitrogen-containing molecules (N_2O, NO_2, and NH_3), molecules of hydrocarbons (in particular, methane), and so on. These radiation sources are promising for spectral applications, in particular, for ecological and technological control of the environment [1]; in addition, they can be used in medicine, e.g., for measuring the sugar content in blood. There have been attempts to develop LEDs for the spectral range 1.6–2.5 μm on the basis of lattice-mismatched InGaAs/GaAs heterostructures [2]; however, these heterostructures exhibited a low efficiency due to the formation of misfit dislocations in the stressed layers. Heterostructures based on GaSb solid solutions are lattice-matched to the GaSb substrate, have a low density of misfit dislocations, and exhibit an enhanced resistance to degradation.

Gallium antimonide is a direct-gap semiconductor with the band gap E_g = 0.725 eV at room temperature. The GaSb energy-band structure includes Γ, *L*, and *X* valleys with the band gaps E_g^Γ = 0.727 eV, E_g^L = 0.753 eV, and E_g^X = 1.032 eV at 300 K. As a result of the small Γ–*L* energy spacing in GaSb and much lower density of states in the Γ minimum at room temperature, a major portion of the electrons occupies states in the *L* valley. The spin–orbit splitting in GaSb amounts to 0.76 eV (i.e., exceeds E_g at room temperature), which is favorable for a decrease in losses due to absorption and, also, for a reduction in the level of nonradiative Auger recombination.

In LEDs based on GaSb, GaInAsSb is used as the material for the active region and AlGaAsSb is used for wide-gap emitters. The lattice constant of the GaInAsSb

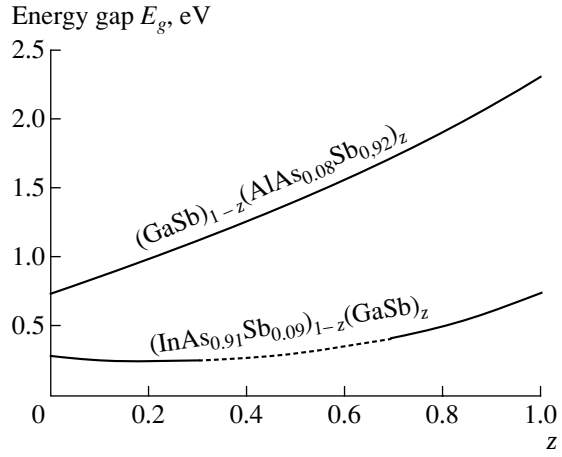

Fig. 1. Dependence of the band gap on the composition of quaternary $(GaSb)_{1-z}(AlAs_{0.08}Sb_{0.92})_z$ and $(InAs_{0.91}Sb_{0.09})_{1-z}(GaSb)_z$ solid solutions, whose lattice constant coincides with that of GaSb at a temperature of 300 K. The miscibility gap for GaInAsSb is represented by the dotted line.

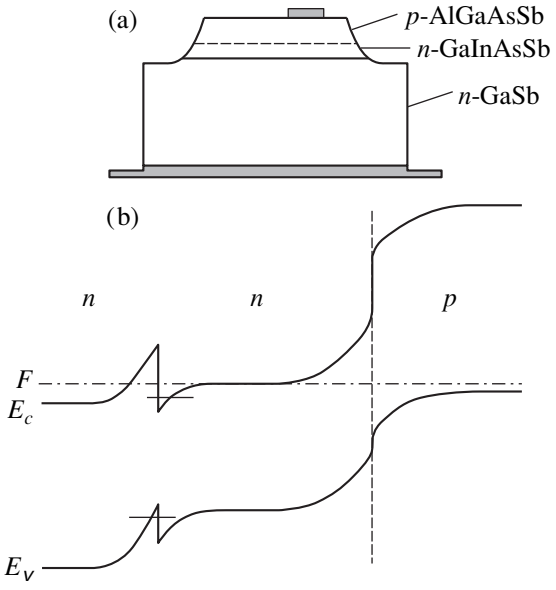

Fig. 2. (a) Schematic representation of a light-emitting diode based on a nonsymmetrical heterostructure with a GaInAsSb active region. (b) The energy-band diagram of the structure: F is the Fermi level, E_c is the conduction-band bottom, and E_v is the valence-band top.

alloy is matched to that of GaSb for the compositions $(GaSb)_z(InAs_{0.91}Sb_{0.09})_{1-z}$. The AlGaAsSb alloy is lattice-matched to GaSb for the compositions $(GaSb)_{1-z}(AlAs_{0.08}Sb_{0.92})_z$. The composition dependences of the band gaps in direct-gap GaInAsSb and AlGaAsSb alloys that are lattice-matched to GaSb are shown in Fig. 1 [3].

Data on fabrication and the results of studies of LEDs based on GaInAsSb were reported for the first time by Dolginov *et al.* [4]. A *p*-GaInAsSb semiconductor grown on a *p*-GaSb substrate was used as the material for the active (emitting) region and *n*-GaSb was used for the wide-gap emitter. An external quantum yield of 1–1.5% was attained at room temperature for these LEDs; the response time was ~10^{-7} s.

This paper is a review of the available publications concerning the development and study of LEDs based on GaSb and its solid solutions. The review consists of an introduction, six main sections, and a conclusion.

In Section 2, the simplest asymmetric LED structures that include a GaSb substrate as one wide-gap emitter and an AlGaAsSb alloy layer as the other wide-gap emitter are considered. These LEDs are most promising for the wavelength range λ = 1.8–2.5 μm.

In Section 3, we consider LEDs with symmetric emitters based on AlGaAsSb alloys. Symmetric heterostructures are found to operate well at the wavelengths of 1.94 and 2.35 μm, which correspond to the absorption lines related to water and methane vapors, respectively.

Section 4 is devoted to the efforts to modify the design of LEDs based on symmetric AlGaAsSb/GaInAsSb/AlGaAsSb heterostructures that emit in the wavelength range 1.9–2.1 μm at room temperature with the aim of attaining a higher emission power.

In Section 5, we describe LEDs that emit at relatively long wavelengths (at λ = 3.4–4.4 μm), are based on symmetric AlGaAsSb/GaInAsSb/AlGaAsSb heterostructures grown on GaSb substrates, and feature an unprecedentedly high efficiency in the spectral range under consideration.

In Section 6, we consider the special features of the design of LEDs that operate at various wavelengths in the range 1.6–2.5 μm. We report the attained parameters of the LEDs.

In Section 7, we describe studies aimed at increasing the quantum yield of the emission by electrochemical faceting the substrate part of the LED.

2. LIGHT-EMITTING DIODES BASED ON AN ASYMMETRIC GaSb/GaInAsSb/AlGaAsSb HETEROSTRUCTURE FOR THE SPECTRAL RANGE 1.8–2.5 μm

The active *p*-GaInAsSb region was formed between a *p*-GaSb substrate and an *n*-GaSb wide-gap emitter in the LED design reported by Dolginov *et al.* [4], whereas, in the LEDs we fabricated, the AlGaAsSb alloy was used as the wide-gap emitter in order to improve the electron confinement [5]. The LEDs were based on a structure (Fig. 2a) [5] that consisted of an active *n*-GaInAsSb 2–3-μm-thick layer ($E_g \approx 0.58$ eV) grown on a (111)B *n*-GaSb substrate (here, B stands for the Sb sublattice) doped with Te so that the charge-carrier concentration was (7–9) × 10^{17} cm^{-3} and a wide-gap *p*-AlGaAsSb emitter layer (E_g = 1.2 eV) doped with Ge so that the carrier concentration was 5 ×

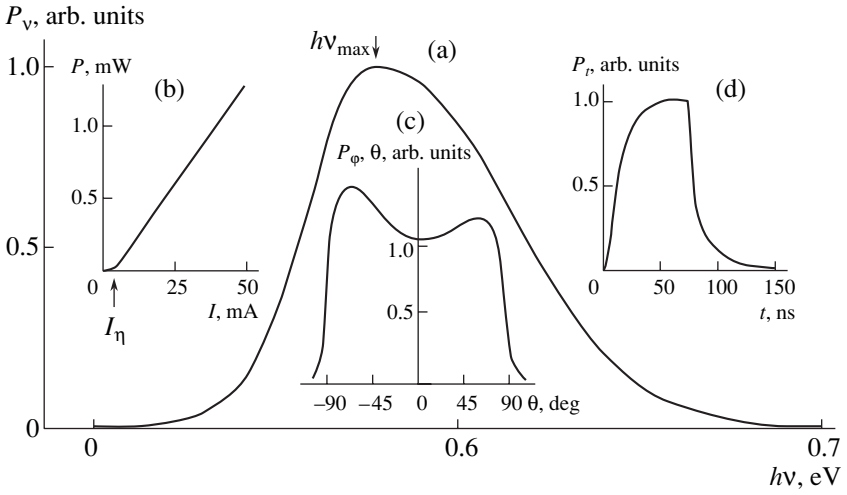

Fig. 3. Electroluminescent characteristics of GaSb/GaInAsSb/AlGaAsSb light-emitting diodes at room temperature. (a) The emission spectrum; (b) the dependence of the emission power P on the current I (I_η is the threshold current that corresponds to a drastic increase in the emission power with the current); (c) the directivity pattern of emission; and (d) the dependence of the emission intensity on time t in the case where rectangular current pulses with an amplitude of 50 mA and duration of 70 ns are applied to the structure.

10^{18} cm^{-3}. We studied structures in which the level of active-region doping with Te varied in the range of carrier concentrations of (5–7) × 10^{17} cm^{-3}. We used this structure to fabricate mesa LEDs (with a diameter of 300 μm) with a continuous deposited ohmic contact to *n*-GaSb (Au + 5% of Te) and a local 50-μm-diameter ohmic deposited contact (Au + 5% of Ge) to *p*-AlGaAsSb.

The energy-band diagram of the LED is shown in Fig. 2b. As can be seen, there is a type II *n*–*n* heterojunction at the interface between the *n*-GaSb substrate and the active region.

The LED characteristics, emission spectra, and directivity patterns were measured under the application of meander-type rectangular current pulses with a duty factor of 0.5 to the LED. The repetition frequency was chosen to be 40–1000 Hz; this frequency was sufficiently low for a steady state in the LED to be established during the effect of each pulse. Therefore, we henceforth refer to this mode of operation as the quasi-continuous wave (CW) mode. In order to obtain LED characteristics at higher currents without heating, we decreased the duty factor to 0.03–0.01. In this case, the pulse width was decreased to 0.2–10 μs. In what follows, we will give only the amplitude values of the current and emission power. The response time was determined from the curve of the growth or decay of the emission pulse when current pulses were applied to the LED.

The results of experimental study of the LEDs are shown in Fig. 3. The emission spectrum $P_\nu(h\nu) = dP/dh\nu$ incorporates a single band whose full width at half-maximum is δ = 0.06–0.07 eV (Fig. 3a). The emission power P (Fig. 3b) increases superlinearly as the current increases, $P \sim I^m$, while, at low currents, $I < I_\eta$ = 4–8 mA; here, m = 4–5 and I_η is the threshold current that corresponds to a drastic increase in the quantum yield of emission. At high currents, $I > I_\eta$, m = 1.1–1.3 in the current range 10–100 mA. The directivity pattern of emission (Fig. 3a) corresponds to the emission-power dependence per unit solid angle ($P_{\varphi,\theta}$) on the angle in the active-region plane φ and the angle θ with respect to the perpendicular to this plane. The total emission power is $P = \int_0^{2\pi} d\varphi \int_0^{\pi} P_{\varphi,\theta} \sin\theta d\theta$. The power of the emission in the direction perpendicular to the *p*–*n*-junction plane (θ = 0°) is 20–30% lower than that at angles θ = 70°–80° (Fig. 3c) for all values of φ. This behavior is attributed to the fact that radiation exits both through the front surface of the crystal with the mesa structure and through side surfaces. Emission from only the front surface is observed at an angle θ = 0°, whereas the emission through the side surfaces is added at larger angles. The angular distribution of emission through each surface is found to follow the cosine law closely. The response speed of a LED affects the dependence of the current emission power P_t on time t when the LED is fed with rectangular current pulses (Fig. 3d). The resulting emission pulse features three stages. Initially, a delay in the appearance of emission is observed; this delay is caused by charging of the *p*–*n*-junction capacitance. The emission intensity then increases with a time constant that is close to the lifetime of the minority charge carriers (τ); when the current is switched off, the emission intensity decays with almost the same time constant. The current-pulse duration is chosen so that it exceeds τ in order for the emission to have time to attain the steady-state value by the instant of current-pulse termination. This steady-state power represents the amplitude emission power *P*. The

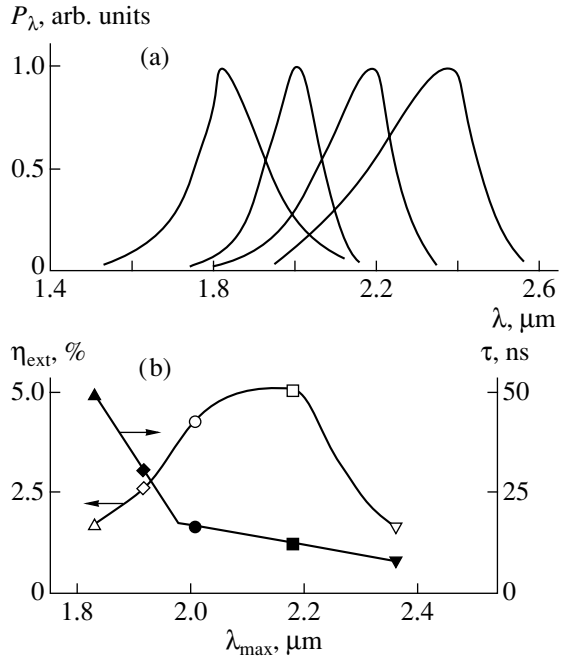

Fig. 4. The main parameters of the light-emitting diode: (a) the emission spectra of four diodes and (b) the dependences of the external quantum yield of emission η_{ext} and the time constant of the emission decay τ on the wavelength that corresponds to the peak λ_{max} of the spectral band.

emission pulse (Fig. 3d) grows and decays with virtually the same time constant of 10–15 ns. The minority-carrier lifetime, determined from the value of the extracted charge when the forward current is changed to the reverse current, has approximately the same value (9–11 ns).

The voltage drop across the LED at high currents ($I > I_\eta$) is expressed by the empirical dependence

$$U = \frac{kT}{e}\ln\frac{I + I_1}{I_1} + \frac{kT}{e}\ln\frac{I + I_2}{I_2} + IR_s, \qquad (1)$$

where I_1 = 0.001–0.1 μA, I_2 = 0.2–0.9 mA, R_s = 1–2 Ω, T is temperature, k is the Boltzmann constant, and e is the elementary charge. The first term on the right-hand side represents the voltage drop across the *p*–*n* junction, the second term represents the voltage drop across the *n*–*n* junction, and the third term represents the voltage drop across the series resistance R_s of the diode.

The external quantum yield of emission was measured using a calibrated photodiode in the case of exit of radiation through both the front face and the lateral faces in combination with exit from the front face. The quantum yield of emission through the front face ranged from 1.3 to 3.5%, while the total quantum yield of emission ranged from 3.0 to 4.5% for a current of 30 mA and was virtually independent of the active-region doping level. The attainment of a higher external quantum yield of emission (η_{ext} > 1.5%) compared to that reported by Dolginov *et al.* [4] is related not only to a high internal quantum yield of radiative recombination but also to the exit of a major part of the radiation due to the process of multiple reflection of light in the mesa structure. Since we used *n*-GaInAsSb (rather than *p*-GaInAsSb as in [4]), we can expect that the contribution of nonradiative recombination becomes much smaller due to the lower rate of impact recombination. As a result, this behavior can lead to a general decrease in the recombination rate in the thin (with the thickness $d \le 3$ μm) active layer and to the appearance of recombination via potential wells at the *n*–*n* heterojunction.

A number of facts indicate that recombination via quantum states at the *n*–*n* heteroboundary can occur in the diodes under consideration. The large width of the emission spectrum (δ = 70 meV) is possibly related to the fact that the degree of degeneracy in the quantum well for electrons at the *n*–*n* heteroboundary is higher than that in the active-region bulk. The independence of the minority-carrier lifetime from the degree of the active-region doping also supports the concept of recombination via quantum states at the *n*–*n* heteroboundary. In addition, the drastic increase in the external quantum yield of emission as the current increases and an increase in the slope of the current–voltage (*I*–*V*) characteristic at currents of 4–8 mA can also be related to radiative recombination via the quantum states at the *n*–*n* heteroboundary.

Further studies of the LEDs based on GaSb/GaInAsSb/AlGaAsSb were carried out in a wide range of compositions, values of the active region thickness, and charge-carrier concentrations in this region [6]. The LED structure was the same as in [5] (see Fig. 2); however, an *n*-GaSb:Te (100) substrate with a charge-carrier concentration of $(5–9) \times 10^{17}$ cm^{-3} was used in [6]. The wide-gap *p*-AlGaAsSb emitter (E_g = 1.27 eV) was doped with Ge so that the acceptor concentration was 5×10^{18} cm^{-3}.

The $Ga_{1-x}In_xAs_ySb_{1-y}$ alloy composition was varied in the ranges $0.05 \le x \le 0.24$ and $0.04 \le y \le 0.22$ in the narrow-gap active layer, while the layer thickness was varied from 0.4 to 6 μm. In this case, the mismatch between the lattice parameters of the substrate and layer ($\Delta a/a$) was no larger than $(1–3) \times 10^{-3}$. The active layer of the structure was doped with tellurium, and the charge-carrier concentration in the layer varied in a wide range, from 1×10^{16} to 2×10^{18} cm^{-3}. Mesa LEDs 300 μm in diameter were provided with a "point" ohmic contact (with a diameter of 40 μm and Au + 5%Ge composition) to *p*-AlGaAsSb and a grid ohmic contact (Au + 3%Te) to *n*-GaSb.

The emission spectra $P_\lambda = dP/d\lambda$ of the LEDs at room temperature (Fig. 4a) include a single band; the wavelength corresponding to the peak of this band λ_{max} increases almost linearly as the composition parameters of the alloy (x and y) in the active region increase. The value of λ_{max} is nearly independent of the level of active-region doping but depends on the thickness of

this region and decreases by 0.05–0.1 μm as the thickness decreases from 5 to 0.4 μm.

The external quantum yield of the emission η_{ext} depends on the charge-carrier concentration n in the active region (Fig. 5a). For all the LEDs, this dependence is bell-shaped with a peak at $n \approx 1 \times 10^{17}$ cm^{-3}. The dependence of the external quantum yield on the active-region thickness d was also represented by a curve with a peak. The highest efficiency was observed at d = 2–3 μm; the efficiency decreased especially drastically (by almost an order of magnitude) as the thickness decreased to 0.7–0.4 μm (Fig. 5b). The external quantum yield η_{ext} attained a maximum of 5% for LEDs with λ_{max} = 2.0–2.2 μm and decreased gradually to 1% for LEDs that emit either at shorter wavelengths (λ_{max} = 1.8 μm) or at longer wavelengths (λ_{max} = 2.4 μm). The measurements were carried out in the range of currents I = 30–300 mA, in which case the value of η_{ext} attained a maximum and the current dependence of the emission intensity was linear. The observed sharp increase in the external quantum yield as the wavelength λ_{max} varied from 1.76 to 2.0 μm is probably caused by an increase in the efficiency of radiative recombination as the energy gap between the Γ and L valleys in the alloy increases as a result of an increase in the In content and eventual increase in the carrier concentration in the direct Γ valley. Further decrease in the radiative-recombination efficiency with increasing wavelength in the range λ_{max} = 2.2–2.4 μm apparently has a complex character. One of the causes of this decrease could be an increase in the degree of disordering of the alloy as the miscibility gap is approached. Another cause might be the effect of interfacial recombination of charge carriers at the *n*–*n* heteroboundary. In a series of LEDs operating at different wavelengths, the magnitudes of the offsets in the conduction band (ΔE_c) and the valence band (E_v) increase; as a result, the depth of the potential wells at the *n*–*n* heteroboundary increases. In this case, if there are imperfections at the *n*–*n* heteroboundary, the efficiency of the radiative recombination can be reduced. Such a conclusion is supported by experimental data on a decrease in the external quantum yield of emission and an increase in the spread in the values of this yield as the active-region thickness decreases and the *p*–*n* junction approaches the *n*–*n* heteroboundary.

The transient electroluminescent characteristics of the structures subjected to rectangular current pulses (I = 200 mA) depend on the alloy composition in the active region. The minority-carrier lifetime τ (Fig. 4b), determined from the emission-decay time constant when the current was switched off and, also, from the value of the extracted charge as the forward current was changed to the reverse current, was the longest for the LEDs with λ_{max} = 1.8 μm and equal to ~50 ns and decreased gradually by an order of magnitude (to 3–5 ns) for a LED with λ_{max} = 2.4 μm.

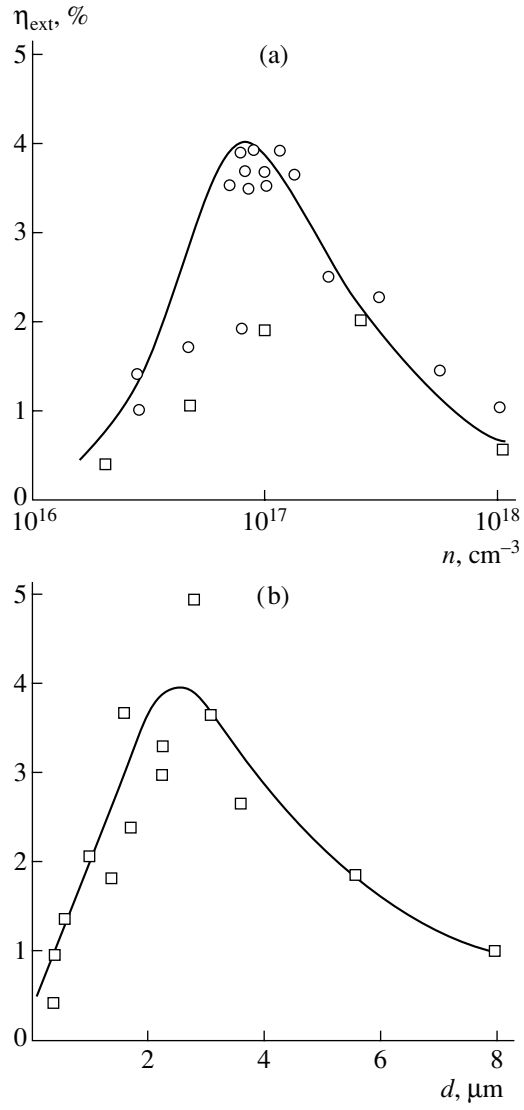

Fig. 5. Dependences of the external quantum yield of emission η_{ext} on (a) the electron concentration n in the active layer and (b) the layer thickness d. T = 295 K.

We managed, later on, to use structures based on GaSb and the GaInAsSb and AlGaAsSb alloys to fabricate LEDs that emitted in a spectral region corresponding to longer wavelengths (λ = 2.5 μm) in the vicinity of the miscibility-gap boundary for the GaInAsSb alloy [7]. Interest in spontaneous optical sources in this spectral region is caused by the fabrication of optical fibers (fluorite) for which an ultralow level of losses (~0.025 dB/km) has been already attained at a wavelength of 2.5 μm.

The light-emitting structure (Fig. 6) was formed by liquid-phase epitaxy (LPE) on an *n*-GaSb (111)B substrate (here, B indicates the Sb sublattice). The active region of the structure consisted of an *n*-$Ga_{0.75}In_{0.25}As_{0.22}Sb_{0.78}$ alloy in the vicinity of the miscibility gap; one side of this region bordered an *n*-GaSb layer ($n \approx 5 \times 10^{17}$ cm^{-3}) and the other side bordered a

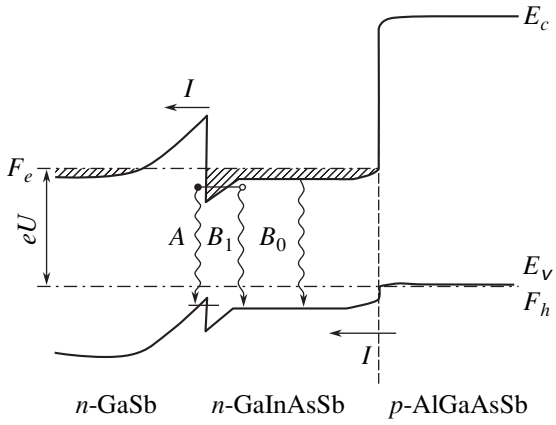

Fig. 6. Energy-band diagram of a nonsymmetrical heterostructure: B_0 denotes band-to-band recombination, and A and B_1 represent two types of interfacial recombination, i.e., (A) between the levels at the heteroboundary and (B_1) between a level at the heteroboundary for electrons and a level of holes attracted to electrons. F_e and F_h are the quasi-Fermi levels for electrons and holes and U is the external voltage.

wide-gap *p*-AlGaAsSb layer (E_g = 1.2 eV, $p = 2 \times 10^{18}$ cm^{-3}). The active region of the structure was doped with tellurium so that the charge-carrier concentration was equal to $(1–8) \times 10^{16}$ cm^{-3}; the active-region thickness was varied in the range 0.4–5 μm. We used this structure to fabricate mesa LEDs (with a diameter of 300 μm) with a grid ohmic contact (Au + 5%Te) to *n*-GaSb and a "point" (with a diameter of ~40 μm) ohmic contact (Au + 5%Ge) to *p*-AlGaSbAs.

The dependence of the LEDs' emitting properties on the active-region thickness was studied.

The emission spectra of the LEDs with a thick active region (d = 5 μm) (Fig. 7a, curves *1*, *1*') feature only an interband emission band (transitions B_0 in Fig. 6) with the wavelengths of the peak λ_{max} = 2.32 and 2.12 μm at 295 and 77 K, respectively. The emission is nonpolarized in any direction of light propagation. The electroluminescence (EL) spectra of the LEDs with a thin active region (d = 0.4 μm) (Fig. 7a, curves *2*, *2*') are shifted to longer wavelengths by 0.15 μm (at 77 and 295 K) owing to the generation of emission with a different physical origin: λ_{max} = 2.42–2.47 μm (295 K) and 2.17–2.21 μm (77 K). The long-wavelength part of the band exhibits TE polarization when emission is observed in the *p*–*n*-junction plane (the vector **E** of the emission electric field is parallel to the *p*–*n*-junction plane). The degree of polarization is as high as 0.1–0.2. The radiation is nonpolarized in a direction perpendicular to the plane of the *p*–*n* junction.

This new emission corresponds to interfacial transitions between the levels for electrons and holes at a *p*–*n* heteroboundary of type II (transitions A in Fig. 6) and between the level for electrons and the level for holes attracted to these electrons (transitions B_1 in Fig. 6).

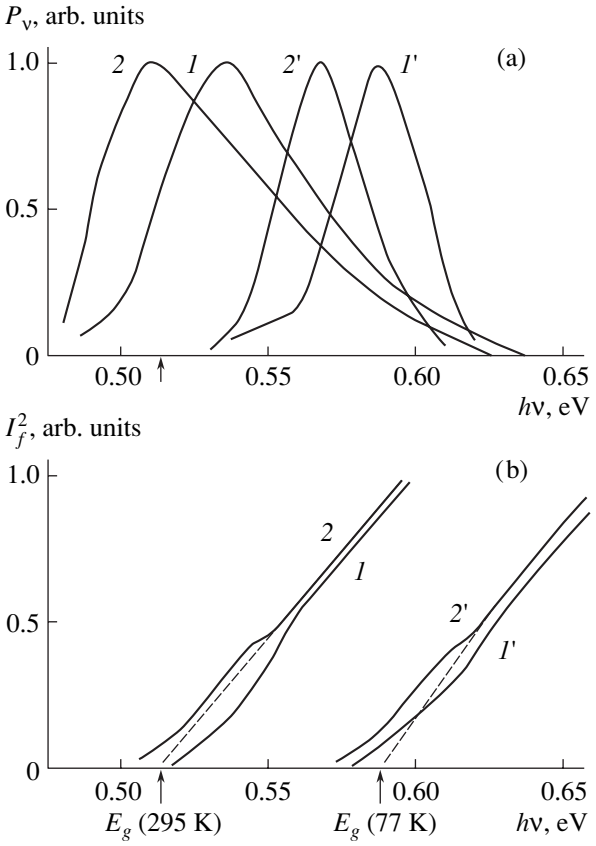

Fig. 7. The spectra of (a) emission P_ν and (b) photocurrent I_f for structures with the thick (*1*, *1*') and thin (*2*, *2*') active regions. T = (*1*, *2*) 295 and (*1*', *2*') 77 K. d = (*1*, *1*') 5 and (*2*, *2*') 0.4 μm.

We studied the long-wavelength edge of photoresponse in the case where the *p*-AlGaAsSb side of the structure was illuminated (Fig. 7b). The shapes of the photoresponse spectra are nearly parabolic for the samples with thin and thick active regions; i.e., the photocurrent $I_f \propto (h\nu - h\nu_f)^{0.5}$, where $h\nu_f$ = 0.51 eV at 295 K and 0.58 eV at 77 K. Such a form photoresponse corresponds to the absorption edge in a lightly doped direct-gap semiconductor, and the value of $h\nu_f$ corresponds to the band gap of the active region.

At the same time, the spectrum of the photoresponse I_f (Fig. 7b) for the structures with a thin active region is shifted to longer wavelengths owing to the appearance of photosensitivity at photon energies $h\nu < E_g$. This additional photosensitivity is probably caused by electron transitions originating near the *n*-GaSb–*n*-GaInAsSb interface.

The external quantum yield of emission at the edge of the miscibility gap for the solid solution (Fig. 8, curve *1*) at room temperature increases almost fivefold as the active-region thickness decreases from 5 to 0.4 μm. It is worth noting that the active-region thickness becomes smaller than the hole diffusion length L = 3 μm. However, the maximum value of the external

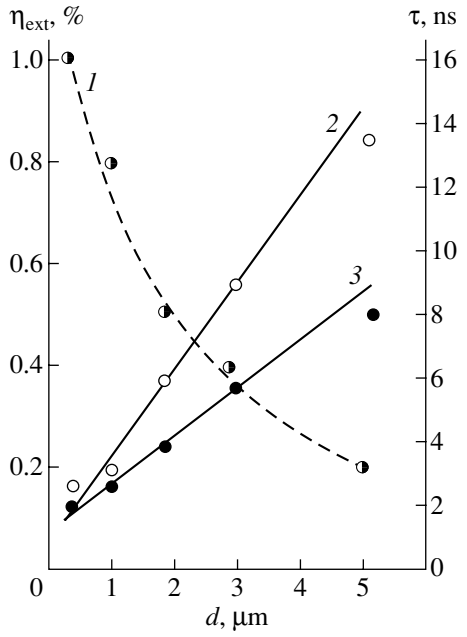

Fig. 8. Dependences of (*1*) the external quantum yield of emission at the edge of the miscibility gap η_{ext} and (*2*, *3*) the time constant of the emission-intensity decay τ on the thickness of the narrow-gap layer *d* at *T* = (*1*, *2*) 295 and (*3*) 77 K.

quantum yield (η_{ext} = 1%) remains lower, by a factor 2–3, than the corresponding yield for the structures with λ_{max} = 2.0–2.2 μm [5]. The external quantum yield at 77 K is a factor of 20–30 higher than that at room temperature.

The most significant changes are observed in the lifetime of minority charge carriers (Fig. 8, curves *2*, *3*) as the active-region thickness is varied: the lifetime decreases by nearly an order of magnitude (from 10^{-8} to 10^{-9} s) as the thickness decreases and the *p*–*n* junction approaches the *n*–*n* heteroboundary.

All the above dependences on the active-region thickness indicate that the radiative-recombination mechanism changes radically and the role of interfacial recombination is prevalent in structures with a thin active region. It is noteworthy that the content of arsenic decreases at the edge of the miscibility gap as the layer thickness increases; as a result, the concentration of defects in the layer increases. This circumstance brings about a decrease in η_{ext} as *d* increases.

Later [8], the nature of the radiative recombination in the heterostructures under consideration was studied in detail. To this end, the temperature and current dependences of the EL spectra, quantum yield of emission, and the lifetime of minority charge carriers in LEDs similar to those considered in [5, 6] were studied. In addition, the lifetime of minority charge carriers was studied in relation to the difference between the band gap of GaSb and that of the narrow-gap GaInAsSb layer.

According to the EL characteristics, all the diodes can be divided into two groups: short-wavelength LEDs

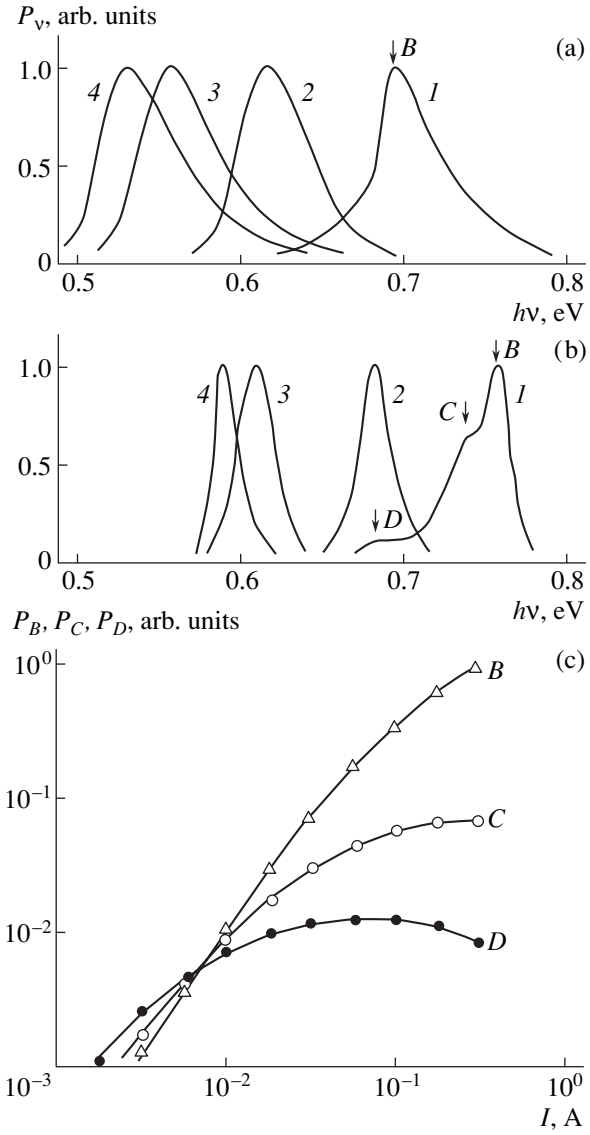

Fig. 9. The emission spectra of four GaSb/GaInAsSb/AlGaAsSb LEDs designed for operation at wavelengths of 1.8–2.4 μm (*1*–*4*) at (a) 295 and (b) 77 K. (c) The dependences of the intensities of bands *B*, *C*, and *D* (P_B, P_C, and P_D) for a light-emitting diode designed for operation at a wavelength of 1.8 μm on the current at 77 K.

with an emission wavelength λ_{max} < 2 μm and long-wavelength LEDs with λ_{max} > 2 μm. The emission spectra of all the LEDs at room temperature (Fig. 9a) are represented by a band with a width of 0.04–0.06 eV and an energy of the peak $h\nu_{max}$ close to E_g of the narrow-gap layer. Spectral dependences of emission for the LEDs designed for the wavelengths of 1.8, 2.0, 2.2, and 2.4 μm (0.69, 0.62, 0.56, and 0.52 eV) at *T* = 295 K are shown in Fig. 9a.

As the temperature is varied from 295 to 77 K, the emission spectra of the long-wavelength LEDs do not radically change: they still include a single band. Low-intensity bands *C* and *D* are clearly observed in the

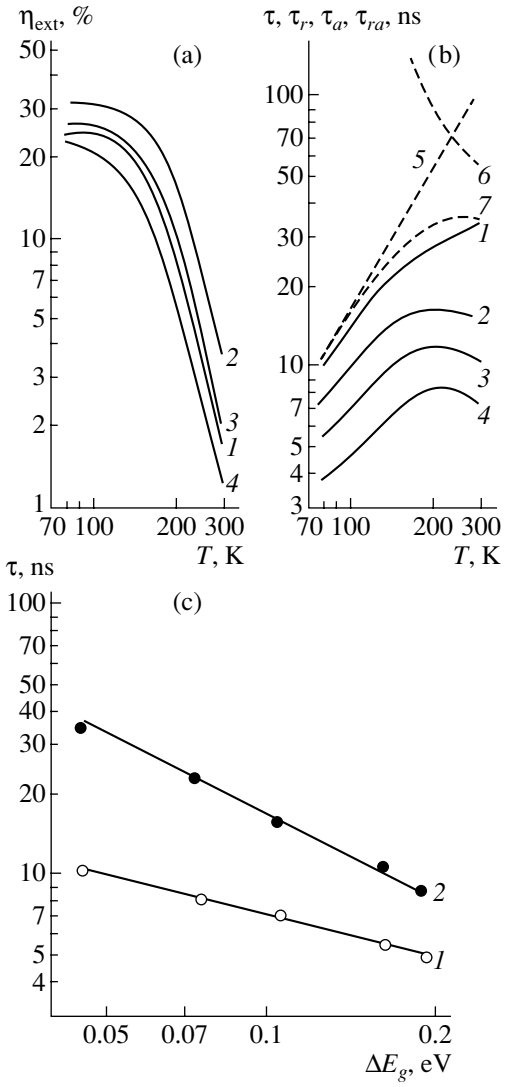

Fig. 10. Temperature dependences of (a) the external quantum yield of emission for LEDs and (b) the charge-carrier lifetime. Curves *1–4* correspond to the LEDs with the emission spectra (*1–4*) in Fig. 9. (b) The dashed lines correspond to the results of calculations of (*5*) τ_r, (*6*) τ_a, and (*7*) τ_{ra}. (c) The dependences of the charge-carrier lifetime on the difference between the band gaps of GaSb and the narrow-gap GaInAsSb layer ΔE_g at (*1*) 77 and (*2*) 295 K for an electron concentration in the narrow-gap layer equaling ~10^{17} cm^{-3}.

spectra of short-wavelength LEDs as the temperature is varied from 295 to 77 K (Fig. 9b). The energies corresponding to the peaks of bands *C* and *D* are smaller than E_g by 20 and 80 meV, respectively; the intensities of the bands depend heavily on current. Bands *C* and *D*, located at longer wavelengths, are prevalent in the spectra at low currents (Fig. 9c). As the current is increased, the emission intensity in these bands attains a maximum (band *C*) or even becomes slightly lower after attaining a maximum (band *D*); at the same time, the emission intensity in the short-wavelength band (band *B*) increases steadily as the current is increased, with the current dependence of the intensity being transformed gradually from superlinear to linear. As the temperature increases, the contribution of band *B* increases; this band is prevalent at room temperature even at low currents.

The temperature dependences of the energies corresponding to the peaks of the emission bands for short- and long-wavelength LEDs are radically different. For all the short-wavelength LEDs, we have $dh\nu_{max}/dT \approx dE_g/dT$ for all the bands.

The energy position and shape of band *B* are characteristic of band-to-band radiative recombination taking into account the degeneracy of electrons. Bands *C* and *D* have features that are characteristic of recombination via doubly charged acceptors. The difference $E_g - h\nu_{max}$ is close to the ionization energy of a singly charged acceptor for short-wavelength band *C* and is approximately fourfold larger for band *D*, which should be expected for a doubly charged acceptor. In the short-wavelength LEDs at temperatures close to 77 K, the minority-carrier recombination is mainly radiative and occurs owing both to band-to-band transitions and to transitions to the levels of inherent doubly charged acceptors; in contrast, at $T > 200$ K, nonradiative Auger recombination begins to play an important role along with the band-to-band radiative recombination. In semiconductors with *n*-type conductivity, the Auger process is most probable; in this process, a minority carrier (hole) recombines with an electron and transfers the released energy to another electron in the conduction band (the CHCC process).

The external quantum yield of emission features a maximum (up to 6%) in the LEDs designed for wavelengths of 2.0–2.2 μm and decreases to 1% for the LEDs designed for either shorter (λ_{max} = 1.8 μm) or longer (λ_{max} = 2.4 μm) wavelengths. As the temperature is increased, the external quantum yield of emission decreases in all the LEDs at a fixed current (30 mA) (Fig. 10a). In the temperature range 77–150 K, the external quantum yield depends on temperature only slightly, whereas this dependence is heavy at higher temperatures.

We calculated the radiative (τ_r) and nonradiative (τ_a) lifetimes of minority charge carriers in the case of band-to-band recombination. In order to calculate τ_r, we chose the formula derived by Gel'mont and Zegrya [9] taking into account the nonparabolicity of the energy bands and the spin–orbit splitting of the valence band; this formula is written as

$$\tau_r = \left[\left(\frac{2\pi}{m_c kT}\right)^{3/2}\frac{\sqrt{\varepsilon_\infty}E_g^2}{c^3} \times \frac{e^2 h}{m_c}\frac{E_g+\Delta}{3E_g+2\Delta}\frac{\mu_h^{3/2}+\mu_l^{3/2}}{m_h^{3/2}+m_c^{3/2}}\right]^{-1} n^{-1}, \quad (2)$$

where

$$\frac{1}{\mu_l} = \frac{1}{m_l} + \frac{1}{m_c}; \quad \frac{1}{\mu_h} = \frac{1}{m_h} + \frac{1}{m_c};$$

m_c, m_l, and m_h are the effective masses of an electron and light and heavy holes, respectively; ε_∞ is the high-frequency permittivity; c is the speed of light; and Δ is the magnitude of the spin–orbit splitting of the valence band.

The temperature dependence of τ_r for a short-wavelength LED was calculated using formula (2) and is shown in Fig. 10b (curve *5*). At a temperature of 77 K, the calculated value of τ_r exceeds the experimental value by no more than ~20%. As the temperature increases, the calculated τ_r increases in proportion to $T^{3/2}$; in contrast, experimental values increase much less rapidly, which indicates that other recombination mechanisms come into effect with an increase in temperature.

In order to calculate the nonradiative hole lifetime in this process, we use the Beattie–Landsberg formula for a CHCC process [10–12]:

$$\tau_a = \left[\frac{8\sqrt{2}\pi^{5/2}e^4h^3|F_1F_2|^2\exp\left(-\frac{\mu}{1+\mu}\frac{E_g}{kT}\right)}{\varepsilon^2 m_c^{1/2}m_h^{3/2}(kTE_g)^{3/2}(1+\mu)^{1/2}(1+2\mu)}\right]^{-1} n^{-2}. \quad (3)$$

Here, $\mu = m_c/m_h$ and ε is the permittivity.

The squared product of the overlap integrals $|F_1F_2|^2$ is calculated using the formula

$$|F_1F_2|^2 = \left(1 + \frac{m_h}{m_c}\right)\frac{\mu(1-\mu)}{1+3\mu+2\mu^2}. \quad (4)$$

The Beattie–Landsberg theory was favored over the more rigorous theory given in [9] because, in the former, the quantity $|F_1F_2|^2$ is calculated in the context of the one-dimensional Kronig–Penney model rather than the three-dimensional model as in [9]. Apparently, the one-dimensional model corresponds satisfactorily to the conditions in the crystals under study; these crystals are heavily compensated and involve high electric fields along which the law of conservation of momentum can be violated. The more rigorous theory [9] yields a value of $|F_1F_2|^2$ that is a factor of E_g/kT smaller and a value of τ_a that is an order of magnitude larger than those calculated using the Beattie–Landsberg theory [10].

The temperature dependence of τ_a for a short-wavelength LED was calculated with formula (3) and is shown in Fig. 10b (curve *6*).

At a temperature of 300 K, the calculated lifetime τ_a exceeds the experimental value by a factor of ~1.5 and is shorter than the radiative lifetime τ_r by a factor of ~2. As the temperature decreases, the value of τ_a increases rapidly. The resulting lifetime, $\tau_{ra} = \tau_a\tau_r/(\tau_a + \tau_r)$ (Fig. 10b, curve *7*), exceeds the experimental value (τ) by no more than 10–25%; therefore, we may assume that radiative recombination is prevalent in short-wavelength LEDs at low temperatures.

The calculated internal quantum yield $\eta_{ra} = \tau_{ra}/\tau_r$ for short-wavelength LEDs is equal to 98% at 77 K and decreases as the temperature increases to 35% at 300 K. The experimental external quantum yield differs from the calculated value, being equal to 30–40% at 77 K, and decreases drastically as the temperature increases (to 1–2% at 300 K) (Fig. 10a). Probably, the experimental value of the external quantum yield is much smaller than the calculated internal quantum yield mainly as a result of absorption of radiation in the crystal. Furthermore, there are some additional mechanisms of nonradiative recombination. At temperatures in the vicinity of 300 K, the external quantum yield can be affected to some extent by nonradiative recombination via the *L* valley of the conduction band as a result of the narrow energy gap (100 meV) between the Γ and *L* valleys.

In addition, the interfacial recombination at the *n*–*n* heteroboundary can make some contribution to the recombination process.

In the long-wavelength LEDs, the external quantum yield of radiation is equal to 20–30% at 77 K, which corresponds to the prevalence of radiative recombination if we take into account absorption of radiation in the crystal. At room temperature, the external quantum yield is an order of magnitude lower than at 77 K; correspondingly, the lifetime of minority charge carriers is controlled by a nonradiative process.

According to expression (2), the radiative lifetime in the case of band-to-band bulk recombination should increase by 40% as E_g decreases from 0.7 to 0.5 eV, irrespective of temperature, while the nonradiative lifetime, according to expression (3), should decrease by a factor of 2 when the temperature is increased to 300 K. However, the experimental lifetime does not increase as E_g decreases from 0.68 to 0.53; rather, the lifetime decreases by a factor of 2.5–5. This circumstance suggests that there is interfacial recombination (in addition to band-to-band bulk recombination) in the long-wavelength LEDs.

Since the lifetime of minority charge carriers should depend on the charge at the heteroboundary, we plotted the dependence of the experimental lifetime τ on ΔE_g, i.e., on the difference between the band gaps of GaSb and GaInAsSb (Fig. 10c). The value of ΔE_g is linearly related to the magnitude of the conduction-band offset ΔE_c at the *n*–*n* heteroboundary; the space charge at this boundary N depends on ΔE_c as $N \propto \sqrt{\Delta E_c}$. Therefore, the radiative lifetime should be inversely proportional to $\sqrt{\Delta E_g}$, which is precisely what is observed for experimental τ at 77 K (Fig. 10c, curve *1*). At the same time, we have $\tau \propto (\Delta E_g)^{-1}$ at room temperature, which is quite possible in the case of a nonradiative CHCC process at the heteroboundary (Fig. 10c, curve *2*).

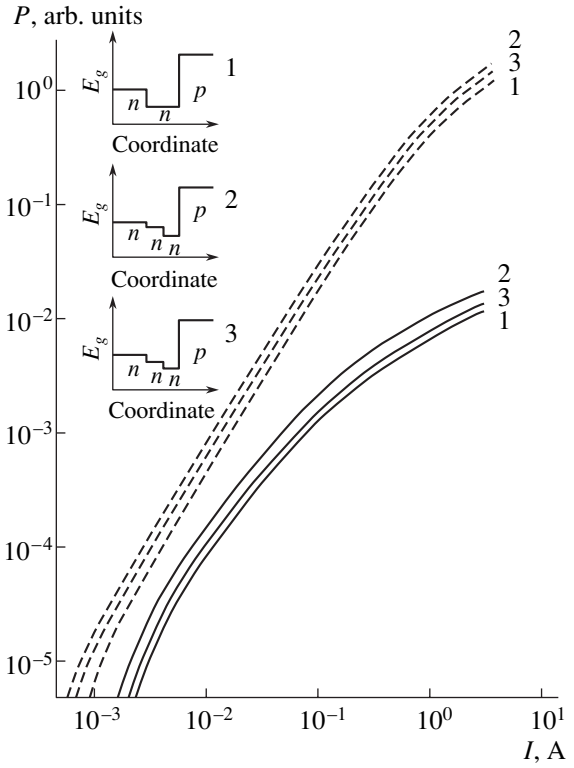

Fig. 11. The current dependences of the optical output power for light-emitting diodes of three types (1–3) at T = 77 K (dashed lines) and 300 K (solid lines). The energy-band diagrams for studied heterostructures 1–3 with various heights of the *n*-GaSb/*n*-GaInAsSb heterobarriers at the boundary with the active region are shown in the inset; these heights amount to (1) 100%, (2) 54%, and (3) 27% of the original value.

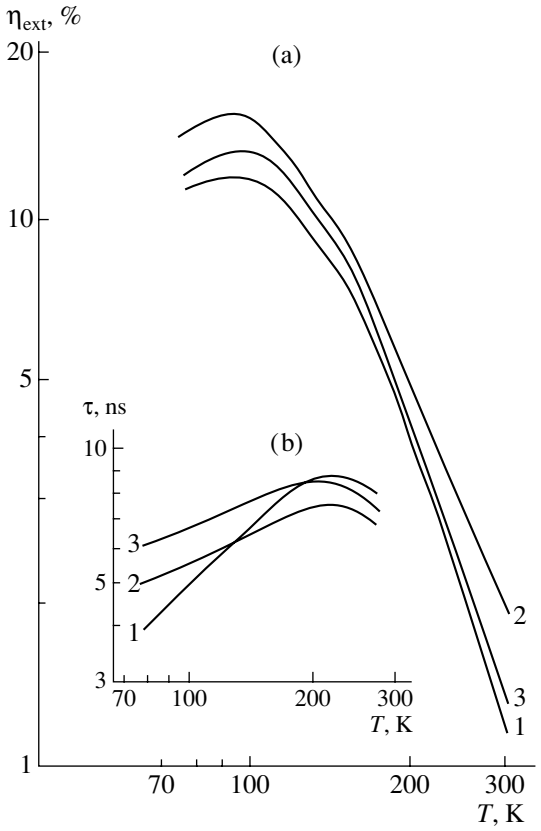

Fig. 12. Temperature dependences of (a) the external quantum yield of emission η_{ext} and (b) the lifetime of minority charge carriers at a pulsed current of 100 mA for structures 1, 2, and 3 (see Fig. 11).

Later on, we studied the effect of the band offset at an *n*-GaSb/*n*-GaInAsSb type II heterojunction on the efficiency of radiative recombination in LEDs based on *n*-GaInAsSb [13]. We studied three types of individual heterostructures (see the inset in Fig. 11) based on the $Ga_{0.79}In_{0.21}As_{0.19}Sb_{0.81}$ alloy (E_g = 530 meV and T = 300 K). In a type 1 structure, a narrow-gap *n*-GaInAsSb layer was confined by an *n*-GaSb:Te substrate (E_g = 726 meV and $n = 3 \times 10^{17}$ cm^{-3}) and a wide-gap *p*-$Al_{0.34}Ga_{0.66}As_{0.02}Sb_{0.98}$:Ge emitter ($E_g$ = 1.27 eV and $p = 5 \times 10^{18}$ cm^{-3}). The structures of types 2 and 3 differed from the type 1 structure in that they included an intermediate *n*-$Ga_{1-x}In_xAs_ySb_{1-y}$ layer introduced between the substrate and narrow-gap *n*-$Ga_{1-x}In_xAs_ySb_{1-y}$; the In content in this intermediate layer amounted to x = 0.10 and 0.15 for the structures of types 2 and 3, respectively. The active and intermediate layers of the structures were doped with tellurium to produce an electron concentration of 8×10^{16}–1×10^{17} cm^{-3}.The narrow-gap layer was 1.5 μm thick, the intermediate layer was 2.0 μm thick; and the emitter layer was 2.5 μm thick. The magnitude of the lattice mismatch between the substrate and the layers was no larger than $\Delta a/a = 5 \times 10^{-4}$. These structures were used to fabricate mesa LEDs 300 μm in diameter with a grid contact (Au + 3%Te) to the *n*-GaSb substrate and a "point" contact (40 μm in diameter, Au + 5%Ge) to *p*-AlGaAsSb. The *p*–*n*-junction area was 3×10^{-3} cm^2.

The current dependences of the optical power (Fig. 11) are similar for the three types of structures. In the entire range of currents and temperatures, the type 2 structures exhibited the highest optical power and the type 1 structures featured the lowest optical power. The external quantum yield of emission η_{ext} (Fig. 12a) first increased by 5–10% as the temperature was increased in the range T = 77–110 K and, then, decreased drastically at temperatures higher than 110 K for all the types of structures. The quantum yield decreased in the vicinity of room temperature.

The lowest quantum yield was observed for the structures without an intermediate layer (type 1) and the highest yield was observed in the structures that incorporated an intermediate layer with x = 0.10 (type 2).

The temperature dependence of the lifetime of minority charge carriers (Fig. 12b) exhibited a maximum at T = 220 K. The temperature dependence of the lifetime for the structures with the intermediate layer was less steep than that for the structures without an

intermediate layer. The temperature at which the carrier lifetime was longest depended on the structure type. The lifetime becomes identical for the structures of types 1 and 2 at 130 K and for the structures of types 1 and 3 at 190 K. At room temperature, the lifetime in the structures with an intermediate layer is 10–15% shorter than that in the structures without an intermediate layer.

The emission characteristics of the LEDs studied exhibit some common features that should be related to recombination in the bulk of the active region; this recombination is similar in the three types of heterostructures under consideration. Differences in the emission characteristics of the LEDs are related to the corresponding differences in the energy-band diagrams. The $Ga_{0.75}In_{0.25}As_{0.19}Sb_{0.81}$ alloy forms a biased heterojunction (type II) with the *n*-GaSb substrate, and the offsets of the conduction band ΔE_c and the valence band ΔE_v are of the same sign and are equal to 370 and 170 meV [14]. The introduction of a $GaIn_xAsSb$ intermediate layer with $x = 0.10$ ($E_g = 630$ meV) divides the barrier at the *n*–*n* heteroboundary according to the relation $\Delta E_{c1}/\Delta E_{c2}$ = (170/200) meV [14]. Introduction of an intermediate layer with $x = 0.15$ ($E_g = 570$ meV) makes this ratio equal to $\Delta E_{c1}/\Delta E_{c2}$ = (270/100) meV [14]. The introduction of an intermediate layer leads to a decrease in the depth of the potential wells at the *n*–*n* heteroboundary with the active region and to a decrease in the role of radiative and nonradiative recombination processes at this heteroboundary. The radiative lifetime of the minority charge carriers in the case of recombination in the region of the heteroboundary is proportional to the surface charge density and is related to the conduction-band offset in the form $\tau \propto (\Delta E_c)^{-1/2}$. An increase in temperature brings about an activation of nonradiative recombination both in the bulk and in heteroboundary region. As ΔE_c increases, the efficiency of the radiative process lowers as a result of intensification of the nonradiative Auger process; therefore, the structures without intermediate layers exhibit longer lifetimes and a lower efficiency at room temperature (Fig. 12). As follows from the experimental data, recombination of charge carriers in the region of the *n*–*n* heterojunction directly affects the efficiency of radiative Auger recombination in the LEDs based on *n*-GaInAsSb. The effect of the *n*–*n* heteroboundary was observed in the entire range of temperatures (77–300 K) and pump currents ($I < 6$ A) under consideration and manifested itself in the ratio between the efficiencies of the mechanisms of radiative and nonradiative recombination processes. The introduction of the intermediate layer ($\Delta E_c/E_g = 40\%$) made it possible to increase the emission external quantum yield by a factor of 1.5–2 compared to that in the structures without an intermediate layer.

Thus, we fabricated and studied LEDs that were designed for the 1.6–2.5-μm spectral range and had a lowered potential barrier at the *n*–*n* boundary of the active region. The *n*–*n* type II heterojunction acted as a lower confining energy barrier. The LEDs of this design featured a quantum yield no lower than 5–6% in the pulsed mode at room temperature. In addition, studies of these LEDs made it possible to gain insight into the properties of a type II *n*–*n* heterojunction for a GaSb/GaInAsSb system. We showed that there is an optimal value of the conduction-band offset ΔE_c at which the external quantum yield reaches a maximum. This value is equal to 200 meV for the LEDs under consideration. It was of great interest to us to compare the developed structures of asymmetric LEDs that include a type II *n*–*n* heterojunction with a symmetric LED structure that does not include a type II heterojunction.

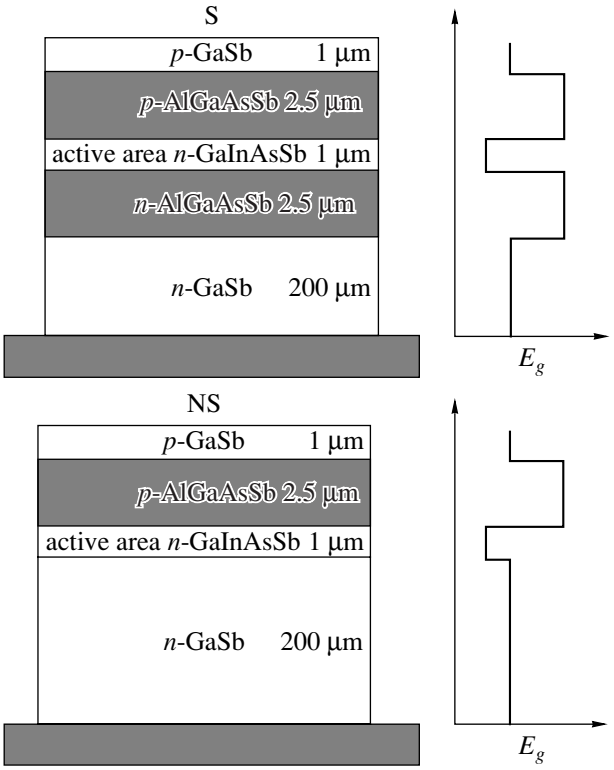

Fig. 13. Schematic representation of light-emitting double heterostructures: symmetric (S) and nonsymmetrical (NS).

3. LIGHT-EMITTING DIODES BASED ON A SYMMETRIC AlGaAsSb/GaInAsSb/AlGaAsSb STRUCTURE AND DESIGNED FOR THE WAVELENGTHS OF 1.94, 2.2, AND 2.35 μm

Popov *et al.* [15] carried out a comparative study of the design of two types of LEDs based on symmetric and asymmetric heterostructures. The LEDs emitted at the wavelength $\lambda_{max} = 2.2$ μm. The measurements were carried out in the continuous-wave (CW) mode at room temperature. The aim of the study was to fabricate high-power LEDs for the above wavelength in order to measure the absorption spectra of nitrogen-containing mol-

ecules (N_2O, NO_2, and NH_3). The structures of these LEDs are shown in Fig. 13.

The LEDs were grown by LPE on an *n*-GaSb (100) substrate. The heterostructure of the first type (symmetric (S)) consisted of four epitaxial layers. The active *n*-GaInAsSb layer was confined by two wide-gap *n*- and *p*-AlGaAsSb emitters with a thickness of 2.5 μm. A heavily doped 0.5-μm-thick *p*-GaSb layer was grown on top in order to provide a low-resistance contact. The active GaInAsSb layer had a high indium content ($x = 16\%$, $E_g = 0.57$ eV) and was doped with Te to a concentration as high as $(1–2) \times 10^{17}$ cm^{-3}. The wide-gap confining AlGaAsSb layers with an Al content of 50% ($E_g = 1.11$ eV) were doped with Te and Ge to the concentrations of $(2–4) \times 10^{18}$ and $(6–8) \times 10^{18}$ cm^{-3} for the *n*- and *p*-type layers, respectively. The lattice constants of all the layers were matched to that of the GaSb substrate. The structure of the second type (nonsymmetrical (NS)) was different in that there was no *n*-AlGaAsSb layer.

We studied circular mesa diodes obtained using photolithography and deep etching of the substrate. The mesa diameter (300 μm) defined the area of the emitting surface (7×10^{-4} cm^2). The chip of an individual LED was square-shaped and had an area of 500–500 μm^2. The semiconductor chip was mounted within a standard TO-18 transistor case. The TO-18 case also included a parabolic reflector that made it possible to collimate the LED emission within an angle of 10°–12°. The total LED size was 9 mm in diameter and 5.5 mm in length.

The *I–V* characteristics of the two types of structures differed from each other in relation to the cutoff voltage, which was equal to 0.27 V for structure S and 0.23 V for structure NS. The series resistances at a forward bias were in the range 1.3–1.4 Ω for both structures.

For both the S and NS structures, the spontaneous-emission spectrum had a shape typical of infrared diodes, exhibiting a characteristic thermal broadening.

Emission was observed under a forward bias when the current was no higher than 5 mA. A steep rise in the power was observed for injection currents in excess of 10 mA.

The emission spectrum of a symmetric structure S at room temperature consisted of a single band that had a peak at the wavelength $\lambda_{max} = 2.173$ μm (0.571 eV) at a current of 120 mA and the full width at half-maximum of 0.23 μm (0.060 eV). The emission spectrum of a nonsymmetrical (NS) structure at room temperature and the same current of 120 mA had a peak shifted by 0.02 μm to longer wavelengths (compared to the emission peak for an S structure) and a spectrum width of 0.28 μm (0.074 eV). If the LEDs were cooled to 77 K, the peak of the emission spectrum of structure S shifted to shorter wavelengths, to $\lambda_{max} = 1.989$ μm (0.623 eV), with the average rate of 0.82 nm/K and the emission-spectrum width decreased to 0.07 μm (0.022 eV). The peak in the spectrum of an NS structure shifted to shorter wavelengths, to 1.997 μm (0.621 eV), as a result of cooling to 77 K. This spectrum had a larger width (0.105 μm, i.e., 0.033 eV), even at liquid-nitrogen temperature. It is worth noting that the total temperature-related shift of the emission-spectrum peak for both LED types was found to be smaller than the calculated thermal-induced variation in the band gap. A weakening of the temperature dependence of the energy corresponding to the emission-spectrum peak is characteristic of band-to-band radiative recombination, in which case the energy of the peak exceeds the band gap E_g by ~kT. The excess of the emission-spectrum over the value of $1.5kT$, which corresponds to the Boltzmann distribution of the charge carriers, is attributed to the heavy doping of the active region with donors. For both structures, the position of the emission peak depends only slightly on the value of the injection current. The shift to longer wavelengths was observed with an average rate of 0.05 nm/mA.

The current dependence of the output optical power is shown in Fig. 14. The optical power P increased for both types of structures in the entire range of currents and can be described by the power-law dependence $P \propto I^m$. For a symmetric structure, the current dependence follows the law $P \propto I$ in the initial region of currents up to 90 mA and transforms into the dependence $P \propto I^{0.87}$ at higher pump currents. For a nonsymmetrical NS structure, the corresponding values of m were equal to ~0.93 and ~0.76 for low and high currents, respectively. For the LEDs of type S, the current dependence exhibited a higher output power in the entire current range. The highest optical power of 1.7 mW in the quasi-CW mode was attained at an injection current of 120 mA (we refer to the pulsed values of the emission power and current). At higher currents, the emission–current characteristic leveled off owing to heating of the LED. The symmetric (S) LEDs exhibited a higher output power in comparison with the nonsymmetrical NS LEDs in the entire range of currents under consideration. The symmetric LED heterostructures of type S were studied in more detail. In particular, we studied the output-power dependence on current at various values of active-region thickness d (Fig. 14b). The maximum value of the optical power was attained at the active-region thickness of 0.7 μm; an increase or a decrease in the layer thickness led to a decrease in the output power. The optimal thickness of the active-region layer was found to be much smaller than the diffusion length for nonequilibrium charge carriers (~2 μm) in the GaInAsSb alloys. This result means that the carrier distribution within the active region is independent of the coordinate perpendicular to the plane of the *p–n* junction.

Thus, from the standpoint of spectral and power characteristics, a symmetric GaAlAsSb/GaInAsSb/GaAlAsSb semiconductor structure with a conduction-band offset that is comparable to the active-region band gap is found to be the most attractive for attaining the highest

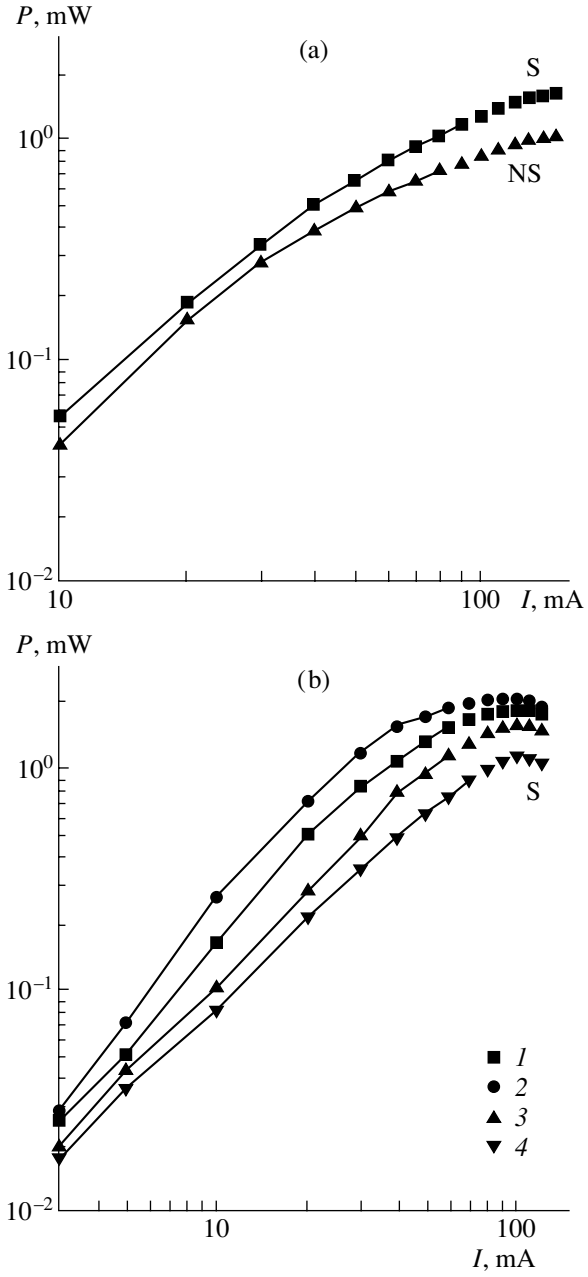

Fig. 14. The current dependences of the optical output power for light-emitting diodes based on double heterostructures fed by meander current pulses with a frequency of 512 Hz. (a) Light-emitting diodes based on symmetric (S) and nonsymmetrical (NS) double heterostructures with an active-region thickness of 0.8 μm. (b) Light-emitting diodes based on a symmetric (S) heterostructure with the active-region thickness d = (*1*) 0.5, (*2*) 0.7, (*3*) 1.2, and (*4*) 16 μm. T = 300 K and λ_{max} = 2.18 μm.

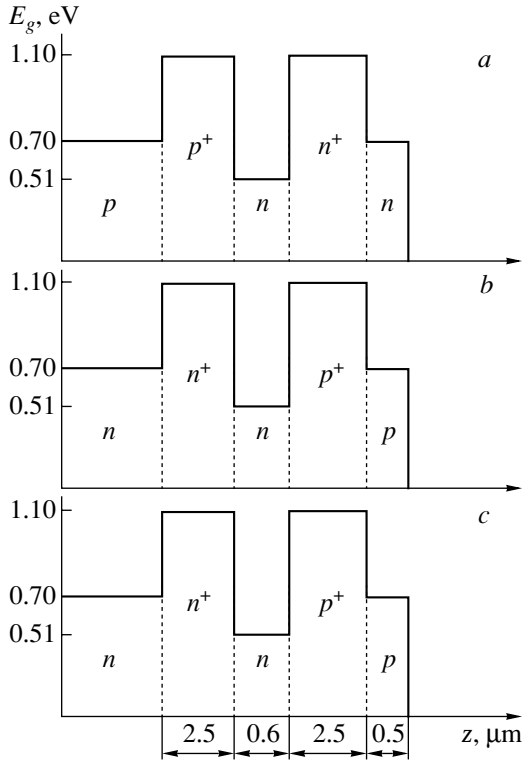

Fig. 15. The energy-band diagrams of LED heterostructures of three types designed for operation at the wavelength λ_{max} = 2.35 μm. Structures *a* and *b* contain 50% of Al in the emitter layers and structure *c* contains 34% of Al in this layer. The coordinate in the direction of the layer growth is denoted by *z*.

emission spectral density. This parameter was found to be most important for practical implementation of this class of infrared LEDs in spectroscopy.

Symmetric heterostructures were used to fabricate LEDs for measuring humidity (at a wavelength of 1.94 μm) [16] and methane content (at a wavelength of 2.35 μm) [17]. The external quantum yield of these devices is higher than that of nonsymmetrical LEDs [6] for the above wavelengths by a factor of 1.8 (1.94 μm) and 1.4 (2.35 μm), respectively.

LEDs emitting at a wavelength of 1.94 μm [16], similarly to those designed for a wavelength of 2.2 μm [15], were formed by LPE on an *n*-GaSb (100) substrate. GaSb (100) substrates with *n*- and *p*-type conductivity were used for LEDs designed for a wavelength of 1.35 μm [17]. Three variants of heterostructure (*a*, *b*, and *c*) were used; the corresponding energy-band diagrams are shown in Fig. 15. As can be seen, these structures do not include a GaSb/GaInAsSb type II heterojunction and differ with regard to the characteristics of the emitter layers. The active region in all the symmetric structures under consideration with an In content of 8 and 21% had *n*-type conductivity as a result of doping with Te (the electron concentration was $(1–2) \times 10^{17}$ cm^{-3}). The optimal thickness of the active region (~0.6 μm) was used [15]. The wide-gap confining layers grown on *n*- and *p*-GaSb substrates in structures *a* and *b* (see Fig. 15) contained 50% of Al (E_g = 1.11 eV) and were doped with Te and Ge so that the charge-carrier concentration was $(2–4) \times 10^{18}$ and $(6–8) \times 10^{18}$ cm^{-3} in the *n*- and *p*-type layers, respec-

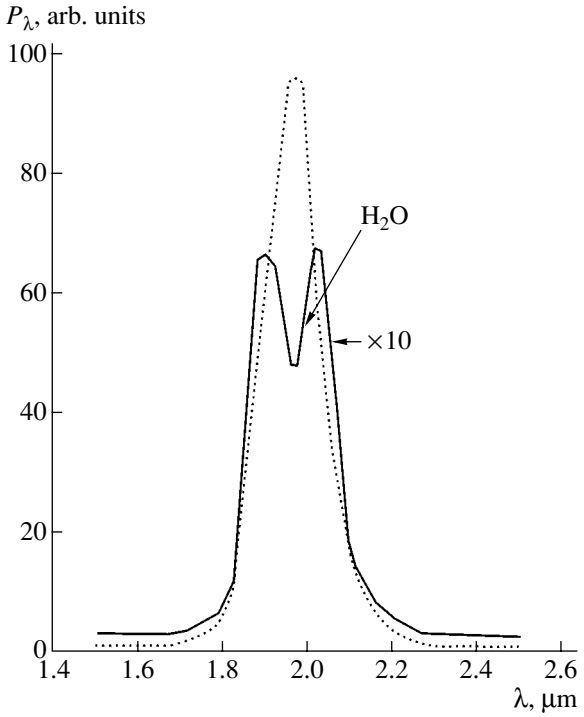

Fig. 16. The emission spectrum of a LED designed for operation at a wavelength of 1.94 μm in the quasi-continuous power-supply mode at a current with the amplitude of 50 mA at room temperature (dashed line) and the spectrum of the same emission after transmission through a water layer with a thickness of 5 μm (solid line). The repetition frequency for the current pulses was 512 Hz and the off-duty factor was equal to 2.

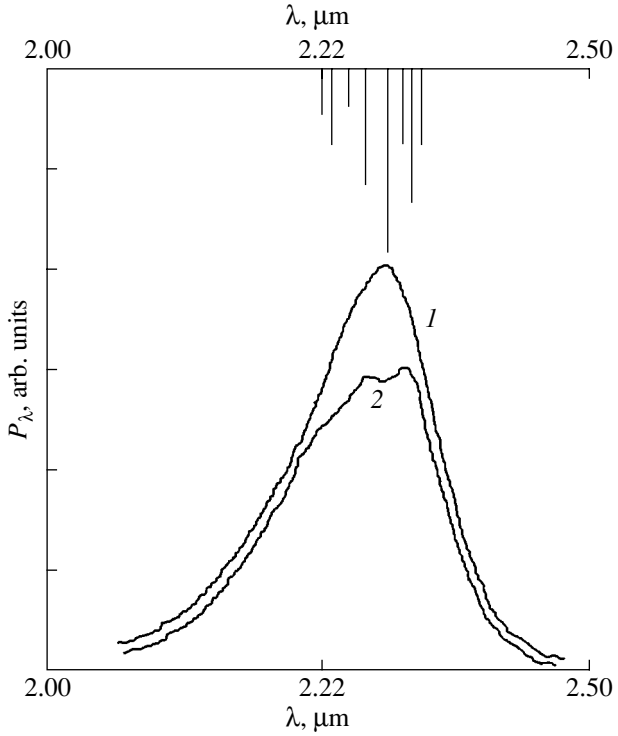

Fig. 17. (*1*) The emission spectrum of a LED designed for operation at a wavelength of 2.35 μm and fed by a current with an amplitude of 50 mA under the quasi-continuous mode of power supply at room temperature and (*2*) the spectrum of the same emission passed through a 2.5-cm-long cell with methane at atmospheric pressure. The position and intensity of the methane absorption lines are indicated in the upper part of the figure. The repetition frequency of the pulses was 512 Hz and the off-duty factor was equal to 2.

tively. The Al content was lowered to 34% (E_g = 1.0 eV) in the emitter regions of structure *c*.

Semiconductor chips were installed into corresponding LED cases in the same way as in [15].

The *I–V* characteristics of the LEDs were of a diode type, with the cutoff voltage of 0.50 V at room temperature and 0.75 V at liquid-nitrogen temperature. The reverse leakage current was equal to 0.8 mA at a voltage of 1 V. The series resistance under forward bias was no higher than 2.4 Ω.

In Fig. 16, we show the emission spectrum of a LED in the quasi-continuous mode at room temperature; the LED was designed to operate at a wavelength of 1.94 μm. The spectrum of this emission after transmission through a 5-μm water layer is also shown in Fig. 16. The width of the emission spectrum is 0.12 μm and that of the water-absorption spectrum is 0.03 μm. The injection current was 50 mA. In Fig. 17 (curve *1*), we show the emission spectrum of a LED that was designed for a wavelength of 2.35 μm and operated under the continuous supply mode, injection current of 50 mA, and at room temperature. The emission-spectrum width is 0.22 μm. The spectrum of absorption of the LED emission by methane at atmospheric pressure was measured under the same conditions and is also shown in Fig. 17 (curve *2*).

As a result of using the optimal values of charge-carrier concentration and active-region thickness (see [6]) and, also, other means for structure optimization for practical implementation, we attained larger values of the external quantum yield for the LEDs designed for the wavelengths of 1.94 and 2.35 μm. A continuous optical power of 3.7 mW and peak power of 90 mW were obtained at room temperature.

Studies of the three types of LEDs designed for emission in the region of 2.35 μm (Fig. 15) made it possible to reveal the dependence of the optical-power characteristics on the parameters of the emitter layers (Fig. 18). Incorporation of an additional wide-gap AlGaAsSb emitter on both sides of the active region (a symmetric structure) brought about an increase in the external quantum yield from 1.25% (for a nonsymmetric structure with a type II heteroboundary [6]) to 1.75% (Fig. 15, structure *c*) [17]. A further increase in the height of the heterobarriers (Fig. 15, structures *a*, *b*) made it possible to increase the efficiency of radiative recombination to 2–2.5%. The structures grown on an *n*-type substrate (Fig. 15, structure *b*) were found to be

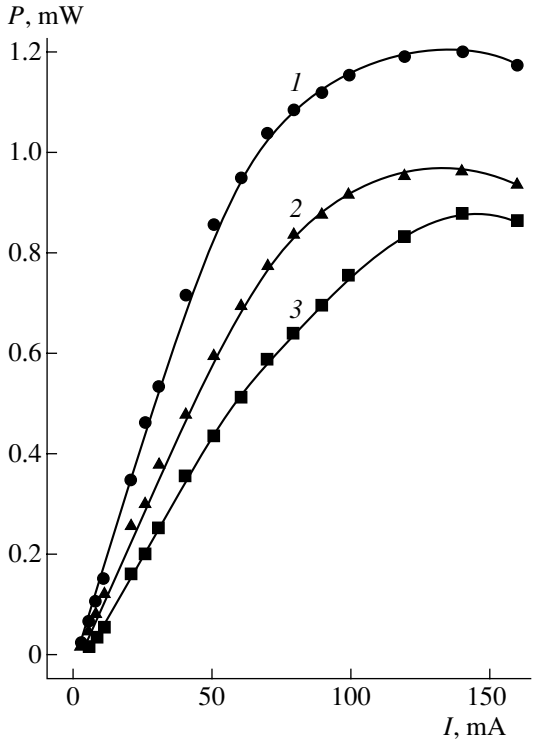

Fig. 18. Dependences of the pulsed optical power on the amplitude of current at $T = 300$ K. Curves (*1*–*3*) correspond to samples *a*, *b*, and *c* in Fig. 15. The repetition frequency of the pulses was 500 Hz, and the off-duty factor was equal to 2.

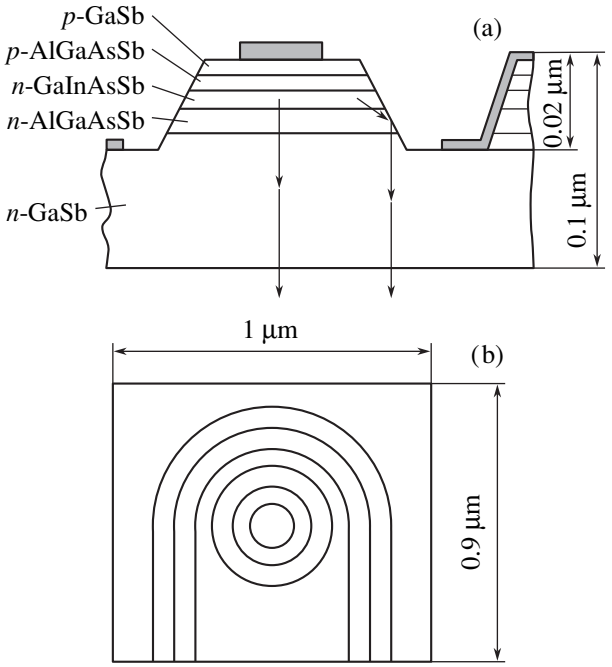

Fig. 19. Optimized structure of a light-emitting diode for obtaining the maximum optical power: (a) the arrangement of layers in the structure and (b) the view from the side of the contact pads. The arrows indicate the direction of exit of radiation from the structure.

more efficient than those grown on a *p*-type substrate (Fig. 15, structure *a*). Curve *1* in Fig. 18 corresponds to structure *b* (Fig. 15). However, for all the structures considered in [17], the transition from a superlinear current dependence of the optical power ($m > 1$) to a sublinear dependence ($m < 1$) indicates that nonradiative losses are enhanced significantly as the injection current increases. A decrease in the efficiency of radiative recombination should be related primarily to overheating of the active region due to both an increased thermal resistance for the heat transfer to the substrate through the quaternary solid solution and an increase in the injection of hot charge carriers. In addition, heavy doping of emitters is conducive to an increase in the tunneling leakage currents and reduces the density of the forward injection current into the active region. The symmetric AlGaAsSb/GaInAsSb/AlGaAsSb semiconductor structure of type *b* (Fig. 15) is found to be most attractive from the standpoint of attaining the maximum spectral density of the emission power. It is the presence of large conduction-band offsets that exceed the active-region band gap that is found to be the most important feature for the development of infrared LEDs. In the wavelength region of 2.3 μm, an amplitude optical power of 1.2 mW was attained in the continuous-wave (CW) mode at room temperature; it was shown that it is promising to use LEDs for detection of hydrocarbon molecules using absorption spectroscopy.

4. HIGH-POWER LIGHT-EMITTING DIODES OPERATING IN THE WAVELENGTH REGION OF 1.9–2.1 μm

Further refinement of the LEDs based on GaInAsSb/AlGaAsSb heterostructures and emitting in the wavelength region 1.9–2.1 μm was related to an increase in their optical power as a result of a more efficient heat removal and a decrease in the contact resistance, which made it possible to increase the external quantum yield and widen the current range in which the emission intensity is proportional to the current [18]. The structure of such a LED corresponds to the well-known flip-chip technology and is shown schematically in Fig. 19. First, photolithography combined with deep etching (into the substrate) is used to form circular mesa diodes on the grown epitaxial structures. Contacts are deposited onto the diode structure in such a way that the *n*- and *p*-type contacts are on the same surface. A view of the LED from the side of the contact pads is shown in Fig. 19b. A silicon wafer with a high thermal conductivity was used for electrical connection of the contacts. The contact layers were first deposited photolithographically onto this wafer and were then aligned and, finally, soldered to the LED contact layers by heating. Light emitted from the active region leaves the structure through the substrate (as indicated by the arrows in Fig. 19a), which is completely unobscured by the contact pads.

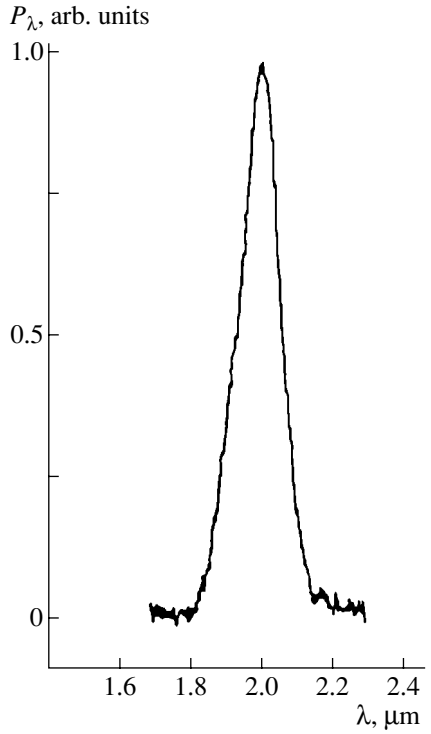

Fig. 20. The emission spectrum of LED E-21 No. 21 fed with a pulsed current with an amplitude of 100 mA, an off-duty factor equal to 2, and a repetition frequency of 400 Hz at room temperature.

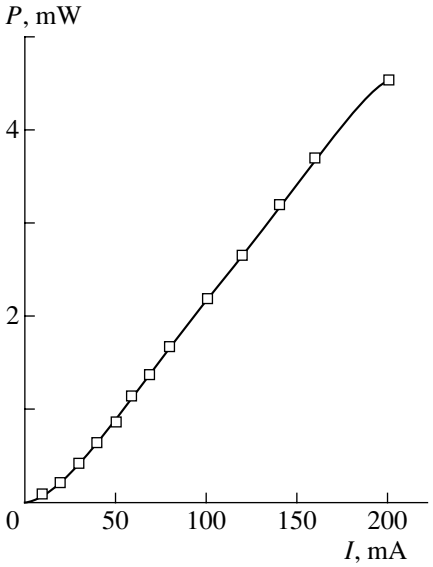

Fig. 21. Dependence of the pulsed emission power on current for LED E-41 No. 21 at room temperature (the off-duty factor was 2 and the repetition frequency equaled 400 Hz).

An epoxy compound in the shape of a lens with a height of 2–4 mm was deposited on the exterior surface of the LED; this lens ensured that the divergence of the luminous flux at half of the maximum intensity amounted to 16°–20°.

The LED structures under study were fabricated by LPE and consisted of GaInAsSb/AlGaAsSb heterostructures grown on an *n*-GaSb (100) substrate doped with Te to attain a free-electron concentration of (8–9) × 10^{17} cm^{-3}. The LEDs' structure (Fig. 19a) included a narrow-gap active layer surrounded by wide-gap emitters. The advantage of a LED structure with two wide-gap emitters was expounded by Popov *et al.* [15]. All the grown layers were lattice-matched to the substrate. The mismatch between the lattice parameters of the substrate and the narrow-gap layer $\Delta a/a$ = (8–9) × 10^{-4} and that of the substrate and the wide-gap layer $\Delta a/a$ = 1.3 × 10^{-3}. The narrow-gap $Ga_{1-x}In_xAs_ySb_{1-y}$ layer with $x \approx 0.1$ and $y \approx 0.08$ was doped with Te to obtain a free-electron concentration of (7–8) × 10^{16} cm^{-3}. The thickness of the narrow-gap layer was 2 μm. The wide-gap layers were grown with a higher Al content than this in the corresponding layers previously studied [6, 8, 15, 16] and had the $Al_{0.64}Ga_{0.36}As_{0.44}Sb_{0.56}$ composition. The *n*-type wide-gap layer was doped with Te; as a result, the free-electron concentration in the layer was 6 × 10^{17} cm^{-3}. The *p*-type wide-gap layer was doped with Ge to obtain a free-hole concentration of ~10^{18} cm^{-3}. The thickness of the *n*-type layer was 1.5 μm and that of the *p*-type layer was 1.7 μm. In order to form a low-resistance contact, we coated the wide-gap *p*-type layer with a p^+-GaSb layer possessing a high concentration of free holes (~10^{19} cm^{-3}); the thickness of this coating layer was ~3 μm.

The calculated value of the band gap at room temperature is $E_g \approx 0.64$ eV in the narrow-gap region and $E_g = 1.23$ eV in the wide-gap region.

The emission spectra of the LEDs with the above parameters consisted of a single band at room temperature (Fig. 20). The emission wavelength at the band peak depended almost linearly on the solid-solution composition in the active region and varied from 1.9 to 2.1 μm. The width of the emission band was 0.17 μm at a current of 50 mA and 0.18 μm at a current of 200 mA. As the current was increased from 50 to 200 mA, the peak of the emission band shifted to longer wavelengths by 0.015–0.017 μm.

The current dependence of the pulsed optical-emission power for a duty factor of 0.5 for the pulse train and repetition frequency of 400 Hz for the LEDs studied is shown in Fig. 21. The maximum value of optical power P (4.6 mW) was obtained at the current I = 200 mA. In the current range 50–200 mA, the dependence $P(I)$ is nearly linear. At higher currents, the measurements were carried out using a pulsed power supply (Fig. 22); the pulse width was no larger than several microseconds. In this case (see Fig. 22), the dependence $P(I)$ was almost linear at currents up to ~520 mA. At higher currents, the dependence becomes sublinear for all three pulse widths τ_p represented in Fig. 22 (τ_p = 5, 10, and 20 μs). The maximum attained peak power of

emission was 190 mW at a current of 1.4 A, pulse width of 5 μs, and repetition frequency of 1 kHz. The external quantum yield for the LEDs studied was equal to ~4% at room temperature.

Measurements of the *I–V* characteristics showed that the LEDs had a cutoff voltage of 0.5 V and series resistance of 2.2–2.8 Ω at room temperature.

Thus, we managed to obtain a high optical power for LEDs designed for the wavelength range 1.8–2.2 μm. Compared to the LEDs that we previously fabricated, these LEDs have two refinements. First, they incorporate emitters with a wider band gap and Al content of ~64%, which is unprecedentedly high for AlGaAsSb layers grown by LPE. Second, the design of these LEDs makes it possible to position the active region closer to the device case, which acts as a heat sink, and let out the emission that is not screened by the contact through the substrate. The values of the series resistance in the LEDs indicate that, despite an increase in the band gap of the emitter layers, the use of a heavily doped p^+-type layer in the near-contact region was found to be sufficient for preventing the series resistance from increasing with respect to its value in the LEDs fabricated in [16]. Nevertheless, heating of the active region in the LEDs studied is noticeable, since the spectral band shifts by 10% of its width to longer wavelengths as the current increases from 50 to 200 mA in the quasi-continuous mode with a duty factor of 0.5 for the pulse train. However, this heating is not intense because the current dependence of the power remains virtually linear (Fig. 21). This linearity is retained even if the current is increased to ~520 mA in the pulsed mode when microsecond pulses are used at a period-to-pulse duration ratio ≥50 (Fig. 22). The appearance of a sublinear dependence $P(I)$ as the current is increased further could be caused by two factors: either by heating of the active region or by an increase in the current losses as a result of Auger recombination. If we represent the dependence $P(I)$ in the form of $P \propto I^m$, m should be equal to 2/3 in the case where the sublinear behavior is governed by Auger recombination. An analysis showed that, in the pulsed mode at $I > 520$ mA, $m = 2/3$ at $\tau_p = 5$ μs, $m = 11/21$ at $\tau_p = 10$ μs, and $m = 2/7$ at $\tau_p = 20$ μs. This means that the sublinear character of the dependence $P(I)$ is governed by Auger recombination if the pulse duration is 5 μs. A decrease in the pulse duration does not result in extension of the linear portion of the dependence $P(I)$ to the current region $I > 520$ mA. If the pulse widths are $\tau_p = 10$ and 20 μs, the sublinear character of the dependence $P(I)$ is caused not only by Auger recombination but also by heating.

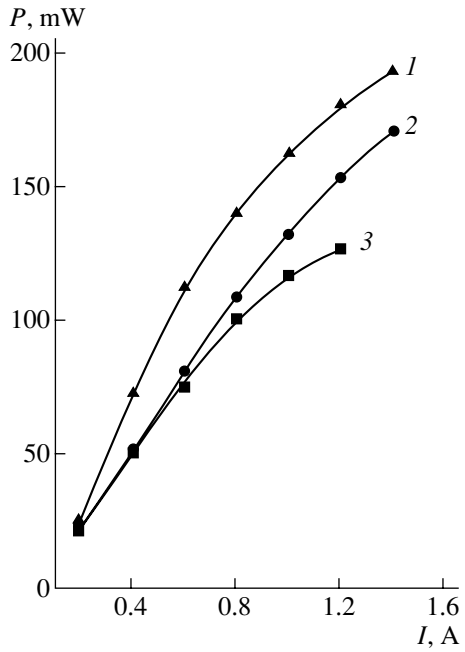

Fig. 22. Dependence of the pulsed emission power on current for LED E-41 No. 21 at room temperature, the repetition frequency of the current pulses was 1 kHz, and the duration of pulses τ_p = (*1*) 5, (*2*) 10, and (*3*) 20 μs.

5. HIGH-EFFICIENCY LIGHT-EMITTING DIODES OPERATING IN THE WAVELENGTH RANGE 3.4–4.4 μm AT ROOM TEMPERATURE

The above-considered advantages of heterostructures based on GaInAsSb/AlGaAsSb and designed for the wavelength range 1.7–2.5 μm allowed us to turn our attention to the development of spontaneous-emission sources formed on GaSb substrates and designed for operation at longer wavelengths (3–5 μm) [19]. LEDs based on InAsSb/InAsSbP heterostructures grown on an InAs substrate have typically been fabricated for this spectral region. A common disadvantage of structures with a ternary solid solution consists in the fact that the epitaxial layers and the substrate, made of a III–V compound, are lattice-mismatched. In addition, the small difference between the band gaps of InAs and InAsSb brings about a small barrier height, which, however, is large enough for efficient confinement of nonequilibrium charge carriers in the active region. Other consequences of the above small difference are intense absorption and an appreciable impact ionization due to the effect of the energy band split-off as a result of spin–orbit interaction. Considering the three above characteristics, AlGaAsSb/GaInAsSb/AlGaAsSb heterostructures offer some advantages over InAsSb/InAsSbP heterostructures. Fabricated AlGaAsSb/GaInAsSb/AlGaAsSb structures emitting in the wavelength range 3–5 μm [19] exhibited a room-temperature optical-emission power and external quantum yield (~1%) that exceeded the corresponding characteristics of the well-known InAsSb/InAsSbP heterostructure grown on an InAs substrate by a factor of 3 [20]. Structures based on AlGaAsSb/GaInAsSb were formed by LPE on a *p*-GaSb (100) substrate and incorporated four epitaxial layers: *p*-AlGaAsSb/*n*-GaInAsSb/*n*-AlGaAsSb/*n*-GaSb. The composition of the narrow-gap GaInAsSb layer corresponded to the middle of the spectral range under

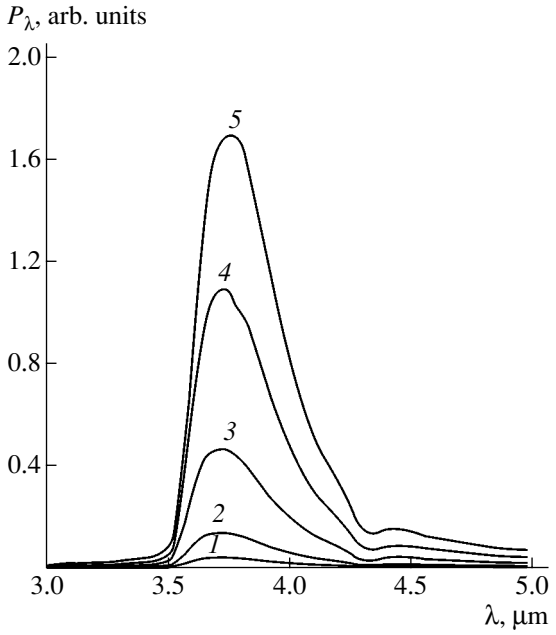

Fig. 23. The emission spectra of LED 9602 at room temperature in the pulsed mode with a pulse duration of 20 μs and an off-duty factor of 49 at the current amplitudes I = (*1*) 200, (*2*) 300, (*3*) 500, (*4*) 700, and (*5*) 1000 mA.

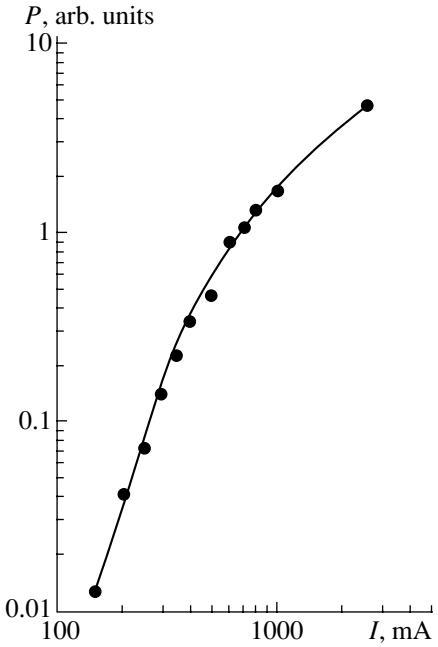

Fig. 24. Dependence of the emission intensity of LED 9602 on current with a pulse duration of 20 μs and off-duty factor of 49 at room temperature.

consideration. The *p*-GaSb substrate was nominally undoped and had an equilibrium-hole concentration of (1–2) × 10^{17} cm^{-3}. The wide-gap *n*- and *p*-type layers were grown with an Al content that was higher than the Ga content; the *p*-type layer was nominally undoped, while the *n*-type layer was doped with Te. The wide-gap layers were 1.5-μm thick. The narrow-gap $Ga_{0.066}In_{0.934}As_{0.83}Sb_{0.17}$ layer of the active region had a thickness of 1.5 μm, was nominally undoped, and had a free-electron concentration of 10^{18} cm^{-3}. The *n*-GaSb contact layer was heavily doped with Te. The specific feature of the structure consisted in the fact that it was basically lattice-matched to the GaSb substrate. The measured value of relative mismatch of the lattice constants $\Delta a/a$ was equal to 2×10^{-4} to within the experimental accuracy.

The sample was installed into a LED case that included a parabolic reflector. The LED had the shape of a parallelepiped. The *p*–*n* junction was square-shaped and had an area of 0.5 × 0.5 mm^2. The parallelepiped height was 0.1 mm. The light was emitted in the reflector direction and was transmitted mainly through the side faces of the parallelepiped.

The spectral and emission–current characteristics of the LEDs were measured at room temperature in the pulsed mode. The emission spectra typically consisted of a single band (Fig. 23). The wavelength corresponding to the intensity maximum was equal to λ_{max} = 3.7–3.8 μm. The absorption line of CO_2 gas (λ = 4.27 μm), contained in air, is perceptible in the long-wavelength wing of the band. The energy corresponding to the peak in the emission spectrum was found to be larger (by 20–30 meV) than the band gap of the narrow-gap material at room temperature, which may indicate that band-to-band recombination of nonequilibrium charge carriers dominates over impurity-related and interfacial recombination in the structures studied. The large difference between the energy corresponding to the emission-band peak and the band gap can be attributed to a high concentration of nonequilibrium electrons in the active region. The short-wavelength wing of the emission band was steeper than the long-wavelength wing. The band shape was nearly independent of the current. The gentle long-wavelength slope of the band indicates that there are tails of the density of states in the band gap; however, these tails do not affect the spectral position of the band peak. It is worth noting that the band width at the half-maximum is equal to 30–35 meV, which is a factor of 1.5–2 smaller than the band width typical of LEDs at room temperature. This narrowing of the band may be caused by absorption of short-wavelength radiation in the active region itself, since the emission towards the parabolic reflector traverses a distance of several tens of micrometers in the active region. In this situation, the short-wavelength radiation is absorbed owing to band-to-band transitions with subsequent partial reradiation. The latter effect is conducive to superlinear increase in the emission intensity with current (Fig. 24). Apparently, the main cause of the superlinear increase in the emission intensity at low currents (<0.5 A) is occupation of deep levels. At currents I > 0.5 A (>200 A/cm^2), the deep levels become almost

completely occupied. The current range from 0.5 to 2.5 A corresponds to a high external quantum yield of emission. The pulsed emission power P is governed by the main band and increases superlinearly as the current I increases (Fig. 24). In the current dependence of the power $P \propto I^m$, the exponent m decreases from $m = 3$ at a current of 150 mA to $m = 1.2$ at a current of 2500 mA. The pulsed emission power (the average power measured using a Nova instrument and multiplied by the off-duty factor) is equal to 3.2 mW at a pulsed current of 1 A with a pulse duration of 20 μs and duty factor of 1/49. In this situation, the external quantum yield of emission is equal to 1%, which exceeds, at least threefold, the corresponding yield for a conventional InAsSb/InAsSbP heterostructure grown on an InAs substrate.

6. HIGH-EFFICIENCY LIGHT-EMITTING DIODES OPERATING IN THE WAVELENGTH RANGE 1.6–2.4 μm AT ROOM TEMPERATURE

In order to solve the problem of developing high-quality LEDs, we continued our efforts concerning the refinement of LEDs based on GaInAsSb/AlGaAsSb heterostructures that are grown on a GaSb substrate and emit in the wavelength range 1.6–2.4 μm. As a result, we fabricated LEDs that completely span the above range with a spectral step of 0.1 μm [21]. In the LED structures designed for the emission wavelengths 2.05, 2.15, 2.25, and 2.35 μm, the emission was extracted through the substrate, since the GaSb absorption edge is located at $\lambda = 1.72$ μm. Absorption in the substrate at the wavelengths of 2–2.35 μm is caused only by free charge carriers. In LEDs operating at shorter wavelengths (1.65–1.75 μm), the radiation is almost completely absorbed in the GaSb substrate. Therefore, in these LEDs, we used heterostructures with two-sided wide-gap confinement and extracted the emission through the confining p-type layer rather than through the substrate. In order to increase the quantum yield of emission, we had to reduce the deleterious effect of deep levels of a doubly charged structural defect in the crystal lattice. Previous studies of GaAs and quaternary GaInAsSb alloys have shown [22] that both a nominally undoped GaSb epitaxial layer grown by LPE and bulk GaSb grown by the Czochralski and Bridgman–Stockbarger methods invariably exhibit p-type conductivity. The hole concentration in the layer equals $p = (1–2) \times 10^{17}$ cm^{-3} at $T = 300$ K. It was also established that there existed three acceptor levels: a shallow level with the activation energy $E_1 = 11–17$ meV and two deep levels with the energies $E_2 = 30–35$ meV and $E_3 = 70–90$ meV; these deep levels are assigned to a structural crystal-lattice defect that consists of a gallium vacancy and a gallium atom at an antimony site ($V_{Ga}Ga_{Sb}$). The concentration of these structural defects governs the concentration of holes and their mobility in GaSb. As gallium atoms are replaced by indium atoms in the lattice of quaternary alloys, the probability of formation of structural defects decreases and the concentration of deep acceptor levels is lowered. In all the cases of growing LED structures, we used n-GaSb substrates with a (100) orientation and an electron concentration of 2×10^{17} cm^{-3}. The concentration of intrinsic structural defects related to the stoichiometry depends on the ratio between the content of Sb and Ga atoms in the solution–melt. Voronina *et al.* [22] suggested a method for changing this ratio by introducing a certain amount of Pb into the melt as a neutral solvent. First, using Pb as a neutral solvent, we grew a buffer n-GaSb layer on an n-GaSb substrate; this layer was (6–10) μm thick and had its concentration of intrinsic defects reduced by an order of magnitude. An active $Ga_{0.95}In_{0.05}AsSb$ layer was then grown over the buffer layer; the active layer had the thickness of 1.5 μm and was doped with Te to obtain the electron concentration $n \sim 10^{17}$ cm^{-3}. The LED structure also included a p-$Al_{0.34}Ga_{0.66}AsSb$ layer (3 μm) as a wide-gap barrier for electrons and a contact GaSb layer (0.5 μm) doped with acceptors to obtain the hole concentration $p \sim 10^{19}$ cm^{-3}.

The LED structure with a thick buffer layer had a better internal quantum yield and integrated output optical power than the structure without a buffer layer corresponding to 13% and a factor of 2, respectively. The spectrum width was 0.18 μm for a structure without a buffer layer and 0.13 μm for a structure with a thick buffer layer. This observation indicates that we managed not only to decrease the concentrations of deep and shallow acceptors in the active region but also to reduce the tails of the density of states responsible for the spectrum broadening. The increase in the spectrum width as the current increases in excess of 3 A in the pulsed mode is most likely caused by the fact that the process of radiative recombination involves charge carriers not only near the conduction-band bottom and the valence-band top but also carriers with higher energies since, the current density is as high as 111 A/cm^2 at $I = 10$ A. The maximum internal quantum yield was as high as 82% at a current of 2 A (with the off-duty factor $Q = 1000$).

In the actual structures, the ability of LEDs to operate at high currents is limited not only by an increase in the role of Auger recombination but also by the probability of a pinch breakdown or overheating as a result of local inhomogeneities in the crystal or the chip surface. The high quality of the structures made it possible to appreciably increase the operating power of the LEDs by increasing the currents at which they operate stably. For example, we obtained the optical power $P = 1.66$ mW in the quasi-steady mode ($Q = 2$) at a current of 400 mA and $P = 60$ mW in the pulsed mode ($Q = 100$, $\tau_p = 200$ ns) at a current of 10 A.

In order to attain a higher emission power, we accomplished yet another modification of the LED structure optimized for the water-absorption line at 1.95 μm. We first used the same technology to grow a buffer layer with a thickness of 10 μm. A 0.5-μm-thick

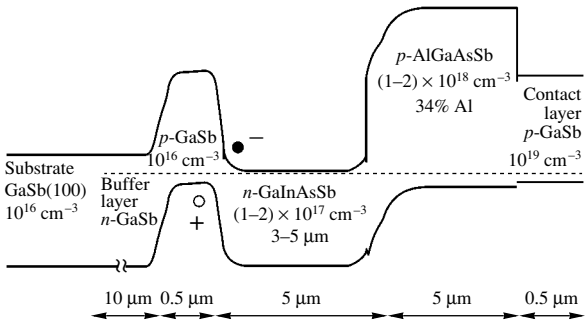

Fig. 25. The energy diagram of thyristor-type LED structure E-816, designed for operation at a wavelength of 1.95 μm.

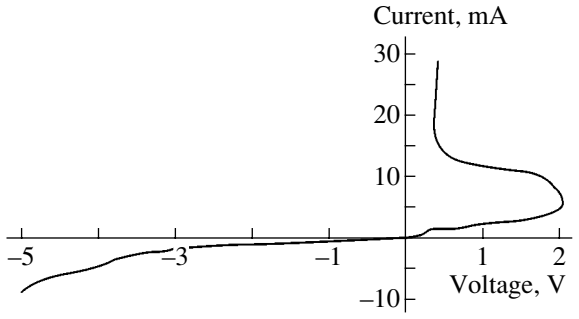

Fig. 26. The current–voltage characteristic of thyristor-type LED structure E-816 at room temperature.

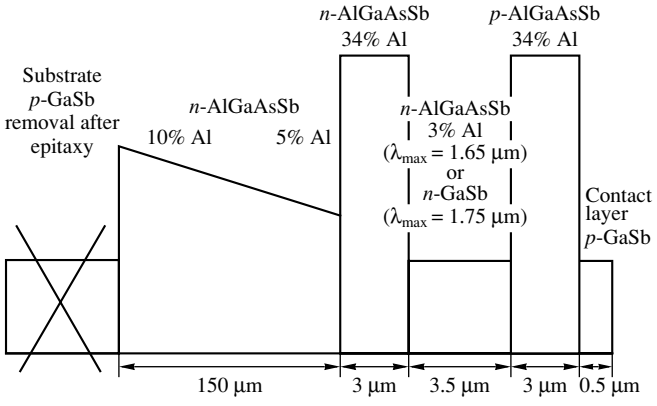

Fig. 27. Energy diagram of LED structures E-832 and E-833, emitting at wavelengths of 1.75 and 1.6 μm, respectively. The structures include a thick wide-gap buffer layer with gradient of composition.

p-GaSb layer was then incorporated between the buffer and active layers (Fig. 25). As a result, we obtained an *n–p–n–p* structure with an *I–V* characteristic that had a shape typical of thyristor structures (Fig. 26). The voltage for switching on the structure was equal to 1.9 V. In the ON state, the voltage decreased abruptly to 0.45 V. As is well known from the theory of thyristor structures, the height of a reverse-connected barrier decreases drastically in the course of switching as a result of the charge of holes and electrons (positive charge in the *p*-type material and negative charge in the *n*-type material) accumulated on both sides of the boundary (in this case, a type II heteroboundary between *p*-GaSb and *n*-GaInAsSb).

In the LEDs with a thyristor structure, we obtained a maximum internal quantum yield of 52% in the quasi-steady mode at a current of 250 mA and the corresponding yield of 77% at a current of 3 A in the pulsed mode ($Q = 1000$). The maximum pulsed optical power was 2.5 mW at the off-duty factor $Q = 2$ and 71 mW at $Q = 1000$.

We used yet another method for fabricating high-efficiency structures that emit at wavelengths of 1.65 and 1.75 μm [21]. Since (as was mentioned above) the emission of these LEDs is almost completely absorbed in the GaSb substrate, the GaSb substrate was removed after the epitaxial layers of the LED heterostructure had been grown (Fig. 27). This method has previously been used [23–27] in fabrication of LEDs based on binary heterostructures in an AlAs–GaAs system. For the substrate to be removed, the structure should have a fairly large thickness (50–100 μm). In the case under consideration, GaSb was first overgrown with a thick (150 μm) *n*-AlGaAsSb layer with a wider band gap and an Al content that decreased gradually from 10% at the boundary with the GaSb substrate to 5% at the boundary with the wide-gap *n*-AlGaAsSb emitter layer. This thick layer had a much higher structural quality than the GaSb substrate. Correspondingly, the active region was free of deep acceptor levels related to defects in the crystal structure.

The emission spectra of the LEDs fabricated by the above-described method consisted of a single band at all the currents under consideration. The width of the emission band was 0.13–0.14 eV in the quasi-steady mode. The internal quantum yield was as high as 60%. A broadening of the spectrum was observed at currents higher than 4 A in the mode of short pulses. It was assumed that the increase in the spectrum width is related to the involvement of charge carriers with a relatively high energy in the process of radiative recombination. The integrated optical power in the mode of short pulses (an off-duty factor equal to 1000) was equal to 140–170 mW. Under these conditions, the internal quantum yield of emission was as high as 100%. In the current range of 1–5 A, the radiative-recombination rate was much higher than the rate of nonradiative processes according to the Shockley–Read–Hall model and the rate of Auger recombination.

7. AN INCREASE IN THE EXTERNAL QUANTUM YIELD OF EMISSION FROM LIGHT-EMITTING DIODES BY CHEMICAL FACETING OF THEIR SUBSTRATE PART

Our further efforts concerning the fabrication of LEDs grown on a GaSb substrate and emitting in the

mid-infrared region of the spectrum (1.6–2.4 μm) were directed at an increase in the emittance of a LED chip by shaping it so that extraction of radiation became more efficient.

A large refractive index of electroluminescent semiconductors ($n \approx 4$) makes the exit of emission from the LED crystal bulk difficult because the angle of internal total reflection with respect to the normal to the surface is equal to n^{-1} (in radians). In a crystal with the shape of a parallelepiped, only 8% of the radiation can cross six facets at the first incidence on these facets.

Various methods for texturing a semiconductor surface (forming a system of depressions) in order to change the angle of reflection back into the crystal bulk have previously been discussed [27–29]. Using these methods, after several passages within the semiconductor, radiation can be incident on the surface at an angle that is smaller than the angle of the total internal reflection and, thus, can partially exit from the sample. Using these methods, one can increase the fraction of outgoing radiation in the visible and near-infrared spectral regions to ~30% [28, 29]. In the mid-infrared region of the spectrum, the multipass approach does not yield good results, since the radiation absorption by free charge carriers is proportional to $\propto\lambda^2$. A decrease in the crystal size in order to reduce the propagation distance of radiation in the crystal leads to degradation of the heat removal and to a decrease in the LED power. However, for the LEDs corresponding to the mid-infrared region, one can expect an increase in the yield of emission from the crystal by making the shape of this crystal close to spherical, which ensures the exit of radiation after its first incidence on the exterior surface [30]. To this end, chemical faceting was used to shape the near-substrate part of the LED structure into a truncated cone–pyramid figure positioned on a pedestal that contained the epitaxial part. Installation of such a crystal on the crystal holder with the epitaxial part facing downwards ensures higher operating currents.

The LED structures under study were formed by LPE on 400-μm-thick *n*-GaSb substrates oriented in the (100) crystallographic plane. The substrates were doped with Te in order to obain an electron concentration of 8×10^{17} cm^{-3}. First, an active undoped GaSb layer, with the addition of the rare-earth element gadolinium in order to improve to crystalline quality of the layer, was grown. The grown layer was 1.5 μm thick and had the *p*-type conductivity that is inherent to undoped GaSb layers. The active region was the same in all the structures. We then grew a confining *p*-$Ga_{0.66}Al_{0.34}SbAs$ layer that had a wider band gap, was doped with Ge to generate a hole concentration of 1×10^{18} cm^{-3}, and had a thickness of 3.5 μm. A contact *p*-GaSb layer with a hole concentration of 8×10^{18} cm^{-3} was grown over the confining layer. Finally, the wafer thickness was reduced to 220 μm by lapping and polishing.

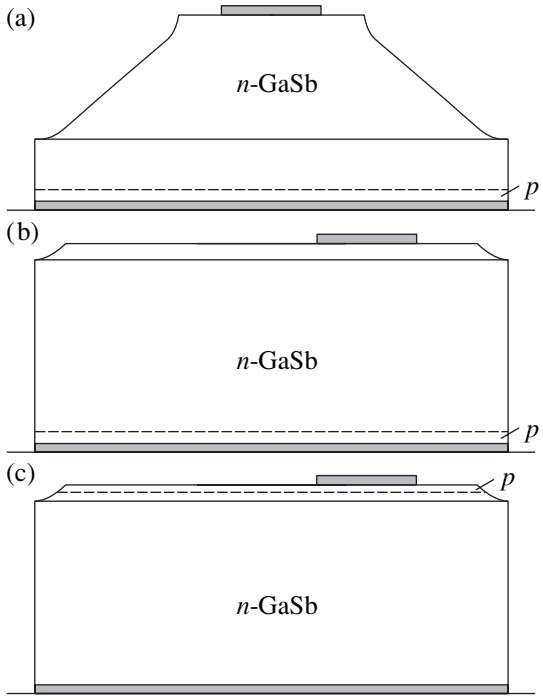

Fig. 28. Three types of structures of LED crystals: structure (a), with conical–pyramidal substrate part; structure (b), in the shape of a parallelepiped with its epitaxial part soldered to the crystal holder; and structure (c), shaped like a parallelepiped with the substrate part soldered to the crystal holder. The dashed line indicates the *p*–*n* junction that represents the boundary between the *n*-GaSb substrate and the epitaxial *p*-type part of the structures.

Chemical faceting was carried out using contact photolithography in three stages. In the first stage of the photolithography, we produced a pattern in the form of squares with a side of 480 μm and a step of 500 μm on the near-substrate side for subsequent separation of the wafer into individual chips. The boundary channels were etched off to a depth of 70 μm; the width of the channels was 160 μm. In the second stage, a pattern in the form of a circle with a diameter of 300 μm was formed in the center of open squares. After etching these circles in the same way as in the case of the squares, we obtained a figure with a height of 140 μm that was pyramid-shaped at its base and in the form of a truncated cone at its apex, with the upper area having a diameter of 200 μm (Fig. 28a). In the third stage, a window for an ohmic contact with a diameter of 100 μm was formed photolithographically at the center of the upper pad.

Contact layers were formed by using a VUP-4 system for consecutive deposition of Cr, Au + Te alloy, and Au on the *n*-type region and Cr, Au + Ge alloy, and Au on the *p*-type region. The contact layers were then fused to the material for 1 min at 250°C. The wafers were further separated into individual chips by cleaving. Each chip was mounted by its epitaxial-layer side in a TO-18 LED crystal holder with a flat table.

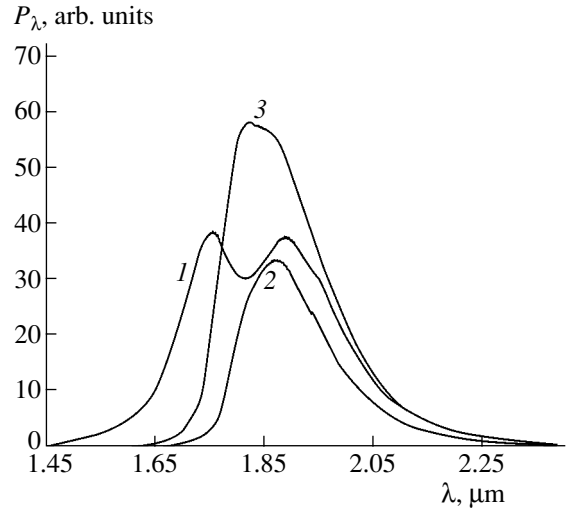

Fig. 29. The emission spectra at a current of 150 mA for LEDs of three configurations: (*1*) parallelepiped with the substrate part soldered to the crystal holder (Fig. 28c); (*2*) parallelepiped with the epitaxial part soldered to the crystal holder (Fig. 28b); and (*3*) with a conical–pyramidal deeply etched substrate part (Fig. 28a).

In order to compare these LEDs with the LEDs produced by deep etching, we fabricated devices with standard geometric parameters (Figs. 28b, 28c). In this case, the above-mentioned squares were formed and channels were etched in the first stage to a depth of 15 μm (in order to obtain the separating grid) on the *n*-type side of one wafer (Fig. 28b) and on the *p*-type side of the other wafer (Fig. 28c). After a repeat photolithography treatment, circular contacts with a diameter of 100 μm were formed on this side. The ohmic contact to the opposite side was formed over the entire area. After dividing the wafer into separate chips, the latter were installed with their continuous contact close to the crystal holder.

First, we determined how the emission spectrum for the deeply etched pyramidal crystals differs from that for the parallelepiped-shaped crystals.

The spectra of the original recombination emission are distorted to the least extent in the crystals mounted with their substrate part on the crystal holder (i.e., with the epitaxial emitting part facing outwards) (Fig. 28c). Emission exits from these crystals mainly through the wide-gap epitaxial layer. These crystals emit a spectral doublet with peaks at the wavelengths of 1.76 μm (0.705 eV) and 1.9 μm (0.65 eV) and band widths of 0.06 and 0.07 eV, respectively (Fig. 29, curve *1*). The differences between the band gaps and the peaks of the short- and long-wavelength bands are equal to the ionization energy of a single-charged acceptor (0.02 eV) and (approximately) to its fourfold value, respectively. This observation suggests that doubly charged acceptors are involved in the generation of radiation. As was already mentioned, the doubly charged acceptors are formed when Ga atoms occupy the Sb sites in the crystal lattice. Such a process is characteristic of GaSb, which is noted for its large deviation from stoichiometry. The presence of other acceptors was unlikely since they were not introduced intentionally and the epitaxial layer was purified using gadolinium.

A similar sample with its epitaxial layer soldered to the crystal holder emits a single band (Fig. 29, curve *2*) with almost the same parameters as those of the long-wavelength band of the doublet emitted by the crystal whose substrate part was soldered to the crystal holder. The peak of this band is located at a wavelength of 1.87 μm (0.66 eV); the width of the band is 0.06 eV. The presence of virtually only a single long-wavelength band in the emission spectrum in the case where the epitaxial-layer side of the LED crystal is soldered to the crystal holder indicates that the short-wavelength emission is absorbed strongly in the bulk of the GaSb substrate. Evidently, this absorption is mainly caused by quasi-interband transitions between the tails of allowed energy bands; these tails are caused by randomly located doubly charged acceptors. The absorption coefficient for the long-wavelength emission band is much smaller. Only the radiation generated near the side faces of the crystal has a short optical path; however, the contribution of this radiation is small.

The emission spectrum of the LEDs obtained by chemical faceting of the substrate part features a single broad band with a nearly flat top in the region of the wavelength 1.83 μm (0.66 eV) and a width of 0.08 eV (Fig. 29, curve *3*) at a current of 150 mA. By representing this spectrum as a superposition of two bands, we reveal a short-wavelength band that is found to be only a factor of 2 less intense than the long-wavelength band. This result indicates that deep etching shortens the optical path of radiation.

The current dependence of the emission intensity for a deeply etched pyramidal crystal (Fig. 30, curve *3*) is steeper (due to the shortened optical path) than that for a LED shaped as a parallelepiped and also soldered by its epitaxial-layer side to the crystal holder (Fig. 30, curve *2*). However, since the optical path for a deeply etched pyramidal crystal is much larger than that for a LED shaped as a parallelepiped and soldered by its substrate to the crystal holder (Fig. 30, curve *1*), the pyramidal LED ranks below the parallelepiped-shaped LED at low currents (<200 mA). At currents of 200–250 mA and higher, the emission intensity of the parallelepiped-shaped LEDs whose substrate is soldered to the crystal holder ceases to increase with current and their emission intensity becomes lower than that of the LEDs with a deeply etched substrate part. The observed tendencies can be explained in the following way. In the LEDs with an emitting layer close to the exterior surface at which the ohmic contact is located, an unwanted phenomenon is observed; i.e., the emission is concentrated under the contact, which appreciably reduces the differential efficiency as the current is increased and increases the current density under the contact. As a result,

the superlinear portion of the emission–current characteristic ceases to exist at low currents. The share of nonradiative Auger recombination increases as well owing to an increase in the concentration of nonequilibrium charge carriers. The emission efficiency becomes lower.

The approximate formula that relates the recombination current I_c concentrated under the circular contact with a much smaller area than the emitting-layer area to the current I_b outside the contact is written as

$$I_b = 4\pi I_\sigma(1 + \sqrt{1 + I_c/4\pi I_\sigma}), \quad (5)$$

where $I_\sigma = \sigma b\beta kT/e$, σ is the average electrical conductivity of the *p*-type region, *b* the thickness of this region, and β is a factor that indicates either the monomolecular ($\beta = 1$) or bimolecular ($\beta = 0.5$) character of the recombination process. Assuming that $\beta = 1$, $kT/e = 0.0256$ V, $b = 5$ μm, and $\sigma = 200\ \Omega^{-1}\ \text{cm}^{-1}$, we obtain $I_\sigma = 2.5$ mA. According to formula (5), for these transport parameters of the epitaxial layer, the concentration of current under the contact sets in at a current of 100 mA, in which case 20% of the current is found to be under the contact; at a current of 250 mA, half of the current is found to be under the contact. This inference is consistent with experimental data. At low currents, $I < 8\pi I_\sigma = 64$ mA, in which case the spreading of the current is total, formula (5) is inapplicable and the ratio of the currents under and outside the contact is equal to the ratio between the area of the contact and the area of the remaining (uncovered by the contact) surface of the GaSb contact layer. In the case under consideration, this ratio is equal to 3%. The phenomenon of emission concentration under the contact makes a small-area ohmic contact to a thin *p*-type region undesirable.

Heat removal was considered for the fabricated and studied LEDs installed in a TO-18 crystal holder; this heat removal is controlled by the thermal resistances of the crystal and crystal holder used.

If the heat is released uniformly in the emitting layer and the crystal is mounted on the crystal holder with the substrate facing downwards, the thermal resistance of the crystal shaped as a parallelepiped is expressed by the formula

$$R_T = \frac{H}{S\chi}, \quad (6)$$

where *H* is height of the parallelepiped, *S* is its area, and χ is the thermal conductivity. At $H = 220$ μm, $S = 0.0025\ \text{cm}^2$, and $\chi = 0.336$ W/(cm K), we obtain $R_T = 26$ K/W. Concentration of recombination under the contact brings about a severalfold increase in the thermal resistance.

Heat is released in the emitting layer mainly as a result of nonradiative recombination; therefore, thermal resistance should be calculated using formula (6). If the internal quantum yield of emission is high, heat is mainly released as a result of emission absorption in the semiconductor bulk. If the emission is absorbed uniformly, the thermal resistance becomes a factor of 2 lower than that given by formula (6), irrespective of the emitting-layer position. This circumstance provides a wide margin for choosing the shape of the LED crystal.

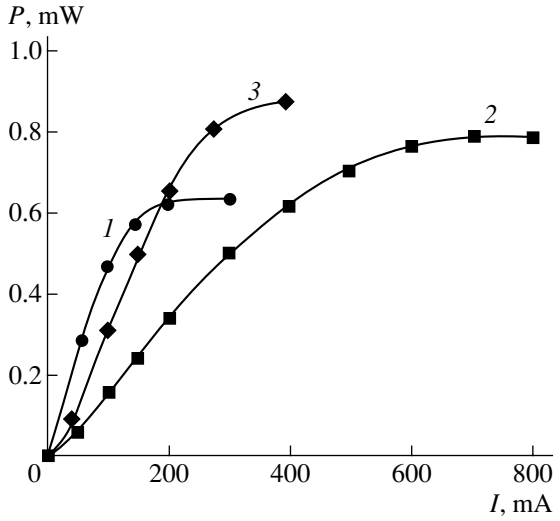

Fig. 30. Dependences of the pulsed emission power on current for three LEDs with different configurations (see Fig. 28). The repetition frequency of the current pulses was 512 Hz and the off-duty factor was 2. The numbers next to the curves correspond to those in Fig. 29.

The thermal resistance of the crystal holder we used (TO-18, gold-plated, and Au layer thickness of ~0.2 μm) is mainly determined by the nickel table, which has a thickness $\delta = 0.02$ cm and diameter $D = 0.4$ cm. This resistance can be expressed by the approximate formula

$$R_H = \frac{1}{2\pi\chi\delta}\ln\frac{\pi D}{l}, \quad (7)$$

where *l* is the crystal perimeter. At $l = 0.2$ cm and the Ni thermal conductivity $\chi = 0.59$ W/(cm K), we obtain $R_H = 25$ K/W, i.e., approximately the same value as is yielded by formula (6) for the semiconductor crystal. The thermal conductivity of the thin Au coating (0.2 μm) can be disregarded. The above estimate is indicative of the important role of the crystal-holder thermal resistance in the shift of the long-wavelength band with an increase in current in the LED crystals of pyramidal–conical and parallelepiped-like shape at high currents (>200 mA) (Figs. 31–33). The shift of the short-wavelength band to longer wavelengths observed even at low currents is attributed to concentration of emission under the contact; this concentration is accompanied by a corresponding increase in the optical path of radiation.

Deep etching of the substrate part of the wafer so that the LED crystal acquires a pyramidal–conical shape and, also, installation of the crystal in a case with the epitaxial-layer side in contact with the crystal holder ensure a higher yield of long-wavelength emis-

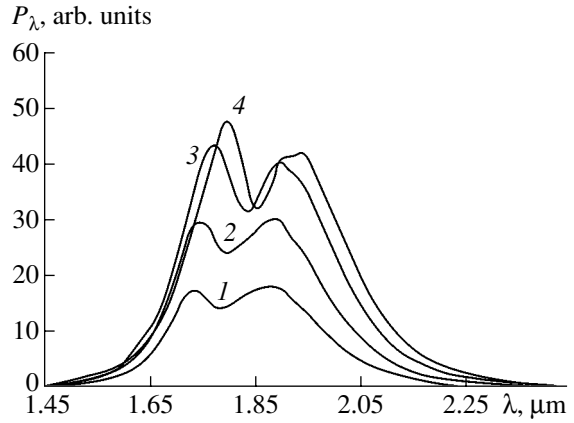

Fig. 31. The emission spectra of a LED shaped like a parallelepiped with the substrate part soldered to the crystal holder (Fig. 28c) at the currents I = (*1*) 50, (*2*) 100, (*3*) 200, and (*4*) 300 mA.

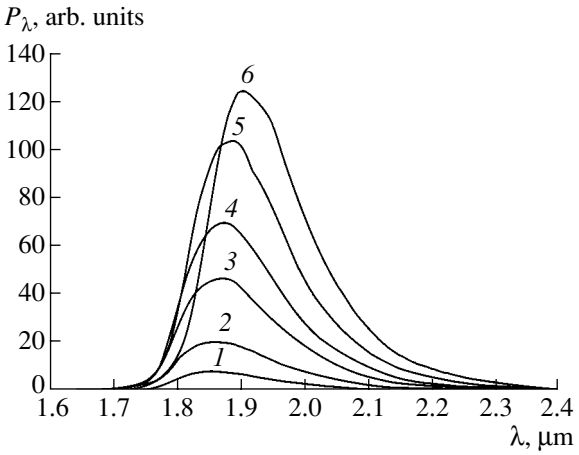

Fig. 32. The emission spectra of a LED shaped like a parallelepiped with the epitaxial part soldered to the crystal holder (Fig. 28b) at the currents I = (*1*) 50, (*2*) 100, (*3*) 200, (*4*) 300, (*5*) 500, and (*6*) 800 mA.

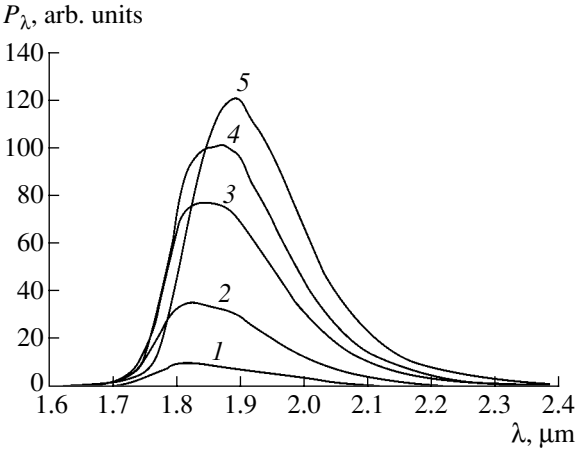

Fig. 33. The emission spectra of a LED with a conical–pyramidal deeply etched substrate part (Fig. 28a) at the currents I = (*1*) 40, (*2*) 100, (*3*) 200, (*4*) 275, and (*5*) 395 mA.

sion than in the case of the standard configuration, especially at high currents.

A weak angular dependence of emission (Fig. 34) is characteristic of the crystals with a deeply etched substrate part and whose epitaxial layer is soldered to the crystal holder (Fig. 28a). As the angle θ increases from 0° to 70°–80°, the emission intensity first increases by 10–15% and then decreases abruptly to zero at 110°; i.e., a plateau is virtually observed in the range of angles from –80° to +80°, with the result that the emission is found to be nondirectional. This phenomenon can be accounted for by an increase in the number of light-transmitting faces from five to nine and by the fact that four of these faces are inclined at an angle of ~45° to the emitting region. The inclined faces are fairly convex, which is conducive to an increase in the efficiency of exit of radiation through these faces and to a decrease in both the directivity and multipass effect. In the case of the standard configuration, the parallelepiped-shaped LED, the emission intensity at the center of the directivity pattern is determined only by the radiation exit through the LED front surface, which is parallel to the crystal-holder table. Emission through the side faces is added to the total emission at the angles $\theta \neq 0°$. In the case of scanning in the planes parallel to the side faces, a single side face is involved in the total emission; two faces are involved if the scanning is carried out over the diagonal. As a result, the emission intensity is higher in the diagonal direction. An analysis of the directivity-pattern shape shows that the distribution of emission through each face follows the cosine law. Chemical faceting of the LED crystal made the directivity pattern of emission closer to that characteristic of a spherical crystal, which increases the exit of emission from the crystal.

The maximum differential external quantum yield of emission for a LED with the simplest geometric form (Fig. 28c) is equal to 0.78% and corresponds to an internal quantum emission yield of 58%.

At high currents (I > 200 mA), a LED with a deeply etched substrate part features the highest quantum yield of emission owing to better heat removal, absence of the current concentration under the contact, and presence of additional rounded faces.

Continuation of the efforts related to electrochemical faceting of LED crystals resulted in the obtaining of a developed convex–pyramidal surface using multistage electrochemical etching. The internal reflection of radiation from the developed surface at random angles gives rise to the multipass phenomenon with reradiation and to transformation of the short-wavelength band into the long-wavelength band without any significant losses in the total number of photons.

For experiments with electrochemical faceting of semiconductor crystals, we formed a wafer with epitaxial layers similar to that described in [30]. This large wafer was then divided into several fragments; contact photolithography was subsequently used to fabricate

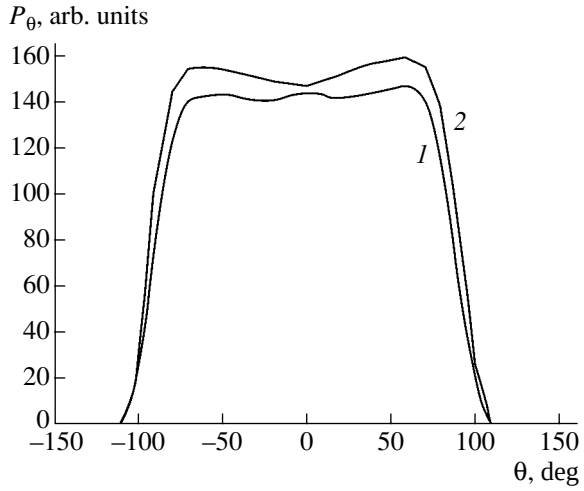

Fig. 34. The directivity patterns of a light-emitting diode with a conical–pyramidal and deeply etched substrate part (Fig. 28a) at a current of 50 mA. The patterns were measured in two planes perpendicular to the *p*–*n*-junction plane: (*1*) the plane of measurements was parallel to the side faces of the LED crystal and (*2*) the plane of measurements included the diagonal of the *p*–*n*-junction plane.

LEDs with crystals of different configurations from these fragments (Fig. 35).

The semiconductor LED crystals of type I (Fig. 35a) had a thickness of ~380 μm. A VUP-4 setup was used to form contacts 100 μm in diameter on the epitaxial-layer side (i.e., the *p*-type region); the contacts were obtained by consecutive deposition of Cr, Au + Ge alloy, and Au. Chromium, Au + Te, and Au were deposited on the substrate side (the *n*-type region). After deposition, the contact layers were then fused by heating for 1 min at a temperature of 250°C.

A pattern in the shape of squares with a side of 480 μm and a step of 500 μm was then formed on the epitaxial-layer side. This operation preceded the division of the structure into separate chips. In the next stage, mesas 300 μm in diameter and 10 μm in height were formed at the center of the squares; the previously fused contacts 100 μm in diameter were located at the center of these mesas.

The LED devices of type II (Fig. 35b) were fabricated so that the point contacts, mesas, and separating grooves were formed on the side of the *n*-type region (i.e., on the substrate side), while a continuous contact layer was formed on the epitaxial (*p*-type) side of the crystal.

The LED chips of types I and II had a conventional flat–rectangular configuration and differed from each other only with regard to the extraction of emission. Emission left the crystal mainly through the epitaxial layers in the chips of type I, whereas it left through the substrate in the case of the type II chips.

The LED devices of type III had a developed surface (Fig. 35c) and were fabricated on the basis of the same structure as LEDs I and II; electrochemical faceting of

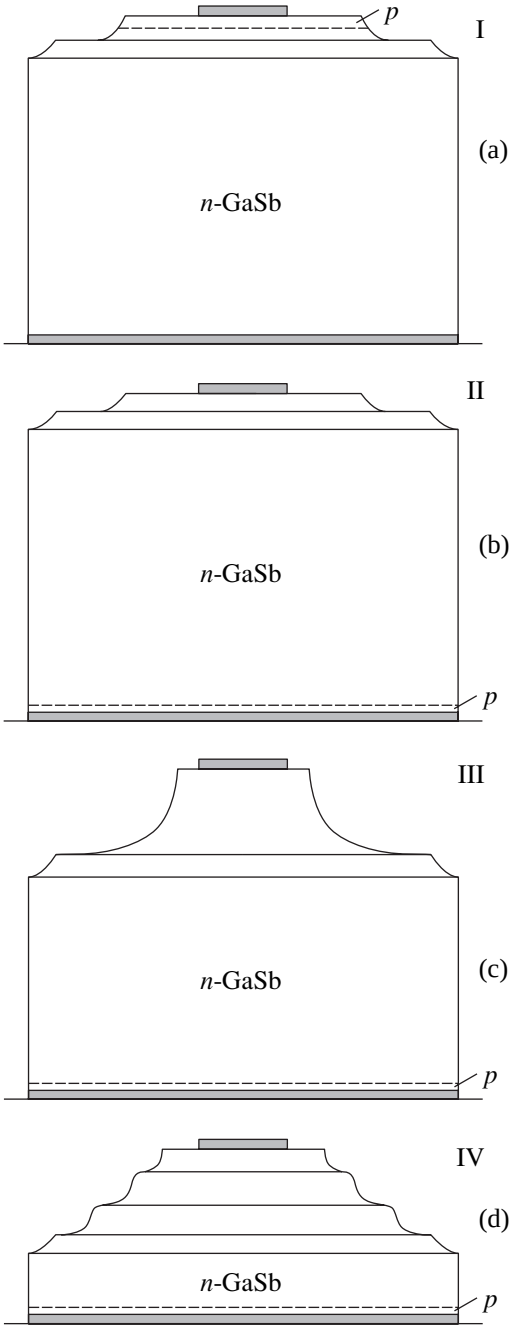

Fig. 35. Four configurations of LED crystals: (a) parallelepiped with the substrate part soldered to the crystal holder (crystal I); (b) parallelepiped with the epitaxial part soldered to the crystal holder (crystal II); (c) a crystal with a conical–pyramidal substrate part (crystal III); and (d) a crystal in the shape of a stepped pyramid with smoothed steps (crystal IV).

the LED crystal by contact photolithography was used repeatedly. The windows for ohmic contacts 100 μm in diameter were formed photolithographically on the side of the chemically cleaned substrate with *n*-type conductivity. The contact to the *p*-type region was formed over the entire surface of the *p*-type epitaxial layer. In

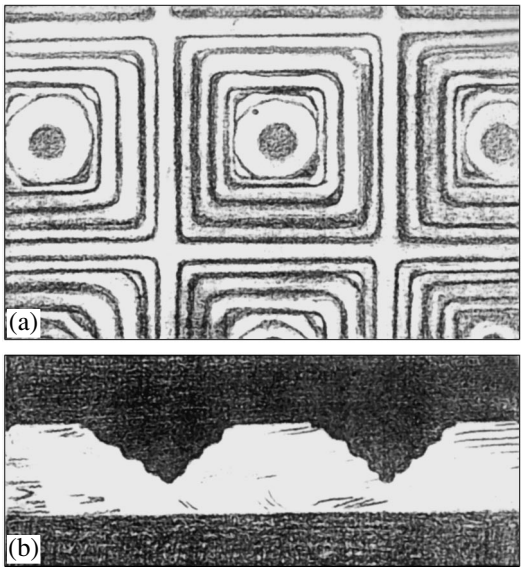

Fig. 36. Photograph of a wafer with LED crystals in the shape of stepped pyramids with smoothed steps formed by etching: (a) the view from the substrate side and (b) the profile obtained by cleaving.

order to delimit separate chips, we formed a pattern in the form of squares with a side of 480 μm and a step of 500 μm on the substrate side of the semiconductor crystal and electrochemically etched off the boundary grooves to a depth of 70 μm using an etchant based on CrO_3; the width of the grooves was 160 μm. In the next stage of the photolithographic process, a pattern in the form of circles 300 μm in diameter was formed at the center of the open squares. We etched this pattern in a way similar to the etching of the squares and obtained a figure 140 μm in height shaped like a pyramid at its base and a truncated cone at the vertex, which had a flat top 200 μm in diameter.

In order to decrease the optical path of radiation, the substrate part of the structure was thinned to 200 μm in the LED devices of type IV (Fig. 35d). The thickness was decreased by grinding and subsequent chemical polishing of the substrate. The LED structures were fabricated using multistage deep etching.

The first stage of fabrication consisted in the formation of ohmic contacts 100 μm in diameter on the substrate side of the structure.

In the second stage of photolithography, i.e., in the stage of the pattern formation on the substrate side of the LED structure, the duration of etching of a specific pattern was reduced. As a result, the squares, circles, etc., obtained had a smaller depth than in the case of the type III LEDs.

The sharp edges that are inevitably obtained when multistage etching is used (four photolithographic stages) were rounded and smoothed. To this end, in the fifth stage, a mesa 200 μm in diameter was formed photolithographically when the size of the flat top of the

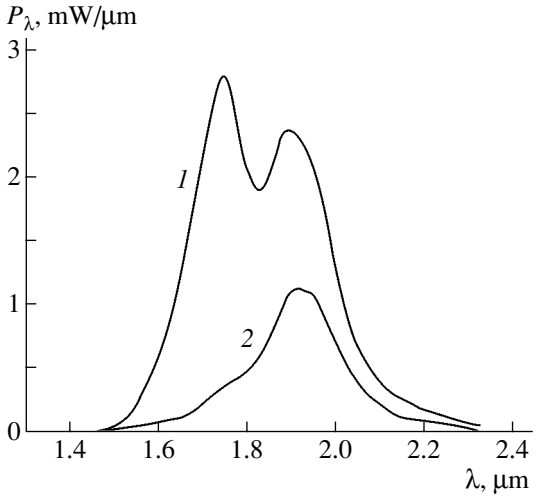

Fig. 37. The emission spectra of type I LEDs measured in two directions: (*1*) perpendicular and (*2*) parallel to the *p*–*n*-junction plane.

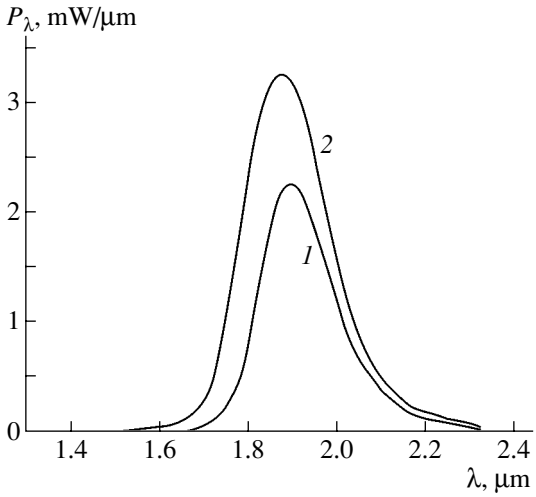

Fig. 38. The emission spectra of type II LEDs measured in two directions: (*1*) perpendicular and (*2*) parallel to the *p*–*n*-junction plane.

structure was 200 μm. All the features that were found beyond this 200-μm-diameter circle were etched off electrochemically for 20 s. As a result, we obtained a figure 120 μm in height in the shape of a stepped pyramid with smoothed steps (Fig. 36).

All the LED crystals were separated into individual chips by cleaving. The chips of the type I crystals were mounted with the substrate facing downwards on the LED TO-18 crystal holder with a flat table, whereas the chips of the crystals of types II, III, and IV were mounted with the epitaxial side facing downwards.

We measured the spectra and directivity patterns of emission at various pulsed currents with amplitudes from 10 to 300 mA, a repetition frequency of 512 Hz,

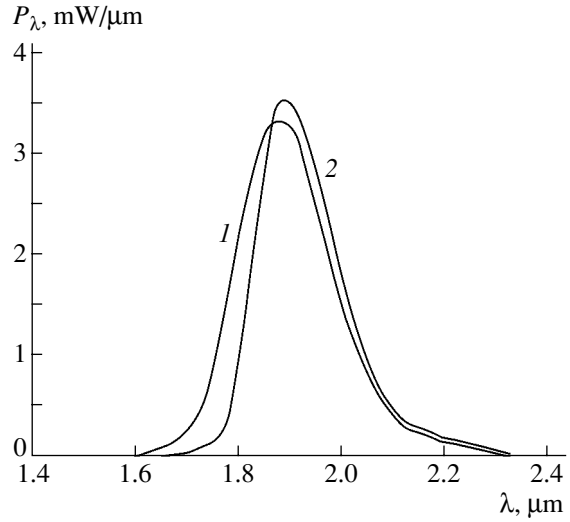

Fig. 39. The emission spectra of type III LEDs measured in two directions: (*1*) perpendicular and (*2*) parallel to the *p–n*-junction plane.

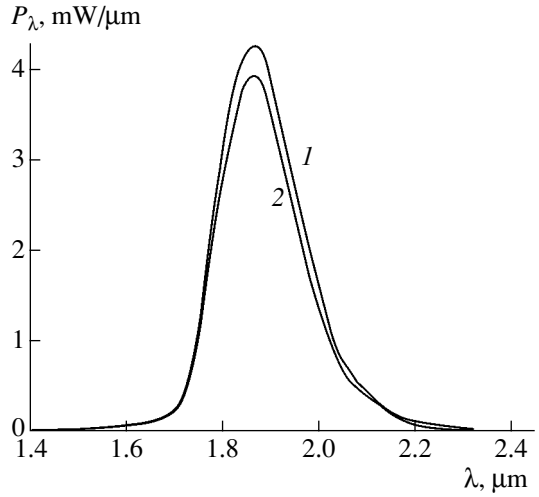

Fig. 40. The emission spectra of type IV LEDs measured in two directions: (*1*) perpendicular and (*2*) parallel to the *p–n*-junction plane.

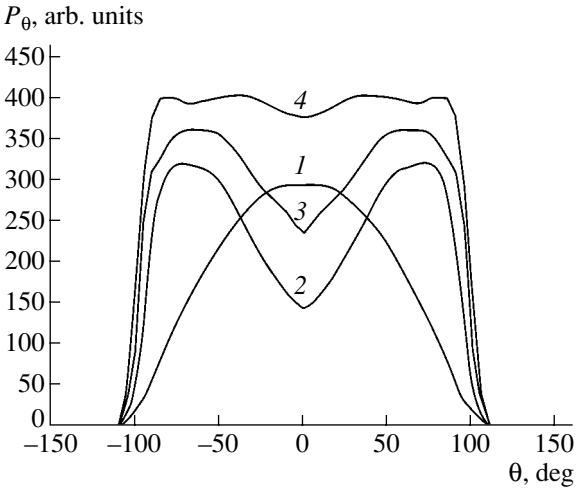

Fig. 41. The directivity pattern of emission in the plane parallel to the side face for LEDs with different crystal shapes: (*1*) crystal I, (*2*) crystal II, (*3*) crystal III, and (*4*) crystal IV.

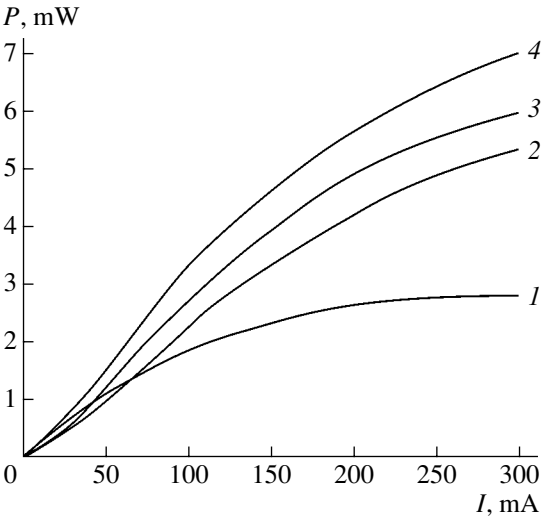

Fig. 42. The current dependence of the emission power for the LEDs with different crystal shapes: (*1*) crystal I, (*2*) crystal II, (*3*) crystal III, and (*4*) crystal IV.

and an off-duty factor of 2. The measurements were carried out at room temperature; the LEDs were cooled using a household fan. The emission transmitted through an MDR-2 grating monochromator (used for measuring the spectra) was calibrated in units of power per unit wavelength range. In order to calculate the emission power, we measured the spectra in two directions: one direction was perpendicular to the *p–n*-junction plane, while the other was parallel to this plane but perpendicular to one of the crystal faces. The power in the parallel direction was doubled when the total emission power was calculated, which corresponded exactly to the directivity pattern for the parallelepiped-shaped LEDs of types I and II. The method of calculation was the same for the other LED types as well, since the base of these was also shaped like a parallelepiped.

The LEDs of types I, II, and III were similar in their structure to the LEDs studied by Grebenshchikova *et al.* [30] (Fig. 28); however, the structures were grown on a thicker substrate. The LED of type I features a spectrum (Fig. 37, curve *1*) that is similar to spectrum *1* (in Fig. 29) measured in the direction perpendicular to the *p–n*-junction plane; i.e., this spectrum consists of a doublet with peaks at wavelengths of 1.76 and 1.9 μm. In the direction lying in the *p–n*-junction plane (Fig. 37, curve *2*), the long-wavelength band of the doublet is prevalent in the emission spectrum. The short-wavelength band is almost beyond detection. The intensity of

the long-wavelength band is two times lower than that in the direction perpendicular to the *p–n*-junction plane.

The LEDs of types II, III, and IV, in which the epitaxial side of the structure is soldered to the crystal holder, emit virtually only a single band, whose parameters were close to those of the aforementioned long-wavelength band (Figs. 38–40).

The emission intensity for a type II LED (Fig. 38) in the direction perpendicular to the *p–n*-junction plane is slightly lower than that in the direction parallel to this plane. The LEDs of types III and IV featured almost the same emission intensities in both directions (Figs. 39, 40). This equality of intensities is caused by the small average thickness of the crystal in the LEDs of types III and IV and indicates that the emission flux is uniform in the crystals. The nondirectivity of light fluxes in the LEDs of types III and IV is also provided by reflection of radiation from the smoothed joints of the faces.

A specific distribution of emission in the far-field zone is characteristic of each LED crystal shape (Fig. 41). As the angle of the observation direction with the normal to the substrate plane becomes larger than 90°, the emission intensity decreases abruptly for the LEDs of all types as a result of shading by the crystal holder.

The type I LEDs emit with the highest intensity in the direction perpendicular to the *p–n*-junction plane (Fig. 41, curve *1*). The emission intensity decreases gradually as the angle θ of deviation from this direction increases and amounts to 10–20% of the intensity at the zero angle at $\theta = 90°$.

The directivity patterns for the LEDs of types II, III, and IV, in which the epitaxial side of the crystal is soldered to the crystal holder, feature a minimum at $\theta = 0°$ (Fig. 41, curves *2–4*). This behavior is most clearly pronounced for the type II LEDs (Fig. 41, curve *2*) that are parallelepiped-shaped with a square base 500×500 μm and height of 380 μm. The intensity at the angle $\theta = 75°$ is a factor of 2.2 higher than that at the zero angle and is a factor of 1.5 higher at the angle $\theta = 90°$.

Smaller angles ($\theta \approx 60°$) at which the emission intensity is at a maximum are characteristic of the type III LEDs whose substrate part was subjected to a deep etching (Fig. 41, curve *3*). The intensity at the maximum exceeds that at the zero angle only by a factor of 1.5.

The minimum at center of the directivity pattern is least pronounced for the type IV LEDs (Fig. 41, curve *4*) with the crystal in the shape of a stepped pyramid with the total height of 200 μm. A weak dependence of the emission intensity on the angle θ is characteristic of these LEDs.

The current dependence of the emission power for the LEDs under study is shown in Fig. 42. At low currents (no higher than 10 mA for the type II LEDs and no higher than 75 mA for other LEDs), the dependence is superlinear and transforms into a sublinear dependence at high currents. At currents $I > 250$ mA, the emission power of the type I LEDs begins to decrease as the current increases, which is caused by concentration of emission under the ohmic contact and a corresponding increase in the rate of Auger recombination. Among the LEDs with different configurations, the type I LEDs exhibit the lowest emission power at currents in excess of 70 mA (Fig. 42, curve *1*). The highest emission power was attained for the type IV LEDs (Fig. 42, curve *4*): this power was equal to 7 mW at a current of 300 mA. The type IV LEDs also exhibited the highest differential quantum yield of photons; this yield was as high as 5.1% at a current of 75 mA. At the same current, the LEDs of types II and III featured quantum yields of 3.2 and 4.1%, respectively. The highest differential quantum yield of photons for the type I LEDs was 3.8% at a current of 10 mA. We can conclude that the external quantum yield of emission for the type I LEDs is approximately equal to that of the type II LEDs; this circumstance implies that the contacts covering the entire *p*-type surface in the type II LEDs and only a small part of this surface in the type I LEDs are virtually nonabsorbing. In addition, the contacts reflect photons diffusely, since the interface between the semiconductor and metal is not optically smooth. As a result, the metal contacts contribute to a situation in which the light flux in the crystal is not directional.

We derived theoretical formulas for the spectrum of outgoing radiation and the external quantum yield of photons; these formulas are based on the fact that the emission spectrum is determined by the spectrum of original recombination emission and the absorption spectrum of the crystal. The derived expressions show that the external quantum yield depends mainly on the ratio of the light-emitting area of the crystal to its volume.

Under operating conditions, photons are first emitted in the crystal, and only a fraction of them exit from the crystal. If we denote the total number of photons in the crystal by Φ, the emission spectrum is represented by the function $d\Phi/d\lambda$. The photons arise as a result of recombination of electron–hole pairs formed due not only to injection related to a passage of electric current I but also to the interband and quasi-interband absorption of photons that circulate in the crystal. The generation rate for electron–hole pairs as a result of photoactive absorption can be expressed by the definite integral $\int_0^\infty \alpha c\,(d\Phi/d\lambda)d\lambda$, where α is the photoactive-absorption coefficient averaged over the crystal and c is the speed of light in the crystal. The absorption spectrum of the crystal is contributed to by photoactive absorption, absorption related to losses (including absorption in the metallic contacts) α_d, and the effective absorption α_e that characterizes the exit of radiation from the crystal. The spectral distribution of original recombination radiation is expressed by the function $d\eta_{in}/d\lambda$, where $\int_0^\infty (d\eta_{in}/d\lambda)d\lambda = \eta_{in}$ is the internal quantum yield of emission. It is assumed that radiation in the crystal is

not directional. The resulting balance equation for the spectral distribution of photons is written as

$$\frac{d(d\Phi/d\lambda)}{dt} = \frac{d\eta_{in}}{d\lambda}\left(\frac{I}{e} + \int_0^\infty c\alpha\frac{d\Phi}{d\lambda}d\lambda\right) - c(\alpha - \alpha_d + \alpha_e)\frac{d\Phi}{d\lambda} = 0. \quad (8)$$

Equation (8) is used to determine the spectrum of the radiation flux that leaves the crystal:

$$\frac{dP_e}{d\lambda} = c\alpha_e\frac{d\Phi}{d\lambda} = \frac{d\eta_{in}}{d\lambda}\alpha_e\left(\frac{I}{e} + \int_0^\infty c\alpha\frac{d\Phi}{d\lambda}d\lambda\right)(\alpha + \alpha_d + \alpha_e)^{-1}. \quad (9)$$

It follows from expression (9) that the spectrum of radiation emerging from the crystal is independent of the reradiation effect, since this effect is represented in expression (9) by the definite integral of λ between the limits 0 and ∞; i.e., the reradiation effect has a certain numerical magnitude. The spectrum of radiation leaving the crystal depends on the spectrum of original recombination radiation $d\eta_{in}/d\lambda$ and on the spectrum of absorption in the crystal ($\alpha + \alpha_d + \alpha_e$). The quantities α_d and α_e vary only slightly within the range of wavelengths of most of the original recombination radiation. The photoactive-absorption coefficient α increases substantially as the wavelength decreases, which can reduce the fraction of short-wavelength photons in the outgoing radiation. This effect is significant in the wavelength region $\lambda < \lambda_b$ (λ_b is a boundary wavelength) where $\alpha > \alpha_d + \alpha_e$. Such a division of the integration domain makes it possible to approximately calculate the definite integral that appears in expression (9) by multiplying (9) by α/α_e and integrating with respect to λ. As a result, we obtain the expression

$$\int_0^\infty c\alpha\frac{d\Phi}{d\lambda}d\lambda = \frac{\eta_s I}{1 - \eta_s e}, \quad (10)$$

where η_s is the internal quantum yield of short-wavelength photons with $\lambda < \lambda_b$. After substituting expression (10) into (9), integrating with respect to λ, and dividing the result by I/e, we obtained the following expression for the external quantum yield of photons:

$$\eta_{ext} = \frac{\eta_l}{1 - \eta_s}\frac{1}{1 + \alpha_d/\alpha_e}. \quad (11)$$

Here, η_l is the internal quantum yield of long-wavelength photons with $\lambda > \lambda_b$.

It follows from expression (11) that, in order to increase the external quantum yield of photons η_{ext}, we have to increase not only the internal quantum yield of long-wavelength photons (η_l) and short-wavelength photons (η_s) but also the effective absorption coefficients α_e that characterize the exit of photons from the crystal. In the case of $\eta_s + \eta_l = 1$ and $\alpha_d/\alpha_e \ll 1$, the value of η_{ext} is close to unity, which indicates that it is possible to transform the short-wavelength band into the long-wavelength band without any loss in the number of photons. In order to determine α_e, we take into account that a different photon density $d\Phi/dV$ can be observed in the vicinity of different areas of the crystal surface dS. Taking into account that the photons cross the surface only within the angle of the total internal reflection and experience partial reflection back into the crystal, we derived the following expression for α_e in the case where the refractive index of the crystal $n \gg 1$:

$$\alpha_e = \frac{1}{\Phi}\int_S \frac{d\Phi}{dV}\frac{dS}{n(n+1)^2}. \quad (12)$$

If the photons and optical inhomogeneities in the crystal are distributed uniformly, expression (12) can be simplified and written as

$$\alpha_e = \frac{S}{Vn(n+1)^2}. \quad (13)$$

It follows from formula (13) that the value of α_e can be increased by increasing the S/V ratio, e.g., by making the crystal thinner. The value of α_e increases by a factor of 1.5 if the cubic shape of the crystal is replaced by a hemispherical shape. Curvature of a spherical surface is conducive to the uniformity of the emission distribution and makes the emission nondirectional in the crystal, whereas the flat orthogonal faces in the cubic structure are conducive to making the emission directional and decrease the value of α_e. A mesa structure obtained by etching one of the LED faces is conducive to making the emission nondirectional. The directionality could be further radically reduced by forming convexities or depressions over the entire crystal surface, which increase the real crystal surface and give rise to an additional increase in α_e. Metallic contacts cover a part of the surface and, thus, decrease the value of α_e. In addition, these contacts can absorb radiation and, as a result, substantially increase the value of α_d. The diffuse reflection of radiation from the metallized surface can represent a beneficial effect, as this reflection reorients the photon fluxes. The small average crystal thickness in the LEDs of types III and IV ensures the equality of the radiation intensities in the directions that are perpendicular and parallel to the *p–n*-junction plane (Figs. 38, 39). This equality indicates that the radiation flux is uniform in the crystals. The absence of a directional distribution of emission in these crystals is ensured by the reflection of radiation from the smoothed joints of their faces. As a result, the conditions for applicability of the above theoretical analysis

can be considered as satisfied for the LEDs of types III and IV. Formulas (13) and (11) were used to calculate the equivalent coefficient of absorption caused by the exit of radiation from the crystal and the external quantum yield, respectively.

In the calculations, we used the typical values of the internal quantum yield of photons $\eta_{in} = 58\%$, the ratio between the generated fluxes of the short- and long-wavelength photons $\eta_s/\eta_l = 2$ [30, 31], the coefficient of nonphotoactive absorption $\alpha_d = 8$ cm^{-1}, and the refractive index $n = 3.9$ [32]. The effective absorption coefficient calculated with formula (13) and related to the exit of radiation from the crystal was found to be 1.13 cm^{-1} for the LEDs of types I and II, 1.3 cm^{-1} for the type III LEDs, and 1.79 cm^{-1} for the type IV LEDs. The theoretical external quantum yield of photons was found to be close to the value measured for all the types of LEDs.

Notwithstanding the fact that the LEDs of types III and IV emit only in the long-wavelength band, in contrast to the type I LEDs, which emit, in addition, (and more intensely) in the short-wavelength band, these LEDs have a higher external quantum yield of emission. This observation indicates that the short-wavelength band is transformed into the long-wavelength band with the total number of photons not only conserved but even increased. This increase is attributed to an effective process of reradiation. The external quantum yield of photons increases as the ratio between the area of the surface through which the radiation exits and the volume of the LED crystal increases.

8. CONCLUSION

The main results obtained from a series of our studies relate to the development and investigation of light-emitting diodes (LEDs) based on the GaSb semiconductor compound and its GaInAsSb and AlGaAsSb solid solutions and designed for operation in the middle-infrared region of the spectrum (1.6–4.4 μm). The LED structures were fabricated using the method of liquid-phase epitaxy (LPE); this method made it possible to grow layers that were lattice-matched to the substrate and had a reasonably large thickness.

The GaInAsSb and AlGaAsSb alloys that form the active and confining layers can basically be lattice-matched in a wide range of compositions to the GaSb substrate. The experimental values of the lattice-constant mismatch were in the range $\Delta a/a = 2 \times 10^{-3}$–$2 \times 10^{-4}$. The LED structures were grown on *n*-GaSb substrates doped with Te (resulting in an electron concentration that was $(7–8) \times 10^{17}$ cm^{-3}) and oriented, in the majority of cases, parallel to the (100) crystallographic plane. The grown structures were either nonsymmetrical (first, the active GaInAsSb layer was grown on the substrate and, then, the wide-gap AlGaAsSb layer was grown) or symmetric, in which case the active layer was surrounded on both sides with wide-gap AlGaAsSb layers. The wide-gap layers were grown with a high Al content, up to 64%, which is unprecedentedly high for the LPE method.

The studies showed that the symmetric type of LED heterostructure had an advantage over the nonsymmetrical type. This advantage manifests itself in a higher optical power and a smaller width of the emission spectrum in the entire range of pump currents.

The active GaInAsSb was doped with Te in all cases. It is experimentally established that the dependence of the external quantum yield of emission on the charge-carrier concentration in the active *n*-type region has a maximum at about $n = 10^{17}$ cm^{-3} for all wavelengths. As the In content in the active region was varied from 0 to 24%, the emission wavelength increased from 1.6 to 2.4 μm. LPE gives no way of growing layers with an In content in the range 25–70%. Emission with the wavelength in the range 3.4–4.4 μm was obtained when the In content exceeded 75%. These LEDs emitted at the longest wavelength among the LEDs grown on an GaSb substrate.

The external quantum yield of emission is highest if the active-region thickness is 2–3 μm, which coincides with the charge-carrier diffusion length.

The lifetime of minority charge carriers decreases from 50 to 5 ns as the In content in the active region increases, corresponding to an increase in the emission wavelength from 1.8 to 2.4 μm.

The current and temperature dependences of the emission intensity indicate that the prevalent recombination processes are band-to-band radiative recombination and the CHCC nonradiative Auger process; in the latter case, one electron executes an interband transition, while the other electron executes an intraband transition, with the result that the energy and momentum are conserved. We calculated (and compared with experimental data) the radiative (τ_r) and nonradiative (τ_a) lifetimes of minority charge carriers in the case of band-to-band recombination. Within the entire temperature range of 77–300 K, the resulting lifetime τ_{ra} is close to the experimentally measured time constant for the decay of the emission intensity when the current is switched off. As the temperature T is increased, the calculated values of τ_r increase in proportion to $T^{3/2}$, while τ_a decreases, on average, according to $T^{-3/2}$. These lifetimes are equal to each other at temperatures of 200–300 K. In this case, the theoretical internal quantum yield is equal to 50%.

In order to improve the efficiency of extracting the generated radiation from the crystal, we used various methods. For example, we installed a parabolic reflector in the TO-18 case, which made it possible to collimate the LED emission within the angle of 10°–12°; introduced an epoxy compound shaped in the form of a lens, which ensured divergence of the radiation flux

equaling 16°–20° at the level corresponding to the half of the maximum intensity; and used a flip-chip structure, which made it possible to position the active region close to the heat-removing case base and extract the light flux through the substrate, which is not screened by the contact. In the case of the LEDs designed for the shortest wavelengths (λ_{max} = 1.65–1.75 μm), we used a structure with removed substrate and extraction of radiation through a wide-gap *n*-type layer, which made it possible to appreciably reduce the absorption in the crystal. We developed a method for treating LED crystals by chemically faceting their substrate part, which made it possible to form this part into a conical–pyramidal shape and increase the number of crystal faces. The chemical faceting of crystals increases the external quantum yield of emission and makes the directivity pattern correspond nearly to that of a hemispherical crystal. Shaping the LED crystals into a stepped pyramid with smoothed steps leads to transformation of the short-wavelength emission band, related to a doubly charged intrinsic acceptor, into a long-wavelength band. It is shown both experimentally and theoretically that an increase in the area of a LED crystal in comparison to its volume increases the external quantum yield of photons.

Optimization of the LED structures made it possible to obtain an external quantum yield of photons at the level of 5.5–6% at 300 K. We attained an optical power of 3.7 mW in the continuous mode. The maximum power in a pulse was as high as 7 mW at an off-duty factor equal to 2, repetition frequency of 512 Hz, and current of 300 mA and was as high as 190 mW at an off-duty factor of 200, repetition frequency of 1 kHz, and current of 1.4 A. For the LEDs emitting in the spectral range 3.4–4.4 μm, we found that the optical emission power and external quantum yield (~1%) exceed the known values for an InAsSb/InAsSbP heterostructure grown on an InAs substrate by a factor 3.

The developed and studied LEDs find wide use in systems of ecological monitoring and medical diagnostics, as well as in all cases where it is necessary to determine the absorption lines of water vapors, methane, carbon dioxide, carbon oxide, acetone, ammonium, and many other inorganic and organic substances.

ACKNOWLEDGMENTS

This study was supported in part by the Russian Foundation for Basic Research (project no. 04-02-17655) and in part by the Civilian Research & Development Foundation (grant no. RPO-1407-ST-03).

REFERENCES

1. A. Mabbit and A. Parker, Sens. Rev. **16** (3), 38 (1996).
2. M. R. Murti, B. Grietens, C. Van Hoof, and G. J. Borghs, J. Appl. Phys. **78**, 578 (1995).
3. I. Vurgaftman, J. R. Meyer, and R. Ram-Mohan, J. Appl. Phys. **89**, 5815 (2001).
4. L. M. Dolginov, L. V. Druzhinina, M. G. Mil'vidskiĭ, *et al.*, Izmer. Tekh., No. 6, 65 (1981).
5. A. Andaspaeva, A. N. Baranov, A. A. Guseĭnov, *et al.*, Pis'ma Zh. Tekh. Fiz. **14**, 845 (1988) [Sov. Tech. Phys. Lett. **14**, 377 (1988)].
6. A. Andaspaeva, A. N. Baranov, A. A. Guseĭnov, *et al.*, Pis'ma Zh. Tekh. Fiz. **15** (18), 71 (1989) [Sov. Tech. Phys. Lett. **15**, 734 (1989)].
7. A. Andaspaeva, A. N. Baranov, E. A. Grebenshchikova, *et al.*, Fiz. Tekh. Poluprovodn. (Leningrad) **23**, 1373 (1989) [Sov. Phys. Semicond. **23**, 853 (1989)].
8. A. Andaspaeva, A. N. Baranov, A. A. Guseĭnov, *et al.*, Fiz. Tekh. Poluprovodn. (Leningrad) **24**, 1708 (1990) [Sov. Phys. Semicond. **24**, 1067 (1990)].
9. B. A. Gel'mont and G. G. Zegrya, Fiz. Tekh. Poluprovodn. (Leningrad) **22**, 1381 (1988) [Sov. Phys. Semicond. **22**, 876 (1988)].
10. P. T. Landsberg and A. R. Beattie, J. Phys. Chem. Solids **8**, 73 (1959).
11. A. R. Beattie and P. T. Landsberg, Proc. R. Soc. London **249**, 16 (1959).
12. J. S. Blakemore, *Semiconductor Statistics* (Pergamon, Oxford, 1962; Mir, Moscow, 1964).
13. A. A. Andaspaeva, A. N. Imenkov, N. M. Kolchanova, *et al.*, Pis'ma Zh. Tekh. Fiz. **19** (24), 5 (1993) [Tech. Phys. Lett. **19**, 776 (1993)].
14. M. Nakao, S. Yashida, and S. Gonda, Solid State Commun. **49**, 663 (1986).
15. A. A. Popov, V. V. Sherstnev, and Yu. P. Yakovlev, Pis'ma Zh. Tekh. Fiz. **23** (18), 12 (1997) [Tech. Phys. Lett. **23**, 701 (1997)].
16. A. A. Popov, V. V. Sherstnev, and Yu. P. Yakovlev, Pis'ma Zh. Tekh. Fiz. **23** (20), 19 (1997) [Tech. Phys. Lett. **23**, 783 (1997)].
17. A. A. Popov, V. V. Sherstnev, and Yu. P. Yakovlev, Pis'ma Zh. Tekh. Fiz. **24** (2), 72 (1998) [Tech. Phys. Lett. **24**, 73 (1998)].
18. T. N. Danilova, B. E. Zhurtanov, A. P. Zakgeĭm, *et al.*, Fiz. Tekh. Poluprovodn. (St. Petersburg) **33**, 239 (1999) [Semiconductors **33**, 206 (1999)].
19. B. Zhurtanov, É. V. Ivanov, A. N. Imenkov, *et al.*, Pis'ma Zh. Tekh. Fiz. **27** (5), 1 (2001) [Tech. Phys. Lett. **27**, 173 (2001)].
20. A. Krier, H. H. Gao, V. V. Sherstnev, and Yu. P. Yakovlev, J. Phys. D: Appl. Phys. **32**, 3117 (1999).
21. N. D. Stoyanov, B. E. Zhurtanov, A. P. Astakhova, *et al.*, Fiz. Tekh. Poluprovodn. (St. Petersburg) **37**, 996 (2003) [Semiconductors **37**, 971 (2003)].
22. T. I. Voronina, B. E. Zhurtanov, T. S. Lagunova, *et al.*, Fiz. Tekh. Poluprovodn. (St. Petersburg) **32**, 278 (1998) [Semiconductors **32**, 250 (1998)].
23. Zh. I. Alferov, V. M. Andreev, D. Z. Garbuzov, *et al.*, Pis'ma Zh. Tekh. Fiz. **2**, 1066 (1976) [Sov. Tech. Phys. Lett. **2**, 420 (1976)].

24. Zh. I. Alferov, V. M. Andreev, D. Z. Garbuzov, *et al.*, Zh. Tekh. Fiz. **45**, 374 (1975) [Sov. Phys. Tech. Phys. **20**, 234 (1975)].
25. Zh. I. Alferov, V. M. Andreev, D. Z. Garbuzov, *et al.*, Fiz. Tekh. Poluprovodn. (Leningrad) **9**, 1265 (1975) [Sov. Phys. Semicond. **9**, 837 (1975)].
26. V. B. Khalfin, D. Z. Garbuzov, and N. Yu. Davidyuk, Fiz. Tekh. Poluprovodn. (Leningrad) **10**, 1490 (1976) [Sov. Phys. Semicond. **10**, 884 (1976)].
27. Zh. I. Alferov, V. G. Agafonov, D. Z. Garbuzov, *et al.*, Fiz. Tekh. Poluprovodn. (Leningrad) **10**, 1497 (1976) [Sov. Phys. Semicond. **10**, 888 (1976)].
28. I. Schnitzer, E. Yablonovitch, C. Caneau, *et al.*, Appl. Phys. Lett. **63**, 2174 (1993).
29. R. Windisch, P. Heremans, A. Knobloc, *et al.*, Appl. Phys. Lett. **74**, 2256 (1999).
30. E. A. Grebenshchikova, A. N. Imenkov, B. E. Zhurtanov, *et al.*, Fiz. Tekh. Poluprovodn. (St. Petersburg) **37**, 1465 (2003) [Semiconductors **37**, 1414 (2003)].
31. E. A. Grebenshchikova, A. N. Imenkov, B. E. Zhurtanov, *et al.*, Fiz. Tekh. Poluprovodn. (St. Petersburg) **38**, 745 (2004) [Semiconductors **38**, 717 (2004)].
32. O. Madelung, *Physics of III–V Compounds* (Wiley, New York, 1964; Mir, Moscow, 1967).

Translated by A. Spitsyn

Semiconductors, Vol. 39, No. 11, 2005, pp. 1267–1274. Translated from Fizika i Tekhnika Poluprovodnikov, Vol. 39, No. 11, 2005, pp. 1312–1319.

ATOMIC STRUCTURE AND NONELECTRONIC PROPERTIES OF SEMICONDUCTORS

Growth Kinetics of Thin Films Formed by Nucleation during Layer Formation

V. G. Dubrovskiĭ*^ and G. E. Cirlin**

**Ioffe Physicotechnical Institute, Russian Academy of Sciences, Politekhnicheskaya ul. 26, St. Petersburg, 194021 Russia*
^e-mail: dubrovskii@mail.ioffe.ru

***Institute of Analytical Instrument Making, Russian Academy of Sciences, Rizhskiĭ pr. 26, St. Petersburg, 198103 Russia*

Submitted March 3, 2005; accepted for publication March 15, 2005

Abstract—A kinetic model of thin-film growth on a solid surface is investigated. This model is valid in the case where the layers are formed as a result of two-dimensional nucleation. Under conditions of high supersaturation of a gaseous phase, solutions are obtained for an island-size distribution function at the initial stage of growth, the degree of filling of a substrate by islands at the coalescence stage, the vertical-growth rate of a film, and its surface roughness. These solutions express the structural characteristics of a growing film in terms of physical constants (the interphase energy on the gas–solid interface and the activation barriers of diffusion and desorption) of the system and the growth parameters (the surface temperature and the material-deposition rate). The obtained results make it possible to calculate the growth dynamics for thin films in particular systems.

1. INTRODUCTION

Investigations of the formation of thin films deposited on a solid surface from a gaseous phase are extremely important for developing technologies for the fabrication of semiconductor epitaxial structures used in microelectronics and optoelectronics [1]. For controllable growth of structures with the desired properties, it is necessary to develop a detailed kinetic theory of thin-film growth. A large number of publications devoted to various aspects of this problem are reviewed, for example, in [2]. In the case of singular surfaces, the basic mechanism of formation of layers is two-dimensional nucleation [2–4]. At the present time, the initial stage of condensation of thin films, involving the nucleation and independent growth of two-dimensional islands (described most fully in [2, 5–7]) and the stage of Ostwald ripening of islands [8], have been reasonably thoroughly studied. The theoretical description of these stages is based on the kinetic theory of first-order phase transitions [9] and certain general theoretical approaches developed by Livshits and Slezov [10], Kuni [11, 12], Binder [13], and some other authors. For investigating the coalescence of islands, the geometrical probabilistic model of crystallization proposed by Kolmogorov [14] and applicable to the case of two-dimensional growth [15–17] is used. The theory of polylayer growth of films is based on the Kashchiev model [18] and its generalizations [19]. In [20, 21], we used computer simulation to investigate thin-film growth during molecular-beam epitaxy (MBE) and its variants. Despite the abundance of models, the problem of constructing a unified theoretical description of the growth that makes it possible to obtain simple approximations for the structural characteristics of a film is still far from being solved.

The purpose of this work is to construct and investigate a model of the autoepitaxial growth of a film deposited on a solid surface from a gaseous phase. We give special attention to finding physically transparent expressions for calculating a film's structural characteristics that are convenient for comparison with the experimental data and enable us to calculate the growth dynamics in particular systems.

2. THEORETICAL MODEL

The basic processes occurring in the formation of thin films are the adsorption, desorption, nucleation, and growth and coalescence of two-dimensional islands. Vertical growth proceeds because of a consecutive filling of layers (Fig. 1). Conditions of growth depend on the surface temperature T and material-deposition rate V. We hereafter consider both these parameters as constant. If V is measured in monolayers per second (ML/s), $V = \sigma J$, where σ is the surface area occupied by an atom and J is the atomic flux to the surface. Material characteristics depend on the critical temperature T_c of the phase transition between rarefied and dense phases of the adsorbate; the activation barriers E_D and E_A of adatom diffusion and desorption, respectively; and the interphase energy γ of the gas–crystal interface per unit length. We consider as known [2] the equilibrium adatom density $n_{eq} = (1/\sigma)\exp(-\lambda/k_BT)$ ($\lambda = 2k_BT_c$ is the phase-transition heat), the adatom lifetime $\tau_A = \nu_A^{-1}\exp(E_A/k_BT)$ on the surface, and the diffusion time

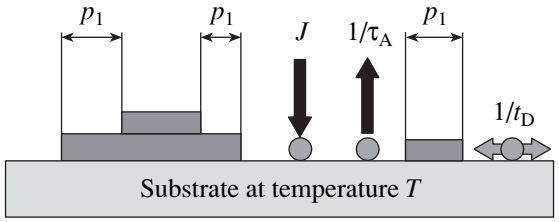

Fig. 1. Schematic representation of thin-film growth: J is the intensity at which atoms arrive from the gaseous phase, $1/\tau_A$ is the probability of adatom desorption per unit time, $1/t_D$ is the probability of a diffusion jump per unit time, $\psi(t)$ is the degree of filling of the surface at the moment of time t, $H(t)$ is the average film height, $R(t)$ is the surface roughness, and $p_k(t)$ is the probability of finding a random point on the film surface at the height of the kth monolayer.

$t_D = \nu_D^{-1} \exp(E_D/k_BT)$, where ν_A and ν_D are the preexponential factors and k_B is the Boltzmann constant.

As was shown in [17], in the case of coalescence by the mechanism of solid-state sintering [15] and the "free-molecular" mode of growth of two-dimensional islands (the growth rate di/dt of the number i of atoms in a supercritical island is proportional to its perimeter [2]), the adatom concentration n on a free surface area obeys the equation [17]

$$n(t) = \int_0^t dt' \left(J - \frac{n(t')}{\tau_A} \right) - \frac{g(t)}{\sigma}. \quad (1)$$

Here,

$$g(t) = 4 \int_0^t dt' I(t') r^2(t', t) \quad (2)$$

is the degree of filling of the surface at the moment of time t when disregarding the coalescence, $I(t)$ is the nucleation rate (intensity), $r(t', t)$ is the linear size of an island formed at the moment of time t' determined according to

$$r(t't) = \int_{t'}^t dt'' v(t''). \quad (3)$$

The rate of lateral growth of the islands is described by the expression

$$v(t) = \frac{r_0}{\tau_D} \zeta(t), \quad (4)$$

where $r_0 \equiv \sigma^{1/2}/2$, $\tau_D \equiv t_D/\sigma^{1/2} l_D n_{eq} \sim t_D/\theta_{eq}$ is the characteristic growth time, l_D is the diffusion-jump length, $\theta_{eq} \equiv \sigma n_{eq}$ is the equilibrium filling of the surface by adatoms, and $\zeta \equiv n/n_{eq} - 1$ is the supersaturation by adatoms. Equations (1)–(4) are written for the case of a square nucleus ($\sigma = 4r^2$), where r is the half-length of the square's side. For another shape, the shape constant c replaces factor 4 in Eq. (2). For low degrees of filling, the physical meaning of Eq. (1) is obvious: it is the material-balance equation on the surface. Here, the integral term on the right-hand side gives the number of atoms that have arrived at the surface at time t, and the second term is the number of atoms in islands per unit surface area. Equation (4) takes into account the arrival of adatoms at an island due to surface diffusion towards a step formed by its boundary. If degree of filling of the surface increases, Eq. (1) is found to be the consequence of the Kolmogorov formula [14] for a true degree of filling,

$$\psi(t) = 1 - \exp[-g(t)], \quad (5)$$

and the balance equations taking into account a nonzero filling [17].

The nucleation rate is described by the Zel'dovich formula [2]

$$I(\zeta) = \frac{n_{eq}}{\sigma} \frac{l_D^2}{2\sqrt{\pi} t_D} (\zeta + 1) \times \ln^{1/2}(\zeta + 1) \exp\left[-\frac{a}{\ln(\zeta + 1)} \right]. \quad (6)$$

Here, $a \equiv 4\sigma(\gamma/k_BT)^2$ is the squared dimensionless interphase energy on the gas–crystal interface, which is large for the majority of materials (~10).

The vertical-growth rate V_s of a film depends on the filling time t_{ML} of one monolayer according to Kolmogorov Eq. (5) [3]:

$$V_s = 1/t_{ML}, \quad g(t_{ML}) = 1. \quad (7)$$

For a low-temperature polylayer growth in which the subsequent layers are formed on unoccupied areas of the previous layers, the average height and roughness of the film surface can be found on the basis of the Kashchiev model [18, 19].

The described pattern represents a reasonably general model of autoepitaxial growth of a film at all its stages (nucleation, independent island growth, coalescence, and growth of subsequent layers), but it disregards the Ostwald-ripening stage [10]. However, it is known that the islands merge together earlier than the point when critical size attains an average nucleus size $r_*(t)$, and no Ostwald ripening is observed [2]. Then, these equations represent a self-consistent system that enables us to determine the structural characteristics of a film in relation to the temperature T; flux J; and physical constants λ, E_A, and E_D. We now investigate the described model at various stages of growth.

3. ISLAND-NUCLEATION STAGE

For investigating the island-nucleation stage, we use the Kuni method [11, 12], which enables us to derive an analytical solution to the nucleation problem under

dynamic conditions. In terms of a supersaturation ζ by adatoms, material-balance Eq. (1) becomes

$$\zeta(t) + G(t) = \frac{1}{\tau_A}\int_0^t dt'[\Phi_{max} - \zeta(t')] - 1. \quad (8)$$

Here, $G(t) \equiv g(t)/\theta_{eq}$ is the number of atoms in the islands per unit surface area expressed in terms of an equilibrium adatom concentration. The quantity Φ_{max} is the gaseous-phase supersaturation and involves both the growth controlling parameters T and V (we give various ways of writing Φ_{max}):

$$\Phi_{max} = \frac{J\tau_A}{n_{eq}} - 1 = \frac{V\tau_A}{\theta_{eq}} - 1 = \frac{V}{\nu_A}\exp\left(\frac{E_A + \lambda}{k_B T}\right) - 1. \quad (9)$$

In technologically important cases, the supersaturation Φ_{max} is always high (about several tens) because adsorption always dominates over desorption during the film growth [2, 4]. The major parameter in the theory is an ideal supersaturation $\Phi(t)$, i.e., the supersaturation in the absence of nucleation, for which it follows from Eq. (8) at $G = 0$ that

$$\Phi(t) = (\Phi_{max} + 1)\left[1 - \exp\left(-\frac{t}{\tau_A}\right)\right] - 1. \quad (10)$$

Expression (6) for the nucleation rate has an extremely sharp peak at the point of the highest supersaturation. Following [11, 12], we present $I(\zeta)$ near the peak as

$$I(\zeta) = I(\Phi_*)\exp\left[-\frac{\Gamma}{\Phi_*}(\Phi_* - \zeta)\right]. \quad (11)$$

Here,

$$\Gamma = \frac{\Phi_*}{\Phi_* + 1}\frac{a}{\ln^2(\Phi_* + 1)} = \frac{\Phi_*}{\Phi_* + 1} i_c(\Phi_*) \gg 1 \quad (12)$$

is a large parameter of the theory and, in order of magnitude, is equal to the critical number i_c in the classical theory of nucleation for $\zeta = \Phi_*$.

Taking into account the main exponential dependence of the nucleation rate on the supersaturation near its peak, other functions near the time instant t_* at which highest supersaturation is attained can be replaced by their linear approximations. Then, we use formula (10) to obtain the following expression for the ideal supersaturation:

$$\Phi(t) = \Phi_* + \alpha(t - t_*). \quad (13)$$

Here, $\alpha \equiv (\Phi_{max} - \Phi_*)/\tau_A$. For the size $r(t', t)$, it follows from Eqs. (3) and (4) that

$$r(t', t) = \frac{r_0\Phi_*}{\tau_D}(t - t'). \quad (14)$$

Material-balance Eq. (8) near $t = t_*$ becomes

$$\Phi_* - \zeta(t) = G(t) - \alpha(t - t_*). \quad (15)$$

Substituting Eqs. (11) and (14) into Eq. (2), taking into account that $G(t) \equiv g(t)/\theta_{eq}$, and using Eq. (15), we obtain a closed integral equation for $G(t)$:

$$G(t) = \frac{I(\Phi_*)}{n_{eq}}\left(\frac{\Phi_*}{\tau_D}\right)^2 \times \int_{-\infty}^{t - t_*} dt'(t - t_* - t')^2 \exp\left[\frac{t'}{\Delta t} - \frac{\Gamma}{\Phi_*}G(t')\right]. \quad (16)$$

Here, we introduce $\Delta t \equiv \Phi_*/\Gamma\alpha$ and solve Eq. (16) by iterations, which alternately majorize the solution from above and from below so that the solution is rapidly approached. For practical purposes, the accuracy of the first iteration is sufficient:

$$G(t) = \frac{\Phi_*}{\Gamma}\exp\left(\frac{t - t_*}{\Delta t}\right). \quad (17)$$

When finding the normalizing constant in Eq. (17), we took into account that $G'(t_*) = (\Phi_{max} - \Phi_*)/\tau_A$ at the point of the highest supersaturation; as a result, we obtain

$$\frac{2}{n_{eq}}\Phi_*^2\frac{(\Delta t)^3}{\tau_D^2} I(\Phi_*) = \frac{\Phi_*}{\Gamma}. \quad (18)$$

Using Eq. (6) for $I(\Phi_*)$ and taking into account the definitions for Δt and τ_D from Eq. (18), we can obtain the following equation for the highest supersaturation:

$$\frac{2\sqrt{\pi}a(\sqrt{\sigma}/l_D)^2}{\Phi_*^2(\Phi_* + 1)^3\ln^{9/2}(\Phi_* + 1)}\left(\frac{\Phi_{max} - \Phi_*}{\Phi_{max} + 1}\right)^3 \times \frac{(Vt_D)^3}{\theta_{eq}^5}\exp\left[\frac{a}{\ln(\Phi_* + 1)}\right] = 1. \quad (19)$$

For $a \gg 1$, $\Phi_{max} \gg 1$, and $\Phi_* \sim 1$, Eq. (19) involves two multipliers, whose magnitudes differ appreciably from unity: $(Vt_D)^3/\theta_{eq}^5$ (small value) and the exponential function of the activation barrier of nucleation (large value). The first two multipliers can be set equal to unity with logarithmic accuracy. Hence, it follows that the approximated solution to Eq. (19) is

$$\Phi_* = \exp\left(\frac{a}{3\ln Q}\right) - 1. \quad (20)$$

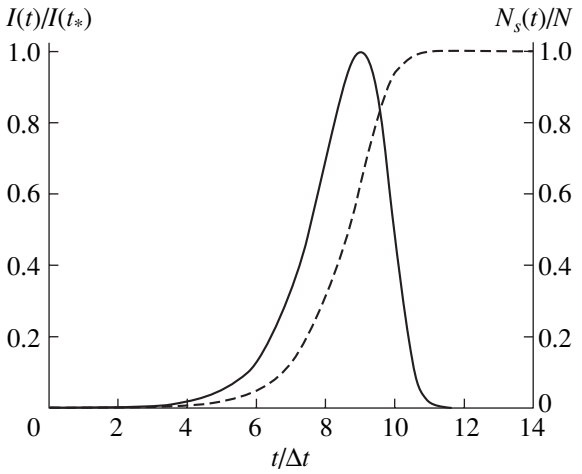

Fig. 2. Reduced nucleation rate $I/I(\zeta_*)$ (the solid line) for two-dimensional islands and their reduced surface density N_s/N (the dashed line) in relation to the dimensionless time $t/\Delta t$ for $t_*/\Delta t = 9$.

Here, Q is the kinetic control parameter [22] defined as

$$Q = \frac{1}{(\Phi_{\max}+1)Q_{\rm eq}^{1/3}}\frac{\tau_{\rm A}}{\tau_{\rm D}} = \frac{\theta_{\rm eq}^{2/3}}{V\tau_{\rm D}} = \frac{\theta_{\rm eq}^{5/3}}{Vt_{\rm D}} = \frac{\nu_{\rm D}}{V}\exp\left(\frac{-(5/3)\lambda - E_{\rm D}}{k_{\rm B}T}\right). \quad (21)$$

The applicability condition for the classical theory of condensation is a large value of the activation barrier of nucleation [11]. Therefore, the range of applicability of the theory is defined by the strong inequality $3\ln Q \gg 1$. We estimate the magnitude of Q for the growth conditions typical in the MBE and the material parameters corresponding to GaAs [20]: $T = 580$°C, $V = 0.1$ ML/s, $T_c = 2200$ K, $E_D = 0.8$ eV, $\nu_D = 3\times10^9$ s^{-1}, and $\sqrt{\sigma} = l_D$. In this case, $\theta_{\rm eq} = 6\times10^{-3}$, $t_D = 1.8\times10^{-5}$ s, $\tau_D = 3\times10^{-3}$ s, $Q = 110$, and $3\ln Q = 14.1$.

The substitution of Eq. (17) into Eq. (11) for the nucleation rate yields

$$I(t) = I(\Phi_*)\exp\left[\frac{t-t_*}{\Delta t} - \exp\left(\frac{t-t_*}{\Delta t}\right)\right]. \quad (22)$$

We find the island density N_s by integrating the nucleation rate over time:

$$N_s(t) = N\left\{1 - \exp\left[-\exp\left(\frac{t-t_*}{\Delta t}\right)\right]\right\}. \quad (23)$$

After completing the nucleation stage, the island density becomes a constant value $N = I(\Phi_*)\Delta t$, for which it follows from Eqs. (18) and (21) that

$$N = n_{\rm eq}\frac{\Gamma(1-\varepsilon)^2}{\theta_{\rm eq}^{2/3}2\Phi_*^3Q^2}. \quad (24)$$

In Eq. (24), we introduced the notation

$$\varepsilon \equiv \frac{\Phi_*+1}{\Phi_{\max}+1} = \frac{n_*}{J\tau_{\rm A}}. \quad (25)$$

The physical meaning of ε is the ratio of the highest adatom concentration n_* to its value $J\tau_A$, which would be established on the surface in the absence of nucleation. In the complete-condensation mode [2, 17], the value of ε is much smaller than unity. The time

$$\Delta t = \frac{\varepsilon}{1-\varepsilon}\frac{\Phi_*}{\Phi_*+1}\frac{\tau_{\rm A}}{\Gamma} \quad (26)$$

corresponds to the duration of the nucleation-stage. Finally, we found the time in which the supersaturation peak from Eq. (10) is attained to be

$$t_* = \tau_{\rm A}[-\ln(1-\varepsilon)]. \quad (27)$$

The obtained expressions solve the problem of an analytical description of the nucleation stage for the island growth of a film. For the model system with the parameters $T = 580$°C, $V = 0.1$ ML/s, $T_c = 2200$ K, $E_D = 0.8$ eV, $E_A = 2.1$ eV, $\nu_D = 3\times10^9$ s^{-1}, $\nu_A = 10^{12}$ s^{-1}, $a = 15$, and $\sqrt{\sigma} = 0.4$ nm, the island-nucleation characteristics are as follows: $\tau_A = 2.6$ s, $\Phi_{\max} = 43$, $\Phi_* = 1.9$, $\varepsilon = 0.065$ (the complete-condensation mode), $i_c(\Phi_*) = 14$, $\Gamma = 9.2$, $\Delta t = 0.011$ s, and $t_* = 0.17$ s. The island nucleation proceeds in a very narrow time interval, $2\Delta t \approx 0.02$ s, after the time $t_* \approx 0.2$ s following the onset of deposition of the material necessary for attaining the highest supersaturation by adatoms. After completing the nucleation, the island density attains the value $N = 5.5\times10^9$ cm^{-2}. In the complete-condensation mode, $t_* \approx \varepsilon\tau_A$; therefore,

$$\Delta t/t_* \sim 1/\Gamma \ll 1. \quad (28)$$

Inequality (28) shows that the duration of the nucleation-stage is much shorter than the nucleation-delay time τ_*. We show the typical time dependences for the nucleation rate and the surface island density in Fig. 2. From Eqs. (24), (21), and the Arrhenius temperature dependences for $n_{\rm eq}$ and t_D for $\Phi_* \sim 1$, it follows that the island density obtained in [23] depends on the deposition rate and temperature in the following way:

$$N \propto V^2\exp\left(\frac{3\lambda + 2E_{\rm D}}{k_{\rm B}T}\right). \quad (29)$$

Thus, the island density increases with as the deposition rate increases and surface temperature decreases.

4. STAGE OF INDEPENDENT ISLAND GROWTH

Since the equation of evolution for the size distribution function for supercritical islands is a first-order equation with a stationary boundary condition at zero and the growth rate of the islands is independent of their

size, we can immediately determine the size distribution of the islands [11] on the basis of the solution to (22). In terms of the size $\rho \equiv r/r_0 = t^{1/2}$, the distribution function is given by

$$f(\rho, t) = cN\exp\{c[\rho - \rho_*(t)] - e^{c[\rho-\rho_*(t)]}\}. \quad (30)$$

Here, $\rho_*(t)$ is the average size of islands nucleated for the highest supersaturation:

$$\rho_*(t) = \frac{1}{\tau_D}\int_{t_*}^{t} dt'\zeta(t'). \quad (31)$$

The constant c is determined from the condition $\int_0^\infty d\rho f(\rho) = \int_0^t dt' I(t')$:

$$c = \frac{\tau_D}{\Phi_*\Delta t} = (1-\varepsilon)\frac{\Gamma}{\Phi_*^2}\frac{1}{\theta_{eq}^{1/3}Q}. \quad (32)$$

Obviously, near the peak of $\rho_*(t)$, distribution function (30) has approximately a Gaussian form. The width of the size distribution

$$\Delta\rho \approx \frac{2\sqrt{2}}{c} \propto \frac{1}{V}\exp\left(-\frac{2\lambda - E_D}{k_B T}\right) \quad (33)$$

decreases as the deposition rate increases and temperature decreases. For the above model parameters, we have $c = 0.14$ and $\Delta\rho = 20$, which corresponds to $\Delta r = 8$ nm.

For a complete description of the island-growth process, it is necessary to find the island mean size as a function of time. Since the distribution function is rather narrow, we can use the δ approximation for $I(t)$ in an expression for the number of atoms in the islands at the independent-growth stage:

$$G(t) = \frac{N}{n_{eq}}\rho_*^2(t). \quad (34)$$

Substituting Eq. (34) into material-balance Eq. (8) and taking into account that $\zeta(t) \approx \Phi(t)$ for $t \le t_*$ and Eq. (31), we obtain an equation for an island average size:

$$\tau_D\frac{d\rho_*}{dt} + \frac{N}{n_{eq}}\rho_*^2 + \frac{\tau_D}{\tau_A}\rho_* = \Phi_* + \frac{\Phi_{max}}{\tau_A}(t - t_*). \quad (35)$$

In this case, the initial condition $\rho(t_*) = 0$. The exact solution to Eq. (35) is

$$\rho_*(t) = \rho_0[U(z) - \delta], \quad (36)$$

where the parameters are defined as follows:

$$\rho_0 \equiv \left(\frac{n_{eq}}{N}\right)^{2/3}\left(\frac{\tau_D}{\tau_A}\Phi_{max}\right)^{1/3}, \quad (37)$$

$$\delta \equiv \frac{1}{2^{2/3}(1-\varepsilon)^{2/3}\Gamma^{1/3}}\frac{\Phi_*}{\Phi_{max}^{1/3}(\Phi_{max}+1)^{2/3}}. \quad (38)$$

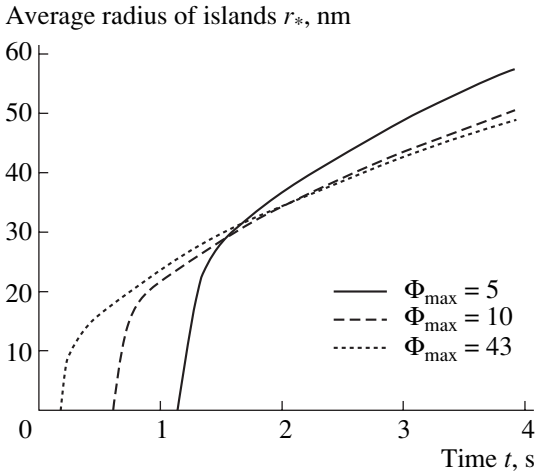

Fig. 3. Time dependences of the average lateral size $r_* = \sqrt{\sigma\rho_*}$ of the islands calculated using Eqs. (21), (22), (26), and (38)–(44) for the three different values of the highest gaseous-medium supersaturation $\Phi_{max} = 5$, 25, and 43, corresponding to different deposition rates V and the fixed surface temperature $T = 580°C$. The values of the parameters used in the calculation are given in the text. The case of $\Phi_{max} = 43$ corresponds to the average-size evolution for $V = 0.1$ ML/s and the distribution function shown in Fig. 4.

The function $U(z)$ in Eq. (36) is the ratio between linear combinations of the Airy functions Ai(z) and Bi(z) (Ai decreases and Bi increases at infinity [24]) and their derivatives

$$U(z) = \frac{\mathrm{Bi}'(z) - k|\mathrm{Ai}'(z)|}{\mathrm{Bi}(z) + k\mathrm{Ai}(z)},$$
$$k \equiv \frac{\mathrm{Bi}'(z_0) - \delta\mathrm{Bi}(z_0)}{|\mathrm{Ai}'(z_0)| + \delta\mathrm{Ai}(z_0)}. \quad (39)$$

The variable z linearly depends on time,

$$z(t) = \beta\left(1 + \mu + \frac{\Phi_{max}}{\Phi_*}\frac{(t - t_*)}{\tau_A}\right), \quad (40)$$

with the coefficients

$$\beta \equiv \left(\frac{\Gamma}{2}\right)^{1/3}\left(\frac{\Phi_{max}+1}{\Phi_{max}}\right)^{2/3}(1-\varepsilon)^{2/3}, \quad (41)$$

$$\mu \equiv \frac{\varepsilon^2}{2\Gamma}\left(\frac{\Phi_*}{\Phi_*+1}\right)^2\frac{1}{(1-\varepsilon)^2}, \quad (42)$$

and $z_0 \equiv z(t = 0) = \beta(1 + \mu)$. We show the results obtained by solving Eqs. (36)–(42) for various parameters in Fig. 3.

Let us consider the obtained solution in the complete-condensation mode ($\varepsilon \ll 1$). Then, $\delta \sim \varepsilon/\Gamma^{1/3} \ll 1$ and $\mu \sim \varepsilon^2/\Gamma \ll 1$, while the parameter β always exceeds 1.5 (in our example, $\beta = 1.62$) for large Γ and small ε. Therefore, we can pass to the limit $\delta \longrightarrow 0$ and $\mu \longrightarrow 0$.

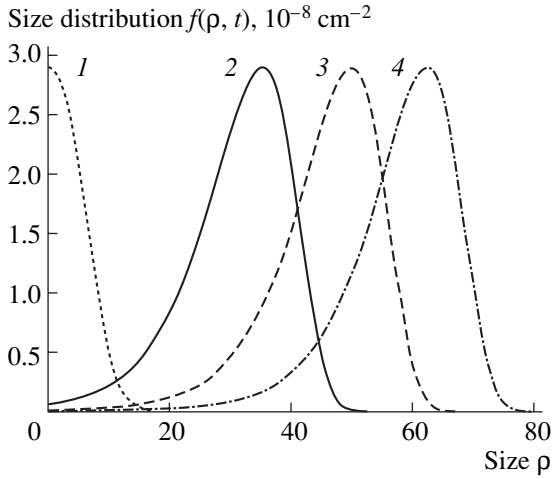

Fig. 4. Size distribution function for islands at the time t = (*1*) t_*, (*2*) $t_* + 0.5t_g$, (*3*) $t_* + t_g$, and (*4*) $t_* + 2t_g$. The values of the parameters used in the calculation are given in the text.

Because $z > \beta$, it is possible to use the asymptotic functions for the Airy functions at large z: $\mathrm{Ai}(z) = (1/2)\pi^{1/2}z^{1/4}\exp[-(2/3)z^{3/2}]$ and $\mathrm{Bi}(z) = (1/\pi^{1/2}z^{1/4})\exp[(2/3)z^{3/2}]$ [24]. As a result, the solution for the average size is greatly simplified:

$$\rho_*(x) = \sqrt{\frac{\Phi_*\theta_{eq} + x}{\sigma N}}\tanh\left\{A\left[\left(\frac{\Phi_*\theta_{eq} + x}{\Phi_*\theta_{eq}}\right)^{3/2} - 1\right]\right\}. \quad (43)$$

Here,

$$A \equiv \frac{2}{3}\beta^{3/2} = \frac{\sqrt{2\Gamma}}{3}\left(\frac{\Phi_{max}}{\Phi_{max} + 1}\right)(1 - \varepsilon). \quad (44)$$

In Eq. (43), we introduced the dimensionless variable x, which is related to the deposition time as follows:

$$x \equiv (1 - D)V(t - t_*). \quad (45)$$

Here, $D \equiv n_{eq}/J\tau_A = \theta_{eq}/V\tau_A$ is the desorption term. The physical meaning of the variable x is obvious: it is the number of material monolayers formed on the surface in the time t taking into account the desorption (D) and the island-nucleation delay (t_*). Solution (45) for the average size shows that, at the very beginning of growth, the islands grow very rapidly and, for the time $t_g \approx (\Phi_*/\Phi_{max})\tau_A \sim \varepsilon\tau_A$, follow the asymptotic dependence

$$\rho_*(x) = \sqrt{\frac{\Phi_*\theta_{eq} + x}{\sigma N}}. \quad (46)$$

After the time $t_{diff} \sim 5t_g$, following the onset of nucleation, the law for which the island radius grows proportionally to $(t - t_*)^{1/2}$: $\rho = (x/\sigma N)^{1/2}$ comes into effect. The average size of the islands at the fixed instant of time t decreases as the deposition rate increases and increases with the surface temperature as follows:

$$\rho_* \propto \sqrt{\frac{Vt}{N}} \propto \frac{1}{V^{1/2}}\exp\left(\frac{-(3/2)\lambda - E_D}{k_B T}\right)t^{1/2}. \quad (47)$$

The evolution of the size distribution function for the islands at the independent-growth stage for the model system is shown in Fig. 4.

5. THREE-DIMENSIONAL FILM GROWTH

Using Eqs. (5), (34), and (46) and taking into account that $g = \theta_{eq}G$, we obtain the following elementary formula for the degree of filling of the surface in the complete-condensation mode:

$$\psi(x) = 1 - e^{-x}. \quad (48)$$

The monolayer-formation time is

$$t_{ML} = t_* + \frac{1}{(1 - D)V}. \quad (49)$$

For the model system under consideration, the values of D and t_* are small: $D = 2.3 \times 10^{-2}$ and $t_* = 0.17$ s; therefore, the monolayer-formation time only slightly differs from $1/V$: $t_{ML} = 10.4$ s.

In the case of pure layer-by-layer high-temperature growth, the vertical-growth rate of a film is determined from Eqs. (7) and (49) as

$$V_s = \frac{(1 - D)V}{1 + (1 - D)Vt_*}. \quad (50)$$

For investigating a three-dimensional film surface, we introduce the probabilities $p_k(t)$ for detecting a random point on the film surface at a height of k monolayers at the moment of time t [19]. According to Fig. 1, if the layers do not overhang each other, we have

$$p_k(t) = \psi_k(t) - \psi_{k+1}(t) \quad (\psi_0 \equiv 1), \quad (51)$$

where $\psi_k(t)$ is the surface filling fraction by the kth film layer at the moment of time t. The average thickness $H(t)$ and the surface roughness $R(t)$ of a film expressed in terms of the monolayer height are determined according to the expressions

$$H(t) = \sum_{k \geq 1} k p_k(t), \quad R^2(t) = \sum_{k \geq 1} k^2 p_k(t) - H^2(t). \quad (52)$$

For pure layer-by-layer growth, it suffices to consider only $k = 0$ and $k = 1$ in Eq. (51). Then, $p_0(t) = 1 - \psi(t)$, $p_1(t) = \psi(t)$, and $H(t) = \psi(t)$, and the filling of one layer over another periodically repeats. The film-surface roughness $R(t)$ is a periodic function of time with a period approximately equal to the monolayer growth rate t_{ML}. As a function of x, the squared roughness is expressed as

$$R^2(x) = (1 - e^{-x})e^{-x}. \quad (53)$$

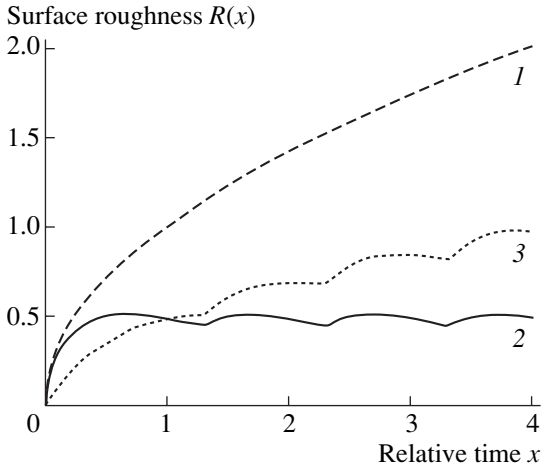

Fig. 5. Roughness as a function of the dimensionless time x (in units of the monolayer growth time) for the cases of (*1*) low-temperature polylayer growth, (*2*) high-temperature layer-by-layer growth, and (*3*) an intermediate mode.

In the case of low-temperature polylayer growth, the following integral relations [18] connect the degrees of filling of the surface by various layers:

$$\psi_{k+1}(x) = \int_0^x dx' F_{k+1}(x-x')\psi_k(x'), \qquad (54)$$

$$F_{k+1}(x) = -\frac{d}{dx}\exp[-g_{k+1}(x)].$$

Here, $g_k(x)$ is a function describing the filling kinetics of the kth layer over the completely filled previous layer. In the complete-condensation mode during autoepitaxy, all $F_k(x) = e^{-x}$; we then use Eqs. (54) and (51) to find that $dp_k/dx = p_{k-1} - p_k$. This set of equations gives a Poisson height distribution for film-surface points:

$$p_k(x) = \frac{x^k}{k!}e^{-x}. \qquad (55)$$

In this case, the film height is equal to the square of the roughness of its surface:

$$H(x) = R^2(x) = x. \qquad (56)$$

Figure 5 illustrates two limiting cases for the behavior of the average height and roughness of the film surface. In the same figure, we qualitatively show the intermediate mode, in which the surface roughness behaves in time in the form of a function of $t^{1/2}$ with oscillations imposed on it. Data from direct computer simulation, including the autoepitaxial growth of GaAs [19, 21], corroborate such behavior of the surface roughness during MBE growth. It should also be noted that MBE allows in situ visualization of the surface state in the reciprocal space using reflection high-energy electron diffraction (RHEED) [4]. The character of the dynamic dependence of the mirror reflection during the layer-by-layer growth (or close to it) is oscillatory, with the period being equal to the layer-formation time. In addition, the peak in this dependence corresponds to a virtually filled layer, while the lowest diffraction intensity reflects the presence of unfilled layer areas. Thus, the obtained time dependences of the surface roughness can be made to conform to dynamic RHEED dependences transformed into the direct space.

6. CONCLUSIONS

We now formulate the main physical results of the performed theoretical consideration of thin-film growth. At the stage of nucleation of two-dimensional islands, which occurs in very narrow time interval, the size distribution function for islands is formed. The surface island density attains its maximum upon completing the nucleation stage, remains constant at the stage of isolated island growth, and decreases only after the onset of coalescence. The island density increases and their size decreases as the surface temperature decreases and deposition rate increases. At the stage of isolated island growth, the size distribution of the islands does not change its shape and shifts as a whole along the size axis. The spread in sizes decreases as the deposition rate increases and the surface temperature decreases. The average size of the islands grows proportionally to $t^{1/2}$ in the complete-condensation mode typical of the MBE for most of the time. The coalescence of the islands results in the formation of a continuous layer; the degree of filling of the surface depends on time in the following way: $1 - \exp(-t/t_{ML})$. For high-temperature pure layer-by-layer growth, the filling of the layers periodically repeats. The average film height increases linearly with time, and the roughness is a periodic function of time. During low-temperature polylayer growth, a Poisson surface profile is formed for which the square of roughness is equal to the average height, and both these quantities increase proportionally to the deposition time. In the intermediate mode, the surface roughness varies in proportion to $t^{1/2}$, with oscillations imposed on this dependence.

Thus, in this paper, we have presented a kinetic model of formation of thin films that enables us to describe all the stages of film formation in an analytical form in relation to the conditions of growth and physical parameters of the system. We show that the stages of nucleation, independent growth, and coalescence of islands are essentially separated in time for the complete-condensation mode characteristic of the MBE and its variants, which greatly facilitates finding solutions to the problem of theoretical description of the growth process. The obtained analytical expressions for the average sizes of the islands, their surface density and the spread in their sizes, and the film-surface average height and roughness can be used in calculations and for optimization of the growth modes in particular systems.

ACKNOWLEDGMENTS

This study was supported by the Russian Foundation for Basic Research, project no. 05-0216568.

REFERENCES

1. Zh. I. Alferov, Fiz. Tekh. Poluprovodn. (St. Petersburg) **32**, 3 (1998) [Semiconductors **32**, 1 (1998)].
2. S. A. Kukushkin and A. V. Osipov, Usp. Fiz. Nauk **168**, 1083 (1998) [Phys. Usp. **41**, 983 (1998)].
3. A. A. Chernov, E. I. Givargizov, Kh. S. Bagdasarov, *et al.*, in *Modern Crystallography*, Vol. 3: *Crystal Growth*, Ed. by B. K. Vaĭnshteĭn, A. A. Chernov, and L. A. Shuvalov (Nauka, Moscow, 1980; Springer, Berlin, 1984).
4. A. Y. Cho and J. R. Arthur, Prog. Solid State Chem. **10**, 157 (1975).
5. A. V. Osipov, Thin Solid Films **277**, 111 (1993).
6. S. A. Kukushkin and A. V. Osipov, J. Chem. Phys. **107**, 3247 (1997).
7. S. A. Kukushkin and A. V. Osipov, Fiz. Tverd. Tela (St. Petersburg) **38**, 443 (1996) [Phys. Solid State **38**, 244 (1996)].
8. S. A. Kukushkin and V. V. Slezov, *Disperse Systems on Solid Surfaces* (Nauka, St. Petersburg, 1996) [in Russian].
9. D. Kashchiev, *Nucleation: Basic Theory with Applications* (Butterworth Heinemann, Oxford, 2000).
10. I. M. Lifshits and V. V. Slezov, Zh. Éksp. Teor. Fiz. **35**, 479 (1958) [Sov. Phys. JETP **8**, 331 (1959)].
11. F. M. Kuni, Preprint No. 84-178.E (Inst. of Theoretical Physics, Kiev, 1984).
12. F. M. Kuni and A. P. Grinin, Kolloidn. Zh. **46**, 23 (1984).
13. K. Binder, Phys. Rev. B **15**, 4425 (1977).
14. A. N. Kolmogorov, Izv. Akad. Nauk SSSR, Ser. Mat. **3**, 355 (1937).
15. V. Z. Belen'kiĭ, *Geometric–Probabilistic Models of Crystallization* (Nauka, Moscow, 1980) [in Russian].
16. V. I. Trofimov and V. A. Osadchenko, *Growth and Morphology of Thin Films* (Énergoatomizdat, Moscow, 1993) [in Russian].
17. V. G. Dubrovskii, Phys. Status Solidi B **171**, 345 (1992).
18. D. Kashchiev, J. Cryst. Growth **40**, 29 (1977).
19. V. G. Dubrovskiĭ and G. E. Cirlin, Zh. Tekh. Fiz. **67** (11), 136 (1997) [Tech. Phys. **42**, 1365 (1997)].
20. A. G. Filaretov and G. E. Cirlin, Fiz. Tverd. Tela (Leningrad) **33**, 1329 (1991) [Sov. Phys. Solid State **33**, 751 (1991)].
21. G. E. Tsyrlin, Pis'ma Zh. Tekh. Fiz. **23** (4), 61 (1997) [Tech. Phys. Lett. **23**, 154 (1997)].
22. V. G. Dubrovskiĭ, Yu. G. Musikhin, G. E. Cirlin, *et al.*, Fiz. Tekh. Poluprovodn. (St. Petersburg) **38**, 342 (2004) [Semiconductors **38**, 329 (2004)].
23. V. G. Dubrovskii, J. Phys.: Condens. Matter **16**, 6929 (2004).
24. *Handbook of Mathematical Functions*, Ed. by M. Abramowitz and I. A. Stegun (Dover, New York, 1971; Nauka, Moscow, 1979).

Translated by V. Bukhanov

Semiconductors, Vol. 39, No. 11, 2005, pp. 1275–1279. Translated from Fizika i Tekhnika Poluprovodnikov, Vol. 39, No. 11, 2005, pp. 1320–1324.

ATOMIC STRUCTURE AND NONELECTRONIC PROPERTIES OF SEMICONDUCTORS

Hydrogen Desorption from the Surface under the Conditions of Epitaxial Growth of Silicon Layers from Monosilane in Vacuum

L. K. Orlov*^ and T. N. Smyslova**

**Institute for Physics of Microstructures, Russian Academy of Sciences, Nizhni Novgorod, 603950 Russia*

^e-mail: orlov@ipm.sci.-nnov.ru

***All-Russia Research Institute of Experimental Physics, Sarov, 607190 Russia*

Submitted February 10, 2005; accepted for publication March 22, 2005

Abstract—For the first time, the desorption coefficient of hydrogen and activation energy of desorption are directly determined during the growth of an Si epitaxial layer from silane in vacuum using experimental data on the degree of surface coverage of an Si wafer with hydrogen. The results obtained are compared with earlier results obtained under low-temperature conditions, for example, by thermodesorption spectrometry. The found values are used to calculate the crystallization coefficient and its dependence on the growth temperature and decomposition rate for monosilane at the growth surface. © *2005 Pleiades Publishing, Inc.*

In recent years, the effect of hydrogen on the characteristics of materials has been widely discussed in the literature in relation to the development of methods for detecting hydrogen in crystals and its role in the formation of microdefects in Si [1]. The spectroscopy of hydrogen bound in Si crystals is of special interest, in particular, the spectroscopy of the rotational–vibrational lines of SiH_n molecules captured by the surface or incorporated into Si crystals. These lines are located in the mid-IR and far-IR spectral regions [2–4]. Analysis of the properties and characteristics of hydrogen complexes is impossible without the development of methods for determining their surface or bulk concentrations and the parameters that determine these concentrations, specifically, the desorption coefficient of hydrogen. These methods can sometimes be very indirect.

In practice, the emergence of hydrogen in epitaxial Si is associated with the metal–hydride technology used for film growth. The accumulation of hydrogen on the surface during such growth also leads to its emergence in the layer. This phenomenon leads to passivation of dangling bonds at the defects in the crystals and to improvement of its electrical characteristics, which most clearly manifests itself for hydrogenated amorphous Si. At the same time, passivation of the surface bonds with hydrogen under low-temperature epitaxial conditions results in a substantial decrease in the film growth rate, thereby restricting the potential of using metal–hydride vacuum epitaxy to grow multilayer heterostructures, including quantum-dimensional structures.

In this context, the development of methods for directly analyzing the characteristics of the surface hydrogen under technological conditions and for determining the hydrogen desorption characteristics, along with the problem of hydrogen dissolution in Si, is of fundamental importance (in addition to the application-oriented importance). The reason is that these aspects are important if we are to gain a deeper insight into such phenomena and to study the surface physicochemical processes often under strongly nonequilibrium conditions. However, there is a considerable spread of data on the hydrogen desorption rate in the relevant publications. Temperature dependences of the hydrogen desorption coefficient that have been obtained or used in reports by various authors are given in [5]. It follows from these data that the spread of the parameter χ at a specific growth temperature for the same activation energy is at least two orders of magnitude of the quantity $\chi_0 = 8 \times 10^{13 \pm 1}$ s^{-1}. Subsequently, using the suggested calculation procedure and data on hydrogen desorption from the Si surface, we refined the value of the desorption parameter experimentally determined in the temperature range 450–650°C under real growth conditions [6]. This procedure allowed us to predict the temperature dependence of this parameter for the region of higher temperatures.

According to the above, the purpose of this study was to analyze the kinetics of the pyrolytic decomposition of hydrides on the epitaxial Si surface so as to subsequently determine the surface concentration of hydrogen, the characteristics of the bond between hydrogen and the surface, the effects of incorporation of hydrogen atoms into the crystals, and mechanisms of hydrogen dissolution in Si. In contrast to other studies, where, in particular, the methods of thermally controlled desorption spectroscopy were used to determine the hydrogen desorption coefficient [7, 8], the specific feature of this study is that we used data from technological experiments, which are widely available in the literature for several aspects of the problem.

As the main method of solving the specified problem, we used a set of kinetic equations that describes

Table

T_{gr}, °C	V_{gr}, Å/s	$\theta_H = n_{sH}/n_s$
800	0.39	
750	0.373	
700	0.328	
650	0.250	0.02
600	0.183	0.05
550	0.109	0.22
500	0.049	0.5
450	0.0167	0.8

the chain of physicochemical processes involved in a molecule's decomposition on a hot surface. This set relates variations in the dimensionless concentrations θ_i of atoms and molecules adsorbed by the growth surface to the molecular flow of hydride that reaches the surface [9]. In order to solve the problem adequately and to calculate the surface concentrations of hydride-decomposition products it is necessary, in most cases, to determine or refine the constants that appear in the kinetic equations and are responsible for the rate of a particular process on the growth surface. These constants can be found by including expressions that determine the growth and composition of the growing epitaxial layer in the main equations of the set. The final choice of the operational set of equations used to analyze pyrolysis and crystallization is governed by the composition or types of gases employed as well as by the selection of a specific scheme of their decomposition.

We previously considered a general set of equations that describes, in particular, the effect of the decomposition kinetics for hydrides on the surface of an epitaxial film on the steady-state growth of a $Si_{1-x}Ge_x$ layer [10, 11]. In the most general case, the set includes a large number of equations that are specified by the type of surface reactions. These reactions can include both monomolecular and bimolecular decomposition, with undefined kinetic coefficients being present in an overwhelming number of cases. At this stage, we considered the simplest system with only one gas, specifically, silicon monohydride. Experimental data relating to this gas are widely available in publications.

In this study, along with the simplest scheme (model) of silane decomposition [10],

$$\begin{gathered}SiH_4(g) + \underline{2} \longrightarrow \underline{Si}H_3 + \underline{H}, \quad \underline{Si}H_3 + \underline{3} \longrightarrow \underline{Si} + 3\underline{H}, \\ \underline{Si} \longrightarrow Si(cr), \quad \underline{H} \longrightarrow 1/2H_2(g),\end{gathered} \tag{1}$$

which is most often used for calculations, we considered other schemes (models) of decomposition of a SiH_4 molecule suggested in previous publications (see, for example, [12]):

$$\begin{gathered}SiH_4(g) + \underline{1} \longrightarrow \underline{Si}H_2 + \underline{H}_2(g), \\ \underline{Si}H_2 + \underline{2} \longrightarrow \underline{Si} + 2\underline{H}, \\ \underline{Si} \longrightarrow Si(cr), \quad \underline{H} \longrightarrow 1/2H_2(g),\end{gathered} \tag{2}$$

$$\begin{gathered}SiH_4(g) + \underline{1} \longrightarrow \underline{Si}H_2 + \underline{H}_2(g), \\ 2\underline{Si}H_2 + \underline{2} \longrightarrow 2\underline{Si} + 2\underline{H} + H_2(g), \\ \underline{Si} \longrightarrow Si(cr), \quad \underline{H} \longrightarrow 1/2H_2(g),\end{gathered} \tag{3}$$

$$\begin{gathered}SiH_4(g) + \underline{3} \longrightarrow \underline{Si}H_2 + 2\underline{H}, \\ \underline{Si}H_2 \longrightarrow \underline{Si} + H_2(g), \\ \underline{Si} \longrightarrow Si(cr), \quad \underline{H} \longrightarrow 1/2H_2(g),\end{gathered} \tag{4}$$

$$\begin{gathered}SiH_4(g) + \underline{3} \longrightarrow SiH + 2\underline{H} + 1/2H_2(g), \\ SiH \longrightarrow Si + 1/2H_2(g), \\ \underline{Si} \longrightarrow Si(cr), \quad \underline{H} \longrightarrow 1/2H_2(g).\end{gathered} \tag{5}$$

In models (1)–(5), the underlined chemical symbol indicates that an atom is bonded to the surface, and the underlined digit indicates the number of free bonds on the surface that are necessary for the reaction to proceed.

The presented reactions are based on different assumptions related to the surface concentration of hydrogen atoms and hydride radicals, which play the most important role in surface processes. The choice of the corresponding molecule in models (1)–(5) is associated with the assumption that this molecule decomposes the most slowly on the growth surface.

The main parameters that should be determined in this problem are the surface dimensionless atomic and molecular concentrations θ_{Si}, θ_H, and θ_{SiH_n} in reference to the concentration of surface bonds $n_s = 6.78 \times 10^{14}$ cm^{-2}, the hydride decomposition frequency $\nu = \nu_0 \exp(-E^a_{SiH_n}/kT)$, the hydrogen desorption rate $\chi = \chi_0 \exp(-E^a_H/kT)$, and the crystallization coefficient of the Si atoms $r(\theta_j, T)$. Several free parameters of the problem, particularly r and χ, can be redefined using experimental data, for example, on the temperature dependences of the film growth rate $V_{gr} = (n_s/n_0) r \theta_{Si}$ and the surface hydrogen concentration. Here, $n_0 = 5.5 \times 10^{22}$ cm^{-3}.

The corresponding data, obtained by analysis of numerous reports on the determination of the growth rate of Si film (see, for example, [13]) and reports on the measurement of the surface hydrogen concentration during growth [6, 14, 15], are given in the table. The tabulated data were chosen according to the most frequently used silane pressure in the reactor: $P_{SiH_4} \approx 0.3$ mTorr. The experimental values of the quantity θ_H

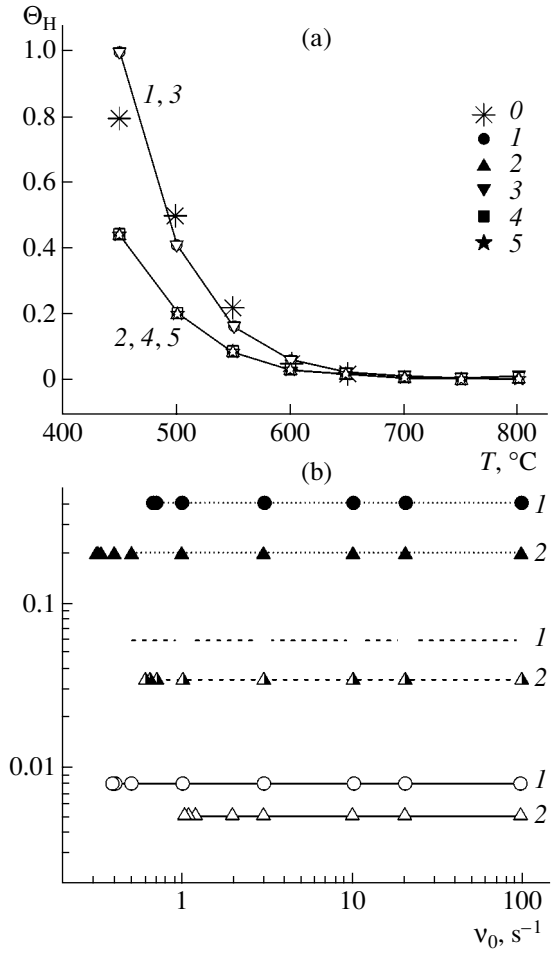

Fig. 1. Dependences of the surface concentration of hydrogen on (a) temperature and (b) monosilane decomposition frequency. (a) Points *0* are the experimental data [6], and the lines represent calculated curves *1–5*, obtained in the context of models 1–5, for $\nu_0 = 96\ s^{-1}$ and $\chi_0 = (1)\ 8 \times 10^{11}$; (*3*) 2×10^{11}; and (*2*, *4*, and *5*) $4 \times 10^{11}\ s^{-1}$. (b) The dependences calculated in the context of models 1 (curve *1*, $\chi_0 = 8 \times 10^{11}\ s^{-1}$) and 2 (curve *2*, $\chi_0 = 4 \times 10^{11}\ s^{-1}$) are represented by solid lines and open symbols at 700°C, by dashed lines and half-closed symbols at 600°C, and dotted lines and closed symbols at 500°C. The values used in calculations were $P = 0.3$ mTorr, $E^a_{SiH_3} = 0.08$ eV, and $E^a_H = 1.755$ eV.

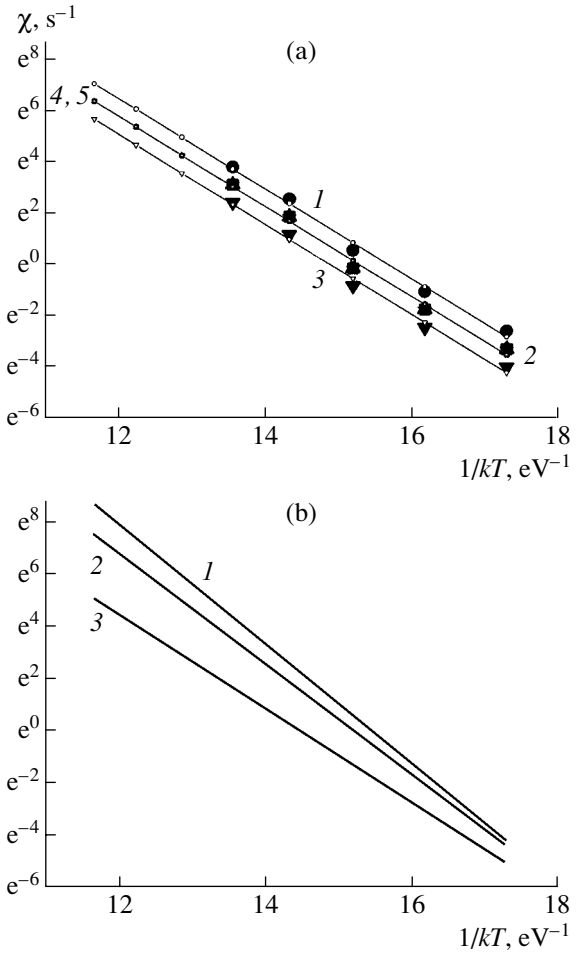

Fig. 2. Temperature dependences of the hydrogen desorption coefficient χ. (a) Calculation using model 1 (curve *1*, $\chi_0 = 8 \times 10^{11}\ s^{-1}$); models 2, 4, and 5 (curve *2*; symbols *2*, *4*, and *5*; $\chi_0 = 4 \times 10^{11}\ s^{-1}$); and model 3 based on the experimental data [6] $P = 0.3$ mTorr, $E^a_{SiH_3} = 0.08$ eV, $\nu_0 = 96\ s^{-1}$, and $E^a_H = 1.755$ eV (curve *3*, $\chi_0 = 2 \times 10^{11}\ s^{-1}$). (b) The previous experimental data corresponding to $\chi_0 = 2.1 \times 10^{15}\ s^{-1}$ and $E^a_H = 2.28$ eV [16] (curve *1*), $\chi_0 = 8 \times 10^{13}\ s^{-1}$ and $E^a_H = 2.1$ eV [5] (curve *2*), and $\chi_0 = 2.2 \times 10^{11}\ s^{-1}$ and $E^a_H = 1.8$ eV [17] (curve *3*).

listed in the table were taken from [6]. These data are shown in Fig. 1a (symbol *0*).

In order to solve the problem defined in the kinetic equations written for the above-mentioned growth models, the quantity χ was chosen as the desired function. The concentration of adsorbed hydrogen θ_H was considered as a parameter of the problem. Using these values of θ_H as one of the main parameters of the problem, it was easy to determine the desorption coefficient χ for all the growth temperatures listed in the table on the basis of the corresponding set of kinetic equations. This calculation procedure is possible for an unambiguous determination of the hydrogen desorption coefficient, since, as follows from Fig. 1b, the surface concentration of hydrogen is completely independent of the monosilane decomposition rate ν for various decay models in a wide range of growth temperatures. The values of the hydrogen desorption parameter χ, which were calculated on the basis of the experimental data in the context of the used models, are shown by closed symbols in Fig. 2a. In the context of the activation dependence of the hydrogen desorption coefficient χ =

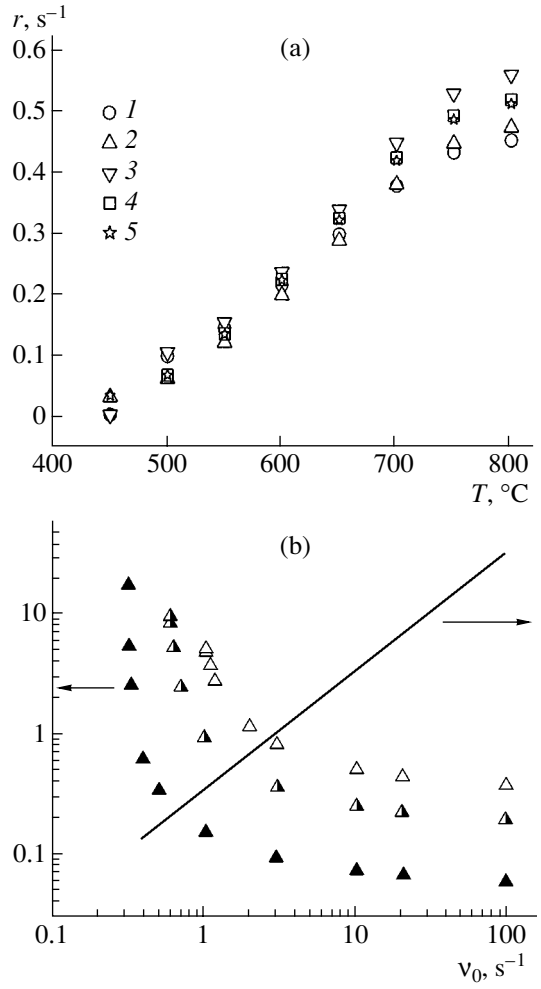

Fig. 3. Dependences of the crystallization coefficient r on (a) temperature and (b) monosilane decomposition frequency. (a) Calculated curves obtained for $\nu_0 = 96\ s^{-1}$ on the basis of the dependence $\chi = \chi_0 \exp(-E_H^a/kT)$ in the context of various models. Model 1, with $\chi_0 = 8 \times 10^{11}\ s^{-1}$, corresponds to symbol *1*; model 3, with $\chi_0 = 2 \times 10^{11}\ s^{-1}$, corresponds to symbol *3*; and models 2, 4, and 5, with $\chi_0 = 4 \times 10^{11}\ s^{-1}$, correspond to symbols *2*, *4*, and *5*, respectively. (b) Dependences calculated in the context of model 2, with $\chi_0 = 4 \times 10^{11}\ s^{-1}$, at three growth temperatures are shown by the open symbols *2* at 700°C; half-closed symbols *2* at 600°C; and closed symbols, $\nu = \nu_0 \exp(-E^a_{SiH_n}/kT)$, at 500°C. The values of the parameters used in the calculations were $P = 0.03$ mTorr, $E^a_{SiH_3} = 0.08$ eV, and $E^a_H = 1.755$ eV. The straight line shows the relation between ν and ν_0.

$\chi_0 \exp(-E_H^a/kT)$, for example, using the method of conjugate gradients, it is easy to choose the parameters χ_0 and E_H^a and to construct the dependences $\chi(T)$ that most closely coincide with the values of χ obtained on the basis of the experimental data. The corresponding dependences are shown in Fig. 2a (straight lines and open symbols). For all the models, we obtained an approximately identical activation energy $E_H^a = 1.75$–1.76 eV and determined the preexponential factor, which was found to be equal to $8 \times 10^{11}\ s^{-1}$ for model 1; $4 \times 10^{11}\ s^{-1}$ for models 2, 4, and 5; and $2 \times 10^{11}\ s^{-1}$ for model 3. The activation-energy dependences of the hydrogen desorption coefficient, which were obtained by other authors using methods distinct from our method, are shown in Fig. 2b for comparison. Comparison of the curves shows that the results obtained in [5, 16] most closely agree, with regard to the absolute value of the coefficient χ, with the results of the calculations we carried out in the context of models 1, 2, 4, and 5. However, there are large distinctions in the activation energies of this process. The results of calculations carried out in the context of model 3 are close to the results of [7, 17] in relation to both the activation energy and the preexponential factor. The performed calculations and comparative analysis allows us to conclude that the coefficient of hydrogen desorption from the Si surface has an activation energy close to $E_a \approx 1.7$–1.8 eV and a preexponential factor χ_0 in the range $(2$–$4) \times 10^{11}\ s^{-1}$.

Using the found values of the hydrogen desorption coefficient and taking into account that θ_H is independent of the silane decomposition frequency, it is easy to solve an inverse problem and recalculate the temperature dependence of the surface concentration of hydrogen over the entire range of growth temperatures most relevant from a technological standpoint in the context of the models under consideration (Fig. 1a). Comparison of the theoretical curves with the experimental points shows that the best agreement of the experimental data with the calculated curves obtained in the context of models 1 and 3 is observed at temperatures above 500°C. In particular, Fig. 1 shows that, below 500°C, the coverage of the surface with hydrogen tends to the upper limit $\theta_H \approx 1$. It is noteworthy that the absence of any dependence of surface hydrogen coverage on the monosilane decomposition rate is not related to the possible considerable difference between the rates of each of these processes. For example, this inference can be derived from a comparison of the dependence $\chi(T)$ in Fig. 2 with the dependence $\nu(\nu_0, T)$, which is shown in Fig. 3b. It can be seen that the abovementioned quantities have comparable values in a wide temperature range.

Another important parameter of the system, which depends strongly on the degree of coverage of the surface with hydrogen, is the crystallization coefficient of the Si atoms. However, in contrast to θ_H, this coefficient is very sensitive both to the growth temperature and to the hydride decomposition frequency on a hot surface. As an example, Fig. 3a shows the dependence $r(T)$ for various schemes of monohydride decomposition at $\nu = \nu_0 \exp(-E^a_{SiH_m}/kT)$ with $\nu_0 = 96\ s^{-1}$ [18] and $E^a_{SiH_m} =$

0.08 eV [19]. For the chosen values of the parameters, the characteristic decomposition rate, $\nu \approx 36\ s^{-1}$, far exceeds the crystallization rate r. According to Fig. 3b, the value of r in the temperature range $T_{gr} = 500$–$800°C$ varies in the range $r = 0.05$–0.5. A decrease in the preexponential factor ν_0 to a value of ≤ 1 leads to a considerable increase in the crystallization coefficient, as there is an increase in the concentration of dangling bonds on the growth surface.

It is noteworthy that, when carrying out the analysis, we exclusively considered the desorption component in the term describing hydrogen escape from the surface. We completely disregarded the possibility that hydrogen atoms are incorporated into the growing layer. However, experience shows that the hydrogen concentration in Si is rather high. It is possible that consideration of this effect could help to eliminate the difficulties encountered when determining the hydrogen absorption coefficient by this method and by thermal desorption spectroscopy.

We thank Cand. Sci. (Phys.–Math.) A.V. Potapov for her contributions to discussions and useful comments and S.A. Nikitina for help with the calculations.

This study was supported by the International Science and Technology Center (project no. 2372).

REFERENCES

1. V. I. Talanin, I. E. Talanin, and D. I. Levinson, in *Proceedings of 4th International Conference on Single Crystal Growth and Heat and Mass Transfer* (Obninsk, Russia, 2001), Vol. 1, p. 205.
2. G. Weirauch, A. Campargue, and H. Burger, J. Mol. Spectrosc. **218**, 256 (2003).
3. M. C. McCarthy and P. Thaddeus, J. Mol. Spectrosc. **222**, 248 (2003).
4. M. Shinohara, T. Kuwano, Y. Kimura, and M. Niwano, Thin Solid Films **435**, 13 (2003).
5. C. M. Greenlief and M. Lier, Appl. Phys. Lett. **64**, 601 (1994).
6. K. J. Kim, M. Suemitsu, M. Yamanaka, and N. Miyamoto, Appl. Phys. Lett. **62**, 3461 (1993).
7. R. W. Price, E. S. Tok, and J. Zhang, J. Cryst. Growth **209**, 306 (2000).
8. M. C. Flowers, N. B. H. Jonathan, Y. Liu, and A. Morris, J. Chem. Phys. **102**, 1034 (1995).
9. D. W. Greve, Mater. Sci. Eng. B **18**, 22 (1993).
10. A. V. Potapov, L. K. Orlov, and S. V. Ivin, Thin Solid Films **336**, 191 (1999).
11. L. K. Orlov, S. V. Ivin, A. V. Potapov, and T. L. Ivina, Zh. Tekh. Fiz. **71** (4), 53 (2001) [Tech. Phys. **46**, 417 (2001)].
12. S. M. Gates, C. M. Greenlief, and D. B. Beach, J. Chem. Phys. **93**, 7493 (1990).
13. E. V. Thomsen and C. Christensen, Thin Solid Films **294**, 72 (1997).
14. K. Sakamoto, H. Matsuhata, K. Miki, and T. Sakamoto, J. Cryst. Growth **157**, 295 (1995).
15. S. M. Gates and S. K. Kilkarni, Appl. Phys. Lett. **60**, 53 (1992).
16. U. Höfer, L. Li, and T. F. Heinz, Phys. Rev. B **45**, 9485 (1992).
17. K. Sinniah, M. G. Sherman, L. B. Lewis, *et al.*, Phys. Rev. Lett. **62**, 567 (1989); J. Chem. Phys. **92**, 5700 (1990).
18. T. R. Bramblett, Q. Lu, T. Karasawa, *et al.*, J. Appl. Phys. **76**, 1884 (1994).
19. A. Vittadini and A. Selloni, Phys. Rev. Lett. **75**, 4756 (1995).

Translated by N. Korovin

Semiconductors, Vol. 39, No. 11, 2005, pp. 1280–1284. Translated from Fizika i Tekhnika Poluprovodnikov, Vol. 39, No. 11, 2005, pp. 1325–1330.

ATOMIC STRUCTURE AND NONELECTRONIC PROPERTIES OF SEMICONDUCTORS

Adsorption, Desorption, and Contact and Thermal Transformation of C_{60} Molecules on a Ta(100) Surface

N. R. Gall'^, E. V. Rut'kov, and A. Ya. Tontegode†

Ioffe Physicotechnical Institute, Russian Academy of Sciences, Politekhnicheskaya ul. 26, St. Petersburg, 194021 Russia

^e-mail: gall@ms.ioffe.ru

Submitted March 15, 2005; accepted for publication March 29, 2005

Abstract—The adsorption, desorption, initial film growth, and contact and thermal transformation of C_{60} molecules on a Ta(100) surface in ultra high vacuum at temperatures from 300 to 2000 K are investigated. It is shown that C_{60} molecules from the first adsorption layer undergo a significant transformation even at room temperature, forming a loose monolayer. The subsequent growth of fullerite occurs in accordance with the Stranski–Krastanov mechanism and results in the formation of compact islands. The thermal stability ranges of fullerite films on tantalum are determined and it is shown that decomposition occurs in the temperature range 850–950 K mainly due to decomposition of the molecules (induced by the catalytically active surface) rather than thermal desorption. © *2005 Pleiades Publishing, Inc.*

1. INTRODUCTION

Interaction of fullerenes with the surface of solids is interesting from a scientific point of view and important in practice, since this process provides the key to technological application of fullerenes. To date, there are at least several tens of studies in which fullerene–surface interaction was analyzed by different methods (both theoretically and experimentally) for silicon [1–7], noble metals [8–12], and refractory metals [13–17]. Previously, we performed a detailed study on the regularities of such interaction between C_{60} molecules and the surfaces of Ir [11, 12], Re [14], W [16, 17], Si [7], and Mo [15]. C_{60} molecules, adsorbed at room temperature, retain their structure on the surfaces of Ir, Re, Si, and Mo. At the same time, on the W surface, fullerenes are significantly transformed, even at room temperature. According to modern concepts, tantalum is much more chemically and catalytically active in comparison with all the previously studied metals [18]. Thus, we believe it is important to gain insight into the transformation of the known regularities of fullerene–surface interaction for the Ta surface.

2. EXPERIMENTAL

The experiments were performed in a high-resolution Auger spectrometer (see [19] for details) in ultrahigh vacuum ($p \approx 10^{-10}$ Torr). Auger spectra were measured in a direction close to the normal to the surface. There was a possibility of recording Auger spectra directly from heated samples in the temperature range 300–2100 K. The samples consisted of filamentary Ta ribbons $0.05 \times 1 \times 40$ mm^3 in size. They were cleaned by successive annealing in oxygen ($p \approx 10^{-7}$ Torr and T = 1500 K for 30 min) and ultrahigh vacuum ($p \approx 10^{-10}$ Torr and T = 2600 K for 5 h). The Auger spectrum of the as-annealed surface contained only Ta peaks. Along with cleaning, a ribbon became textured after the appearance of the (100) face on the surface. The work function of the surface was $e\varphi$ = 4.15 eV (this value corresponds to the (100) face, according to [20]). The surface was homogeneous in the work function. It has previously been shown that the C_{KVV} Auger peak of C_{60} molecules has an energy of 269 eV, i.e., almost 3 eV lower than, for example, the carbon Auger peak in the spectra of graphite, metal carbides, or adsorbed carbon clusters. This Auger peak energy is characteristic of both thick films of adsorbed C_{60} molecules (5–10 monolayers) and submonolayer coatings on iridium, rhenium, and silicon. We used this factor to distinguish adsorbed fullerenes from carbon in other possible states.

The C_{60} molecules were deposited on the entire surface of a ribbon from a Knudsen cell, into which a weight of fullerenes with a purity of 99.5% was loaded. After aging, the cell yielded a stable and easily controlled flux of C_{60} molecules with the density $\nu_{C_{60}} = 10^{10}$–10^{13} molecule/cm^2 s. To carry out absolute calibration of the flux density, an iridium ribbon was installed near a tantalum ribbon (parallel to it). The calibration was performed using the technique we proposed in [16]. The error of absolute calibration was estimated to be 15–20%.

3. ADSORPTION AT ROOM TEMPERATURE

Figure 1 shows the changes occurring in the carbon and tantalum Auger signals during the adsorption of C_{60} molecules under the effect of a constant flux on the Ta(100) surface at room temperature. As can be seen, the tantalum Auger signal monotonically decreases but

†Deceased.

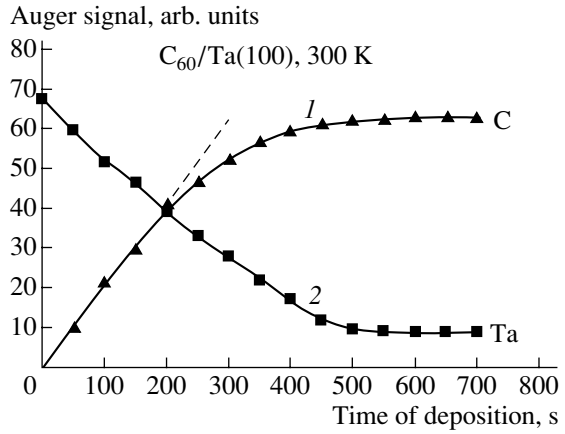

Fig. 1. Dependences of the (*1*) carbon and (*2*) tantalum Auger signals on the time of deposition of C_{60} molecules on Ta(100) at room temperature. The flux density $\nu_{C_{60}} = (4 \pm 0.5) \times 10^{11}$ molecule/cm^2 s.

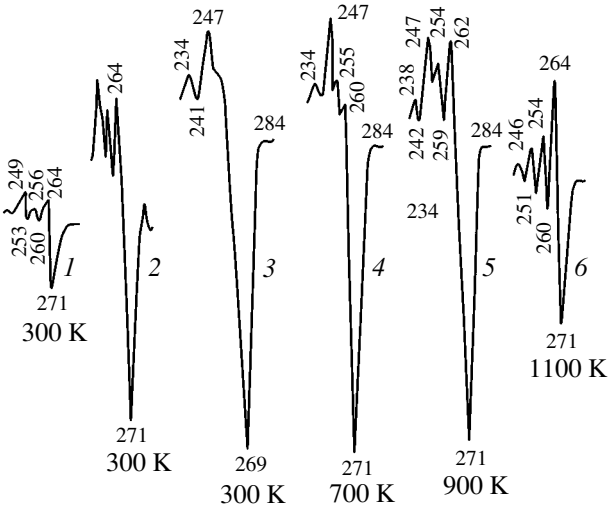

Fig. 2. Shapes of the C_{KVV} Auger line for different adsorption states of C_{60} molecules on tantalum: (*1*) 0.3 monolayers deposited at 300 K, (*2*) a monolayer deposited at 300 K, (*3*) a multilayer (~4 monolayers) fullerene film deposited at 300 K, (*4*) the same film annealed at 700 K for 20 s, (*5*) the same film annealed at 900 K for 20 s, and (*6*) the same film annealed at 1100 K for 20 s. The numbers indicate the energies (in eV) of the corresponding peaks.

does not vanish: it attains some measurable value after the deposition for approximately 500 s and then stops changing. The carbon Auger signal increases almost linearly during the deposition for about 200 s. Then, its growth slows, and, at t = 500–600 s, the intensity of this signal reaches a constant value. This result indicates that, beginning with $t \approx 200$ s, new C_{60} molecules arriving at the surface screen not only the substrate signal but also the carbon Auger signal of the previously adsorbed molecules, and, beginning from deposition times of 500–600 s, the thickness of the fullerene layer formed on the substrate becomes comparable with the escape depth of the Auger electrons of carbon (15–20 Å). Thus, we can state that, after a deposition lasting for about 200 s, the first monolayer becomes filled and the subsequent monolayers begin to grow. During the deposition of C_{60} molecules, the shape of the C_{KVV} Auger line is gradually transformed: spectrum *1* in Fig. 2, measured after the first ~60 s of deposition, changes to spectrum *2* in Fig. 2 (deposition for 200 s) and, then, to spectrum *3* in the same figure (deposition for 12 min).

The following question arises: how should we characterize the monolayer of C_{60} molecules grown at 300 K on Ta(100)? As can be seen from Fig. 2, the carbon Auger signal from the first monolayer of C_{60} molecules has an energy of 271 eV and does not correspond to the fullerene Auger signal. A similar phenomenon has previously been observed on the W(100) surface [16, 17]. Note that the first fullerene monolayer screens the Auger signal of the Ta substrate more weakly (only by a factor of 1.75) than the tungsten Auger signal [17] and even more weakly than the molybdenum [15] or silicon [7] signals. Nevertheless, this screening value of 1.75 significantly exceeds the degree of screening obtained, for example, for surface layers of tungsten or molybdenum carbides and is close to the degree of screening characteristic of a two-dimensional graphite film with respect to molybdenum, rhenium, or iridium Auger signals (1.6). Recall that the energies of the Auger peaks of all the metals considered here are close to each other (within 15 eV), which makes it possible to directly compare the degrees of screening. We believe that fullerene, in contact with a Ta surface that has a high catalytic activity, does not completely lose its individuality and structure but is significantly transformed. Indeed, one would hardly expect fullerene to undergo a complete decomposition into atoms at room temperature even on such a chemically active surface as the Ta surface. For example, we earlier showed [21] that the Auger line of a carbon film deposited in ultrahigh vacuum has a shape characteristic of carbon clusters and that this film is thermally stable up to 900 K. The transformation of C_{60} molecules makes it possible for some C atoms to be involved in strong chemisorption interaction with the metal surface, which is the likely reason for the complex partly carbide-like shape of the Auger line of adsorbed submonolayer and monolayer films of C_{60} molecules (see spectra *1* and *2* in Fig. 2). Somewhat arbitrarily, we propose to characterize this state as a "loose ball" (a schematic diagram of the processes occurring during the deposition of fullerenes on Ta(100) at 300 K is shown in Fig. 3a). Previously, we developed similar concepts for the transformation of fullerenes on the W(100) surface [17].

Let us estimate the concentration of C_{60} molecules in the first monolayer. On the basis of the absolute flux calibration, we can state that $(0.8–1.1) \times 10^{14}$ molecules are deposited on a surface area of 1 cm^2 for 200 s. This means that the first monolayer of the C_{60} molecules on Ta(100) is rather loose in comparison with similar layers on metals of group VI (see table).

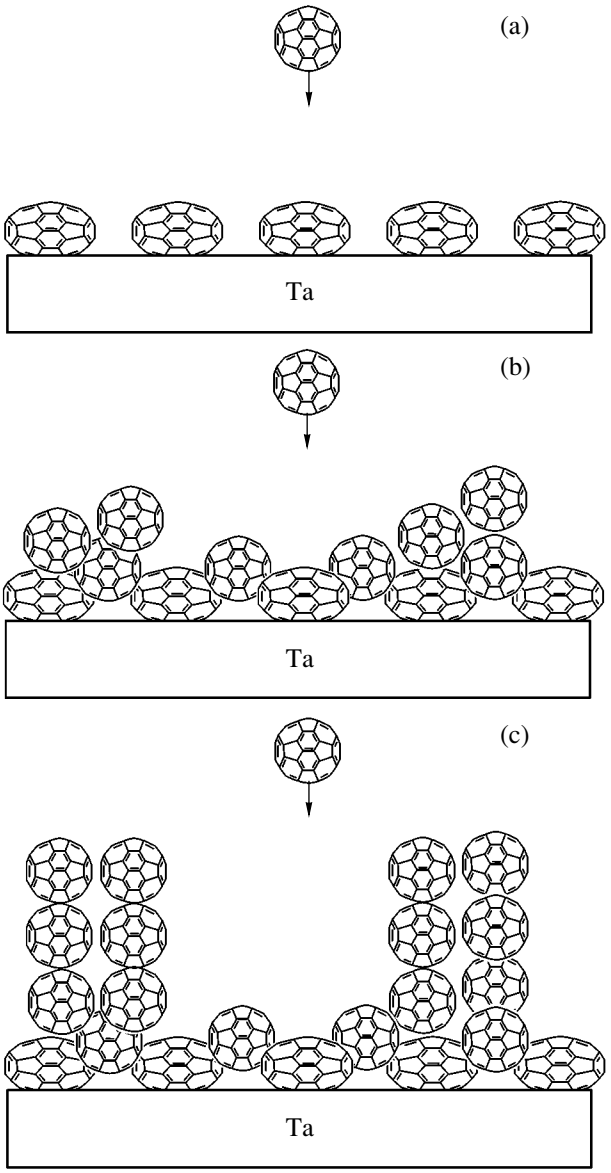

Fig. 3. Schematic diagram of the processes occurring during the deposition of C_{60} molecules on Ta(100) at room temperature: (a) submonolayer coating, (b) beginning of the second-layer growth, and (c) growth of a multilayer film.

Let us consider the further growth of fullerene films. Some conclusions can be drawn on the basis of the Auger data. First, the growth of a fullerene film on tantalum is distinctly not of the layer-by-layer type (as it is on molybdenum or tungsten). It is more likely of an island type, as on silicon and rhenium. Second, the observed changes in both Auger signals can be made consistent with the model only by assuming that the growing fullerite islands leave some part of the first monolayer open, while the density of these islands is higher than in the first monolayer and is close to the volume density of the fullerite. A hypothetical schematic diagram of the successive growth stages of a fullerite film on Ta(100) is shown in Fig. 3. In surface science, this mechanism of film growth is referred to as the Stranski–Krastanov mechanism.

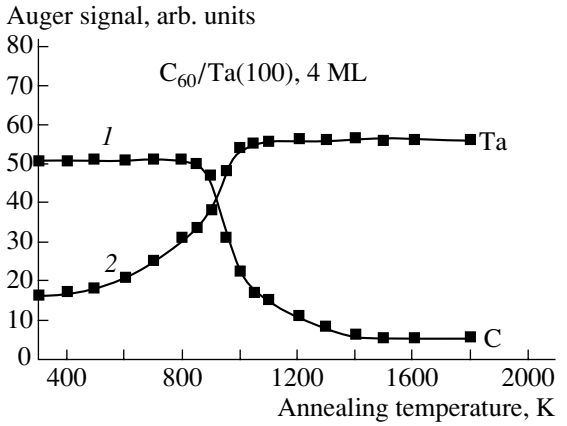

Fig. 4. Changes in the (*1*) carbon and (*2*) tantalum Auger signals during the step annealing of a film of C_{60} molecules with a thickness of about four monolayers on Ta(100). The initial state is the film of C_{60} molecules deposited at room temperature. The annealing time at each point is 20 s.

In addition, we should note that, up to the end of the formation of the first monolayer, the shape of the carbon Auger line hardly changes (it is present in spectrum *1* in Fig. 2). In contrast, for a three- of four-layer film, the line shape is typical of fullerenes (spectrum *3* in Fig. 2), since the Auger electrons from the first layer are strongly absorbed in higher lying layers and make almost no contribution to the total signal.

4. THERMAL TRANSFORMATION OF A FULLERITE FILM ON Ta(100)

Figure 4 shows the changes in the carbon and tantalum Auger signals upon annealing of multilayer fullerite films with a total thickness of four layers. The change in the shape of the carbon Auger line upon such heating is shown in Fig. 2. As can be seen, up to 800 K, the adsorbate Auger signal hardly changes, whereas the substrate Auger signal increases significantly from the beginning. The shape of the carbon Auger line is also transformed, which is indicative of changes in the chemical state of C atoms entering the composition of fullerenes. Even at 700 K, the energy of the carbon Auger peak changes to the value of 271 eV, and a number of specific features arise in the low-energy part of the spectrum that are typical of carbide structures rather than fullerenes.

This trend is even more pronounced at 900 K, although the Auger peak amplitude changes very little. At high temperatures, the shape of the Auger peak becomes very similar to that of carbides (Fig. 2, spectrum *6*) and does not change upon further heating; only the peak amplitude decreases. In the temperature range 850–950 K, fast reconstruction of the adsorption layer occurs: the carbon Auger signal sharply decreases and

the substrate Auger signal increases by a factor of almost 2. With a further increase in temperature, the carbon Auger signal continues to decrease, remaining similar to the carbide Auger line in shape, and the substrate Auger signal continues to increase. Both Auger signals attain constant values at $T = 1700$–1800 K at the level characteristic of the tantalum carbide surface [21].

Apparently, this complex behavior of the Auger signals is the result of a number of processes, occurring simultaneously and competing with each other. In the temperature range 300–800 K, the catalytic action of the metal surface, leading to decomposition of fullerenes from the first and next layers, increasingly manifests itself during the heating. The released C atoms are incorporated into carbide-like structures on the surface and yield the Auger peak of the corresponding shape. The sharp change in the amplitudes of both Auger spectra at 800–900 K is apparently due to two processes occurring almost simultaneously: desorption of undecomposed C_{60} molecules from the upper layers and intense decomposition of C_{60} molecules and their fragments with dissolution of the released carbon in the substrate volume.

Indeed, the upper layers of the film initially contain unstrained fullerenes (as indicated by an Auger peak energy equal to 269 eV). However, even at 700 K, their number is very small (if there any are at all): the Auger peak energy is characteristic of carbides. Apparently, this phenomenon is related to the further decomposition of the fragments of fullerenes and the replacement of a significant fraction of C–C bonds by C–Ta chemisorption bonds. For all the previously studied substrates (Mo, Re, Ir, W, Si, and SiC), the thermal desorption of fullerenes from multilayer films has been observed in the temperature range 750–850 K. It is reasonable to suggest desorption of undecomposed C_{60} molecules in this case. At the same time, as was shown in [21], the atomization of almost all forms of the adsorbed carbon and the dissolution of the released carbon in the Ta substrate, accompanied by the formation of a solid solution, finish at 900 K. Apparently, in the case under consideration, a large fraction of the deposited fullerenes are partially decomposed even at 400–700 K and lose the ability to be desorbed. At 850–900 K, all these molecules are decomposed into atoms and the released C atoms penetrate the surface region of the substrate to cause a significant supersaturation and form grains of volume carbide. Heating to higher temperatures leads to a gradual dissolution of these grains, and, at 1700–1800 K, the surface contains only the equilibrium surface carbide, as one would expect from the data of [21].

It is of interest to compare the data in Fig. 4 with the results of annealing of one monolayer of fullerenes (Fig. 5). It can be seen that the picture is qualitatively very similar: radical changes in the intensities of the Auger signals occur at the same temperatures, although the thermal desorption of decomposed fullerenes seems to be very unlikely. It is noteworthy that the state of the surface carbide is attained at lower temperatures (apparently, due to the smaller total amount of carbon in the system, smaller grains of volume carbide are formed and they can be more easily dissolved).

Data on the surface concentration of C_{60} molecules and the degrees of screening of the substrate Auger signal for monolayers of C_{60} molecules on different substrates

Substrate	Concentration of C_{60} molecules in a monolayer, cm^{-2}	Degree of screening	$S_{C_{60}}(1-\sigma)$, cm^2
Mo(100)	$\sim 1.6 \times 10^{14}$	2.9	0.41×10^{-14}
W(100)	$\sim 1.6 \times 10^{14}$	2.8	0.40×10^{-14}
Si(100)	$(7–8) \times 10^{13}$	~1.9	0.63×10^{-14}

It is also of interest to determine the limiting depth at which this surface effect exists, causing the decomposition of fullerenes. Special experiments were carried out in which fullerite films with thicknesses ranging from 300 to 1000 atomic layers were deposited on the Ta surface. Then, the films were heated in vacuum, and the products of thermal desorption were deposited on a closely located substrate and analyzed by Auger electron spectroscopy. It was found that, at such film thicknesses, fullerenes are not decomposed but are thermally desorbed, retaining their shape. Apparently, the effect of the surface, leading to the decomposition of fullerenes, covers depths no larger than several (maximum several tens) atomic layers.

5. RESULTS AND DISCUSSION

Let us estimate the concentration of fullerenes in the first layer using the data on their screening ability for other substrates. We assume that the screening ability of C_{60} molecules weakly changes as a result of the above-described transformation and is the same for tan-

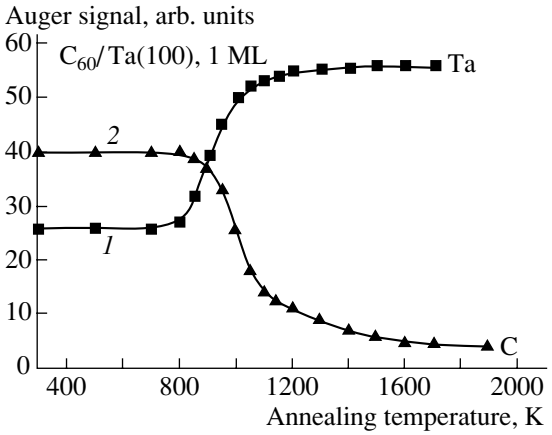

Fig. 5. Changes in the (*1*) tantalum and (*2*) carbon Auger signals during the step heating of films of C_{60} molecules with a thickness of one monolayer on Ta(100). The annealing time at each point is 20 s.

talum, tungsten, and molybdenum. In addition, we assume that one fullerene decreases the flux of substrate Auger electrons passing through it by a factor of σ and occupies an area equal to $S_{C_{60}}$ cm^2, the total area from which the Auger signal is collected is equal to S, and the Auger signal intensity of a pure substrate is I_0. Then, the intensity I_N of the substrate Auger signal from a surface with a concentration N of fullerenes can be written as

$$I_N = I_0[(S_{C_{60}}N\sigma) + (1 - S_{C_{60}}N)], \quad (1)$$

where the first and second terms describe the Auger emission through the areas occupied by fullerenes and those free of them, respectively. Let us denote the experimentally observed decrease in the Auger signal as $\delta = I_N/I_0$. Then, it can easily be seen that

$$\delta = 1 + S_{C_{60}}N(\sigma - 1). \quad (2)$$

The experimental data for the substrates previously investigated are listed in the table. As can be seen from formula (2), one can experimentally determine only the product of the area occupied by one fullerene on the basis of its screening ability, $S_{C_{60}}(\sigma - 1)$. For the estimation, let us take the average value from those listed in the table and assume that $S_{C_{60}}(\sigma - 1) = 0.5 \times 10^{-14}$ cm^2. Then, calculation of the surface concentration of fullerenes on Ta(100) by formula (2) yields $N = 0.85 \times 10^{14}$ cm^{-2}, which is in very good agreement with the data of direct measurements (see above).

Let us compare the results obtained for Ta(100) with the specific features of the interaction of fullerenes with other, previously studied, metal substrates. The adsorption of fullerenes on tantalum is very similar to their adsorption on tungsten: on both these substrates, the fullerenes of the first monolayer lose their character even at 300 K. However, the heating of multilayer films on the surface of W, as well as the previously studied Mo, Si, and Re, leads to the thermal desorption of excess C_{60} molecules; only the molecules of the first layer (on W) and some of those from the second layer remain on the surface. However, tantalum, which has a much higher catalytic activity than all the above-mentioned substrates [18], can decompose almost all fullerenes deposited on the surface, including those that are not in direct contact with the metal. Apparently, we are observing here the effect of induced transformation of molecules from the second and subsequent layers (revealed by us in [17]) when the catalytic action of the surface is transferred through the layers of transformed molecules.

6. CONCLUSIONS

The regular features of the interaction between C_{60} molecules and the Ta(100) surface are studied in detail. It is shown that the deposition of fullerenes at room temperature leads to island growth of a fullerite film by the Stranski–Krastanov mechanism with a highly loose first monolayer composed of highly transformed C_{60} molecules. Heating of a multilayer film leads to the induced transformation of C_{60} molecules from the second and subsequent adsorption layers, which apparently makes these molecules unable to undergo thermal desorption.

ACKNOWLEDGMENTS

This study was supported by the program "Controlled Synthesis of Fullerenes," project no. 8C78, and the program "Low-Dimensional Quantum Structures," project no. 9G19. N.R. Gall' also acknowledges the Foundation for the Support of National Science.

REFERENCES

1. C. Gripon, L. Legrand, I. Rosenman, and F. Boue, Fullerene Sci. Technol. **4**, 1195 (1996).
2. Xu Hang, D. M. Chen, and W. N. Creager, Phys. Rev. Lett. **70**, 1948 (1993).
3. Y. Z. Li, M. Chander, J. C. Partin, and J. H. Weaver, Phys. Rev. B **45**, 13837 (1992).
4. T. Sato, T. Sueyoshi, and M. Iwatsuku, Surf. Sci. Lett. **321**, L137 (1994).
5. D. Chen and D. Sarid, Surf. Sci. **318**, 74 (1994).
6. P. H. Beton, A. W. Dunn, and P. Moriarty, Surf. Sci. **361–362**, 878 (1996).
7. N. R. Gall', E. V. Rut'kov, and A. Ya. Tontegode, Fiz. Tekh. Poluprovodn. (St. Petersburg) **36**, 1084 (2002) [Semiconductors **36**, 1008 (2002)].
8. T. Hashizume, K. Motai, X. D. Wang, *et al.*, J. Vac. Sci. Technol. A **12**, 2097 (1994).
9. T. Chen, S. Howelles, M. Gallager, *et al.*, J. Vac. Sci. Technol. B **9**, 2461 (1991).
10. D. K. Kin, Y. D. Suh, K. H. Park, *et al.*, J. Vac. Sci. Technol. A **11**, 1675 (1993).
11. E. V. Rut'kov, A. Ya. Tontegode, and Yu. S. Grushko, Pis'ma Zh. Éksp. Teor. Fiz. **57**, 712 (1993) [JETP Lett. **57**, 724 (1993)].
12. E. V. Rut'kov, A. Ya. Tontegode, and M. M. Usufov, Phys. Rev. Lett. **74**, 758 (1995).
13. G. K. Wertheim, Solid State Commun. **88**, 97 (1993).
14. N. R. Gall, E. V. Rut'kov, A. Ya. Tontegode, and M. M. Usufov, Mol. Mater. **7**, 187 (1996).
15. N. R. Gall', E. V. Rut'kov, A. Ya. Tontegode, and M. M. Usufov, Zh. Tekh. Fiz. **69** (11), 117 (1999) [Tech. Phys. **44**, 1371 (1999)].
16. N. R. Gall, E. V. Rut'kov, and A. Ya. Tontegode, Fullerene Sci. Technol. **9** (2), 111 (2001).
17. N. R. Gall', E. V. Rut'kov, and A. Ya. Tontegode, Fiz. Tekh. Poluprovodn. (St. Petersburg) **38**, 1061 (2004) [Semiconductors **38**, 1023 (2004)].
18. G. K. Boreskov, *Heterogeneous Catalysis* (Nauka, Moscow, 1988; Nova Sci., Hauppauge, N.Y., 2003).
19. N. R. Gall, S. N. Mikhailov, E. V. Rut'kov, and A. Ya. Tontegode, Surf. Sci. **191**, 185 (1987).
20. V. S. Fomenko, *Emission Properties of Materials* (Naukova Dumka, Kiev, 1984) [in Russian].
21. N. R. Gall, E. V. Rut'kov, and A. Ya. Tontegode, Surf. Sci. **472**, 187 (2001).

Translated by Yu. Sin'kov

Semiconductors, Vol. 39, No. 11, 2005, pp. 1285–1289. Translated from Fizika i Tekhnika Poluprovodnikov, Vol. 39, No. 11, 2005, pp. 1331–1335.

ELECTRONIC AND OPTICAL PROPERTIES OF SEMICONDUCTORS

Applicability of a Simplified Shockley–Read–Hall Model to Semiconductors with Various Types of Defects

A. N. Yashin

Institute of Solid-State and Semiconductor Physics, Belarussian Academy of Sciences, ul. Brovki 17, Minsk, 220072 Belarus
e-mail: yash@ifttp.bas-net.by

Submitted January 27, 2005; accepted for publication February 15, 2005

Abstract—Restrictions imposed on the maximum defect concentration at which the conventional assumption of the Shockley–Read–Hall recombination theory (the equality of electron and hole lifetimes) is still applicable are studied. Using the example of doped silicon, the dependence of this concentration on the injection level and various defect parameters is considered. The cases where the semiconductor contains defects of only one type and of several types are investigated. The performed analysis allows us to determine the sample parameters for which the lifetimes of charge carriers can be calculated using a simplified recombination model. © *2005 Pleiades Publishing, Inc.*

1. INTRODUCTION

Measurements of charge-carrier lifetimes in semiconductors are used to determine various defect parameters, in particular, their concentrations and energy-level positions in the band gap. Usually, the results of such measurements are simulated using the Shockley–Read–Hall (SRH) theory [1–3]. Thus, in order to simplify the calculations, it is often assumed that the electron and hole lifetimes τ_n and τ_p or, equivalently, the excess charge carrier concentrations Δn and Δp are approximately equal [2, 4, 5]. In Shockley–Read terminology [1, 6], this condition corresponds to the so-called simplified SRH model. The problem is, however, that the application of such a simplified approach is not always justified. As was shown in [1], the defect concentration N_t must not exceed some critical value N_{crit}; otherwise, the results of the lifetime measurements are not reliable. The higher the concentration N_t, the greater the possible error is. At the same time, the quantity N_{crit} strongly depends on many parameters of both the defects and the semiconductor material. In particular, in [1], the dependence of N_{crit} on the position of the defect level E_t in the band gap was studied for different values of the ratio $\gamma = c_p/c_n$ of carrier capture coefficients with respect to the defect level. However, generally, the plots in [1] allowed only a rough estimation of the quantity N_{crit}, since the calculations were based on the formula of the simplified SRH theory itself. Basically, the case where $\tau_n/\tau_p = \Delta n/\Delta p \approx 1$ was studied. However, the reverse case, where the above quantities are substantially different, is of interest. The approach used in this study, specifically, application of the non-simplified theory, makes it possible to establish the critical concentration at an arbitrary value of the ratio τ_n/τ_p.

According to [7, 8], in *p*-type silicon containing a number of radiation defects, in particular, *E* centers, the carrier lifetimes are substantially different. Therefore, for such samples, one might expect significant restrictions on the defect concentration if the simplified recombination model is used. This issue is considered in this study.

If the injection level is increased, the charge-carrier lifetimes become closer to each other. Accordingly, the restrictions on the defect concentrations should become weaker. In this study, the conditions under which these restrictions are retained, even if injection is not low, are considered.

In [1, 7, 8], calculations were performed for the case in which carrier lifetimes are determined by one defect type only. Here, the applicability of the simplified SRH model is investigated for a more realistic situation in which the levels of different centers contribute simultaneously to recombination.

2. RELATIONS BETWEEN THE PARAMETERS OF THE SEMICONDUCTOR IN THE SRH MODEL

According to the SRH theory of recombination, in the case of defects with one level in the band gap at a given injection level Δp, the quantity Δn is determined by solving a quadratic equation. Knowing this quantity, we can calculate the lifetimes of charge carriers [3, 9]. For electrons, the following relation is valid:

$$\tau_n = N_t^{-1}\left(p_0 + \Delta p + n_0\frac{\Delta p}{\Delta n}\right)^{-1} \times\left(\frac{n_0 + n_1 + \Delta n}{c_p} + \frac{p_0 + p_1 + \Delta p}{c_n}\right). \quad (1)$$

1063-7826/05/3911-1285$26.00 © 2005 Pleiades Publishing, Inc.

Here, n_0 and p_0 are the equilibrium electron and hole concentrations, $p_1 = n_i\exp(-\Delta e_t)$, $n_1 = n_i\exp(\Delta e_t)$,

$$\Delta e_t = \frac{E_t - E_i}{k_B T},$$

n_i and E_i are the carrier concentration and the Fermi level in an intrinsic semiconductor, k_B is the Boltzmann constant, and T is temperature. The hole lifetime can be found from formula (1) using the relation $\tau_n/\tau_p = \Delta n/\Delta p$.

We describe deviations from the condition $\Delta n = \Delta p$ by the parameter $x = 1 - \Delta n/\Delta p$ for a p-type semiconductor and by $x = 1 - \Delta p/\Delta n$ for an n-type semiconductor. Then, instead of (1), we obtain, for an acceptor-doped semiconductor,

$$\tau_n = (c_p N_t)^{-1}\left(p_0 + \Delta p + \frac{n_0}{1-x}\right)^{-1} \times\left[(p_0 + p_1)\left(\frac{n_1}{p_0} + \gamma\right) + \Delta p(\gamma + 1 - x)\right]. \quad (2)$$

It follows that, at a low injection level ($\Delta p \ll p_0$, where p_0 is the equilibrium concentration), the lifetime of minority charge carriers changes only if the quantities Δn and Δp are substantially different (so that $|x| \approx 1$) and only at a rather low doping level. However, the majority-carrier lifetime is more sensitive to the value of x, since

$$\tau_p = \frac{\tau_n}{1-x}.$$

The simplified SRH model corresponds to the approximation $x \approx 0$. The error arising when using this model is determined by comparing carrier lifetimes at $x = 0$ and $x \neq 0$. The error can be substantial if the relaxation of the measured parameter is determined by either majority carriers or carriers of both types. An example is provided by the method used in [1], where the photoconductivity variation under optical injection was measured.

Having fixed x, i.e., having chosen a reasonable ratio of the lifetimes, we can find the corresponding defect concentration N_t. Thus, for a p-type semiconductor, the relation between these quantities is

$$x = \frac{N_t}{p_0 + p_1}\frac{(1-x)p_0 - \gamma p_1}{(p_0 + p_1)(\gamma + n_1/p_0) + \Delta p(\gamma + 1 - x)}. \quad (3)$$

At a low injection level ($\Delta p \ll p_0$), we have

$$N_t = \frac{x(p_0 + p_1)^2(\gamma + n_1/p_0)}{(1-x)p_0 - \gamma p_1}.$$

In [1], the quantity

$$N_{\text{crit}} = \frac{(N_a + p_1)[\gamma(N_a + p_1) + n_1]}{|N_a - \gamma p_1|}$$

was analyzed rather than the quantity N_t. The expression for N_{crit} can be written as $N_t/|x|$ if, following [1], we introduce the additional assumptions

$$x \ll 1, \quad p_0 = N_d \gg p_1.$$

We disregard these conditions, directly using nonsimplified formula (3).

In p-Si, the position of the defect level in the band gap ($E_t = E_i - 0.18$ eV) and the smallness of the coefficient $\gamma \approx 1.8 \times 10^{-3}$ yield a value of x close to unity even for low concentrations of Fe_i defects [1]. At a doping level of $N_a = 10^{15}$ cm^{-3}, injection level $\Delta p < 10^{13}$ cm^{-3}, and defect concentration of $N_t = 10^{14}$ cm^{-3}, we obtain $x \approx 0.99$. Therefore, Fe_i centers can appreciably affect the charge-carrier lifetimes in such a sample.

According to the data from theoretical studies [7, 8], for the parameters N_a, Δp, and N_t, when they are equal to those listed above for Fe_i centers, the presence of radiation-induced E centers (phosphorus–vacancy) in a p-Si crystal should provide an equally large value of $x \approx 0.99$. Note, however, that, at such a concentration, it is not possible to satisfy the electrical neutrality condition using the values of the parameters of the centers ($E_t = E_i + 0.13$ eV and $\gamma = 10$) cited in [7, 8]. A calculation using formula (3) yields a value of $x \approx 0.01$, which is two orders of magnitude smaller. Indeed, in this case, x must be small, since the probability of filling of the E centers by electrons is very small. Thus, for $N_a = 10^{15}$ cm^{-3}, $N_t = 10^{14}$ cm^{-3}, and $\Delta p = 10^{13}$ cm^{-3}, only $10^{-3}N_t$ of the neutral E centers become negatively charged. It is not sufficient to create an appreciable difference in the nonequilibrium concentrations of free carriers in the bands and, respectively, in the carrier lifetimes. We also note that we have succeeded in reproducing the results of [1] for p-Si with Fe_i and FeB centers, in particular, the carrier lifetime data. For this reason, the methods suggested in [7] for finding defect concentrations using the dependence of the carrier lifetimes on the injection level seem to be unjustified.

3. DEPENDENCE OF THE APPLICABILITY OF THE SRH MODEL ON THE DEFECT ENERGY-LEVEL POSITION

Let us consider the dependence $N_t(\Delta e_t)$ of the defect concentration on the position of their energy levels for specific values of x, N_a, and γ using the nonsimplified SRH theory. Thus, we should be able to determine the concentration of defects with a specific value of E_t for which the ratio of the carrier lifetimes is $\tau_p/\tau_n = 1 - x$. In this way, we shall establish the limiting concentration up to which one can use the simplified SRH model before the error does exceeds the specified ratio of the carrier lifetimes.

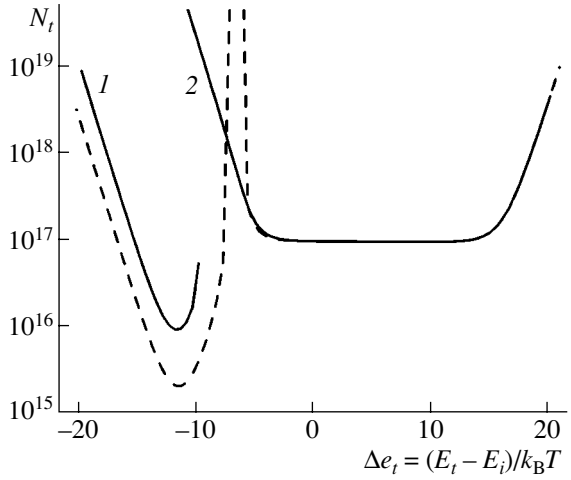

Fig. 1. Dependence of the concentration of (–/0) defects (N_t) in *p*-Si on the position of their energy level (E_t) at γ = 100 and a low injection level. $N_a = 10^{15}$ cm^{-3} and $|x| = 0.5$. Solid curve *1* corresponds to the region $x < 0$; solid curve *2*, to the region $x > 0$; and the dashed curves, to the approximation $p_0 = N_a$.

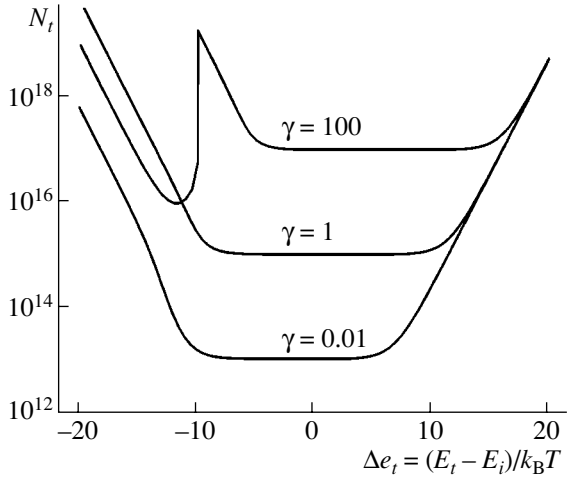

Fig. 2. Dependence of the concentration of (–/0) defects allowed by the simplified SRH model in *p*-Si on the position of the defect energy level for γ = 0.01, 1, and 100 at a low injection level. $N_a = 10^{15}$ cm^{-3} and $|x| = 0.5$.

We use formula (3). To be specific, we consider the case of a *p*-type semiconductor with (–/0) defects, i.e., defects with charge states (–/0). The dependence $N_t(\Delta e_t)$ for a low injection level ($\Delta p \ll N_a = 10^{15}$ cm^{-3}) and different values of γ in *p*-type silicon is shown in Fig. 1 by solid lines *1* and *2*. We set $|x| = 0.5$. We note that, in the sample under study, such a value of x might be provided by radiation-induced $E4$ centers (Δe_t = 5.41, γ = 6.83), for example, at a concentration of $N_t \approx 6.8 \times 10^{15}$ cm^{-3} [10, 11]. At the same doping level in *n*-type silicon, these centers would give $x = 0.5$ at a concentration of $N_t \approx 1.3 \times 10^{14}$ cm^{-3}. For p_0, we use the approximation

$$p_0 \approx N_a + \frac{N_t p_1}{p_0 + p_1}.$$

Curve *1* in Fig. 1 corresponds to values of E_t and N_t that provide $x < 0$, i.e., an excess of nonequilibrium electrons. For curve *2*, we have $x > 0$ and an excess of nonequilibrium holes, accordingly. Compared to the equilibrium value, the occupancy of the defect level by majority carriers increases at $x < 0$ and decreases at $x > 0$.

In Fig. 1, the dotted line corresponds to the same dependence $N_t(\Delta e_t)$ but is calculated under the condition $p_0 = N_a$. Such a simplified electrical-neutrality condition was used when constructing similar dependences in [1]. The authors of [1] would have obtained exactly these curves if they had considered larger values of x. The dependence has a discontinuity near the point

$$\Delta e_0 = \ln\frac{\gamma n_i}{p_0}.$$

It can be shown that the width of the corresponding "gap" is

$$\ln\frac{1 + |x|}{1 - |x|};$$

for example, at $x = 0.5$, this gap is approximately equal to k_BT. We note that the region $x < 0$ lies on the left of the gap whereas the region $x > 0$ is on the right of the gap. In [1], the curves $N_{crit}(\Delta e_t)$ tended to infinity and had no gaps at the points $\Delta e_t = \Delta e_0$. Indeed, the gap disappears as $x \longrightarrow 0$.

It can be seen from Fig. 1 that the dependence of the free-carrier concentration on the defect concentration can strongly modify the curves $N_t(\Delta e_t)$ compared to the approximation $p_0 = N_a$. This statement is particularly true for the region $x < 0$, where the quantity p_1 can assume large values. Now, there is no gap between the regions of negative and positive x. Moreover, the region $x > 0$ extends over the entire band gap, in contrast to the region $x < 0$, which either adjoins the band of the majority charge carriers (as in Fig. 1) or totally disappears. We note that the greater the parameter γ, the bigger the difference from the case $p_0 = N_a$.

The solid curves in Fig. 1 correspond to the nonsimplified SRH model, but this dependence can be compared to calculation within the framework of the simplified model with $x \approx 0$, which is of particular interest to us. In the case where two values of N_t correspond to same value of Δe_t, we must choose the smaller value. Thus, we obtain one of the curves in Fig. 2 (γ = 100) from the solid curve in Fig. 1. Similarly, changing the parameter γ, we can also construct the other curves in Fig. 2. All of them refer to the case of (–/0) centers at a low injection level and a doping level of $N_a = 10^{15}$ cm^{-3}. In this way, for each Δe_t, we find the maximum defect

concentration at which the use of the simplified model is still justified. Up to this concentration, the error does not exceed the chosen limiting value $\tau_p/\tau_n = 1 - x$.

From Fig. 2, we see that the concentration of defects, as allowed by the simplified SRH model with a preset value of $|x| = 0.5$, can be much smaller than N_a. This situation occurs if the coefficient γ is small and a defect has a sufficiently deep level. In contrast, in the case of defects with large γ, the application of the simplified SRH model is usually justified even at low doping levels. We note that our plots are radically different from the corresponding plots presented in [1].

4. INJECTION LEVEL DEPENDENCE OF THE CONDITIONS FOR THE APPLICABILITY OF THE SRH MODEL

It follows from (3) that, at fixed x, the concentration N_t increases as the injection level Δp is increased. Therefore, even if, at small Δp, the concentrations N_t allowed by the simplified model are low, as Δp increases, this restriction is removed [1]. However, for some defects, the dependence $N_t(\Delta p)$ can be weak. In this case, the applicability of the simplified SRH model can be limited in the case of a higher injection level as well.

It can be seen from formula (3) that, in a p-type semiconductor ($n_0 \ll p_0$), the quantity N_t is weakly affected by injection if

$$\Delta p \ll \frac{\gamma(p_0 + p_1) + n_1}{\gamma + 1}.$$

A similar condition for an n-type semiconductor is

$$\Delta n \ll \frac{\gamma^{-1}(n_0 + n_1) + p_1}{\gamma^{-1} + 1}.$$

At the same doping level, this inequality is more easily satisfied for acceptor doping if $\gamma > 1$ and, for donor doping, if $\gamma < 1$. This finding is confirmed by the example of radiation-induced $E4$ centers in p-Si and n-Si [10, 11]. For this case, we obtain

$$\Delta p(\mathrm{cm}^{-3}) \ll 2.9 \times 10^{11} + 0.9 p_0$$

and, respectively,

$$\Delta n(\mathrm{cm}^{-3}) \ll 2.9 \times 10^{11} + 0.1 n_0.$$

Having supplemented the above conditions with the inequalities $\Delta p \ll p_0$ and $\Delta n \ll n_0$, using formula (2), we find the limiting injection level below which the charge-carrier lifetime is independent of the injection level. For p-Si with Fe_i centers, we obtain

$$\Delta p(\mathrm{cm}^{-3}) \ll 1.5 \times 10^{10} + 1.4 \times 10^{-3} p_0.$$

Therefore, in such a sample, the lifetime begins to depend on the injection level at a much lower doping level than in p-Si with $E4$ centers [1, 10].

5. RECOMBINATION CENTERS OF DIFFERENT TYPES

In real semiconductors, recombination centers and traps of different types are usually present. In this case, we can obtain an expression for the parameter x that generalizes formula (3). For a p-type semiconductor, we find

$$x = \sum_k \frac{N_{tk}[(1-x)p_0 - \gamma_k p_{1k}]}{(p_0 + p_{1k})[(p_0 + p_{1k})(\gamma_k + n_{1k}/p_0) + \Delta p(\gamma_k + 1 - x)]}. \quad (4)$$

Here, the index k is used to distinguish between defects of different types if necessary. In [1], the assertion is made that, in the case of numerous defect types, the same restriction on the concentration as in the case of a sample with defects of a given type must be satisfied for each one. In other words, the total allowed concentration N_t is not smaller than the sum of allowed concentrations N_{tk} for each of the defect types. However, it follows from (4) that this is not always the case. Some defects can create an excess of nonequilibrium free electrons, while other defects create an excess of holes.

Now, we consider the example of silicon containing the radiation-induced centers $E1$ and $E4$. In p-Si at all doping levels, defects of both types give rise to an excess of nonequilibrium holes. Therefore, an increase in the concentration of defects of one type actually reduces the allowed concentration of defects of the other type. However, in n-Si, the situation is somewhat different. The $E4$ centers nearly always create an excess of nonequilibrium electrons (at $N_d < 3.3 \times 10^{11}$ cm^{-3}, if we disregard the case of very high defect concentrations). At the same time, the $E1$ centers ($E_t = E_i + 0.40$ eV) can create an excess both of electrons and of holes. In the available publications, there exists a significant scatter in the values of the electron-capture coefficient for these centers, with the result that the possible values of the parameter γ lie in the range 1.8–394 [12]. Accordingly, the $E1$ centers create an excess of holes if N_d is smaller than 2.5×10^{16} cm^{-3} or 1.1×10^{14} cm^{-3} for limiting values of γ in the specified interval, respectively. In this case, the total allowed concentration exceeds the sum of the allowed concentrations for each type of defect. Thus, the use of the simplified

SRH model is justified at concentrations N_t exceeding those in the case of a sample with defects of only one type.

6. CONCLUSIONS

The simplified SRH recombination model can be used to interpret measurements of charge-carrier lifetimes only if the defect concentration does not exceed some limiting value. The latter is determined by the parameters of the centers, the level and type of the semiconductor doping, and the semiconductor temperature. The result depends on the error that is considered to be allowed in finding the lifetime of carriers. The allowed value of the defect concentration can be several orders of magnitude lower than the doping level. At low injection levels, the carrier lifetimes in such samples are substantially different.

When estimating the allowed defect concentration, it is necessary to correctly take into account the role of defects in the balance of charge carriers. Primarily, this concerns defects whose energy levels lie far from the band of minority carriers. Even if the injection level is not low, restrictions on the allowed concentrations of some defects can be substantial. At the same time, in a semiconductor with several defect types, such restrictions can be weaker than in case of the defects of a single type.

The knowledge of a value of the limiting defect concentration is necessary to obtain reliable results when measuring the charge-carrier lifetimes using the method based on the simplified SRH recombination model.

REFERENCES

1. D. Macdonald and A. Cuevas, Phys. Rev. B **67**, 075203 (2003).
2. S. Rein, T. Rehrl, W. Warta, and S. W. Glunz, J. Appl. Phys. **91**, 2059 (2002).
3. J. S. Blakemore, *Semiconductor Statistics* (Pergamon, Oxford, 1962; Mir, Moscow, 1964).
4. H. Bleichner, P. Jonsson, N. Keskitalo, and E. Nordlander, J. Appl. Phys. **79**, 9142 (1996).
5. D. L. Meier, J.-M. Hwang, and R. B. Campbell, IEEE Trans. Electron Devices **35**, 70 (1988).
6. W. Shockley and W. T. Read, Phys. Rev. **87**, 835 (1952).
7. S. Zh. Karazhanov, Semicond. Sci. Technol. **16**, 276 (2001).
8. S. Zh. Karazhanov, J. Appl. Phys. **88**, 3941 (2000).
9. S. C. Choo, Phys. Rev. B **1**, 687 (1970).
10. H. Bleichner, P. Jonsson, N. Keskitalo, and E. Nordlander, J. Appl. Phys. **79**, 9142 (1996).
11. N. Keskitalo, P. Jonsson, K. Nordgren, *et al.*, J. Appl. Phys. **83**, 4206 (1998).
12. H.-J. Schultze, A. Frohnmeyer, F.-J. Niedernostheide, *et al.*, J. Electrochem. Soc. **148**, G655 (2001).

Translated by I. Zvyagin

Semiconductors, Vol. 39, No. 11, 2005, pp. 1290–1293. Translated from Fizika i Tekhnika Poluprovodnikov, Vol. 39, No. 11, 2005, pp. 1336–1339.

SEMICONDUCTOR STRUCTURES, INTERFACES, AND SURFACES

Sensitivity of Insulator–Semiconductor Structures to Time-Dependent Light Fluxes

N. F. Kovtonyuk, V. P. Misnik, and A. V. Sokolov

Kometa Central Research Institute (Federal State Unitary Enterprise), Moscow, 115280 Russia

Submitted February 28, 2005; accepted for publication March 9, 2005

Abstract—The kinetics of the electronic processes in metal–insulator–semiconductor structures in which the insulator layer has low conductivity is considered. When a dc bias voltage is applied to such a structure, a nonequilibrium depletion region appears in the semiconductor layer. The conditions necessary for the formation of a stable depletion region and the appearance of photoelectric signals in this region are analyzed. The duration of transients and the parameters of the structure layers are estimated. © *2005 Pleiades Publishing, Inc.*

"Ideal" insulator layers with low electrical conductivity (10^{-12} Ω^{-1} cm^{-1}) are used in the following photosensitive devices based on metal–insulator–semiconductor (MIS) structures: charge-coupled devices (CCDs), charge injection devices (CIDs), and image converters based on structures that consist of a MIS and a liquid crystal [1]. MIS structures with leakage in their insulator layer have attracted virtually no attention. Nevertheless, such structures are used in vidicon phototargets that are sensitive in the middle infra-red spectral region [2, 3]. In vidicon phototargets, the voltage across the MIS structure continuously decreases because of leakage of the charge supplied by an electron beam. In traditional devices based on MIS structures [1], the power source maintains a strictly controlled voltage across the structure irrespective of the conduction in the insulator layer. The fact that the kinetics of the electronic processes in MIS structures must be somewhat different from similar processes in phototargets is the subject of the present study.

In MIS structures, wide-gap semiconductors with impurities can be used as insulator layers. In this case, a heterojunction consisting of a narrow-gap semiconductor and a wide-gap semiconductor is formed, which, under certain conditions, can exhibit the properties of a MIS structure. Metal oxide and polymer layers possessing the required conductivity can be also used as insulator layers. The concept of an "insulator layer" in such structures has a purely terminological meaning. In what follows, we use the term "MIS structure with leakage." First of all, we consider structures in which, at relatively low voltages, an injection of charge carriers (at least of one sign) across the insulator–semiconductor interface is impossible.

We disregard surface effects related to the contact potential difference between the layers of a structure. This step is possible because the voltage applied to such a structure (>10 V) is much greater than the contact potential difference.

The distribution of charge, a field, and voltage in the layers of a MIS structure with leakage is described by the equations [2, 4]

$$\varepsilon_i E_i = 4\pi e n_0 L + 4\pi e N_s - 4\pi \Delta Q_i, \quad (1)$$

$$U = U_s + U_i, \quad (2)$$

$$U_s = \frac{4\pi e n_0 L^2}{\varepsilon_s}, \quad (3)$$

where ε_i and ε_s are the permittivities of the insulator and semiconductor layers, respectively; n_0 is the concentration of ionized impurities in the semiconductor; L is the length of the depletion region; N_s is the density of free carriers accumulated at the semiconductor–insulator interface; ΔQ_i is the density of the charge passing through the insulator layer; U is the voltage across the layers of the structure; U_s is the voltage across the semiconductor; and U_i is the voltage across the insulator.

We must find the time dependence of the length of the depletion region with regard to the leakage current in the insulator layer as a sufficiently wide voltage pulse is applied to a structure.

Using Eqs. (1)–(3), we can write the expression for the voltage across the layers of a structure as

$$U = \frac{4\pi e n_0 L^2}{\varepsilon_s} - \frac{L_i}{\varepsilon_i}(4\pi e n_0 L + 4\pi e N_s - 4\pi e \Delta Q_i). \quad (4)$$

Differentiating (4) with respect to time t and taking into account that

$$\frac{dN_s}{dt} = GL, \quad \frac{d\Delta Q_i}{dt} = \sigma_i E_i, \quad \frac{dU}{dt} = 0,$$

we obtain

$$\frac{8\pi e n_0}{\varepsilon_s} L \frac{dL}{dt} + \frac{L_i}{\varepsilon_i}\left(4\pi e n_0 \frac{dL}{dt} + 4\pi e G L - 4\pi \sigma_i E_i\right) = 0, \quad (5)$$

where G is the rate of thermal generation in the depletion region and σ_i is the electrical conductivity of the insulator layer. To simplify the solution of Eq. (5), we assume that the current density in the insulator layer is time-independent, i.e., $\sigma_i E_i$ = const.

In the experiment, the insulator thickness $L_i = 10^{-5}$ cm, the voltage applied to the insulator $U_i = 10$ V, and the field $E_i \approx 10^6$ V/cm. Under such high fields, the drift velocity of a charge carrier v_i attains saturation ($v_i = \mu_i E_i$) and the assumption that $\sigma_i E_i = e n_i v_0$ = const is quite justified (μ_i is the mobility of charge carriers in the insulator, and n_i is their concentration).

Equation (5) can be rewritten as

$$\frac{2 e n_0 \varepsilon_i L}{\varepsilon_s L_i (\sigma_i E_i - eGL)} dL + \frac{e n_0}{\sigma_i E_i - eGL} dL = dt. \quad (6)$$

Integrating Eq. (6), we obtain

$$\frac{2\varepsilon_i}{\varepsilon_s L_i}(L - L_0) + \frac{2\varepsilon_i \sigma_i E_i}{\varepsilon_s L_i e G} \ln\frac{\sigma_i E_i - eGL}{\sigma_i E_i - eGL_0} + \ln\frac{\sigma_i E_i - eGL}{\sigma_i E_i - eGL} = \frac{t}{T}, \quad (7)$$

where $T = n_0/G$ and L_0 is the initial length of the depletion region.

For convenience of the analysis, we rewrite Eq. (7) in the form

$$\frac{\sigma_i E_i - eGL}{\sigma_i E_i - eGL_0} \exp\left\{\frac{A(L - L_0)}{B}\right\} = \exp\left\{-\frac{t}{TB}\right\}, \quad (8)$$

where

$$A = \frac{2\varepsilon_i}{\varepsilon_s L_i}, \quad B = \frac{2\varepsilon_i \sigma_i E_i}{\varepsilon_s e G L} + 1.$$

In the steady-state mode ($t \approx \infty$), we find, from Eq. (8),

$$\sigma_i E_i - eGL = 0. \quad (9)$$

This relation implies that, in the steady-state mode, in the presence of a dc current in a MIS structure, a depletion region of length

$$L_{st} = \frac{\sigma_i E_i}{eG} \quad (10)$$

still exists in a layer of the semiconductor near the interface with the insulator.

If the conductivity of the insulator is $\sigma_i \approx 10^{-8}$–$10^{-9}\ \Omega^{-1}\ \text{cm}^{-1}$, $E_i \approx 10^5$ V/cm, and the rate of thermal generation in the semiconductor is $G \approx 10^{19}$–$10^{20}\ \text{cm}^{-3}\ \text{s}^{-1}$, then $L_{st} \approx 10^{-4}$–10^{-3} cm.

Using Eq. (8), at $L_{st} \ll L_0$, we can determine the duration of the transient required for attaining a steady-state value of the depletion region length:

$$T_{st} = \frac{2\varepsilon_i L_0 n_0}{\varepsilon_s L_i G} - \frac{n_0}{G}\left(\frac{2\varepsilon_i \sigma_i E_i}{\varepsilon_s e G L_i} + 1\right)\ln\frac{\sigma_i E_i - eGL_{st}}{\sigma_i E_i - eGL_0}. \quad (11)$$

If the current in the insulator is sufficiently low for the inequalities $\sigma_i E_i \ll eGL_i$, $\sigma_i E_i \ll eGL_{st}$, $\sigma_i E_i \ll eGL_0$, $L_{st} \ll L_0$, and $L_i \ll L_0$ to hold, then we obtain from (11)

$$T_{st} = \frac{2\varepsilon_i L_0 n_0}{\varepsilon_s G L_0} - \frac{n_0}{G}\ln\frac{L_{st}}{L_0} \approx \frac{2\varepsilon_i L_0 n_0}{\varepsilon_s L_i G}. \quad (12)$$

The first term in (12) coincides with a similar expression for the transient obtained for MIS structures with an "ideal" insulator [3]. From (11) and (12), we see that, if we use a MIS structure with leakage in the insulator, the duration of the transient decreases by a quantity determined by the second term in (11) and (12).

Let us determine the time dependence of the length of the depletion region under the conditions $eGL \gg \sigma_i E_i$ and $L \ll L_0$. From Eq. (8), we find

$$\frac{L}{L_0}\exp\left\{-\frac{AL_0}{B}\right\} = \exp\left\{-\frac{t}{TB}\right\}. \quad (13)$$

If $\sigma_i E_i \ll eGL_0$, then $B = 1$ and, using Eq. (13), we can represent the function $L(t)$ as

$$L(t) = L_0 \exp\left\{-\left(\frac{t}{T} - \frac{2\varepsilon_i L_0}{\varepsilon_s L_i}\right)\right\}. \quad (14)$$

Setting the argument of the exponential function in (14) equal to unity, we find that the length of the depletion region decreases by a factor of 2.7 in the time

$$t_H = \left(\frac{2\varepsilon_i L_0}{\varepsilon_s L_i} + 1\right)T. \quad (15)$$

If $L_0 \gg L_i$ and $\varepsilon_i \approx \varepsilon_s$, then $t_H = (2L_0/L_i)T$.

A variation in the photogenerated current I_P in a structure can be determined from the formula

$$I_P = eG_P L S_e = eGS_e L_0 \exp\left\{-\left(\frac{t}{T} - \frac{2\varepsilon_i L_0}{\varepsilon_s L_i}\right)\right\}, \quad (16)$$

where G_P is the photogeneration rate and S_e is the area of the photosensitive element.

The conclusion, following from formulas (8)–(10), that a nonequilibrium depletion region exists in the narrow-gap semiconductor of a MIS structure with leakage when a dc voltage is applied to the structure is of certain practical interest. We consider the possible physical processes resulting in the formation of such a region. It is well known that a nonequilibrium depletion region

appears in MIS structures after applying a voltage pulse. The formation and conservation of a depletion region when a dc voltage is applied to a structure is possible under certain conditions.

Most importantly, there must be no injection of free carriers (at least, of one sign) from the insulator with leakage into the narrow-gap semiconductor. Electrons passing through the insulator layer stop at the interface. To neutralize the interface, holes must come to the interface from the bulk of the semiconductor. However, in our case, the semiconductor is chosen as an *n*-type structure, meaning that there are virtually no free holes. Therefore, the field penetrates into the semiconductor and pushes the equilibrium electrons away from the interface, and a depletion region, in which electron–hole pairs are thermally generated, is formed. If the thermally generated current of minority carriers in the semiconductor exceeds the leakage current in the insulator, then, in a time T_{st}, the depletion region virtually disappears. If the thermally generated current of minority carriers is comparable with the current in the insulator or lower ($eGL \le \sigma_i E_i$), then the nonequilibrium depletion region does not vanish and continues to exist as long as there is a dc voltage across a structure. The hole current thermally generated towards the interface has no time to compensate for the arrival of electrons at the interface, and the electric field penetrates into the boundary layer of the semiconductor, pushing the majority carriers away from the interface.

A similar nonequilibrium depletion has been observed in photosensitive semiconductor structures under the exclusion of minority carriers and in photodiodes under extraction [5]. An exclusion contact (a homojunction formed by the layers of a heavily doped semiconductor and of the same almost intrinsic semiconductor) lets the flux of majority carriers pass and, at the same time, does not inject minority carriers; therefore, finally, a steady-state nonequilibrium depletion region is formed. In [5], it was shown that photodetectors based on the exclusion phenomenon have a lower level of intrinsic noise and higher operation temperature compared to traditional photoresistive detectors.

Let us consider the response of a structure to light pulses that produce the photogeneration current $eG_P LS_e \gg \sigma_i E_i$. Under these conditions, the charge current through the insulator has no time to compensate the charge eN_s of the minority carriers accumulating at the interface, and the thickness of the steady-state region decreases over time to a new value that is smaller than L_{st}. In turn, this process results in a decrease in the photocurrent to a new value determined, according to (10), by the total rate of thermal generation and photogeneration. Therefore, a photocurrent pulse is observed in the circuit. After some time, in spite of the presence of illumination, this photocurrent decreases to a value only a little larger than the dark steady-state current.

Essentially, when a MIS structure is illuminated under a dc voltage, the voltage is redistributed from the semiconductor layer to the insulator layer; this redistribution is accompanied by the appearance of a photocurrent pulse, which decays as a new steady-state voltage distribution is established. If the pulse of light is terminated, the charges that pass through the insulator gradually begin to compensate the accumulated charge, the length of the steady-stae depletion region assumes its initial value, and structure can again record a pulse of light.

In several experimental studies [6, 7], time-dependent radiation has been recorded using MIS structures with leakage. However, the theory of the effect was not completely clear. We compare the above results of theoretical analysis with the experimental data presented in [6–8].

Silicon-based MIS structures with a room-temperature resistivity of about 3×10^3 Ω cm were studied. Deposited layers of titanium dioxide and silicon dioxide with resistivites of ~(10^8–10^9) Ω cm and thicknesses of 10^{-5} cm were used as an insulator. The area of the structures was ~1 mm^2. After the application of a dc voltage of ~30 V, a current appeared in the structures with a current density of ~10^{-2} A/cm^2, which corresponds to a resistivity of the insulator equaling ~10^8 Ω cm. As a source of pulsed radiation, gallium arsenide light-emitting diodes were used.

After the application of a rectangular pulse of light of duration ~10^{-4} s, a rather sharp spike in the photocurrent is observed on the pulse front; after a time of about 10^{-5} s, this spike decays, although the pulse of light is still on. This observation means that the structure responds to time-dependent radiation only. The photocurrent decays exponentially with a time constant that decreases as is the intensity of the pulses of light are increased, in agreement with formulas (15) and (16). The situation is repeated for the subsequent pulses of light. Thus, the theory developed in this study agrees relatively well with the result of the experiment.

Corresponding oscillograms of the photocurrent pulses (see Fig. 1 in [6]) for MIS structures with leakage under different operation modes are reported in [6–8], and it is not necessary to reproduce them here.

The level of intrinsic noise of a photodetector is mainly governed by dark current. In the MIS structures considered, the dark current is controlled by the conductivity of the insulator σ_i, which, for the required value of L_{st}, can be determined from formula (10):

$$\sigma_i = \frac{eGL_{st}}{E_i}. \qquad (17)$$

Using formula (17), we performed a simulation of the required conductivity of the insulator layer of MIS structures based on narrow-gap semiconductors (indium arsenide and indium antimonide), which are sensitive in the middle infra-red spectral region (2.5–5.5 μm). In order to attain a sufficiently high quantum yield in this spectral region, it is necessary for the length of the steady-state depletion region L_{st} to be ~(5–10) μm. In these semiconductors at liquid-nitrogen

temperature, the thermal generation rate is $G \approx 10^{17}$–10^{20} cm^{-3} s^{-1} [7]. In experiments carried out in [4, 6, 7], the voltage applied to the structures was ≥10 V, the insulator thickness was 10^{-5} cm, and $E_i = 10^6$ V/cm. Substituting these values into formula (16), we find that σ_i can vary in the range ~$(10^{-7}$–$10^{-10})$ Ω^{-1} cm^{-1}.

There is a possibility of choosing the minimum value of the conductivity of the insulator layer necessary for the formation of a depletion region of required size in a narrow-gap semiconductor, i.e., there is a possibility of optimizing the noise current. As to the operation temperature of the MIS photodetectors considered, the conclusions of [2, 3, 5] that, in the presence of a nonequilibrium depletion region in a photosensitive structure, the operation temperature of photodetectors is higher than in traditional photoresistors, remain valid.

Since a MIS structure with a dc bias voltage does not respond to a time-independent light flux, specific light modulators must be used at the input. If, for some reason, the signal light flux is already modulated (for example, in laser range meters and in active optical locators) and the background radiation is time-independent, then a background signal is absent in the measured photocurrent and the threshold sensitivity is restricted by the total noise in the dark current and background.

In summary, we note that, if a dc voltage is applied to a MIS structure with leakage, a photosensitive nonequilibrium depletion region, whose length is determined by the ratio of the leakage current density in the insulator to the thermal generation rate in the semiconductor, appears in a boundary layer of the semiconductor. Such structures are photosensitive to pulsed light fluxes and insensitive to time-independent light fluxes. The noise level in MIS structures with leakage is determined by the current in the insulator layer and can be minimized by choosing the parameters of the layers of the structure.

REFERENCES

1. N. F. Kovtonyuk and E. N. Sal'nikov, *Photosensitive MIS Devices for Image Conversion* (Radio i Svyaz', Moscow, 1990), Chap. 4, p. 106 [in Russian].
2. N. F. Kovtonyuk and V. P. Misnik, Radiotekh. Élektron. (Moscow) **47**, 1145 (2002) [J. Commun. Technol. Electron. **47**, 1045 (2002)].
3. N. F. Kovtonyuk, V. P. Misnik, and A. V. Sokolov, Opt. Zh. **71** (5), 17 (2004) [J. Opt. Technol. **71**, 280 (2004)].
4. N. F. Kovtonyuk, G. N. Savkov, and L. I. Vanina, Fiz. Tekh. Poluprovodn. (Leningrad) **9**, 1208 (1975) [Sov. Phys. Semicond. **9**, 805 (1975)].
5. T. Ashley, C. T. Elliott, and A. T. Harker, Infrared Phys. **26** (5), 303 (1986).
6. N. F. Kovtonyuk, V. A. Morozov, V. G. Fadin, *et al.*, Fiz. Tekh. Poluprovodn. (Leningrad) **6**, 575 (1972) [Sov. Phys. Semicond. **6**, 503 (1972)].
7. N. F. Kovtonyuk and V. A. Morozov, Radiotekh. Élektron. (Moscow) **18**, 430 (1983).
8. N. F. Kovtonyuk, G. N. Savkov, A. I. Verov, and L. I. Vanina, Mikroélektronika **5** (2), 196 (1976).

Translated by I. Zvyagin

Semiconductors, Vol. 39, No. 11, 2005, pp. 1294–1298. Translated from Fizika i Tekhnika Poluprovodnikov, Vol. 39, No. 11, 2005, pp. 1340–1344.

SEMICONDUCTOR STRUCTURES, INTERFACES, AND SURFACES

Photosensitivity of Heterostructures Based on Finely Ground Semiconductor Phases

Yu. A. Nikolaev*, V. Yu. Rud', Yu. V. Rud'*^, E. I. Terukov*, and T. N. Ushakova***

**Ioffe Physicotechnical Institute, Russian Academy of Sciences, St. Petersburg, 194021 Russia*

^e-mail: yuryrud@mail.ioffe.ru

***St. Petersburg State Polytechnical University, St. Petersburg, 195251 Russia*

Submitted June 9, 2003; accepted for publication December 25, 2004

Abstract—A new type of heterostructure is suggested and developed. The heterostructures are based on the direct contact of a bulk semiconductor with a dielectric layer in which a finely ground semiconductor phase is dispersed. In Si- and GaAs-based heterostructures of this type, rectification and photovoltaic effects are observed. It is shown that illumination of such structures so that the side of the dielectric layer with the built-in finely ground semiconductor phase is exposed to light induces a broadband photovoltaic effect deep within the fundamental absorption band of the bulk semiconductor. © *2005 Pleiades Publishing, Inc.*

Heterostructures based on diamond-like semiconductors have been, for a long time, one of the most important subjects of investigations in the modern physics of semiconductors and semiconductor electronics [1]. At the present time, the substantial progress that has been made towards the next-generation of optoelectronics is closely related to the development of low-dimensional heterostructures [2–4]. The advent of materials with reduced dimensionalities has led to the emergence of novel technologies for controlling the fundamental properties of semiconductors and to the advent of high-power low-threshold lasers [2, 3]. In this paper, we report the results of the first study of the photosensitivity of a new type of heterostructures that are based on bulk crystals in contact with thin dielectric layers containing a uniformly distributed finely ground semiconductor phase. Silicon and gallium arsenide have been taken as examples.

1. The photosensitive heterostructures were formed on (100)-oriented Si and GaAs wafers with *n*- and *p*-type conductivity. The finely ground phase was prepared by mechanical grinding of the initial single crystals. In order to reduce the dispersion of sizes of the semiconductor particles to be introduced into the dielectric layer, we subjected them to multiple fractional precipitation from mixtures of these particles with alcohol in air. Then, the finely ground phase was introduced into a liquid polymer (*P*), specifically, epoxy resin, to a content of 1–2 wt %, and the mixture was thoroughly stirred so as to eventually provide a uniform distribution of the finely ground semiconductor (*S*) phase over the volume of the liquid dielectric phase. Thereafter, a drop of the liquid epoxy resin was applied to the surface of a semitransparent metal layer (Mo or Ni) thermally deposited on a glass surface. Then, the surface of the epoxy resin drop was brought into direct contact with a semiconductor wafer, after which the semiconductor wafer was slightly pressed so that it could be put on special-purpose bounding dielectric plates placed directly on the metal surface. Eventually, these dielectric plates provided the conditions for obtaining a plane-parallel epoxy resin layer including the embedded disperse semiconductor particles. In the above procedure of fabrication of the structures, the excess liquid mixture was "pressed out" of the gap between the metal (*M*) and semiconductor surfaces, following which the system, consisting of glass, metal, and a mixture of epoxy resin with the finely ground semiconductor phase (*M*/(*P* + *S*)/*S*), was fixed under a mechanical load until the solidification of the epoxy resin was completed. With the entire solidification completed, the resulting structure became monolithic and was supplied with electrical contacts to the semiconductor and metal. The procedure used here for fabrication of the structures is similar to that previously suggested for manufacturing heterocontacts between a natural protein and a semiconductor [5]. The only difference is that an epoxy layer with a built-in finely ground semiconductor phase is used here instead of the protein used in [5]. The thickness of the dielectric layer in the heterostructures under consideration ranged between about 0.1 and 0.05 mm.

Along with the *M*/(*P* + *S*)/*S* structures, we fabricated *M*/(*P* + *S*)/*M* structures in which the epoxy resin layers with the built-in finely ground semiconductor phase were in contact with metal surfaces on both sides of the layers. In this case, the metal layers were deposited on glass surfaces in the same way as for the *M*/(*P* + *S*)/*S* structures.

2. The basic types of structures fabricated by the above procedure and some of the parameters of the

Table

Constituent structural components			R_0, Ω	K, U = 5 V	$\Delta\hbar\omega^{m\,a}$, eV	$S_u^{m\,b}$, V W^{-1}
single-crystal wafer	finely ground phase	sample number				
p-Si	*p*-Si	5	10^6	1	1.7–2.2	
n-Si	*p*-Si	7	5×10^5	10	2.5–2.9	50
n-GaAs	*p*-GaAs	17	10^5	10^2	1.5–2.5	850
p-Si	*p*-GaAs	23	10^6	10	2–3	100

Note: The heterostructures' thin-film component, consisting of a finely ground semiconductor phase embedded in epoxy resin, was illuminated. [a] $\Delta\hbar\omega^m$ refers to the spectral region of high voltage photosensitivity. [b] S_u^m refers to the maximal photosensitivity.

structures are listed in the table. Below, we describe the main experimental results obtained for these structures.

The *M*/*P*/*M* structures, as a rule, exhibited a linear current–voltage behavior under the external biases $U \leq 100$ V ($I \propto U$). At room temperature, the resistance R of structures of this type was typically in the range 10^9–10^{11} Ω, depending on the thickness and area of the epoxy resin layer.

With the finely ground Si and GaAs phases introduced into the epoxy resin, the resistance of the resulting *M*/(*P* + Si)/*M* and *M*/(*P* + GaAs)/*M* structures, containing about 1–2 wt % of the finely ground phase in the resin layer, as a rule, appeared to be several orders of magnitude lower than the resistance of the *M*/*P*/*M* structures. It was possible to estimate the resistance, which was found to be at a level of $R \approx 10^5$–10^7 Ω, from the linear portion of the steady-state current–voltage (*I*–*V*) characteristic of such systems (at $U \leq 50$ V). The resistance is controlled mainly by the geometric dimensions of the layers and by the content of the finely ground semiconductor phase introduced into the resin layer. Under the exposure of such heterostructures to integral radiation from a filament lamp at T = 300 K, positive photoconductivity at a level of $\Delta\sigma/\sigma \approx 1.1$–1.2 was generated.

When studying the steady-state *I*–*V* characteristics of the *M*/(*P*+Si(GaAs))/Si(GaAs) heterostructures, we observed a rectification typical of well-known semiconductor homostructures and heterostructures. The *I*–*V* characteristic of one of the heterostructures under consideration is shown in the inset in Fig. 1. This structure involved a finely ground *p*-Si:B (ρ = 2 Ω cm) phase uniformly distributed in the dielectric layer in contact with the surface of an *n*-Si:P single crystal plate (ρ = 0.1 and 0.01 Ω cm). The rectification factor K, defined as the ratio of direct current to reverse current at $U \approx 100$ V, was as large as $K \approx 10$. In this case, the forward direction corresponded to a positive polarity of the external bias applied to the layer. The residual resistance of the heterostructures in the range of the dependence $I = (U - U_0)/R_0$ was $R_0 \approx 5 \times 10^5$ Ω, while the cutoff voltage was $U_0 \approx 1$ V.

In addition to the well-pronounced rectification, a photovoltaic effect was detected in the *M*/(*P* + *S*)/*M* heterostructures. As a rule, this effect was most pronounced when the side of the structures with thin two-phase layers was illuminated; these layers consisted of a finely ground Si or GaAs phase embedded in the dielectric *P*.

3. We now consider specific features of the spectral dependences of the relative quantum efficiency of photoconversion η, which is defined as the short-circuit

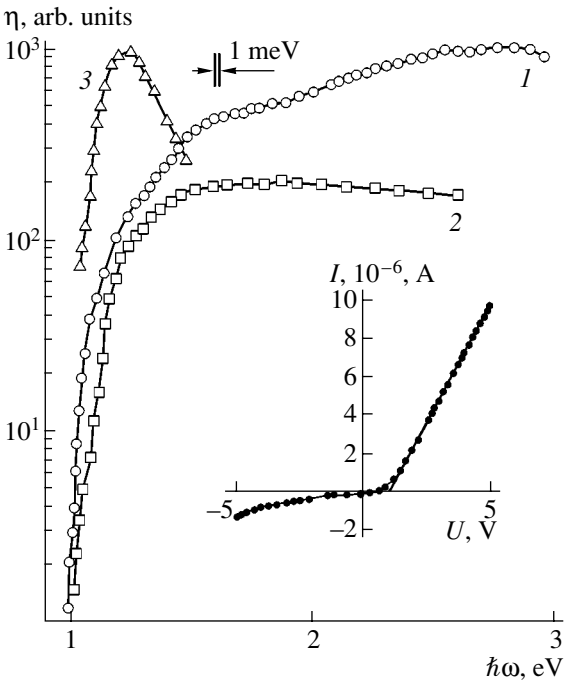

Fig. 1. Spectral dependences of the relative quantum efficiency of photoconversion for the *M*/(*P* + Si)/(*p*-Si) heterostructures in the case where the side of (*1*, *2*) the metal layer and (*3*) *p*-Si crystalline substrate were exposed to unpolarized light at T = 300 K. The substrate thickness was d = 0.3 mm. Curves *1* and *3* refer to sample no. 5, and curve *2* refers to sample no. 7. The inset shows the steady-state current–voltage characteristic of the *M*/(*P* + Si)/(*p*-Si) heterostructures. The forward direction corresponds to a positive polarity of the external bias at the *p*-Si crystalline substrate.

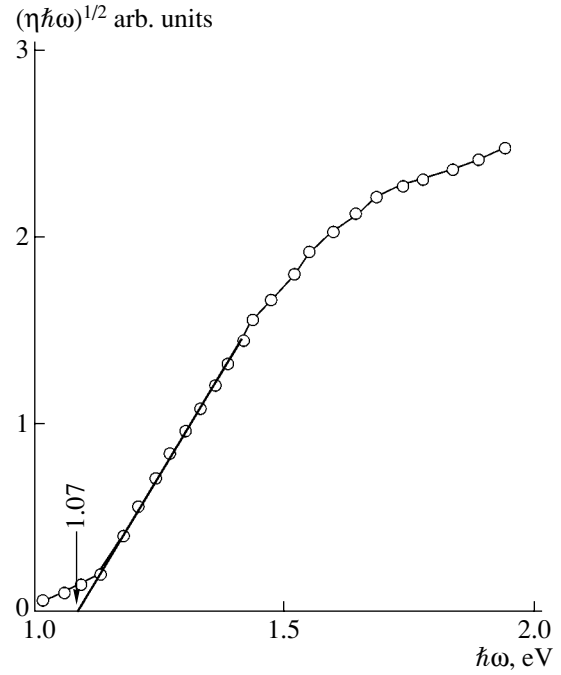

Fig. 2. The dependence $(\eta\hbar\omega)^{1/2} = f(\hbar\omega)$ for the $M/(P + \text{Si})/(p\text{-Si})$ heterostructures in the case where the metal-layer side was illuminated at $T = 300$ K.

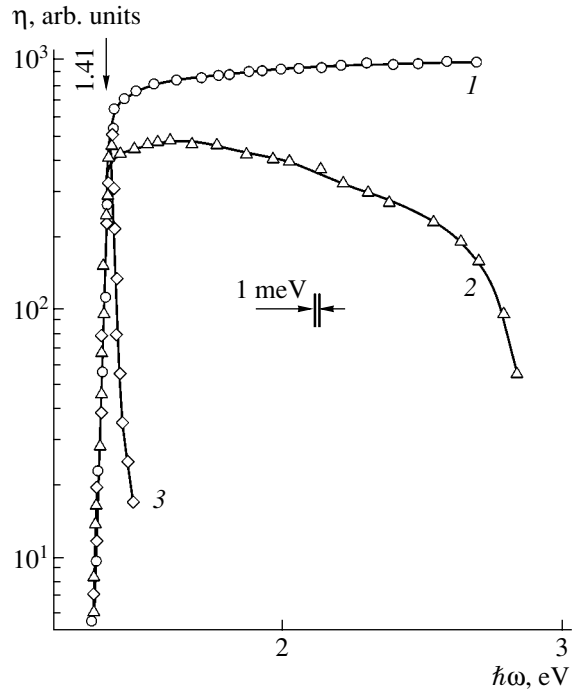

Fig. 3. Spectral dependences of the relative quantum efficiency of photoconversion for the $M/(P + \text{GaAs})/(p\text{-GaAs})$ heterostructures in the case where the side of (*1*, *2*) the metal layer and (*3*) crystalline substrate was illuminated at $T = 300$ K. The substrate thickness was $d = 0.3$ mm. Curve *1* refers to sample no. 11, and curves *2* and *3* refer to sample no. 17.

photocurrent normalized by the number of incident photons. If the side of an $M/(P + \text{Si})/\text{Si}$ heterostructure with its dielectric layer containing a uniformly distributed finely ground *p*-Si phase was illuminated, we observed broadband spectra of photosensitivity, as is shown in Fig. 1 (curves *1*, *2*). For structures of this type, the long-wavelength edges of the spectra of η were similar in shape and could be linearalized when plotted as $(\eta\hbar\omega)^{1/2}$ versus $f(\hbar\omega)$ (Fig. 2). Such a spectral dependence is typical of absorption due to indirect interband transitions [6]. The extrapolation of $(\eta\hbar\omega)^{1/2}$ to zero yielded a cutoff energy that is in agreement with the band gap of bulk crystalline silicon [7].

If the side of the Si $M/(P + \text{Si})/\text{Si}$ heterostructure corresponding to the single crystal substrate (the thickness $d \approx 0.3$ mm) was illuminated, the spectrum of η consisted of a narrow band with a peak around $\hbar\omega \cong 1.24$ eV (Fig. 1, curve *3*). In this case, a short-wavelength decrease in photosensitivity was observed with an increase in the photon energy at $\hbar\omega > 1.24$ eV. This decrease is related to an increase in optical absorption in the Si substrate and to the large spacing between the layer of photoinduced electron–hole pairs and the space-charge region. These circumstances eventually cause the quantum efficiency of photoconversion to decrease. It should be emphasized that, if the dielectric layer with a built-in finely ground Si phase in such structures is illuminated (instead of illumination of the Si substrate), the decrease in photosensitivity in the region of fundamental optical absorption in bulk crystalline Si at $\hbar\omega > 1.24$ eV is virtually nonexistent (Fig. 1, curves *1*, *2*). In this case, it is evident that, in the part of the spectra with shorter frequencies $\eta(\hbar\omega)$ at $\hbar\omega > 1.4$ eV, the photosensitivity of the heterostructures varies only slightly and even exhibits a tendency to decrease in the region $\hbar\omega > 2$ eV (Fig. 1, curve *2*). In the other type of structures (Fig. 1, curve *1*), we observed a steady increase in photosensitivity deep within the fundamental absorption band of bulk silicon; the photosensitivity attained an absolute maximum at $\hbar\omega \approx 2.8$ eV. It should be noted that the heterostructures compared above differ mainly in relation to size, mutual arrangement, and content of the finely ground phase introduced into the epoxy resin layer.

It is worth noting that study of correlation between the short-wavelength spectra of photosensitivity and the real arrangement and size of the particles of the finely ground phase may be of considerable importance for understanding the processes of photoconversion in this new type of heterostructure. At the same time, the lack of short-wavelength decrease in η at $\hbar\omega > E_G^{\text{Si}}$ revealed in the Si-based $M/(P + \text{Si})/\text{Si}$ heterostructures (Fig. 1, curve *1*) may suggest that this result is a manifestation of the reduced dimensions (size-confinement) of the semiconductor particles formed by mechanical

grinding, as in the case of a heterojunction between the nanosized and bulk phases of silicon [8, 9].

As can be seen from Fig. 3, patterns similar to those considered above (Fig. 2) were also observed in the spectra $\eta(\hbar\omega)$ for the $M/(P$ + GaAs)/GaAs heterostructures. In fact, the long-wavelength edge of the photosensitivity of these GaAs-based structures is independent of what side of the structure is illuminated and, in both cases, follows the exponential dependence, with a bend (Fig. 3, curves *1*, *2*) or a peak (curve *3*) at $\hbar\omega \cong 1.41$ eV. This photon energy is consistent with the band gap of GaAs [7]. The steep slope of the long-wavelength edge of photosensitivity, $S = \delta(\ln\eta)/\delta(\hbar\omega) \approx 80\ \text{eV}^{-1}$, corresponds, with regard to [10], to direct interband optical transitions in GaAs [6]. At the same time, the sharp short-wavelength decrease in η at $\hbar\omega > E_G^{\text{GaAs}}$ observed if the substrate side of the structure is illuminated (Fig. 3, curve *3*) is due to a sharp increase in the optical absorption coefficient in this direct-gap semiconductor. From Fig. 3, it is also evident that, if the side with the dielectric layer incorporating a finely ground GaAs phase is illuminated, it is possible to eliminate the short-wavelength decrease in the quantum efficiency at photon energies $\hbar\omega > E_G^{\text{GaAs}}$ (curve *1*) or to shift the high-photosensitivity spectral region much deeper into the fundamental absorption band of GaAs (curve *2*). This finding provides good grounds for believing that, as in the case of the above-discussed heterostructures containing fine Si particles (Fig. 1, curves *1*, *2*), the new approach to fabrication of heterostructures containing fine GaAs particles makes it possible to suppress recombination processes in the depth of the fundamental absorption band of bulk GaAs, in spite of the mechanical grinding of the material used for reducing the dimensionality of the semiconductor.

Figure 4 shows the typical spectral dependence of the photosensitivity of the $M/(P$ + GaAs)/Si heterostructures that involve a contact between two different semiconductors in different states, i.e., between the bulk Si crystal and the finely ground GaAs phase. From Fig. 4 (curve *1*), it is evident that, if the side of the epoxy layer with built-in fine GaAs particles is illuminated, this heterosystem exhibits a high photosensitivity in a wide spectral region, from 1 to 3 eV, and the so-called "window effect" typical of ideal heterojunctions [11]. The long-wavelength edge of the photosensitivity of such heterostructures follows the dependence $\eta\hbar\omega \propto (\hbar\omega - E_G^{\text{Si}})^2$, which is characteristic of indirect interband optical transitions in silicon, and, therefore, can be ascribed to absorption of radiation in the Si substrate (Fig. 4, curve *2*). In turn, the lack of a well-pronounced short-wavelength decrease in photosensitivity when the side of structures with the P + GaAs layer is illuminated may indicate that recombination processes in the region of fundamental absorption of the constituent finely ground semiconductor are suppressed. With regard to the data presented in [8, 9], it can be suggested that one of the possible reasons for widening of the spectral region of photosensitivity in such heterostructures is transformation of the electronic energy spectrum of the semiconductor in its finely ground phase.

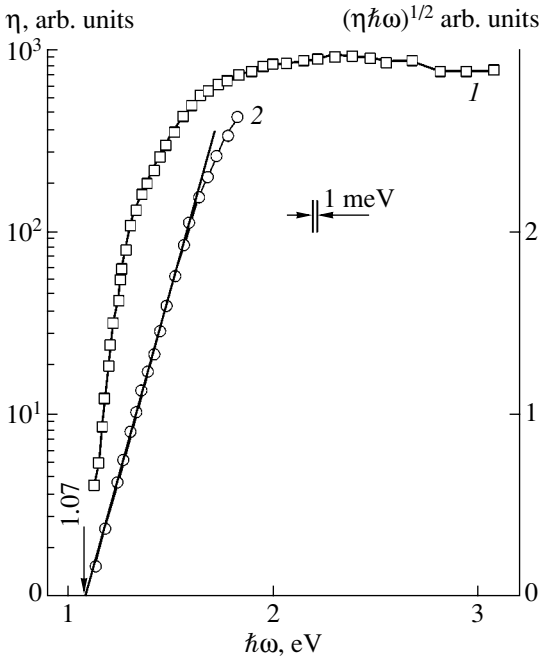

Fig. 4. (*1*) The spectral dependence of the relative quantum efficiency of photoconversion and (*2*) the dependence $(\eta\hbar\omega)^{1/2} = f(\hbar\omega)$ for an $M/(P$ + GaAs)/(p-Si) heterostructure (sample no. 23) in the case where the metal-layer side was exposed to unpolarized light at $T = 300$ K.

Thus, using Si and GaAs as examples, we are first to develop photosensitive structures based on bulk diamond-like semiconductors and finely ground semiconductor phases distributed in a dielectric. With these structures, we have managed to widen the spectral region of high photosensitivity to shorter wavelengths. This result may be due to the reduced dimensionality of the semiconductor crystals achieved by mechanical grinding.

ACKNOWLEDGMENTS

The study was supported by the Department of Fundamental Sciences of the Russian Academy of Sciences program "New Principles of Energy Conversion in Semiconductor Structures."

REFERENCES

1. Zh. I. Alferov, Rev. Mod. Phys. **73**, 767 (2001).
2. J. A. Lott, N. N. Ledentsov, V. M. Ustinov, *et al.*, in *Proceedings of 2000 IEEE LEOS Annual Meeting Conference* (2000), Vol. 1, p. 304.

3. N. A. Maleev, A. R. Kovsh, A. E. Zhukov, *et al.*, in *Proceedings of 10th International Symposium on Nanostructures: Physics and Technology* (St. Petersburg, Russia, 2002), p. 399.
4. L. V. Asryan and R. A. Suris, Fiz. Tekh. Poluprovodn. (St. Petersburg) **38**, 3 (2004) [Semiconductors **38**, 1 (2004)].
5. V. Yu. Rud', Yu. V. Rud', and V. Kh. Shpunt, Zh. Tekh. Fiz. **70** (2), 114 (2000) [Tech. Phys. **45**, 255 (2000)].
6. Yu. A. Ukhanov, *Optical Properties of Semiconductors* (Nauka, Moscow, 1977) [in Russian].
7. *Physicochemical Properties of Semiconductor Materials: A Handbook*, Ed. by A. V. Novoselova and V. B. Lazarev (Nauka, Moscow, 1979) [in Russian].
8. V. Yu. Rud' and Yu. V. Rud', Fiz. Tekh. Poluprovodn. (St. Petersburg) **31**, 254 (1997) [Semiconductors **31**, 197 (1997)].
9. E. V. Astrova, A. A. Lebedev, A. D. Remenyuk, *et al.*, Thin Solid Films **297**, 129 (1997).
10. A. Shileika, Surf. Sci. **37**, 730 (1973).
11. J. I. Pankove, *Optical Processes in Semiconductors* (Prentice-Hall, Englewood Cliffs, N.J., 1971; Mir, Moscow, 1973).

Translated by É. Smorgonskaya

Semiconductors, Vol. 39, No. 11, 2005, pp. 1299–1303. Translated from Fizika i Tekhnika Poluprovodnikov, Vol. 39, No. 11, 2005, pp. 1345–1349.

SEMICONDUCTOR STRUCTURES, INTERFACES, AND SURFACES

Dynamics of Laser-Induced Phase Transitions in Cadmium Telluride

A. A. Kovalev, S. P. Zhvavyĭ^, and G. L. Zykov

Institute of Electronics, Belarussian Academy of Sciences, Minsk, 220090 Belarus

^e-mail: zhvavyi@inel.bas-net.by

Submitted March 14, 2005; accepted for publication March 16, 2005

Abstract—A numerical simulation of the dynamics of phase transitions induced by nanosecond pulsed radiation from a ruby laser in CdTe has been carried out. It is shown that evaporation of Cd atoms results in cooling of the surface; consequently, a nonmonotonic profile of the temperature field is formed, with the maximum temperature being attained in the bulk of the semiconductor at a distance of about 10–30 nm from the surface. At radiation energy densities above the threshold, the molten state formed under the surface extends both to the surface and into the depth of the semiconductor. Crystallization also proceeds in two directions, namely, from the surface into the depth of the samples due to the growth of nucleation centers in the melt, which is highly depleted in Cd atoms under the conditions of intense heat removal, and from the substrate to the surface due to epitaxial growth. © *2005 Pleiades Publishing, Inc.*

At the present time, II–VI semiconductor materials, including cadmium telluride, are extensively used in the production of photoresistors, optical waveguides, detectors of ionizing radiation, solar cells, etc. For the successful use of laser-assisted treatments of such materials within the currently available technologies, it is necessary to gain some insight into the physical processes induced by laser irradiation of these semiconductors.

The regular patterns occurring during modification of CdTe surface layers by irradiation with nanosecond laser pulses have been studied by a number of authors (see, e.g., [1–5]). In such studies, the properties and composition of the surface layers after laser-assisted treatments received the most attention. However, problems concerned with the dynamics and kinetics of the phase transitions induced by laser radiation are not yet adequately understood mainly because there are no data on a number of optical and thermal parameters and their temperature dependences. This is particularly true for the value of the thermal conductivity k_1 and its temperature dependence for molten cadmium telluride. The previously used value, $k_1 = 0.58$ W/(cm K) [1, 6] (accepted as equal to the thermal conductivity of molten silicon), is substantially overestimated; the value $k_1 = 0.011$ W/(cm K), used in [4], refers to the thermal conductivity of crystalline CdTe at its melting point.

Exposure of IV and III–V semiconductors to laser radiation with an energy density above the threshold value induces melting of the surface layer of the material; then, the layer crystallizes in the process of liquid-phase epitaxy at the crystal–melt interface. In the case of II–VI semiconductors, these processes are accompanied by changes in the stoichiometric composition of the surface layer because of evaporation of its components. For instance, during irradiation of the CdTe surface with nanosecond pulses from a ruby laser, the surface layer becomes enriched with tellurium because of an intense evaporation of Cd atoms [7]. In addition, the evaporation profoundly affects the formation of the temperature profile [8] and, thus, influences the dynamics of phase transitions.

In this study, we consider the dynamics of phase transitions initiated in cadmium telluride by nanosecond radiation from a ruby laser (at the wavelength $\lambda = 694$ nm) with regard to the evaporation and shift of the melt–vapor interface. The numerical simulation was carried out on the basis of the one-dimensional heat-transfer equation

$$\rho(T)[c(T) + L_m\delta(T - T_m)]\frac{\partial T}{\partial t} = \frac{\partial}{\partial x}\left[k(x, t)\frac{\partial T}{\partial x}\right] + S(x, t), \quad (1)$$

where ρ is the density, c is the heat capacity, L_m is the latent melting heat, $\delta(T - T_m)$ is the δ function, T_m is the melting temperature, k is the thermal conductivity, t is time, T is temperature, and x is the coordinate in the direction from the surface into the depth of a sample.

In Eq. (1), the function of the heat source $S(x, t)$ describes the heat release on absorption of the laser radiation:

$$S(x, T) = (1 - R)\frac{E(t)}{\tau}\alpha(x, T)\exp\left(-\int_0^x \alpha(x', T)dx'\right). \quad (2)$$

1063-7826/05/3911-1299$26.00

Here, R and $\alpha(x, T)$ are the optical reflection and absorption coefficients, and $E(t)$ and τ are the energy density and the duration of the laser pulse.

The boundary conditions and the initial condition were specified as

$$-k\frac{\partial T}{\partial x}\bigg|_{x=0} = -Q, \quad T(x = d, t) = T_0, \tag{3}$$

$$T(x, 0) = T_0, \tag{4}$$

where d is the thickness of the CdTe layer; T_0 is the initial temperature; and Q is the heat flow from the surface, which is controlled by the flow of evaporating atoms j.

As a rule, when simulating the effect of nanosecond laser radiation on condensed materials, it is assumed that all the energy losses are negligible except the energies expended on evaporation, phase transitions, and chemical reactions (depending on the particular conditions in the problems to be solved). For instance, when the pulse duration $\tau \sim 100$ ns and the intensity of laser radiation is $\sim 10^7$ W/cm^2, the temperature of the surface of the material irradiated is as high as ~2000 K. If the coefficient of the convective heat exchange is taken to be $\alpha_c = 10^{-3}$ W/cm^2 K, the heat flow from the surface is $Q_1 = \alpha_c[T(0, t) - T_0] \sim 2$ W/cm^2, and estimation of the losses for thermal radiation yields the value $Q_2 = \varepsilon\sigma[T^4(0, t) - T_0^4] \sim 100$ W/cm^2 (here, $\sigma = 5.67 \times 10^{-12}$ W/cm^2 K^4 is the Stefan–Boltzmann constant, ε is the reduced emissivity, and T_0 is the ambient temperature). Comparison of these values shows that, in time intervals on the order of 100 ns, the energy losses from the surface due to convective and radiative thermal exchange are small and can be disregarded when simulating the thermal processes induced in semiconductors by nanosecond laser radiation.

For the density of mass flow of the atoms evaporating in vacuum j we used the following dependence [8, 9]:

$$j(T) = 0.435P_s(T)\sqrt{\frac{M}{2\pi k_B T}}. \tag{5}$$

Here, M is the atomic mass, and k_B is the Boltzmann constant. The pressure $P_s(T)$ is defined by the phase equilibrium equation [10]

$$\log P_s(T) = a - b/T. \tag{6}$$

Evaporation of Cd atoms and Te_2 molecules from the surface of both the crystal and the melt was taken into account. The heat flux from the surface was determined by the expression [8]

$$Q = L_{Cd}j_{Cd} + L_{Te}j_{Te}, \tag{7}$$

where L_{Cd} and L_{Te} are the latent evaporation heat for cadmium and tellurium and j_{Cd} and j_{Te} are the mass flow densities for evaporating cadmium and tellurium.

Because of the intensive evaporation of Cd atoms, the surface layer becomes enriched with Te. Therefore, the motion of the vapor–melt phase interface $Z(t)$ is controlled by the flow of evaporating tellurium molecules in accordance with the equation

$$\frac{dZ}{dt} = \frac{j_{Te}}{\rho_{Te}}, \tag{8}$$

where ρ_{Te} is the mass density of tellurium.

Equation (1) was solved numerically using a computational procedure, without considering the melt–crystal phase interface explicitly. When formulating the implicit difference scheme, we used a method of smoothing [11] in which the δ function was approximated by a δ-like function as follows:

$$\delta(T - T_m, \Delta) = \frac{1}{\sqrt{2\pi}\Delta}\exp\left[\frac{(T - T_m)^2}{2\Delta^2}\right]. \tag{9}$$

Here, the initial width $\Delta = 10$ K. The parameter Δ was varied in relation to the temperature gradient in such a way that the interval in which the δ-like function was defined involved no less than three count points. The problem was solved by the sweep method with the use of the iteration procedure. The step along the space coordinate was varied from $h = 0.01$ μm for 0 μm $< x \leq 1$ μm to $h = 0.5$ μm for 20 μm $< x < 35$ μm. The initial step along the time coordinate was 0.2 ns and could be varied depending on the convergence of iterations in the computational process. The optical and thermal parameters of cadmium telluride used to solve the problem are listed in the table. The shape of the laser pulse was specified by the function $\sin^2(\pi t/2\tau)$.

The thermal conductivity of cadmium telluride in its solid state is defined by the expression $k_s(T) = 15.07/T$, with T measured in degrees of kelvin and k_s in W/(cm K) [1]. Such a temperature dependence is typical of the phonon mechanism of heat transport [16]. It is well known that cadmium telluride belongs to the class of materials that melt, following a "semiconductor-to-semiconductor" transition, resulting in the formation of a chain-structured liquid in which charge carriers are located at the ends of the chains [17]. These findings were confirmed by the results by Godlevsky *et al.* [18], who studied the properties of the CdTe melt using the methods of molecular dynamics. It was shown that, when melted, cadmium telluride retained its semiconductor properties and assumed the properties of a metal at higher temperatures. However, the metallization of the CdTe melt is attained due to structural changes, which result in the formation of Te chains, rather than due to an increase in the density of free charge carriers. As the temperature increases further, the Te chains break down into shorter chain fragments, ultimately resulting in the formation of a close-packed metal phase. High-temperature measurements (up to 1825 K) of the electrical conductivity of the CdTe melt were reported in [19]. It was also shown

Optical and thermal parameters of cadmium telluride

Parameter	Crystalline CdTe	Molten CdTe
ρ, g cm^{-3}	$5.887 - 0.1165 \times 10^{-3}T$ [12]	$6.158 - 0.3622 \times 10^{-3}T$ [12]
c, J g^{-1} K^{-1}	$0.205 + 3.6 \times 10^{-5}T$ [13]	0.255 [8]
L_m, J g^{-1}	209 [13]	
T_m, K	1365 [13]	
k, W cm^{-1} K^{-1}	$15.07/T$ [1]	$2 \times 10^{-5}(2.213 - 3.654 \times 10^{-3}T + 1.52 \times 10^{-6}T^2)$
n (λ = 694 nm)	3.04 [14]	3.04 [14]
α, cm^{-1}	$(83.96T + 3.54 \times 10^4)$ [1]	1.5×10^5 [1]
Parameter	Cd	Te
L, J g^{-1}	888 [8]	893 [8]
a*	5.68 [10]	4.72 [15]
b	5720 [10]	5960.2 [15]

* Pressure is measured in atmospheres; n is the refractive index.

that semiconductor properties were retained in the molten state, with further metallization of the melt at higher temperatures. In the context of a double-structure cluster model of the melt [12], the gradual transition to metal-type conductivity was interpreted in [19] as being a consequence of the formation of a chain-structured liquid on melting. This behavior is accompanied by the appearance of charge carriers at the ends of the constituent chains, which results in an increase in the carrier concentration and electrical conductivity.

We used data on the conductivity of the CdTe melt [19] and the Wiedemann–Franz relationship [16] to obtain the temperature dependence of the thermal conductivity for the CdTe melt as follows:

$$k_1(T) = 2 \times 10^{-5}T \times (2.213 - 3.654 \times 10^{-3}T + 1.52 \times 10^{-6}T^2). \quad (10)$$

Since the Wiedemann–Franz relationship for molten II–VI compounds has not been studied due to the lack of experimental data on the electrical conductivity, the Lorentz number was taken to be 2×10^{-8} W Ω/K^2.

Figure 1 shows the time dependences of the CdTe surface temperature (solid line) and of the flux of vaporizing Cd (dashed line) and Te (dashed-and-dotted line) atoms on irradiation of a CdTe sample with pulses from a ruby laser with the energy density E = 0.2 J/cm^2 and pulse duration τ = 80 ns. It is evident that the flux of vaporizing Cd atoms is substantially more intensive than the flux of Te atoms, since the vapor pressure of the Cd atoms is an order of magnitude higher than the pressure of the Te atoms. It is the vaporization of Cd atoms that brings about a rather intensive cooling of the irradiated sample surface and promotes, from the initial stage of heating, the formation of a nonmonotonic temperature profile with a maximum at the depth $x \approx$ (0.01–0.03) μm (Fig. 2). As a result, melting starts near the surface at a depth of ~19.5 nm; then, the molten domain extends to the surface (Fig. 3), with a velocity ~1.5 m/s, and into the depth of the sample, with a velocity ~2.5 m/s.

At the stage during which a sample cools down, the nonmonotonic temperature profile is retained (Fig. 4). Therefore, the crystallization front starts moving both from the surface into the depth of a sample (Fig. 3, curve *2*') and from the maximum depth of the molten domain (~157 nm) to the sample surface (Fig. 3, curve *2*). The velocities of motion of the melt–crystal interfaces are nearly equal, being ~1 m/s. The crystallization process is brought to completion at the moment at which both fronts meet at a depth of ~68 nm. By this time the evaporated-layer thickness is ~6 nm (Fig. 3, curve *2*").

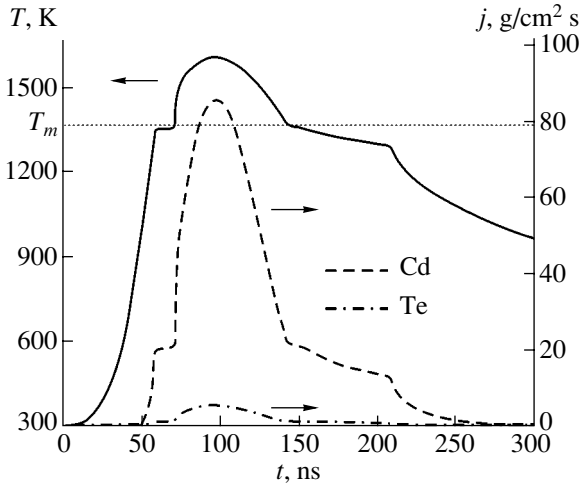

Fig. 1. Time dependences of (solid line) the CdTe surface temperature T and (dashed and dot-and-dashed lines) the fluxes j of the vaporizing (dashed line) Cd and (dot-and-dashed line) Te components at the irradiation energy density E = 0.2 J/cm^2.

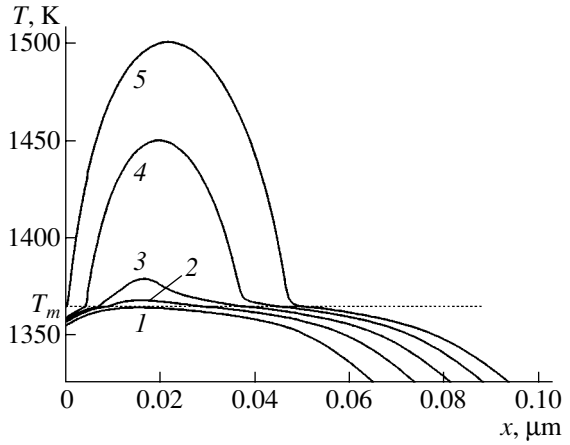

Fig. 2. Calculated temperature profiles during the melting stage of CdTe at the irradiation energy density $E = 0.2$ J/cm^2 at different instants of time: (*1*) 62, (*2*) 64, (*3*) 66, (*4*) 68, and (*5*) 70 ns.

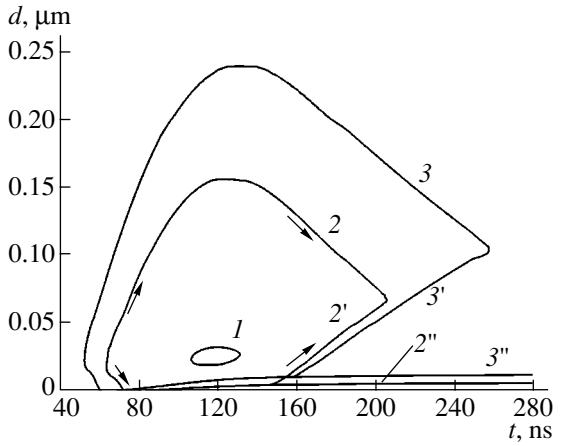

Fig. 3. The time dependence of the thickness of the molten CdTe layer at the irradiation energy densities E = (*1*) 0.1, (*2*, *2*') 0.2, and (*3*, *3*') 0.3 J/cm^2. Lines *2*" and *3*" indicate the thickness of the layer evaporated at $E = 0.2$ and 0.3 J/cm^2, respectively.

It should be noted that, at the depth of the molten layer, recrystallization proceeds via epitaxial growth from the substrate. At the same time, crystallization from the surface proceeds as a result of a three-dimensional growth of nucleation centers in the molten layer, which has a nonstoichiometric composition, under the conditions of strong depletion of Cd atoms from the melt and intensive heat removal. In this case, a fine-grained polycrystalline or amorphous phase is expected to be formed at the surface, depending on the conditions of laser irradiation. As a consequence, the surface layer, ~62 nm in thickness, will contain a large number of defects [5, 7].

The threshold energy density for melting under exposure of the CdTe surface to radiation from a ruby laser with a pulse duration of 80 ns has been determined experimentally at the level of 0.12 J/cm^2 [20]. As follows from the results of optical probing, an increase in the reflectivity and a decrease in the transmittance was observed at $E = 0.1$ J/cm^2. These data were accounted for in [17] by the temperature dependences of the optical parameters of CdTe in its solid state. In accordance with the calculations, at an irradiation energy density of 0.1 J/cm^2, the melt is formed near the surface at a depth of 23.5 nm; it then moves 3.5 nm toward the surface but does not reach it (Fig. 3). The lifetime of the liquid phase is ~25 ns, and the thickness of the evaporated layer after the crystallization process is ~1.1 nm.

The modification of the CdTe surface region as a result of exposure to nanosecond radiation from a ruby laser ($\tau = 20$ ns) was studied experimentally by Golovan' *et al.* [2]. As follows from their experimental data and the theoretical calculations in [6], the threshold energy density is ~40 mJ/cm^2. Studies of laser-induced defect formation [7] have shown that, at $E = 80$ mJ/cm^2, the thickness of the layer in which point defects are

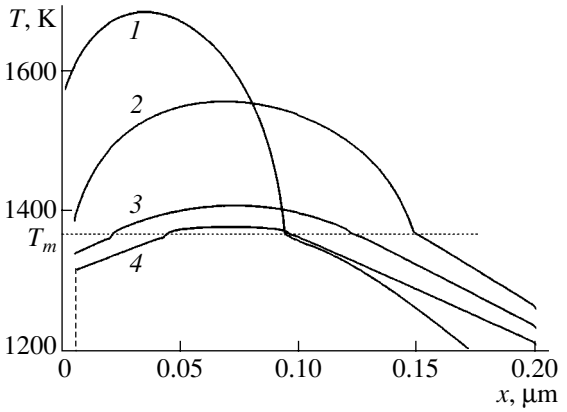

Fig. 4. Calculated temperature profiles at the stage of crystallization for the irradiation energy density $E = 0.2$ J/cm^2 at different instants of time: (*1*) 80, (*2*) 140, (*3*) 160, and (*4*) 180 ns. The dashed line represents the thickness of the evaporated layer.

detected is ~70 nm. At $E = 143$ mJ/cm^2, such a layer is thicker than 100 nm. According to calculations taking into account the experimental conditions in this study, the threshold for melting is ~60 mJ/cm^2. In this case, a molten layer ~22 nm in thickness is formed in the semiconductor at a depth of ~10 nm and does not extend to the surface (Fig. 5). As a sample cools down, this layer is crystallized due to epitaxial growth. At higher energy densities (curves *2*, *3*), the melt reaches the surface. In this case, as the semiconductor cools down, a surface layer containing a large number of defects is formed due to multinucleus crystallization in the surface layer [5]. At $E = 80$ and 120 mJ/cm^2, the thickness of this layer is ~27 and ~47 nm, respectively (curves *2*', *3*'). For the above values of E, the depths of the extension of the melt are 73 and 130 nm, respectively. The intensive

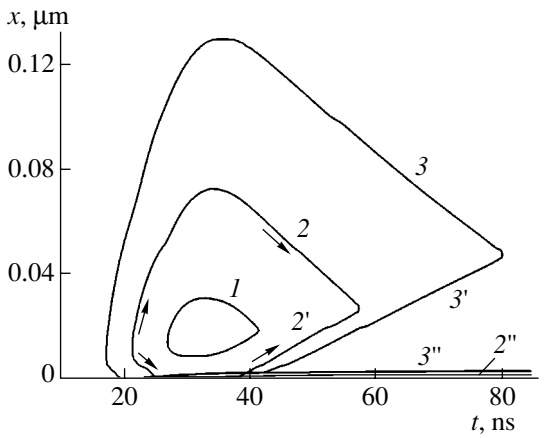

Fig. 5. The time dependence of the thickness of the molten CdTe layer x on exposure to an 20-ns laser pulse with the energy densities E = (*1*) 0.06, (*2*, *2*') 0.08, and (*3*, *3*') 0.12 J/cm^2. Lines *2*" and *3*" indicate the thickness of the layer evaporated at E = 0.08 and 0.12 J/cm^2, respectively.

vaporization from the surface and the high mobility of Cd atoms in the melt (the diffusion coefficient is D_{Cd} = 6.7×10^5 cm^2/s [18]) favor the formation of point defects in the depth of these layers, due to crystallization of the melt to a nonstoichiometric composition. At the energy density 120 mJ/cm^2, the thickness of the evaporated layer is ~3 nm (curve *3*"). The values calculated above are in satisfactory agreement with the experimental data [7].

Thus, a numerical simulation of the influence of radiation from a ruby laser on cadmium telluride shows that vaporization profoundly affects the dynamics of phase transitions in the surface layer. The intensive vaporization results in cooling of the surface of the material; as a consequence, a nonmonotonic profile of the temperature field is formed, with the maximum temperature inside the semiconductor being at a distance of about 20–30 nm from the surface. At above-threshold radiation-energy densities, the melt formed under the surface extends in opposite directions: to the surface and into the depth of the semiconductor sample. Crystallization of the melt proceeds in two directions as well, namely, (i) from the surface into the depth of a sample due to a three-dimensional growth of crystallization nuclei in the molten layer of nonstoichiometric composition under the conditions of depletion of Cd atoms from the melt and intensive heat removal and (ii) from the substrate to the surface due to epitaxial growth.

REFERENCES

1. R. Bell, M. Toulemonde, and P. Sifferent, Appl. Phys. **19**, 313 (1979).
2. L. A. Golovan', V. Yu. Timoshenko, and P. K. Kashkarov, Poverkhnost, No. 10, 65 (1995).
3. Y. Hatanaka, M. Niraula, Y. Aoki, *et al.*, Appl. Surf. Sci. **142**, 227 (1999).
4. V. A. Gnatyuk, T. Aoki, O. S. Gorodnychenko, and Y. Hatanaka, Appl. Phys. Lett. **83**, 3704 (2003).
5. I. L. Shul'pina, N. K. Zelenina, and O. A. Matveev, Fiz. Tverd. Tela (St. Petersburg) **42**, 548 (2000) [Phys. Solid State **42**, 561 (2000)].
6. I. Yu. Viskovatykh, V. M. Lakeenkov, P. K. Kashkarov, *et al.*, Izv. Ross. Akad. Nauk, Ser. Fiz. **57** (9), 12 (1993).
7. L. A. Golovan', P. K. Kashkarov, V. M. Lakeenkov, *et al.*, Fiz. Tverd. Tela (St. Petersburg) **40**, 209 (1998) [Phys. Solid State **40**, 187 (1998)].
8. L. A. Golovan, B. A. Markov, P. K. Kashkarov, and V. Yu. Timoshenko, Solid State Commun. **108**, 707 (1998).
9. S. I. Anisimov, Ya. A. Imas, G. S. Romanov, and Yu. V. Khodyko, *The Effect of High-Power Radiation on Metals* (Nauka, Moscow, 1970) [in Russian].
10. S. Dushman, *Scientific Foundations of Vacuum Technigue*, Ed. by J. M. Lafferty (Wiley, New York, 1962; Mir, Moscow, 1964).
11. A. A. Samarskiĭ and B. D. Moiseenko, Zh. Vychisl. Mat. Mat. Fiz. **5**, 816 (1965).
12. V. M. Glazov and L. M. Pavlova, Zh. Fiz. Khim. **75**, 1735 (2001).
13. K. R. Zanio, in *Semiconductors and Semimetals*, Vol. 13: *Cadmium Telluride*, Ed. by R. K. Willardson and A. C. Beer (Academic, New York, 1978).
14. S. Adachi and T. Kimura, Jpn. J. Appl. Phys. **32**, 3496 (1993).
15. R. Fang and R. F. Brebrick, J. Phys. Chem. Solids **57**, 443 (1996).
16. A. S. Okhotin, A. S. Pushkarskiĭ, and V. V. Gorbachev, *Thermal Properties of Semiconductors* (Atomizdat, Moscow, 1972) [in Russian].
17. A. R. Regel' and V. M. Glazov, *Physical Properties of Electronic Melts* (Nauka, Moscow, 1980) [in Russian].
18. V. V. Godlevsky, M. Jain, J. J. Derby, and J. R. Chelikowsky, Phys. Rev. B **60**, 8640 (1999).
19. V. M. Sklyarchuk, Yu. O. Plevachuk, P. I. Feĭchuk, and L. P. Shcherbak, Neorg. Mater. **38**, 1314 (2002).
20. G. D. Ivlev, E. I. Gatskevich, S. P. Zhvavyi, *et al.*, in *Proceedings of 8th International Conference on Laser and Laser-Information Techologies: Fundamental Problems and Applications* (Plovdiv, Bulgaria, 2003), p. 25.

Translated by É. Smorgonskaya

Semiconductors, Vol. 39, No. 11, 2005, pp. 1304–1307. Translated from Fizika i Tekhnika Poluprovodnikov, Vol. 39, No. 11, 2005, pp. 1350–1353.

LOW-DIMENSIONAL SYSTEMS

Studies of the Electron Spectrum in Structures with InGaN Quantum Dots Using Photocurrent Spectroscopy

D. S. Sizov^, V. S. Sizov, V. V. Lundin, A. F. Tsatsul'nikov, E. E. Zavarin, and N. N. Ledentsov

Ioffe Physicotechnical Institute, Russian Academy of Sciences, Politekhnicheskaya ul. 26, St. Petersburg, 194021 Russia

^e-mail: Dsizov@pop.ioffe.rssi.ru

Submitted February 14, 2005; accepted for publication March 1, 2005

Abstract—Structures with InGaN/GaN quantum dots have been studied using photocurrent spectroscopy. The dynamic range of measurements is found to amount to four orders of magnitude under preservation of the signal-to-noise ratio at a level higher than ten. Within the experimental accuracy, the shape of the spectrum is independent of an applied reverse external bias, whereas the spectrum itself shifts to shorter wavelengths, which is attributed to the Franz–Keldysh effect. Variation of the temperature brings about a change in the spectrum shape. This effect is found to be different for structures grown under different conditions. This behavior can be attributed to homogeneous broadening of the electronic states, the statistics of charge carriers at the levels of quantum dots, and the effect of temperature on the position of these levels. © *2005 Pleiades Publishing, Inc.*

1. INTRODUCTION

For semiconductor light-emitting structures that include *p–n* junctions and contain quantum-dimensional inclusions (such as quantum wells or quantum dots (QDs)) in their active region, only interband absorption occurring in the active region makes a contribution to the photocurrent in measurements of photoconductivity for which the photon energy is smaller than the band gap of the matrix. This circumstance makes it possible to study the electron spectrum in the active region directly [1]. As a rule, other methods used to measure absorption spectra provide no means with which to accurately separate the contribution from passive regions, which detrimentally affects experimental sensitivity. These requirements are especially strict in studies of structures in which the emission originates from deeply localized states whose concentration is lower than that of the states in the matrix. For example, this situation takes place in the structures with QDs. At the same time, any kind of absorption depends on occupancy of the levels that are involved in the transition: in the case where the occupancy of the relevant levels is comparable to unity, the absorption decreases; if the population sign is reversed, amplification is observed in the medium [2]. In addition, when measuring the photocurrent, we should take into account that some of the electron–hole pairs generated during excitation of the photocurrent are separated by a *p–n* junction and the remaining electrons and holes recombine. Under certain conditions, retardation of the charge-carrier extraction from localized levels of a QD for some QD-containing structures and subsequent reradiation of these carriers are possible [1]. The characteristic times of emission of charge carriers from a QD increase exponentially as the depth of charge-carrier localization increases and temperature decreases [3]. In the case where the emission times of charge carriers become comparable to the radiative-recombination times, reradiation of the generated electron–hole pairs is possible. In addition, retardation of extraction for already delocalized charge carriers is possible, which can lead to formation of an excess population in the vicinity of the active region. In this study, we used the photocurrent method to investigate light-emitting diode structures with InGaN/GaN QDs. The system of semiconductor compounds containing Group III nitrides is characterized by a wide band gap. As a result, the band offsets at the heteroboundaries can also be large. At the same time, the current level of insight into the kinetics of relaxation and thermal activation of charge carriers and, also, into the statistics of charge carriers in this system is relatively inadequate.

2. EXPERIMENTAL

The structures under study were grown using an AIX2000HT system and contained five InGaN QD layers that had an average thickness of 3 nm and were separated by 7-nm-thick GaN barriers. A more detailed description of the structure design can be found in [4]; however, in contrast to the structures studied in [4], we used a special technological method (growth interruption) for one of the structures in order to enhance the phase decomposition that initiates QD formation [5]. This interruption should lead to the formation of QDs with a higher depth of localization of their charge carriers. The photocurrent was excited using a gas-discharge xenon lamp and measured with an SR810 DSP

1063-7826/05/3911-1304$26.00

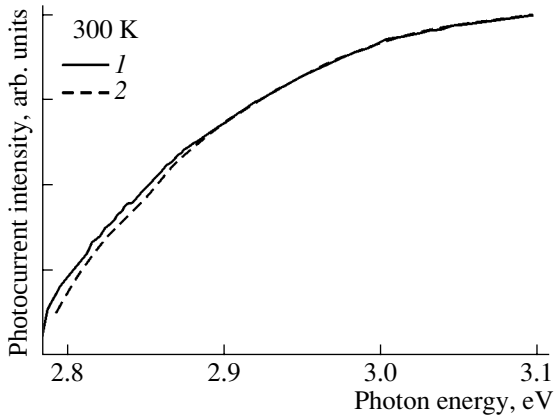

Fig. 1. Photocurrent spectra for the structures with quantum dots. The reverse-bias voltage applied to the structure was $V = (1)$ 0 and (2) –3 V.

synchronous detector. We used a resistive heater in measurements of the photocurrent spectra at temperatures above 295 K (up to 600 K). In the temperature range under consideration, a tin contact was used to measure the current. In order to increase the signal-to-noise ratio, we averaged the signal over a fairly long time interval; at the same time, the stability of the lamp power was also controlled.

3. RESULTS AND DISCUSSION

It is well known that the electron spectrum of structures with InGaN QDs can be described by the error function [5] and the tail of states can be approximated by the Gaussian function. The variance parameter in the latter function can be determined by studying the position of the emission peak as a function of temperature. This approach implies a quasi-equilibrium distribution of charge carriers in the entire temperature range. At the same time, the long-wavelength tail of the photocurrent spectrum can also be approximated by the error function; however, the variance parameter can, in this case, differ from that obtained from temperature dependences of the peak position in the spectrum. This parameter, as obtained from photocurrent measurements and reported by Eliseev [5], was much larger than would be expected from temperature dependences of the position of the peak in the spectrum and was attributed to an appreciable inhomogeneous broadening of the electron spectrum. This broadening corresponds to relaxation times on the order of 10 fs; however, experimental data obtained in studies with time resolution indicate that the relaxation times in a QD are much longer [6]. It is conceivable that structures possessing a radically different rate of charge-carrier relaxation were studied in [6].

In order to reveal a correlation between the photocurrent spectra and the electron spectrum, we measured

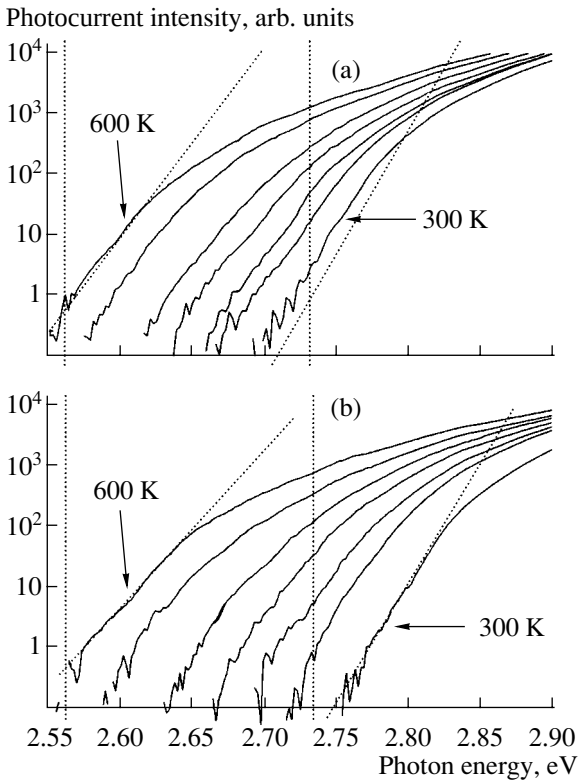

Fig. 2. Photocurrent spectra measured at temperatures ranging from 300 to 600 K for structures grown (a) with a growth interruption, which stimulates the phase separation in InGaN, and (b) without a growth interruption.

the photocurrent in structures that contained QDs. The measurements were carried out at temperatures ranging from 300 to 600 K with (or without) a reverse external bias voltage applied to the structure. Previously, we studied the photocurrent spectra for a structure with a low degree of charge-carrier localization; in that case, an increase in temperature did not result in appreciable changes in the shape of the photocurrent spectrum [4]. An increase in the sensitivity of the experimental setup and a study of QDs with a large depth of charge-carrier localization made it possible to observe and analyze variations in the shape of the photocurrent spectra in the region of long-wavelength tails.

In Fig. 1, we show the photocurrent spectra of a structure with QDs such that the charge carriers were localized at a large depth. As can be seen from Fig. 1, the application of a reverse bias voltage does not affect the spectrum shape within the experimental accuracy; however, a slight shift of the spectrum to shorter wavelengths is observed. Since the photocurrent depends on the light absorption and the efficiency of extraction of photogenerated charge carriers, the above observation indicates that an external bias only slightly affects both the aforementioned processes. The short-wavelength shift of the photocurrent spectrum occurring when an external reverse bias is applied can be attributed to the

Franz–Keldysh effect [7]. At the same time, an increase in temperature leads to an appreciable extension of the long-wavelength tail of the spectrum (Fig. 2). This behavior corresponds to an increase in the variance parameter if the photocurrent spectrum is approximated with a Gaussian function. This phenomenon can be accounted for on the basis of several different standpoints:

(i) An increase in temperature leads to an increase in the homogeneous broadening of the levels, since there is an increase in the rate of interaction between charge carriers and phonons [5]. In this case, the emission times for charge carriers are much shorter than the times of recombination, whose rate, in order of magnitude, is typically equal to 10^9 s^{-1} [6].

(ii) The probability of charge-carrier recombination is comparatively high due to retardation of the carrier emission if the times of carrier emission to QDs with a large depth of localization are relatively long; as a result, the photocurrent efficiency is lowered in structures with deep QDs. As the temperature increases, the role of deep QDs becomes more important owing to an increase in the probability of emission [1].

(iii) An increase in temperature brings about a variation in the electron spectrum of the structure. This phenomenon is related to the different composition dependences of the electronic–optical parameters of GaN and InGaN.

In any of the above cases, the fact that the spectrum shape is not affected by the application of a bias is indicative of a fairly rapid extraction of already delocalized charge carriers from the active region. In other words, this behavior means that the *p–n*-junction field is found to be sufficient for rapid separation of delocalized charge carriers before their recombination in the active region.

We now consider extension of the photocurrent-spectrum tail for structures grown under different conditions in more detail. In Figs. 2a and 2b, we show the photocurrent spectra for structures grown (1) without and (2) with an interruption of the growth process, respectively (the interruption stimulates phase separation). As can be seen, when the temperature is increased, the extension of the spectrum tail is larger for structures 2. In accordance with the above-considered interpretation, this distinction could be caused by the following factors:

(I) A larger relative increase in the rates of emission and capture of charge carriers in a structure of type 2 (Fig. 2b). If the emission rate corresponds to a time of 10 fs, the homogeneous broadening increases more rapidly with temperature. In this case, the statistics of charge carriers in the active region corresponds to the equilibrium state.

(II) When the emission times are much longer than 10 fs, extension of the spectrum tail can mean that the emission in structures 2 is greatly retarded, which, as was considered above, leads to a decrease in the contribution of deeper QDs to the photocurrent. In this situation, the statistics of charge carriers corresponds to a nonequilibrium state. In structures 1 (Fig. 2a), the initial emission rate can be high and its relative variation affects the photocurrent spectra only slightly.

(III) An increase in temperature may affect the spectrum of states in structure 1 to a lesser extent than in structure 2. A variation in the spectrum of states can be caused, for example, by the different sensitivity of built-in fields to temperature at various levels of dimensional quantization [7]. In addition, this variation can be caused by a different rate of decrease in the band gap for the GaN matrix and the InGaN QD layer as the temperature increases.

For the structures under consideration, data obtained from X-ray diffractometry indicate that the average content of In in the InGaN layer of structures 2 is lower than in this layer of structures 1 (10 and 13%, respectively), even though the positions of the emission peaks for these structures were almost identical (2.8 eV) at room temperature. The above structural features could account for the difference between the temperature dependences of the optical properties of the structures under consideration. We can take into account the following factors. In structures grown under certain conditions, homogeneous broadening of the levels can be important. As a result, a quasi-equilibrium distribution of charge carriers can take place even at low temperatures. However, in structures grown under different conditions, the homogeneous broadening can be negligible, while the quasi-equilibrium statistics of charge carriers is established at fairly high temperatures. Therefore, additional experimental data are needed for clarifying the issue of what exactly the absorption and carrier-extraction mechanisms that are in effect in structures with InGaN QDs are.

4. CONCLUSIONS

We studied the photocurrent spectra of structures with InGaN quantum dots; the spectra were measured using a high-sensitivity setup. The application of an external bias voltage did not affect the spectrum shape to within the experimental accuracy. This observation means that the extraction of photogenerated charge carriers is independent of the *p–n*-junction field; instead, this extraction depends on other parameters, for example, the rates of thermal emission of charge carriers from the quantum dots and the rate of the tunneling processes (if these exist). At the same time, the spectrum shape changed appreciably as the temperature was varied. Specifically, the spectrum tails were extended as the temperature was increased. This effect was more pronounced in a structure with a higher degree of phase separation in the active region.

ACKNOWLEDGMENTS

We thank M.A. Yagovkina and V.I. Il'ina for their contribution to the experimental part of this study.

This study was supported by the Russian Foundation for Basic Research.

REFERENCES

1. P. W. Fry, I. E. Itskevich, S. R. Parnell, *et al.*, Phys. Rev. B **62**, 16784 (2000).
2. M. Kubal, E. S. Jeon, Y.-K. Song, *et al.*, Appl. Phys. Lett. **70**, 2580 (1997).
3. L. V. Asryan and R. A. Suris, Semicond. Sci. Technol. **11**, 554 (1996).
4. D. S. Sizov, V. S. Sizov, E. E. Zavarin, *et al.*, Fiz. Tekh. Poluprovodn. (St. Petersburg) **39**, 492 (2005) [Semiconductors **39**, 467 (2005)].
5. P. G. Eliseev, J. Appl. Phys. **93**, 5404 (2003).
6. I. L. Krestnikov, N. N. Ledentsov, A. Hoffmann, *et al.*, Phys. Rev. B **66**, 155310 (2002).
7. S. F. Chichibu, T. Azuhata, T. Sota, *et al.*, J. Appl. Phys. **88**, 5153 (2000).

Translated by A. Spitsyn

Semiconductors, Vol. 39, No. 11, 2005, pp. 1308–1312. Translated from Fizika i Tekhnika Poluprovodnikov, Vol. 39, No. 11, 2005, pp. 1354–1358.

LOW-DIMENSIONAL SYSTEMS

Specific Features of Photoluminescence of InAs/GaAs QD Structures at Different Pumping Levels

V. A. Kulbachinskii^, V. A. Rogozin, R. A. Lunin, A. A. Belov, A. L. Karuzskiĭ, A. V. Perestoronin, and A. V. Zdoroveishchev

Moscow State University, Moscow, 119992 Russia

^e-mail: kulb@mig.phys.msu.ru

Submitted February 22, 2005; accepted for publication March 9, 2005

Abstract—Photoluminescence spectra of InAs/GaAs QD structures have been studied at different pumping powers and temperatures. At low pumping levels, one of the spectral lines in an undoped sample is shifted as the power increases. As the temperature increases, the luminescence intensity in the high-energy portion of the spectrum decreases, and the low-energy spectrum is red-shifted. The presence of QDs of two characteristic sizes is demonstrated. © *2005 Pleiades Publishing, Inc.*

1. INTRODUCTION

Structures with self-organized quantum dots (QDs) are of interest for development of radically new QD devices, such as lasers or memory cells, with parameters superior to the existing ones [1, 2]. Particular attention has been given to studies of the photoluminescence (PL) of these structures [3, 4], as PL studies are the simplest method for confirming the presence of QDs in a sample, estimating their size, and observing quantum confinement [5–7]. Active studies of QD systems and a broad distribution of efficient technologies for the production of quantum-confined structures have drawn attention to development of methods for estimation of structure quality by diagnostics of the electron states using the low-temperature luminescence. Moreover, systems of correlated QDs are of fundamental interest as a model object for investigations of many-particle interactions in strongly correlated systems of a Mott–Hubbard type [8].

The shape of the PL spectra is mainly defined by the intrinsic properties of the samples under study (the electronic structure, distribution of free-carrier density, and the possibility of phonon formation). However, several external factors, such as the temperature of the studied sample and frequency and power of light exciting the PL, exert a strong influence on the obtained data.

The effect of excitation power on the PL spectra was studied in [9–13]. In these studies, the scatter in QD size was small, whereas the process of self-organized QD growth often results in the formation of QDs of different size [14, 15]. Another specific feature of the studies performed so far is the fact that they mainly focused on investigations of the PL spectra at high pumping powers, whereas the effect of low pumping power on the shape of the PL spectra is little understood. Also little known about is the effect of doping on the PL spectra of doped structures.

For example, in [9], increasing the pumping power from 0.5 to 32 W/cm^2 resulted in a blue shift of the PL peak of InAs QDs by 18 meV and in the broadening of this peak. This behavior was explained as follows: at low pumping powers, only a certain portion of QDs are in an excited state, and large-sized QDs are excited first [10]. As the power is increased, a larger amount of small-sized QDs contribute to the PL spectrum. It also follows from [10] that, in doped samples, the initial position of the PL peak must be at a higher energy, since the energy levels of several large-sized QDs are initially filled and smaller QDs contribute to PL even at the lowest pumping power.

As the illumination intensity further increases from 45 to 4500 W/cm^2, the position of the PL peak remains virtually unchanged, since, at this power, all QDs contribute to PL. However, this circumstance gives rise to new higher energy peaks related to the excitation of levels with higher energies in the QDs [11].

In [12], the PL spectra were studied at an optical excitation power ranging from 1 to 1100 W/cm^2. In the power range below 100 W/cm^2, only the amplitude of the spectral lines increased, while the general shape of spectrum remained virtually unchanged. At higher powers, new spectral lines appeared, similarly to [11].

In [13], the PL spectra were studied at extremely high powers of optical excitation, specifically, up to 20 kW/cm^2. A large number of excitons concentrated in the QDs, and the interaction between these excitons are responsible for decreasing the energy of transitions from ground states, whereas the PL peaks related to transitions from excited states are blue-shifted.

Thus, four portions can be distinguished in the dependence of the PL spectra of QD structures on optical excitation power. At low powers, a shift of the spectral peaks related to involvement of new QDs is observed. In addition, the amplitude of the peaks

1063-7826/05/3911-1308$26.00

increases linearly, but the shape of the spectrum is not changed. Then, at a sufficiently high power of optical excitation, new lines arise in the PL spectra. Finally, at extremely high powers, a shift of lines related to inter-exciton interaction is observed.

The additional PL peaks arising in the spectra of QD structures can be related to more than simply the excitation of the next energy levels. For example, the two PL peaks observed in [14, 15] are related to the formation of QDs of two different sizes in the structures under study. The temperature dependence of the PL spectra of such structures was also discussed in [15]. At low temperatures, nonresonant photoexcitation leads to uniform occupation of all QDs. As the temperature increases, the probability of carrier tunneling between the QDs increases, so progressively deeper QDs are preferentially occupied and involved in radiative recombination. Therefore, the red shift of PL lines observed with an increase in temperature is stronger than that predicted by a decrease in the band gap.

This communication reports on a study of PL spectra for doped and undoped samples containing QDs of two different sizes. The spectra were recorded at relatively low optical excitation powers, from 10 mW/cm^2 to 9 W/cm^2, at temperatures between 4.2 K and room temperature.

2. SAMPLES AND EXPERIMENTAL METHODS

The structures for study were grown by MOCVD at 630°C at atmospheric pressure. Sample no. *1* contained a homogeneously Si-doped 1.3-μm-thick GaAs matrix grown on a semi-insulating (001) GaAs substrate. A layer of InAs QDs, formed by depositing 4.5 monolayers (ML) of InAs between two 15-nm-thick undoped InAs spacers, was built into the central part of the matrix. Sample no. *2* was grown on a vicinal semi-insulating (001) GaAs substrate, misoriented by 2° in the [110] direction. It consisted of an undoped GaAs matrix and a layer of InAs QDs formed by depositing 3.3 ML of InAs near the structure surface. Sample no. *3* was grown on a substrate with a 0.14° misorientation. In this sample, the thickness of InAs was 1.4 ML, which was not enough for the formation of QDs. The sample was doped with two δ layers of Si, separated from the QD layer by GaAs spacers of 20 nm in thickness. The total thickness of the sample was 0.8 μm. Thus, PL was studied in samples with doped QDs (sample no. *1*), undoped QDs (sample no. *2*), and with an InAs wetting layer (WL) (sample no. *3*).

The morphology of the surfaces with QDs was studied with an Accurex TMX-2100 atomic force microscope in the contact mode at atmospheric pressure.

The PL spectra were recorded at liquid-helium, liquid-nitrogen, and room temperatures using an MDR-3 spectrometer and an FÉU-62 photomultiplier operating in the photon-counting mode under optical excitation by an CW YAG laser with an LCM-T-111 pumping

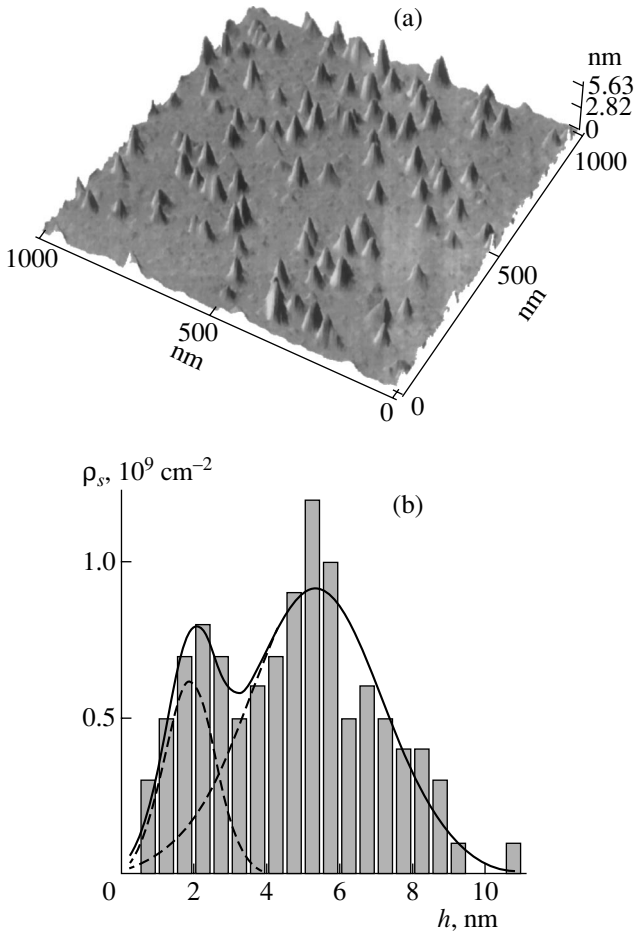

Fig. 1. (a) AFM image of the surface of a sample with QDs revealed by selective chemical etching of the capping layer and (b) histogram of the height distribution of the surface density of QDs for the surface under study.

diode (with a wavelength of 532 nm, emission power of 20 mW, and laser beam divergence θ = 1.4 mrad). The laser beam was focused by a spherical lens with the focal length f = 33.5 cm. The diameter of the light spot d in the focal plane of the lens was determined from the relation $d = \theta f$ [16, p. 525] and was found to be equal to 0.47 mm. The incident power was determined taking into account the reflection from the fused quartz windows of the optical cryostat. During spectral studies in the temperature range ~4.2 K, the optical excitation power was varied from 10 mW/cm^2 to 9 W/cm^2.

3. RESULTS AND DISCUSSION

Figure 1 shows an AFM image of the doped QD layer, obtained after the 15-nm-thick capping layer was removed by selective etching [17]. In spite of possible etching of the clusters, the size and surface density of the QDs can be estimated from this image. Two types of QDs can be seen. The larger dots have a surface density of ~3×10^9 cm^{-2}, average height of ~5 nm, and lat-

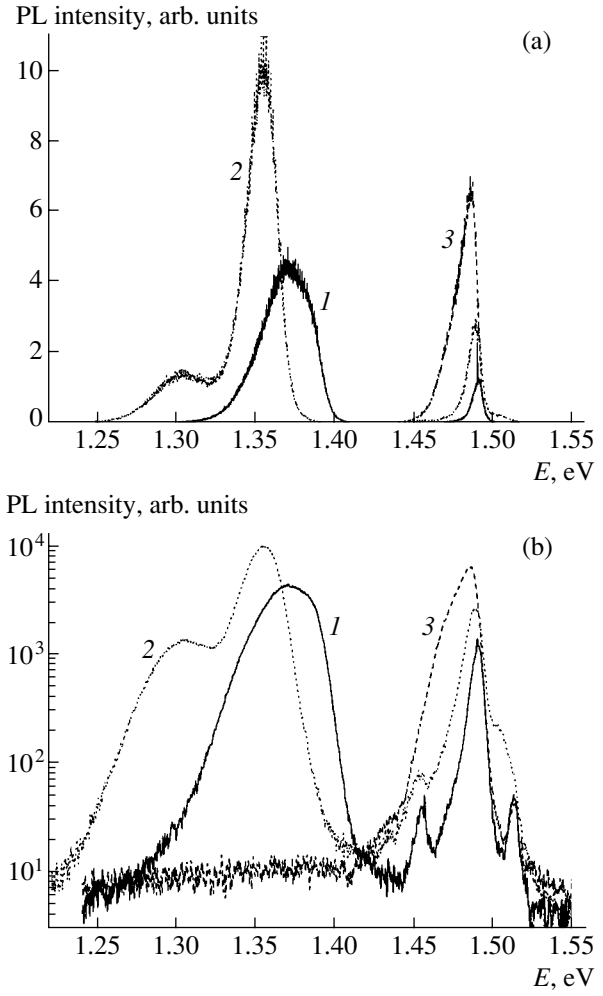

Fig. 2. (a) PL spectra for the samples: (solid line) sample no. *1*, (dotted line) sample no. *2*, and (dashed line) sample no. *3*. (b) The same as (a) but in the logarithmic scale. Temperature $T = 4.2$ K.

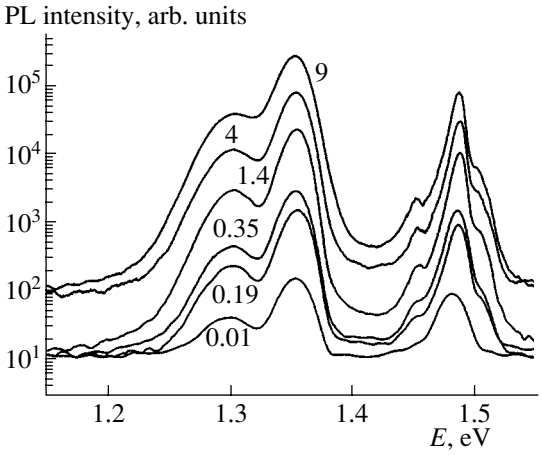

Fig. 3. PL spectra for sample no. *2* recorded at $T = 4.2$ K and different pumping powers P (W/cm^2). $T = 4.2$ K. The noise in the curve tails is smoothed.

eral size of ~40 nm; their typical size matches the data obtained for QD layers without overgrowth. Smaller QDs, which have a similar surface density, demonstrate a larger scatter in size, perhaps due to the stronger effect of etching. Their average lateral size is ~30 nm, and their height is ~2 nm. It is noteworthy that this type of dot is not observed on the surface QD layers formed without overgrowth. We assume that they either disappear on the free surface through coalescence or are formed after deposition of the capping layer as a result of reconstruction of the WL. The last process can enhance elastic stresses in a relatively thick WL grown on a free surface. A simple calculation shows that changing the WL thickness by one ML is enough for the formation of QDs with the above-mentioned size and density.

Figure 2a shows the PL spectra for the three samples at $T = 4.2$ K. For convenience, Fig. 2b shows these spectra on the logarithmic scale. The obtained PL spectra can be conventionally divided into low-energy and high-energy portions with the boundary at about 1.42 eV. In the low-energy portion, the spectral peaks for sample no. *3* can be represented as the sum of two peaks, presumably corresponding to two types of QDs of different size. As an example, Fig. 3 shows the PL spectra for sample no. *2*, recorded at 4.2 K at different pumping powers. Figure 4 shows the energy positions of spectral peaks related to radiative transitions in InAs QDs as a function of the pumping power. It can be seen that, as the pumping power increases, the low-energy peak for undoped sample no. *2* is slightly blue-shifted in the power range $P < 0.4$ W/cm^2. At the same time, the position of the second peak remains virtually unchanged, and its amplitude is higher. This behavior can be attributed to the presence of a large amount of smaller QDs (see Fig. 1), which are occupied nearly uniformly. Among the large-sized QDs, the largest are occupied first, with all the dots being occupied only at higher excitation powers; this behavior should be related to the high probability of tunneling between the large-sized QDs. The presence of a dopant in sample no. *1* means that carriers are already present in the QDs, and, beginning from the lowest excitation intensity, virtually no shifts of the peak positions are observed.

Now, we discuss the high-energy portion of the spectra. As can be seen in Fig. 2, it includes three peaks. The peak with highest energy lies at $E \approx 1.51$–1.52 eV and corresponds to transitions in the GaAs matrix. The central peak of high amplitude can be attributed to transitions in the InAs WL (see, e.g., [18]); the peak that lies at an energy ~0.35 eV lower can be related to radiative transition in the WL, which is accompanied by emission of longitudinal optical phonons in the GaAs matrix [19]. The difference between the positions of the WL peaks in different samples is attributed to difference in the WL thickness. For example, at the nominal thickness of the InAs layer of 1.4 ML, all the deposited

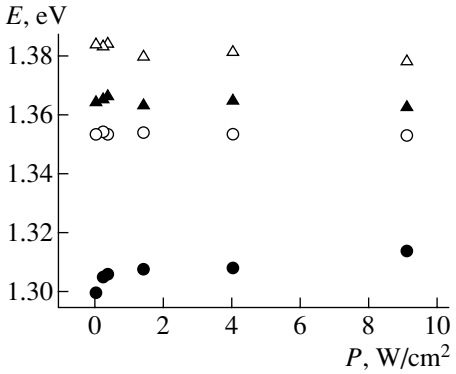

Fig. 4. Energy positions E of two peaks in the low-energy portion of the PL spectrum as a function of the pumping power P. The triangles refer to sample no. *1*, and the circles, to sample no. *2*.

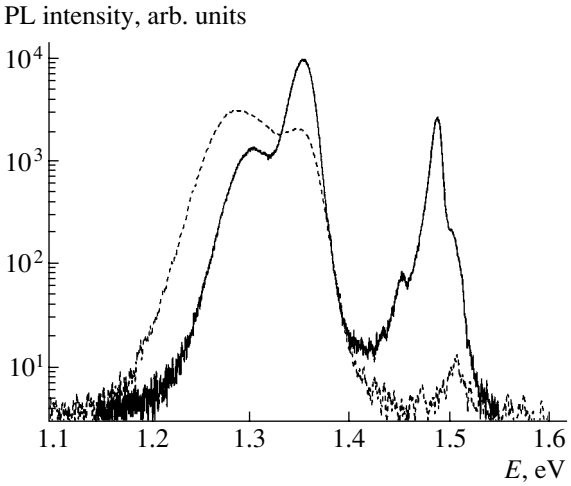

Fig. 5. PL spectra for sample no. *2*. The solid line refers to $T = 4.2$ K, and the dashed line, to $T = 77$ K.

InAs is contained in the WL. When the amount of InAs is increased to 3.3 ML, the WL becomes thinner, since some portion of InAs is redistributed into QD islands. As the amount of InAs further increases, the WL is further thinned.

The large size of the QDs in sample no. *2* can be related to the misorientation of the substrate, which means that it becomes more energetically favorable for InAs to be accumulated on the terrace boundaries and form large QDs [15] than to form multiple small islands distributed uniformly over the entire surface.

Figure 5 shows the PL spectra for sample no. *2* recorded at different temperatures. During the transition from $T = 4.2$ to 77 K, the PL intensity in the high-energy portion of spectrum considerably decreases, which is typical of bulk GaAs, and the low-energy QD peaks are further red-shifted. This behavior can be attributed to an increase in the mobility of carriers in the structure, which leads to entry of the carriers into regions with the deepest energy levels, in which radiative recombination occurs. In the case of doped sample no. *1*, the shift of the low-energy spectrum is smaller; this fact is related to filling of the regions deepest in energy by free carriers. Adequately explainable room-temperature PL spectra could not be obtained because of the large temperature broadening and low intensity of the spectral lines.

4. CONCLUSION

The PL spectra of InAs/GaAs QD structures have been studied at different pumping powers and temperatures. The spectra comprise a low-energy portion related to electron–hole recombination within the QDs and a high-energy one related to transitions in the GaAs matrix and the InAs wetting layer. Analysis of the low-energy portion of the spectra has shown that the structures under study contain QDs of two characteristic sizes. As the pumping power initially increases, one of the PL lines in the undoped sample is shifted; this effect is related to an increase in the number of QDs involved in the PL process. At higher temperatures, the intensity of the high-energy portion of the spectrum decreases, and the low-energy portion is further red-shifted. This effect is related to an increase in carrier mobility in the structure and redistribution of carriers between QDs of different sizes.

ACKNOWLEDGMENTS

This study was supported by the Russian Foundation for Basic Research (project no. 05-02-17029a), the "Scientific Schools" Program (grant no. NSh-2043.2003.2), and the Ministry of Education and Science of the Russian Federation's program "Physics of Solid-State Nanostructures" (project no. 97-1048).

REFERENCES

1. N. N. Ledentsov, V. M. Ustinov, V. A. Shchukin, *et al.*, Fiz. Tekh. Poluprovodn. (St. Petersburg) **32**, 385 (1998) [Semiconductors **32**, 343 (1998)].
2. A. D. Yoffe, Adv. Phys. **50**, 1 (2001).
3. M. Crassi Alessi, M. Capizzi, A. S. Bhatti, *et al.*, Phys. Rev. B **59**, 7620 (1999).
4. D. Bimberg, M. Grundmann, and N. N. Ledentsov, *Quantum Dot Heterostructures* (Wiley, Chichester, 1998).
5. V. A. Kulbachinskii, R. A. Lunin, V. A. Rogozin, *et al.*, Semicond. Sci. Technol. **17**, 947 (2002).
6. M. Bissiri, G. Baldassarri Hoger von Hogersthal, A. S. Bhatti, *et al.*, Phys. Rev. B **62**, 4642 (2000).
7. S. Fafard, Z. R. Wasilewski, C. Ni. Allen, *et al.*, Phys. Rev. B **59**, 15368 (1999).
8. M. Chiba, V. A. Fradkov, A. L. Karuzskii, *et al.*, Physica B (Amsterdam) **302–303**, 408 (2001).
9. J. Z. Wang, Z. M. Wang, Z. G. Wang, *et al.*, Phys. Rev. B **61**, 15614 (2000).

10. A. W. E. Minnaert, A. Yu. Silov, W. van der Vleuten, *et al.*, Phys. Rev. B **63**, 075303 (2001).
11. M. J. Steer, D. J. Mowbray, W. R. Tribe, *et al.*, Phys. Rev. B **54**, 17738 (1996).
12. M. Henini, S. Sanguinetti, S. C. Fortina, *et al.*, Phys. Rev. B **57**, R6815 (1998).
13. R. Heitz, F. Giffarth, I. Mukhametzhanov, *et al.*, Phys. Rev. B **62**, 16881 (2000).
14. H. Kissel, U. Muller, C. Walther, *et al.*, Phys. Rev. B **62**, 7213 (2000).
15. D. G. Vasil'ev, V. P. Evtikhiev, V. E. Tokranov, *et al.*, Fiz. Tverd. Tela (St. Petersburg) **40**, 855 (1998) [Phys. Solid State **40**, 787 (1998)].
16. F. Kaczmarek, *Wstep do Fizyki Laserow* (PWN, Warszawa, 1978; Mir, Moscow, 1981).
17. I. A. Karpovich, A. V. Zdoroveishev, A. P. Gorshkov, *et al.*, Phys. Low-Dimens. Semicond. Struct., No. 1/2, 143 (2003).
18. K. H. Schmidt, G. Medeiros-Ribeiro, M. Oestreich, *et al.*, Phys. Rev. B **54**, 11346 (1996).
19. R. Heitz, I. Mukhametzhanov, O. Steir, *et al.*, Phys. Rev. Lett. **83**, 4654 (1999).

Translated by D. Mashovets

Semiconductors, Vol. 39, No. 11, 2005, pp. 1313–1318. Translated from Fizika i Tekhnika Poluprovodnikov, Vol. 39, No. 11, 2005, pp. 1359–1364.

LOW-DIMENSIONAL SYSTEMS

Interband Light Absorption in Size-Confined Systems in Uniform Electric Fields

É. P. Sinyavskii^, S. M. Sokovnich, and R. A. Khamidullin

Institute of Applied Physics, Academy of Sciences of Moldova, Akademicheskaya 5, Chisinau, MD-2028 Moldova

^e-mail: arusanov@mail.ru

Submitted December 9, 2004; accepted for publication March 15, 2005

Abstract—A simple approach to calculation of the interband absorption coefficient in a uniform electric field is developed. This approach provides a means for studying the special features of electroabsorption in a wide class of semiconductor systems on the basis of the most general relationships. The approach is used to study the electroabsorption in two-dimensional systems with different profiles of their one-dimensional potential, quantum wells, and superlattices in magnetic fields. © *2005 Pleiades Publishing, Inc.*

When studying interband light absorption in semiconductor systems in a uniform electric field, the solution to the Schrödinger equation for an electron is commonly used [1–3]. A large number of studies have dealt with the processes of electroabsorption in a uniform magnetic field. For example, electroabsorption was studied in the special case where the vectors of the strength of the electric (**E**) and magnetic (**H**) fields are parallel [4, 5]. The absorption of electromagnetic waves with $\mathbf{E} \perp \mathbf{H}$ was reported in [6–9]. In that case, it was necessary to exploit the two-band approximation in order to treat the tunneling processes (the Franz–Keldysh effect) consistently.

In this study, we develop a theoretical approach that makes it possible to calculate the coefficient of interband light absorption in a uniform electric field directly from the Kubo formula, with knowledge of only the eigenfunctions and eigenvalues in the absence of an electric field. The prime objective of this study is to illustrate the simplicity of the new approach and its potential for studying the special features of light absorption in size-confined systems.

In what follows, we use the simplest model of a semiconductor with nondegenerate bands and assume that both bands have extrema at the same point of the *k* space. The calculations below are carried out in the single-band approximation, which implies the inequality $cE/SH \ll 1$ in the case of $\mathbf{E} \perp \mathbf{H}$ [7, 10] ($S = \sqrt{\varepsilon_g/4m_c}$, ε_g is the band gap, m_c is the electron effective mass, and c is the speed of light). Hereafter, we will disregard exciton-related effects. The influence of exciton effects on the linear optical properties of semiconductor quantum wells was discussed in [11].

1. In accordance with the Kubo formula [12], the coefficient of interband absorption of light with the frequency Ω is defined by the correlation function for dipole moments and can be written in the secondary-quantization representation as

$$K(\Omega) = \frac{4\pi e^2}{n_0 c\hbar\Omega V}\left|\frac{\mathbf{P}_{cv}\boldsymbol{\xi}}{m_0}\right|^2 \sum_{\substack{\alpha\alpha_1\\ \beta\beta_1}} \langle\alpha^v|\alpha_1^c\rangle\langle\beta^c|\beta_1^v\rangle \times \int_{-\infty}^{\infty} dt \exp(i\Omega t)\langle a_\alpha^{+(v)}(t)a_{\alpha_1}^{(c)}(t)a_\beta^{+(c)}a_{\beta_1}^{(v)}\rangle. \quad (1)$$

Here, we introduce the following notation: $a_\alpha^{+(i)}$ and $a_\alpha^{(i)}$ are the operators of creation and annihilation of an electron in the ith band ($i = c$ and v refer to the conduction and valence bands, respectively), α is a set of quantum numbers that describe the state of the electron, $\alpha^{(i)}$ is the smoothed wave function of the carrier in the ith band in the absence of an electric field, $\mathbf{P}_{cv}$ is the matrix element of the momentum operator in the Bloch functions of the valence and conduction bands, $\boldsymbol{\xi}$ is the unit polarization vector of the electromagnetic wave, V is the volume of the quantum system, e is the elementary charge, m_0 is the free-electron mass, and n_0 is the refractive index. In Eq. (1), the averaging $\langle\ldots\rangle$ is performed with the full density matrix of the system in a uniform electric field,

$$\hat{A}^{(i)}(t) = \exp\left(\frac{it}{\hbar}\hat{H}^{(i)}\right)\hat{A}\exp\left(\frac{-it}{\hbar}\hat{H}^{(i)}\right), \quad (2)$$

with the Hamiltonian

$$\hat{H}^{(i)} = \sum_\alpha \varepsilon_\alpha^{(i)} a_\alpha^{+(i)} a_\alpha^{(i)} + \sum_{\alpha\alpha_1} V_{\alpha\alpha_1}^{(i)} a_\alpha^{+(i)} a_{\alpha_1}^{(i)}, \quad (3)$$

where $\varepsilon_\alpha^{(i)}$ is the energy of an electron in the ith band in the absence of an electric field.

If the electric-field strength **E** is directed along the axis Ox, we have

$$V_{\alpha\alpha_1}^{(i)} = eE\langle\alpha^{(i)}|x|\alpha_1^{(i)}\rangle. \quad (4)$$

According to Eq. (2), the equation of motion for $a_\alpha^{(i)}(t)$ can be written as

$$\dot{a}_\alpha^{(i)}(t) = -\frac{i}{\hbar}\left\{\varepsilon_\alpha^{(i)}a_\alpha^{(i)} + \sum_\beta V_{\alpha\beta}^{(i)}a_\beta^{(i)}(t)\right\}. \quad (5)$$

The solution to Eq. (5) can be found in a manner similar to that used in [13] and is defined by the relation

$$a_\alpha^{(i)}(t) = \sum_\beta\left\langle\alpha^{(i)}\left|\exp\left\{-\frac{it}{\hbar}(\hat{H}_0^{(i)} + \hat{V})\right\}\right|\beta^{(i)}\right\rangle a_\beta^{(i)}, \quad (6)$$

where $\hat{H}_0^{(i)}$ is the Hamiltonian for electrons in the ith band in the coordinate representation in the absence of an electric field, $\hat{V} = eEx$, and $\hat{H}_0^{(i)}|\alpha^{(i)}\rangle = \varepsilon_\alpha^{(i)}|\alpha^{(i)}\rangle$. Substituting the expressions for $a_\alpha^{+(i)}(t)$ and $a_\beta^{(i)}(t)$ into Eq. (1) and taking into account the completeness of the system of wave functions for electrons, we derive the absorption coefficient:

$$K(\Omega) = \frac{4\pi e^2}{n_0 c\hbar\Omega V}\left|\frac{\mathbf{P}_{cv}\boldsymbol{\xi}}{m_0}\right|^2\sum_\alpha\int_{-\infty}^{\infty}dt\exp(i\Omega t)$$
$$\times\left\langle\alpha^c\left|\exp\left\{\frac{it}{\hbar}(\hat{H}_0^{(v)} + \hat{V})\right\}\exp\left\{-\frac{it}{\hbar}(\hat{H}_0^{(c)} + \hat{V})\right\}\right|\alpha^c\right\rangle. \quad (7)$$

Expression (7) is obtained with regard to the relation

$$\langle a_\gamma^{+(v)}a_{\gamma_1}^{(c)}a_\beta^{+(c)}a_{\beta_1}^{(v)}\rangle \approx \delta_{\gamma\beta_1}\delta_{\gamma_1\beta}$$

for a degenerate electron gas in the conduction band (the valence band is completely filled with electrons). In what follows, we consider the case of the Hamiltonian

$$\hat{H}_0^{(i)}(x, y, z) = \hat{H}_0^{(i)}(y, z) + \frac{\hat{P}_x^2}{2m_i}, \quad (8)$$

where $\hat{P}_x$ is the momentum-operator component and m_i is the effective mass of an electron in the ith band.

The Hamiltonian of Eq. (8) describes a wide class of physical problems. If we use the algebra of operators of the coordinate and momentum [14], it can easily be shown that

$$\exp\left\{\frac{it}{\hbar}\left[\frac{\hat{P}_x^2}{2m_i} + eEx\right]\right\} = \exp\left\{\frac{it}{\hbar}\frac{\hat{P}_x^2}{2m_i} - \frac{ieEt^2}{2\hbar m_i}\hat{P}_x\right\}$$
$$\times\exp\left(\frac{ieExt}{\hbar}\right)\exp\left(\frac{ie^2E^2t^3}{6m_i\hbar}\right) = \exp\left(\frac{ieExt}{\hbar}\right) \quad (9)$$
$$\times\exp\left(\frac{ie^2E^2t^3}{6m_i\hbar}\right)\exp\left\{\frac{it}{\hbar}\frac{\hat{P}_x^2}{2m_i} + \frac{ieEt^2}{2\hbar m_i}\hat{P}_x\right\}.$$

With regard to Eq. (9), the absorption coefficient of Eq. (7) takes, after integrating with respect to t, the form

$$K(\Omega) = \frac{8\pi^2e^2}{Vn_0c\hbar\Omega\omega_E}\left|\frac{\mathbf{P}_{cv}\boldsymbol{\xi}}{m_0}\right|^2$$
$$\times\sum_{\alpha,\beta}|\langle\alpha^c|\beta^v\rangle|^2\exp\left\{\frac{iP_x\Delta_{\alpha\beta}}{\hbar eE} + \frac{iP_x^3}{3eE\hbar\mu}\right\} \quad (10)$$
$$\times\mathrm{Ai}\left[-\frac{1}{\hbar\omega_E}\left(\Delta_{\alpha\beta} + \frac{P_x^2}{2\mu}\right)\right],$$

where we introduce the following notation: $\hbar\omega_E = \sqrt[3]{\hbar^2e^2E^2/2\mu}$, $\Delta_{\alpha\beta} = \hbar\Omega + \varepsilon_\beta^v - \varepsilon_\alpha^c$, and $\mu^{-1} = m_c^{-1} + m_v^{-1}$. For writing expression (10), we used an integral representation of the Airy functions Ai(z) [15],

$$\int_{-\infty}^{\infty}dt\exp\left(\frac{it}{\hbar}\Delta + iat^2 - ibt^3\right) = 2\pi(3b)^{-1/3}$$
$$\times\exp\left(\frac{i}{\hbar}\frac{a}{3b}\Delta + i\frac{2}{27}\frac{a^3}{b^2}\right)\mathrm{Ai}\left[-(3b)^{-1/3}\left(\frac{\Delta}{\hbar} + \frac{a^2}{3b}\right)\right].$$

The choice of the Hamiltonian for electrons in the absence of an electric field in form (8) means that, in the eigenvalues $\varepsilon_\alpha^{(i)}$, the term $P_x^2/2m_i$ can be explicitly separated, i.e.,

$$\varepsilon_\alpha^{(i)} = \varepsilon_{\alpha'}^{(i)} + \frac{P_x^2}{2m_i} \quad (11)$$

(α' are quantum numbers that describe, in addition to P_x, the electron state in the ith band).

Thus, the argument of the Airy functions is independent of P_x ($\Delta_{\alpha\beta} + P_x^2/2\mu = \hbar\Omega + \varepsilon_{\beta'}^v - \varepsilon_{\alpha'}^c \equiv \Delta_{\alpha'\beta}$), and the matrix element is $\langle\alpha^c|\beta^v\rangle = \langle\alpha'^c|\beta'^v\rangle\delta_{k_x^c, k_x^v}$ (k_x^i is the wave-vector component for an electron in the ith band). Therefore, we can sum over k_x^i in formula (10) exactly.

As a result, the final expression for the absorption coefficient can be written as

$$K(\Omega) = \frac{8\pi^2 e^2}{L_y L_z n_0 c\hbar\Omega}\left(\frac{2\mu}{\hbar\omega_E}\right)^{1/2}\left|\frac{\mathbf{P}_{cv}\boldsymbol{\xi}}{m_0}\right|^2 \times \sum_{\alpha',\beta'}\left|\langle\alpha'^c|\beta'^v\rangle\right|^2 \mathrm{Ai}^2\left(-\frac{\Delta_{\alpha'\beta'}}{\hbar\omega_E}\right), \quad (12)$$

where L_y and L_z are the corresponding dimensions of the semiconductor system. From expression (12), well-known results for interband light absorption can be derived [1–3]. For absorption in a uniform magnetic field gauged with the vector potential **A**(0, 0, *Hy*), formula (12) directly yields the results obtained in [4, 5] for the coefficient $K(\Omega)$ (**H** || **E**).

2. On the basis of general formula (12), we now examine the special features of electroabsorption in size-confined systems. For quantum-confined systems with an arbitrary one-dimensional potential along the axis *Oz*, we have

$$\varepsilon_{\alpha'}^{(i)} = \varepsilon_n^{(i)} + \frac{\hbar^2 k_y^2}{2m_i}, \quad (13)$$

where $\varepsilon_n^{(i)}$ are the quantum-confined levels in the *i*th band and $n^{(i)}$ is the number of a particular level. For the quantum systems under consideration, the overlap integral for the wave functions can be written as

$$\langle\alpha'^c|\beta'^v\rangle = \langle n^c|n^v\rangle\delta_{k_y^c, k_y^v}. \quad (14)$$

We now substitute expressions (14) and (13) into formula (12) and integrate with respect to the momentum $\hbar k_y^c$ using the relation [16]

$$\int_0^{-\infty}\frac{dx}{\sqrt{x}}\mathrm{Ai}^2(\alpha + x) = \frac{1}{2}\mathrm{Ai}_1(2^{2/3}\alpha) \equiv \frac{1}{2}\int_{2^{2/3}\alpha}^{\infty} dx\,\mathrm{Ai}(x).$$

Then, the absorption coefficient takes the form

$$K(\Omega) = \frac{4\pi e^2\mu}{dn_0 c\hbar^2\Omega}\left|\frac{\mathbf{P}_{cv}\boldsymbol{\xi}}{m_0}\right|^2 \times \sum_{n, n_1}\left|\langle n^c|n_1^v\rangle\right|^2 \mathrm{Ai}_1\left(-2^{2/3}\frac{\Delta_{nn_1}}{\hbar\omega_E}\right). \quad (15)$$

Here, *a* is the thickness of the size-confined system and $\Delta_{nn_1} = \hbar\Omega + \varepsilon_{n_1}^v - \varepsilon_n^c$.

In the absence of an electric field, we have, at $\Delta_{nn_1} > 0$, $\mathrm{Ai}_1(-2^{2/3}\Delta_{nn_1}/\hbar\omega_E) \longrightarrow \Theta(\Delta_{nn_1})$, where $\Theta(x)$ is the unit-step function. Then, according to expression (15), the frequency dependence $K(\Omega)$ has the stepwise shape typical of two-dimensional systems. Specifically, for rectangular quantum wells (QWs) with an infinite barrier height ($\langle n^c|n_1^v\rangle = \delta_{nn_1}$), the well-known results of [17] for the absorption coefficient can be obtained directly from formula (15). As follows from this formula, the frequency dependence of the coefficient of interband absorption of electromagnetic waves at any particular strength of a uniform electric field **E** is the same for different size-confined systems. In this case, only the value (the factor $\langle n^c|n_1^v\rangle$) and position of the absorption peak (the value of $\varepsilon_n^{(i)}$ depends on the shape of the one-dimensional potential) vary. As follows directly from the asymptotic behavior of the Airy function $\mathrm{Ai}_1(x)$ [15] at $\Delta_{nn_1}/\hbar\omega_E > 0$, i.e., in the high-frequency region, the light-frequency dependence of the absorption coefficient is nonmonotonic. In the case of size-confined systems, the oscillatory behavior of $K(\Omega)$ is more pronounced than in bulk materials. In the long-wavelength region of the absorption spectrum ($\Delta_{nn_1} < 0$) at $\Delta_{nn_1}/\hbar\omega_E \gg 1$, the absorption coefficient $K(\Omega)$ follows the exponential frequency dependence and describes the tunneling process (the Franz–Keldysh effect). It is worth noting that all the above calculations were carried out for isotropic bands. Extension of the results to the case of anisotropic masses and consideration of light and heavy holes presents no problems. The latter consideration leads only to quantitative changes in the oscillatory dependence $K(\Omega)$ in the short-wavelength region of the spectrum [17].

We now consider the light absorption in parabolic quantum wells (PQWs) in the case where uniform magnetic and electric fields are directed along the surface of a size-confined system under study (**H** || **E** || *Ox*). When gauging the vector potential **A**(0, *Hz*, 0), the Hamiltonian is given by

$$\hat{H}^{(i)} = \frac{1}{2m_i}\left(\hat{P}_y + \frac{eH}{c}z\right)^2 + \frac{\hat{P}_z^2}{2m_i} + \frac{\hat{P}_x^2}{2m_i} + eEx + \frac{m_i\tilde{\omega}_i^2}{2}z^2, \quad (16)$$

where $\hbar\tilde{\omega}_i = \sqrt{8\Delta E_i\hbar^2/m_i a^2}$ is the quantum-confinement step and ΔE_i is the PQW barrier height for the *i*th band.

In the absence of an electric field, Hamiltonian (16) takes the form given by expression (8). In this case, according to formula (11), we have

$$\varepsilon_{\alpha'}^c = \frac{\hbar^2(k_y^c)^2}{2m_c}\frac{\tilde{\omega}_c^2}{\omega_{0c}^2} + \hbar\omega_{0c}(n^c + 1/2),$$
$$\varepsilon_{\alpha'}^v = -\frac{\hbar^2(k_y^v)^2}{2m_v}\frac{\tilde{\omega}_v^2}{\omega_{0v}^2} - \hbar\omega_{0v}(n^v + 1/2) - \varepsilon_g, \quad (17)$$

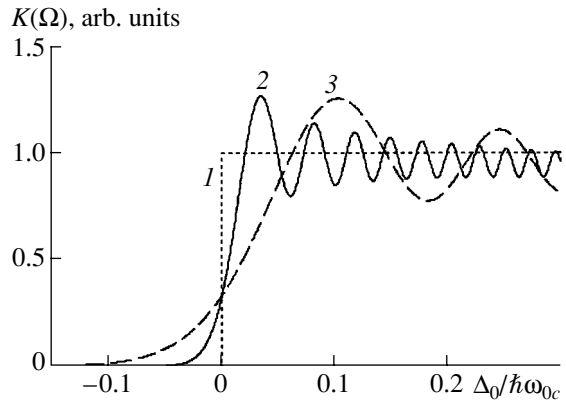

Fig. 1. Frequency dependences of the optical absorption coefficient (in arbitrary units) for a parabolic quantum well in uniform electric and magnetic fields. The dependence for the case of a zero electric field is shown by curve *1*. Curves *2* and *3* refer to $\omega_E/\omega_c = 0.033$ and 0.1, respectively.

where $\omega_{0i}^2 = \tilde{\omega}_i^2 + \omega_i^2$ and ω_i is the cyclotron frequency in the *i*th band.

The square of the matrix element based on the wave functions of an electron in a PQW in a magnetic field [18] can be directly calculated in the simplest case of a transition of a carrier between the lower quantum-confinement magnetic levels ($n^c = n^v = 0$). The expression for absorption coefficient (12) takes the form

$$K(\Omega) = \frac{16\pi e^2\sqrt{M\mu}}{an_0c\hbar^2\Omega}\frac{\sqrt{\lambda_c\lambda_v}}{\lambda_c+\lambda_v}\left|\frac{\mathbf{P}_{cv}\boldsymbol{\xi}}{m_0}\right|^2 \times\int_0^\infty\frac{d\tau}{\sqrt{\tau}}e^{-\beta\tau}\mathrm{Ai}^2\left(-\frac{\Delta_0}{\hbar\omega_E}+\tau\right), \quad (18)$$

with

$$\beta = \frac{2M\omega_E}{m\omega_c}\left[\frac{\omega_c}{\omega_{0c}}\right]^3(p+1)(p-1)^2,$$

$$M^{-1} = \frac{1}{m_v}\delta_v + \frac{1}{m_c}\delta_c, \quad \lambda_i = \frac{|m_i|\omega_{0i}}{\hbar},$$

$$\Delta_0 = \hbar\Omega - \varepsilon_g - \frac{\hbar\omega_{0c}}{2} - \frac{\hbar\omega_{0v}}{2},$$

$$\delta_i = \frac{\tilde{\omega}_i^2}{\omega_{0i}^2}, \quad p = \frac{\lambda_c}{\lambda_v}.$$

In the absence of an electric field, the frequency dependence of the absorption coefficient exhibits a stepwise behavior (Fig. 1, curve *1*). Under a higher magnetic field, the step width spans a wider region of frequencies of the absorbed electromagnetic waves (Fig. 1 shows a part of the first step). This circumstance is due to an increase in the quantum step corresponding to the magnetic-field-induced size confinement. In a constant electric field, light absorption in the long-wavelength spectral region (the Franz–Keldysh effect) becomes possible; in the high-frequency region, the absorption coefficient $K(\Omega)$ is described by an oscillatory dependence (Fig. 1, curves *2*, *3*). The numerical calculations were carried out for typical AlGaAs–GaAs PQWs ($m_c = 0.06m_0$ and $m_v = 0.4m_0$, with, respectively, the offsets of the conduction and valence bands $\Delta E_c = 0.255$ eV and $\Delta E_v = 0.17$ eV). The other parameters were the PQW width $a = 1000$ Å, $\hbar\tilde{\omega}_c = 14.6$ meV, and $\hbar\tilde{\omega}_v = 4.6$ meV. The magnetic field strength corresponded to the relation $\hbar\omega_c = \hbar\tilde{\omega}_c$. In this case, we had $\beta \approx 0.3\omega_E/\omega_c$. Curves *2* and *3* were obtained with $\omega_E/\omega_c = 0.033$ ($E = 125$ V/cm) and $\omega_E/\omega_c = 0.1$ ($E = 650$ V/cm), respectively. As the electric field is increased, the number of oscillations and their amplitude at the step decrease.

3. Using formula (12), we can easily derive an expression for the coefficient of interband absorption in a superlattice (SL) of period *d* in a transverse electric field. With regard to the dispersion relation for charge carriers, the tight-binding approximation yields the following relation for the eigenvalues [19]:

$$\varepsilon_\alpha^{(i)} = \frac{\hbar^2}{2m_i}[(k_x^i)^2 + (k_y^i)^2] + \varepsilon_{si} - \Delta_{si}\cos(k_z^i d). \quad (19)$$

Here, ε_{si} are the quantum-confined levels of the *i*th band and Δ_{si} is the width of the *s*th miniband in the *i*th band.

For the allowed direct transitions ($k_z^c = k_z^v$), it follows from expression (15) that

$$K^{\mathrm{SL}}(\Omega) = \frac{4\pi e^2\mu}{dn_0c\hbar\Omega}\left|\frac{\mathbf{P}_{cv}\boldsymbol{\xi}}{m_0}\right|^2 \times\sum_{s,s',k_z}\left|u_{cv}^{ss'}\right|^2\mathrm{Ai}_1\left(-\frac{2^{2/3}}{\hbar\omega_E}[\hbar\Omega - \tilde{\varepsilon}_g^{ss'} + \Delta_{ss'}\cos(k_z d)]\right), \quad (20)$$

where $u_{cv}^{ss'}$ is the matrix element based on the wave functions of the *s*th miniband of the conduction band and *s*'th miniband of the valence band, $\tilde{\varepsilon}_g^{ss'} = \varepsilon_g + (\varepsilon_{sc} + \varepsilon_{s'v})$, and $\Delta_{ss'} = \Delta_{sc} + \Delta_{s'v}$.

If the width of the minibands can be disregarded ($\Delta_{si} = 0$), expression (20) yields, in the absence of an electric field ($E = 0$), the well-known expression for the interband absorption coefficient [20].[1]

Let the width of the miniband be finite ($\Delta_{sc} \neq 0$ and $\Delta_{sv} \neq 0$). If we disregard the weak dependence on k_z in the overlap integral $u_{cv}^{ss'}$ [21] in this case, we obtain,

[1] The first allowed minibands are rather narrow; therefore, this approximation is often used when studying the optical properties of SLs.

after summing over the momenta, the following expression for the absorption coefficient:

$$K^{\mathrm{SL}}(\Omega) = \frac{8\pi e^2\mu}{dn_0c\hbar^2\Omega}\left|\frac{\mathbf{P}_{cv}\boldsymbol{\xi}}{m_0}\right|^2\sum_{s,s'}\left|u_{cv}^{ss'}\right|^2 I(\gamma, x). \quad (21)$$

Here, we introduced the following notation:

$$I(\gamma, x) = \frac{1}{2}\left\{\mathrm{Ai}_1[-\gamma(x+1)] + \mathrm{Ai}_1[-\gamma(x-1)] - \frac{2\gamma}{\pi}\int_{-1}^{1} d\tau \arcsin\tau \mathrm{Ai}[-\gamma(x+\tau)]\right\}, \quad (22)$$

with $\gamma = \dfrac{2^{2/3}}{\hbar\omega_E}\Delta_{ss'}$ and $x = \dfrac{\hbar\Omega - \tilde{\varepsilon}_g^{ss'}}{\Delta_{ss'}}$.

In the absence of an electric field ($E = 0$ and $\gamma \longrightarrow \infty$), the function $I(\gamma, x)$ is defined by the relation

$$I_0(x) = \left\{\frac{1}{2} - \frac{1}{\pi}\arcsin(-x)\right\}\Theta(-x)\Theta(1+x) + \left\{\frac{1}{2} + \frac{1}{\pi}\arcsin x\right\}\Theta(x)\Theta(1-x) + \Theta(x-1). \quad (23)$$

The function $I_0(x)$ is shown in Fig. 2 (curve *1*). It should be noted that we consider interband optical transitions between the lowest minibands, i.e., $s = s' = 1$. In this case, the frequency dependence $K^{\mathrm{SL}}(\Omega)$ reproduces the behavior of the electron density of states in an SL in relation to Ω [22]. In a nonzero electric field, absorption of electromagnetic waves in the long-wavelength region becomes possible (the Franz–Keldysh effect), and the function $K^{\mathrm{SL}}(\Omega)$ exhibits oscillations at $x > 1$. As the electric field is increased, the oscillatory peaks increase in amplitude and their number decreases. In Fig. 2, curves *2* and *3* are plotted for $\gamma = 3$ and 1, respectively.

We now consider the interband absorption in SLs in a magnetic field directed along the axis of quantum confinement (the axis *Oz*). Let the electric field be parallel to the plane of the size-confined system ($\mathbf{E} \perp \mathbf{H}$). In Landau's gauging for the vector potential $\mathbf{A}(-Hy, 0, 0)$, the Hamiltonian of the system is written as

$$\hat{H}^{(i)} = \frac{1}{2m_i}\left(\hat{P}_x + \frac{eH}{c}y\right)^2 + \frac{\hat{P}_y^2}{2m_i} + \frac{\hat{P}_z^2}{2m_i} + V(z) + eEy, \quad (24)$$

where $V(z)$ is the periodic potential of the SL.

To eliminate the term eEy, we use a unitary transformation of Hamiltonian (24):

$$e^{\hat{S}_i}\hat{H}^{(i)}e^{-\hat{S}_i} = \tilde{H}^{(i)} \text{ with } \hat{S}_i = -\frac{ieE}{m_i\hbar\omega_i^2}\hat{P}_y. \quad (25)$$

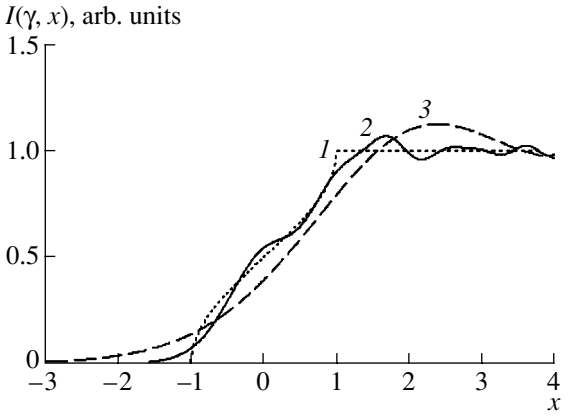

Fig. 2. Frequency dependences of the optical absorption coefficient (in arbitrary units) for a superlattice in a uniform electric field. The dependence for the case of a zero electric field is represented by curve *1*. Curves *2* and *3* refer to $\gamma = 3$ and 1, respectively.

It can easily be shown that

$$\hat{H}^{(i)} = \frac{1}{2m_i}\left(\hat{P}_x - \frac{\hbar}{R^2}y\right)^2 + \frac{\hat{P}_y^2}{2m_i} + \frac{\hat{P}_z^2}{2m_i} + V(z) + \frac{eER^2}{\hbar}\hat{P}_x - \frac{e^2E^2}{2m_i\omega_i^2}. \quad (26)$$

We now perform unitary transformation (25) under the trace sign in expression (7). Taking into account the completeness of the system of wave functions, we obtain the absorption coefficient

$$K_H^{\mathrm{SL}}(\Omega) = \frac{4\pi e^2}{Vn_0c\hbar\Omega}\left|\frac{\mathbf{P}_{cv}\boldsymbol{\xi}}{m_0}\right|^2\sum_{\alpha,\beta}\left|\langle\alpha^c|\exp\{-i\gamma_0\hat{P}_y\}|\beta^v\rangle\right|^2 \times \int_{-\infty}^{\infty} dt\exp\left\{\frac{it}{\hbar}\left[\hbar\Omega - \varepsilon_\alpha^c + \varepsilon_\beta^v + \frac{c^2E^2}{2H^2}(m_c + m_v)\right]\right\}. \quad (27)$$

Here, we introduced the notation $\gamma_0 = eER^2(1/\hbar^2\omega_c + 1/\hbar^2\omega_v)$; $\varepsilon_\beta^v(\varepsilon_\alpha^c)$ is the energy of an electron in the valence band (conduction band) for the SL in a magnetic field. In the tight-binding approximation, this energy is defined as

$$\varepsilon_\alpha^{(i)} = \hbar\omega_i(n + 1/2) + \varepsilon_{si} - \Delta_{si}\cos(k_z^i d). \quad (28)$$

In expression (27), $\langle\alpha^{(i)}|$ are the wave functions of an electron in the *i*th band, which represent the solution to the Schrödinger equation with Hamiltonian (26) (at $E = 0$). These functions are the product of the wave functions for an SL and the wave functions of an electron in a uniform magnetic field (n_i is the Landau level) [23]. The

matrix element involved in expression (28) can easily be calculated as

$$\langle \alpha^c | e^{-i\gamma_0 \hat{P}_y} | \beta^v \rangle = |u_{cv}^{ss'}| \delta_{k_x^c, k_x^v} \delta_{k_y^c, k_y^v} \left(\frac{n_c! 2^{n_v}}{n_v! 2^{n_c}} \right)^{1/2}$$

$$\times \left(-\frac{\hbar \gamma_0}{2R} \right)^{n_c - n_v} L_{n_c}^{n_c - n_v} \left(\frac{\hbar^2 \gamma_0^2}{2R^2} \right) \exp\left(-\frac{\hbar^2 \gamma_0^2}{4R^2} \right) \quad (29)$$

$$\equiv |u_{cv}^{ss'}| \delta_{k_\perp^c, k_\perp^v} W_{n_c n_v} \exp\left(-\frac{\hbar^2 \gamma_0^2}{4R^2} \right), \quad n_c \geq n_v.$$

Let the slight dependence on k_z^c in $u_{cv}^{ss'}$ be disregarded. Then, for the allowed direct optical transitions ($k_z^c = k_z^v$), we obtain, after summing over k_x^c, an expression for absorption coefficient (27) in the form

$$K_H^{\mathrm{SL}}(\Omega) = \frac{2e^2}{n_0 c \Omega R^2 d} \left| \frac{\mathbf{P}_{cv} \boldsymbol{\xi}}{m_0} \right|^2 \exp\left(-\frac{\hbar^2 \gamma_0^2}{2R^2} \right)$$

$$\times \sum_{\substack{n_c, n_v, \\ s, s'}} |u_{cv}^{ss'}|^2 |W_{n_c n_v}|^2 \int_{-\pi}^{\pi} dz \delta\{ \Delta_{n_c n_v} + \Delta_{ss'} \cos z \}, \quad (30)$$

where

$$\Delta_{n_c n_v} = \hbar\Omega - \tilde{\varepsilon}_g^{ss'} - \hbar\omega_c (n_c + 1/2)$$

$$- \hbar\omega_v (n_v + 1/2) + \frac{c^2 E^2}{2H^2} (m_c + m_v).$$

Further calculations can be carried out in the same way as above. As a result, we obtain

$$K_H^{\mathrm{SL}}(\Omega) = \frac{4e^2}{n_0 c \Omega R^2 d} \left| \frac{\mathbf{P}_{cv} \boldsymbol{\xi}}{m_0} \right|^2$$

$$\times \sum_{\substack{n_c, n_v, \\ s, s'}} |u_{cv}^{ss'}|^2 |W_{n_c n_v}|^2 \exp\left(-\frac{\hbar^2 \gamma_0^2}{2R^2} \right) \frac{\mathrm{sgn}(\Delta_{ss'} - \Delta_{n_c n_v})}{\sqrt{\Delta_{ss'}^2 - \Delta_{n_c n_v}^2}}. \quad (31)$$

Formula (31) describes the frequency dependence of the absorption coefficient typical of the behavior in magnetic fields. It should be noted that, at $E \neq 0$, there are no selection rules (as is standard [6]) for the number of Landau levels, and the optical absorption edge shifts to the low-frequency region by the quantity $E^2 c^2 (m_c + m_v)/2H^2$. The magnitude of the absorption coefficient decreases by a factor $\exp\{-\hbar^2 \gamma_0^2 / 2R^2\}$ typical for the case of crossed electric and magnetic fields. The square-root singularity of the absorption coefficient in expression (31) can be eliminated by taking into account, e.g., the interaction of the carriers with lattice vibrations. It should be remembered that all of the above calculations of electroabsorption in SLs were carried out in the effective-mass approximation, so the results are invalid in the limit of high electric fields (the conditions for the Wannier–Stark ladder) [24].

REFERENCES

1. W. Franz, Z. Naturforsch. **132**, 484 (1958).
2. L. V. Keldysh, Zh. Éksp. Teor. Fiz. **34**, 1138 (1958) [Sov. Phys. JETP **7**, 788 (1958)].
3. K. Tharmalingam, Phys. Rev. **130**, 2204 (1963).
4. M. Reine, Q. H. F. Vrehen, and B. Lax, Phys. Rev. **163**, 726 (1967).
5. G. Giobanu, Rev. Roum. Phys. **10**, 109 (1965).
6. A. G. Aronov, Fiz. Tverd. Tela (Leningrad) **5**, 552 (1964) [Sov. Phys. Solid State **5**, 402 (1964)].
7. A. G. Aronov and G. E. Pikus, Zh. Éksp. Teor. Fiz. **51**, 505 (1966) [Sov. Phys. JETP **24**, 339 (1967)].
8. A. G. Aronov and G. E. Pikus, Zh. Éksp. Teor. Fiz. **49**, 1904 (1965) [Sov. Phys. JETP **22**, 1300 (1966)].
9. M. H. Weiler, W. Zawadzki, and B. Lax, Phys. Rev. **163**, 733 (1967).
10. B. Lax, in *Proceedings of 7th International Conference on the Physics of Semiconductors* (Dunod, Paris, 1964), p. 253.
11. S. Schmitt-Rink, D. S. Chemla, and D. A. B. Miller, Adv. Phys. **38** (2), 89 (1989).
12. R. Kubo, J. Phys. Soc. Jpn. **12**, 570 (1957).
13. É. P. Sinyavskiĭ and E. I. Grebenshchikova, Zh. Éksp. Teor. Fiz. **116**, 2069 (1999) [JETP **89**, 1120 (1999)].
14. W. H. Louisell, *Radiation and Noise in Quantum Electronics* (McGraw-Hill, New York, 1964; Nauka, Moscow, 1972).
15. *Handbook of Mathematical Functions*, Ed. by M. Abramowitz and I. A. Stegun (Dover, New York, 1971; Nauka, Moscow, 1979).
16. D. E. Aspnes, Phys. Rev. **147**, 554 (1966).
17. É. P. Sinyavskii, *Optical Properties of Semiconductors and Quasi-two-dimenional Systems* (RIO Pridnestr. Gos. Univ., Tiraspol', 2002) [in Russian].
18. E. P. Sinyavskii, S. M. Sokovnich, and F. I. Pasechnik, Phys. Status Solidi B **209**, 55 (1998).
19. A. P. Silin, Usp. Fiz. Nauk **147**, 485 (1985) [Sov. Phys. Usp. **28**, 972 (1985)].
20. A. Ya. Shik, Fiz. Tekh. Poluprovodn. (Leningrad) **8**, 1841 (1974) [Sov. Phys. Semicond. **8**, 1195 (1974)].
21. V. A. Volkov and T. N. Pinsker, Fiz. Tverd. Tela (Leningrad) **13**, 1360 (1971) [Sov. Phys. Solid State **13**, 1138 (1971)].
22. R. C. Fivaz, J. Phys. Chem. Solids **28**, 839 (1967).
23. L. D. Landau and E. M. Lifshitz, *Course of Theoretical Physics*, Vol. 3: *Quantum Mechanics: Non-Relativistic Theory*, 3rd ed. (Nauka, Moscow, 1974; Pergamon, New York, 1977).
24. S. N. Molotkov, Pis'ma Zh. Éksp. Teor. Fiz. **62**, 318 (1995) [JETP Lett. **62**, 340 (1995)].

Translated by É. Smorgonskaya

Semiconductors, Vol. 39, No. 11, 2005, pp. 1319–1322. Translated from Fizika i Tekhnika Poluprovodnikov, Vol. 39, No. 11, 2005, pp. 1365–1369.

LOW-DIMENSIONAL SYSTEMS

Photoluminescence of Silicon Nanocrystals under the Effect of an Electric Field

E. N. Vandyshev^, A. M. Gilinskiĭ, T. S. Shamirzaev, and K. S. Zhuravlev

Institute of Semiconductor Physics, Siberian Division, Russian Academy of Sciences, Novosibirsk, 630090 Russia

^e-mail: vandyshev@thermo.isp.nsc.ru

Submitted March 10, 2005; accepted for publication April 24, 2005

Abstract—The effect of an electric field on photoluminescence (PL) of silicon nanocrystals formed in silicon dioxide by ion implantation with subsequent annealing has been studied. Application of an electric field leads to an increase in PL intensity by ~10% at low temperatures and an electric field strength of 12 kV/cm and to its decrease at temperatures above 20 K. The increase in exciton PL intensity in an electric field is inconsistent with the model of recombination of quantum-confined excitons in nanocrystals. The effect can be described in terms of a model of recombination of self-trapped excitons formed at the interface between a Si nanocrystal and SiO_2.

The mechanism of radiative recombination in nanosize semiconductor crystals remains an open question in spite of a variety of publications on the subject in recent years. The efficient luminescence from nanocrystals is attributed to quantum confinement in crystallites with sizes smaller than the Bohr radius of an exciton as well as to recombination assisted by defects or foreign substances on the surface of the nanocrystallites. The largest efforts have been applied to study of the recombination mechanism in Si-based nanocrystallites such as porous Si [1] and nanocrystals grown by epitaxy [2] or self-formation [3, 4]; nevertheless, the mechanism of luminescence from Si nanocrystals remains under discussion. For example, the data obtained in [5] indicate that effects on the nanocrystal surface play an important role in the observed photoluminescence (PL), whereas the authors of [3, 6] state that the luminescence of silicon nanocrystals in the visible spectral range is due to quantum confinement. In this study, we present data on the photoluminescence (PL) of Si nanocrystals embedded in a SiO_2 matrix under the action of an external electric field. Our results indicate that the PL from nanocrystals is not related to recombination of excitons via quantum-well levels in a nanocrystal. A mechanism of recombination taking into account structural defects formed in the vicinity of a nanocrystal is discussed in terms of the self-trapped exciton model.

Nanocrystal samples were produced by implantation of Si atoms into a 0.5-μm-thick SiO_2 layer formed by oxidation of a silicon substrate followed by annealing [7]. The implantation energies were 200 and 100 keV at the doses 6.3×10^{16} and 3.9×10^{16} cm^{-2}, respectively. The post-implantation annealing was performed for 5 h at 1130°C.

An electric field was applied in the no-contact configuration. The sample under study was placed at a small distance from the surface of a piezoelectric $LiNbO_3$ crystal, in which interdigitated transducers excited a surface acoustic wave (SAW) [8]. The ac electric field of the SAW was applied to the sample, and the PL was excited and measured through the $LiNbO_3$ crystal, which is transparent in the used spectral range (see the inset in Fig. 1). This method of electric field appli-

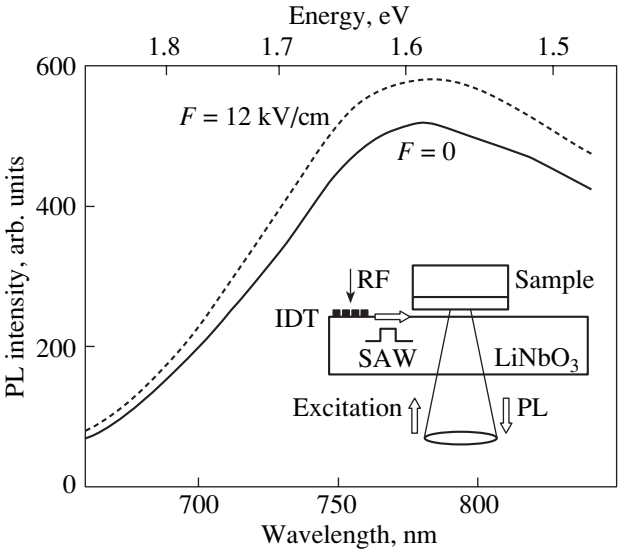

Fig. 1. Spectra of steady PL from silicon nanocrystals measured without an electric field (solid line) and in a field with a strength of 12 kV/cm (dotted line). The spectra are normalized to the spectrum of sensitivity of the recording system. The inset shows the following experimental configuration: IDT is an interdigitated transducer deposited onto the piezoelectric crystal and RF stands for radio-frequency voltage.

1063-7826/05/3911-1319$26.00 © 2005 Pleiades Publishing, Inc.

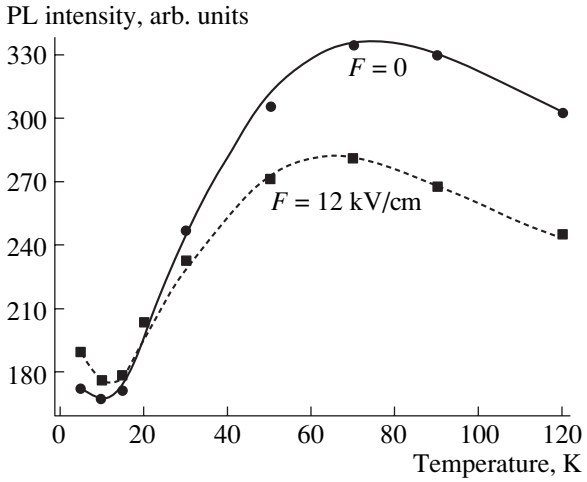

Fig. 2. Temperature dependence of the integral intensity of the PL from a nanocrystal with and without an electric field with a strength of 12 kV/cm. The lines are drawn for convenience.

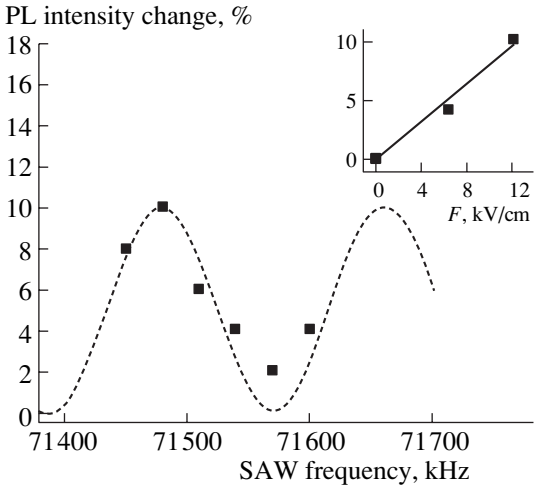

Fig. 3. Frequency dependence of the change in intensity of the PL from a nanocrystal with a SAW applied in the standing wave mode at $T = 5$ K (squares). The dashed line shows the approximation of the frequency response of the light diffraction in the SAW standing mode. Inset: the change in the PL intensity vs. the electric field strength.

cation excludes the process of fabrication of contacts to the sample and makes it possible to study different samples under identical conditions. A drawback of this technique is the limitation imposed on the wavelength of the exciting laser, which should satisfy the condition of transparency of the piezoelectric crystal; in our case, a 337-nm pulsed nitrogen laser was unsuitable for study of the PL kinetics. The measurements were performed in He vapor in the temperature range 5–120 K in the traveling SAW mode; in test measurements, the standing SAW mode could be used. The SAW frequency was ~71 MHz, which corresponds to a wavelength of ~40 μm. The maximum strength of the electric field induced in the sample was calculated from the measured efficiency of the diffraction of light on the SAW and equaled 12 kV/cm. In order to reduce the average power applied to the piezoelectric crystal, the SAW was excited in the pulsed mode with a repetition period and pulse width of 320 μs and 64 μs, respectively. The PL was recorded during the time interval corresponding to propagation of the SAW over the region of PL excitation. Steady PL was excited by an Ar^+ laser (20 mW and 488 nm). Along with steady PL under the electric field, we studied the kinetics of low-temperature PL from nanocrystals, which was excited by an N_2-laser. The PL was recorded using a double monochromator spectrometer with a cooled photomultiplier operated in the photon-counting mode.

Figure 1 shows the most important result of the experiment on the effect of the electric field of the SAW on the PL of nanocrystals. It appeared that, at a temperature of 5 K, the intensity of steady PL from the nanocrystals increases by as much as 10% at an electric field strength of 12 kV/cm. The shape of the PL spectrum, which has a broad band peaked at about 770 nm, remains virtually unchanged. Figure 2 shows temperature dependences of the integral intensity of the nanocrystal PL in an electric field and without it. These dependences are similar. They include a portion of nearly constant intensity at $T = 5$–15 K, a portion of intensity increase at temperatures up to 70 K, and a portion of intensity decrease at $T > 80$ K. As can be seen in Fig. 2, the application of an electric field raises the PL intensity in the first portion of the temperature dependence, whereas, at temperatures above 25 K, the PL is quenched by the electric field.

Since the intensity of PL from nanocrystals increases with temperature (Fig. 2; in addition, see [9, 10]), it might be assumed that the intensity increase observed under a SAW is not related to the electric field but is caused by the heating of the sample due to ohmic loss in the interdigitated transducers formed on the piezoelectric crystal. In order to estimate the effect of heating, we studied the frequency dependence of the change in PL intensity with a SAW excited in the standing wave mode (Fig. 3). In this situation, multiple reflections of the SAW from the interdigitated transducers are responsible for the frequency response being strongly modulated, with a period of about 100 kHz, which is determined by the pitch of the transducers. If the PL intensity is affected by heating of the transducers, the heating of the sample must be independent of the SAW frequency. However, in the experiment, the magnitude of the effect of a standing SAW on the PL intensity varied with the frequency of the exciting RF voltage in synchronism with the efficiency of the light diffraction on the SAW (see Fig. 3). This fact allows us to leave out the effect of heating of the interdigitated transducers. This conclusion is also supported by the nearly linear dependence of the change in PL intensity on the electric field (see the inset in Fig. 3). If sample

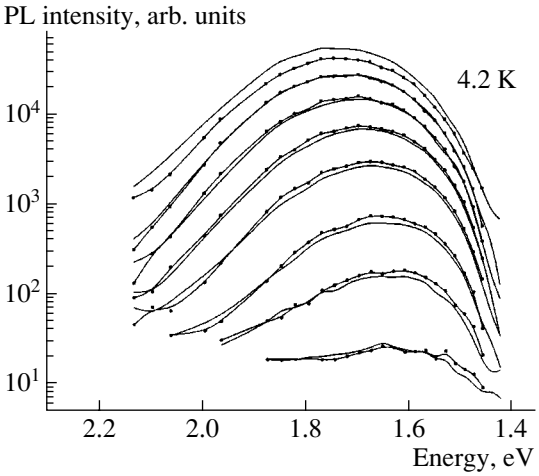

Fig. 4. Evolution of the spectrum of nonsteady PL from nanocrystals recorded with different delays after pulse excitation without a magnetic field (solid lines) and on applying a magnetic field of strength 5.6 T. Temperature equaled 4.3 K, and the delay after the laser pulse, from the top downwards, was 0.2, 1.4, 4, 8.5, 16, 32, 55, and 110 ms.

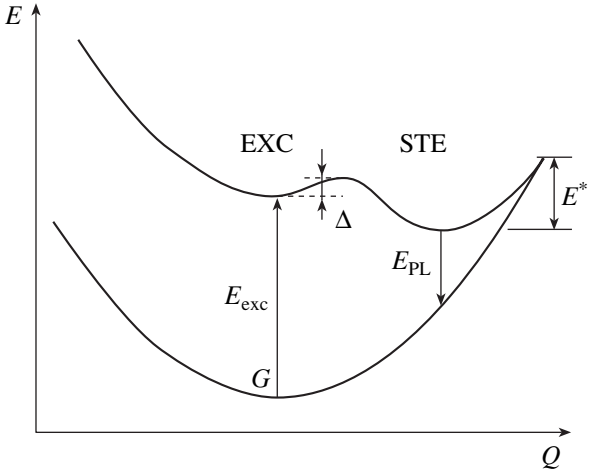

Fig. 5. Configuration diagram of a nanocrystal with an Si–Si dimer at the interface between the nanocrystal and amorphous matrix.

heating were a source of increase in PL intensity, this dependence would be quadratic.

Now, we discuss the problem of correspondence between the observed increase in the PL intensity under the action of an electric field and the model of recombination of quantum-confined excitons in nanocrystals. In the absence of calculations of the radiative recombination efficiency for silicon nanocrystals in an electric field, we rely on results obtained for other systems. First, we disregard the effect of fine structure of the exciton levels. As is well known, in bulk structures and quantum wells, exciton PL is quenched by the applied electric field, which reduces the overlapping of the electron and hole wave functions in an exciton [11, 12]. In particular, similar behavior was predicted for CdS and CdSSe quantum dots (QDs) [13] and experimentally observed during optical absorption by CdS QDs [14] and luminescence from InP QDs [15]. There is no reason to suppose that the effect of an electric field on silicon QDs leads to the opposite result. Now, we take into account the fine structure of exciton states. In silicon QDs, it gives rise to a lower optically inactive triplet state and an optically active singlet state with higher energy [16]. In this case, redistribution of excitons between the states in the magnetic field [17] or at elevated temperatures [6] modifies the probability of radiative recombination and the PL intensity if recombination occurs via several competing channels. As far as we know, data on modification of the time and intensity of exciton transitions in an electric field for silicon nanocrystals that takes into account the fine structure of exciton states has not yet been obtained. Therefore, we examine data obtained for a system in which the radius of the exciton state is close to the nanocrystal size, for example, organic semiconductors, which are being actively studied at present. In organic semiconductor structures, an external electric field quenches the luminescence of singlet excitons [18, 19]. The quenching of the phosphorescence of triplet excitons in an electric field was observed in [20]. Study of the optical absorption by triplet excitons in [21] led to the conclusion that the cross section for their formation is reduced by an applied electric field. On the basis of these data, we conclude that the increase in PL intensity in nanocrystals under the action of an electric field cannot be attributed to effects related to the fine structure of exciton states.

The insignificance of the contribution from the fine structure of exciton levels in the PL of silicon nanocrystals is also confirmed by the kinetics of low-temperature PL from nanocrystals in a magnetic field (Fig. 4). As can be seen from this figure, the application of a magnetic field does not change the kinetics of PL from the nanocrystals, which indicates that excitons are not redistributed between the different spin states.

We may conclude, therefore, that the enhancement of the nanocrystal PL by an electric field is inconsistent with the model of recombination of quantum-confined excitons in nanocrystals. At the same time, the enhancement of the PL may be related to the existence of some kind of potential barrier in the system, which can be more easily overcome by carriers if an electric field is applied. Earlier, we observed a similar effect during study of the PL from GaAs, which is related to electron capture by shallow donors [8]. The observed behavior of the PL of nanocrystals in response to the application of an electric field and variation of the temperature, which is shown in Fig. 2, can be explained in terms of the model suggested in [22]. The model is based on the assumption that a self-trapped exciton is formed on a Si–Si dimer at the nanocrystal boundary. Figure 5 shows the configuration diagram of such a system. Here, Q is the configuration coordinate, which

characterizes the stretching of the Si–Si bond. In the ground (G) and excited (EXC) states, an exciton belongs to a nanocrystal. The self-trapped exciton (STE) state, separated from the excited state by the potential barrier Δ, corresponds to a self-trapped exciton localized on the Si–Si dimer. The self-trapped exciton is formed from an exciton in the excited (EXC) state in the nanocrystal if the exciton overcomes the potential barrier. The probability of overcoming the barrier can be raised by elevating the temperature or reducing the barrier height by applying an electric field. In this situation, the nonzero effect in the time-averaged PL intensity upon application of an ac field is provided by the nonlinear response of the system. It is noteworthy that the presence of a low-temperature portion with constant PL intensity in the temperature dependences shown in Fig. 2 requires that the probability of an exciton tunneling from the EXC to STE state should also be taken into account. It is also necessary to note that a change in the PL intensity is only possible when competing recombination channels are considered. In particular, following an analogy with deep levels in semiconductors, it is necessary to take into account the probability of recombination of an STE exciton via a nonradiative tunneling transition across the barrier E*, which separates the self-trapped exciton state and the ground state [23]. The decrease in the PL intensity observed under the effect of an electric field at temperatures above 25 K is related to the rising efficiency of this recombination channel.

Good agreement between the calculated and experimental curves is reached when the experimental data are described in terms of the self-trapped-exciton model. Nevertheless, the analysis shows that the large number of parameters used in the model hinders an unambiguous determination of the height of the potential barriers and the transition probabilities. In order to determine the numerical values of the model parameters, further study of the kinetics of nanocrystal PL in an electric field is necessary.

We have studied the effect of an ac electric field on the steady PL of silicon nanocrystals formed in a SiO_2 matrix by ion implantation with subsequent annealing. It is shown that the application of the electric field raises the intensity of low-temperature PL and quenches PL at temperatures above 20 K. The analysis of the experimental data shows that the observed enhancement of the PL in the electric field is inconsistent with the model of recombination of quantum-confined excitons in nanocrystals; instead, it can be described in terms of a model of recombination of self-trapped excitons formed at the interface between the silicon nanocrystal and SiO_2.

ACKNOWLEDGMENTS

The study was supported by the Russian Foundation for Basic Research (project no. 02-02-17719 and grant no. 03-02-06874).

REFERENCES

1. A. G. Cullis, L. T. Canham, and P. D. J. Calcott, J. Appl. Phys. **82**, 909 (1997).
2. P. Photopoulos, A. G. Nassiopoulou, D. N. Kouvatsos, and A. Travlos, Appl. Phys. Lett. **76**, 3588 (2000).
3. M. D. Efremov, V. A. Volodin, D. V. Marin, *et al.*, Pis'ma Zh. Éksp. Teor. Fiz. **80**, 619 (2004) [JETP Lett. **80**, 544 (2004)].
4. P. Mutti, G. Ghislotti, S. Bertoni, *et al.*, Appl. Phys. Lett. **66**, 851 (1995).
5. Y. Kanemitsu, Phys. Rev. B **49**, 16845 (1994).
6. V. Vinciguerra, G. Franzo, F. Priolo, *et al.*, J. Appl. Phys. **87**, 8165 (2000).
7. K. S. Zhuravlev, I. E. Tsychenko, E. N. Vandyshev, *et al.*, Acta Phys. Pol. A **102**, 337 (2002).
8. K. S. Zhuravlev, A. M. Gilinskiĭ, A. V. Tsarev, and A. E. Nikolaenko, Fiz. Tekh. Poluprovodn. (St. Petersburg) **35**, 932 (2001) [Semiconductors **35**, 895 (2001)].
9. K. S. Zhuravlev and A. Yu. Kobitskiĭ, Fiz. Tekh. Poluprovodn. (St. Petersburg) **34**, 1254 (2000) [Semiconductors **34**, 1203 (2000)].
10. A. Yu. Kobitsky, K. S. Zhuravlev, H. P. Wagner, and D. R. T. Zahn, Phys. Rev. B **63**, 115423 (2001).
11. C. Rocke, A. O. Govorov, A. Wixforth, *et al.*, Phys. Rev. B **57**, 6850 (1998).
12. K. S. Zhuravlev, D. V. Petrov, Yu. B. Bolkhovityanov, and N. S. Rudaja, Appl. Phys. Lett. **70**, 3389 (1997).
13. G. W. Wen, J. Y. Lin, H. X. Jiang, and Z. Chen, Phys. Rev. B **52**, 5913 (1995).
14. U. Woggon, S. V. Bogdanov, O. Wind, and V. Sperling, J. Cryst. Growth **138**, 976 (1994).
15. M. Sugisaki, H.-W. Ren, S. V. Nair, *et al.*, Phys. Rev. B **66**, 235309 (2002).
16. P. D. J. Calcott, K. J. Nash, L. T. Canham, *et al.*, J. Phys.: Condens. Matter **5**, L91 (1993).
17. H. Heckler, D. Kovalev, G. Polisski, *et al.*, Phys. Rev. B **60**, 7718 (1999).
18. A. Nollau, M. Hoffmann, T. Fritz, and K. Leo, Thin Solid Films **368**, 130 (2000).
19. S. Tasch, G. Kranzelbinder, G. Leising, and U. Scherf, Phys. Rev. B **55**, 5079 (1997).
20. J. Kalinowski, W. Stampor, J. Myk, *et al.*, Phys. Rev. B **66**, 235321 (2002).
21. L. C. Lin, H. F. Meng, J. T. Shy, *et al.*, Phys. Rev. Lett. **90**, 036601 (2003).
22. G. Allan, C. Delerue, and M. Lannoo, Phys. Rev. Lett. **76**, 2961 (1996).
23. S. D. Ganichev, I. N. Yassievich, and V. Prettl, Fiz. Tverd. Tela (St. Petersburg) **39**, 1905 (1997) [Phys. Solid State **39**, 1703 (1997)].

Translated by D. Mashovets

Semiconductors, Vol. 39, No. 11, 2005, pp. 1323–1327. Translated from Fizika i Tekhnika Poluprovodnikov, Vol. 39, No. 11, 2005, pp. 1370–1374.

LOW-DIMENSIONAL SYSTEMS

Circular Polarization of Luminescence Caused by the Current in Quantum Wells

N. S. Averkiev*^ and A. Yu. Silov**

**Ioffe Physicotechnical Institute, Russian Academy of Sciences, Politekhnicheskaya ul. 26, St. Petersburg, 194021 Russia*
^e-mail: Averkiev@les.ioffe.ru
***COBRA Inter-University Research Institute, Eindhoven University of Technology,*
PO Box 513, NL-5600 MB Eindhoven, the Netherlands
Submitted April 25, 2005; accepted for publication May 10, 2005

Abstract—The degree of circular polarization of photoluminescence from an *n*-type III–V-based [001] quantum well (QW) is calculated under an electric current flow in the well plane. It is shown that mixing of the states of light and heavy holes leads to circular polarization of photoluminescence during the propagation of light in the plane of the structure. The role of various terms that are linear in the wave vector in the electron energy spectrum is analyzed for the effects of spin orientation and emergence of circular polarization of radiation in the electric field. © *2005 Pleiades Publishing, Inc.*

1. One of the main specific features of nanosize structures fabricated on the basis of III–V compounds is their gyrotropic properties. From the point of view of symmetry, this fact means that the components of vectors and pseudovectors are transformed by identical representations, and a linear relation is possible between them. Phenomenologically, this circumstance should lead, for example, to the emergence of an average carrier spin (pseudovector) when a constant electrical current flows in a gyrotropic medium [1]. A microscopic cause of the linear relation between the average spin and the electric field is the presence of terms that are linear in the wave vector in the electron or hole spectrum. For gyrotropic bulk Te crystals, the emergence of a uniform spin density under a flow of current was predicted by Ivchenko and Pikus [2] and was detected owing to the additional rotation of the polarization plane of linearly polarized light, which propagates along the main axis of a crystal [3]. For nongyrotropic crystals, the emergence of spin density close to the surface under a flow of current was predicted by Dyakonov and Perel [4]. For AlGaAs-based structures, measurement of the degree of circular polarization of radiation represents a direct observation of the spin orientation [5]. For bulk AlGaAs crystals, the average spin is related to the degree of circular polarization by a numerical factor. However, this is not the case for quantum heterojunctions, and the coefficient depends on the spin orientation relative to crystal axes.

Recently, the effect of spin orientation of charge carriers has been found from the degree of circular polarization in a *p*-AlGaAs asymmetric heterojunction [6]. The purpose of this study is to calculate the degree of circular polarization of photoluminescence (PL) for *n*-type III–V-based [001] Quantum Wells (QWs) when a current flows in the well plane.

2. The symmetry of III–V-based [001] QWs can be D_{2d} or C_{2v}. According to this fact, the average electron spin is oriented in the heterostructure (HS) plane when a current flows through a QW. However, the relative orientation of the average spin and current depends on the relation between various contributions to the Hamiltonian of a two-dimensional (2D) gas that are linear in the wave vector [7]. If the contribution caused by the asymmetry of a QW itself prevails and the Rashba Hamiltonian describes the electron spectrum, the average spin is normal to the current [8].

If the asymmetry of the heterojunction itself is insignificant and the main role belongs to terms that are linear in the wave vector and arise owing to the absence of the center of inversion in a bulk material (the Dresselhaus terms), the spin is not normal to the current, and the angle between them depends on the current direction relative to the crystallography axes [7].

In order to induce PL in *n*-type QWs, it is necessary to generate nonequilibrium holes. Nonequilibrium carriers can be generated by light. In this case, the circular polarization of radiation depends on the spatial localization of the carriers. If the nonequilibrium holes are located in the barrier and their motion is not quantized, the degree of circular polarization is equal to the average spin multiplied by 0.25 [9]. If the recombining holes remain in a QW, their motion is quantized, and, as a result, the total momentum is aligned along the growth axis. Due to this circumstance, the degree of circular polarization is equal to zero if an electron and hole have a zero quasi-momentum. For the entire charge-carrier ensemble, this fact means that the circular polarization of radiation will depend on the electron

and hole distribution, and its magnitude cannot be related to the average spin by a simple numerical factor. When calculating the degree of polarization, we will hereafter assume that the nonequilibrium holes involved in recombination are located at the ground level of the size quantization and can have a nonzero quasi-momentum in the well plane when the concentration of photoexcited electrons is considerably lower than the equilibrium one.

The polarization properties of the emitted optical radiation are determined by the polarization tensor $d_{\alpha\beta}$ [10]:

$$d_{\alpha\beta} = \sum_{\substack{nm \\ n'm'}} V^{*\alpha}_{nm} V^{\beta}_{n'm'} \hat{\rho}^{e}_{nn'} \hat{\rho}^{h}_{m'm}. \quad (1)$$

Here, $\hat{\rho}^{e}$ and $\hat{\rho}^{h}$ are the spin density matrices for electrons and holes, and V^{α}_{nm} are the matrix elements for the operator of the momentum component between the states n for electrons and m for holes. Let us assume that light propagates in the plane (x, y) along the y_1 axis, the z axis is parallel to the growth axis while $x \parallel (100)$ and $y \parallel (001)$, and the electric field has the components $(\mathcal{E}_x, \mathcal{E}_y, 0)$. The problem consists in calculation of $d_{\alpha\beta}$, where $\alpha, \beta = z, x_1$, and $x_1 \perp y_1$. In a general form, an electron-spin density matrix with a definite quasi-momentum can be represented as

$$\rho^{e}_{nn'} = \left(a(k)\frac{1}{2}I + \hat{\boldsymbol{\sigma}}\mathbf{S}(\mathbf{k})\right)_{nn'} = \frac{1}{2}\begin{pmatrix} a + S_z & S_x - iS_y \\ S_x + iS_y & a - S_z \end{pmatrix}, \quad (2)$$

where α and $S_i(k)$ can depend on the electric field and are determined from the solution to the corresponding kinetic equation, and σ_i is the Pauli matrix. Let us assume that the nonequilibrium holes are not oriented by the electric field and their density matrix is diagonal:

$$\rho^{h}_{mm'} = \frac{1}{2}\delta_{mm'} f^{h}(\mathbf{k}). \quad (3)$$

Here, $f^{h}(\mathbf{k})$ is the hole distribution function. In order to simplify the calculation of the wave functions of electrons and holes, let us consider a rectangular QW and disregard the odd terms in the wave vector. It is convenient to write the wave functions for the ground state of the holes in the form [11]

$$\begin{aligned}\psi_{3/2,k} &= e^{i\mathbf{k}\boldsymbol{\rho}}\frac{1}{\sqrt{A}}(-V_0(k)C(z)U_{3/2} + iV_1(k)S(z)e^{i\varphi_k}U_{1/2} \\ &- V_2(k)C(z)e^{2i\varphi_k}U_{-1/2} + iV_3(k)S(z)e^{3i\varphi_k}U_{-3/2}), \\ \psi_{-3/2,k} &= e^{i\mathbf{k}\boldsymbol{\rho}}(V_3(k)C(z)e^{-3i\varphi_k}U_{3/2} \\ &+ V_2(k)C(z)e^{-2i\varphi_k}U_{1/2} + iV_1(k)S(z)e^{i\varphi_k}U_{-1/2} \\ &+ V_0(k)C(z)U_{-3/2}).\end{aligned} \quad (4)$$

Here, $C(z)$ and $S(z)$ are functions that are even and odd relative to the QW center; V_i are the functions of k, with $V_m \propto k^m$ at $k \longrightarrow 0$; $\rho(x, y)$ is the radius vector of a charge carrier in the well plane; U_n are the wave functions at the valence-band top of the bulk material; φ_k is the polar angle of the k vector; and A is the area. In relation (4), no allowance is made for the cubic anisotropy of the valence band.

The electron wave function can be written as

$$\psi_{n,k} = e^{i\mathbf{k}\boldsymbol{\rho}}\frac{1}{\sqrt{A}}f(z)U^{n}_{c}, \quad n = \pm\frac{1}{2}. \quad (5)$$

Here, $f(z)$ is the smooth envelope of the wave function, which depends on the potential barrier shape; and U^{n}_{c} is the Bloch wave function in the conduction band at $\mathbf{k} = 0$. We will further assume that the electrons are located at the ground level and $f(z)$ is an even function relative to the well center. Using a canonical basis for the functions U_m and U^{n}_{c} [10], we can write the matrix elements V^{α}_{nm} in the form

$$\begin{aligned}V^{x_1}_{1/2,3/2} &= \left(\frac{n_x + in_y}{\sqrt{2}}V_0(k) - \frac{n_x - in_y}{\sqrt{3}}V_2(k)e^{2i\varphi_k}\right)DP, \\ \hat{V}^{z}_{1/2,-3/2} &= \sqrt{\frac{2}{3}}e^{-2i\varphi_k}DP, \\ V^{z}_{-1/2,3/2} &= -V^{*z}_{1/2,-3/2}, \\ V^{x_1}_{-1/2,-3/2} &= -V^{*x1}_{1/2,3/2}, \\ P &= \int_{-\infty}^{\infty} f(z)C(z)dz.\end{aligned} \quad (6)$$

Here, D is a real constant, and (n_x, n_y) is the direction of the x_1 vector. We made allowance for the fact that the optical transitions occur with quasi-momentum conservation so that the electron and hole quasi-momenta were identical. Using set (6) and representations of spin matrices for the electron and hole densities (2), (3), we can write expressions for $d_{\alpha\beta}$:

$$\begin{aligned}d_{zz} &= \frac{a(k)f^{k}(k)}{2}D^2P^2\frac{2}{3}V_2^2(k), \\ d_{x_1x_1} &= \frac{a(k)f^{h}(k)}{2}\frac{D^2P^2}{6}[3V_0^2 + V_2^2 \\ &- 2\sqrt{3}V_0V_2\cos 2\varphi_k(n_x^2 - n_y^2) - 4n_xn_y\sqrt{3}V_0V_2\sin 2\varphi_k], \\ d_{x_1z} &= \frac{f^{h}(k)}{2}\frac{D^2P^2}{3}i(V_2^2(k)(n_yS_x - n_xS_y) \\ &- \sqrt{3}V_0V_2[(n_xS_x - n_yS_y)\sin 2\varphi \\ &- (S_yn_x + S_xn_y)\cos 2\varphi]), \\ d_{zx_1} &= d^{*}_{x_1z}.\end{aligned} \quad (7)$$

The circular polarization is defined by the imaginary part of d_{xz}, and it follows from set (7) that, at $k = 0$, we have $d_{xz} \equiv 0$. By order of magnitude, $V_2 \approx E_h/\Delta$, where Δ is the quantum confinement energy for light holes. Since it is possible to expect that, under experimental conditions, there would be few photoexcited holes and their energy E_h would be much lower than Δ, we obtain $V_2 \ll 1$. In further calculations, we will restrict the analysis to this approximation. The magnitudes of S_x and S_y are proportional to the electric-field strength. Therefore, when calculating the degree of circular polarization in the approximation that is linear in E in expressions for $d_{x_1x_1}$ and d_{zz}, there is no need to make allowance for the field dependence of $a(\mathbf{k})$ and $f(\mathbf{k})$. The degree of circular polarization is defined as

$$\mathcal{P}_{circ} = -\frac{4}{\sqrt{3}}\frac{\langle V_0 V_2 P^2 f^h(k)((n_x S_x - n_y S_y)\sin 2\varphi - (S_y n_x + S_x n_y)\cos 2\varphi)\rangle}{\langle P^2 a(k) f^h(k) V_0^2\rangle}. \quad (8)$$

In relation (8), the symbol $\langle\ \rangle$ denotes integration with respect to d^2k, and it is taken into account that the average values of $a(\mathbf{k})f^h(\mathbf{k})\cos 2\varphi$ and $a(\mathbf{k})f^h(\mathbf{k})\sin 2\varphi$ are equal to zero at $\mathscr{E} = 0$. In addition, the integration is carried out here with respect to the frequency of the emitted light, meaning that relation (8) yields the magnitude of the average degree of circular polarization of PL. Thus, it is necessary to determine S_α, $f(\mathbf{k})$, and $f^h(\mathbf{k})$. The form of $f^h(\mathbf{k})$ is determined by the photoexcitation conditions, while S and $a(\mathbf{k})$ should be found by solving the kinetic equation [5]

$$\frac{i}{\hbar}[H_k^{(1)}, \hat{\rho}] + \frac{e\mathscr{E}}{\hbar}\frac{\partial\hat{\rho}}{\partial\mathbf{k}} = St\hat{\rho},$$
$$H_k^{(1)} = \frac{\hbar}{2}(\boldsymbol{\sigma}\boldsymbol{\Omega}_k^{(1)}) = \beta_{ij}\sigma_i\mathbf{k}_j. \quad (9)$$

Here, $[H_k^{(1)}, \hat{\rho}]$ denotes the commutator; $St\rho$ denotes the collision integral; and $H_k^{(1)}$ denotes the Hamiltonian that describes splitting of the levels in the approximation that is linear in the wave vector. A nonequilibrium spin emerges during spin relaxation; therefore, the magnitudes S_i depend on the spin relaxation mechanisms. We will further calculate S_i and $\mathcal{P}_{circ}$ under the assumption that spin relaxation proceeds mainly according to the Dyakonov–Perel kinetic mechanism. To simplify the calculations, we will assume that scattering occurs at the Δ potential, which means that the relaxation times of various harmonics of the distribution function are identical. In this case, the collision integral can be expressed as [5]

$$St\hat{\rho} = -W_0\sum_k\{\delta(E_k - E_k' + H_k^{(1)} - H_{k'}^{(1)}), \hat{\rho}(k) - \hat{\rho}(k')\}. \quad (10)$$

Here, $E_k = \frac{\hbar^2k^2}{2m^*}$, m^* is the effective electron mass, $\{AB\} = (AB + BA)/2$ denotes the anticommutator, and W_0 is the squared absolute value of the matrix element that corresponds to electron scattering by impurities. In the absence of an electric field, the equilibrium density matrix takes the form

$$\rho_0 = \frac{1}{2}f_0(E_k + H_k^{(1)})n. \quad (11)$$

Here, f_0 is the equilibrium electron distribution function, n is the equilibrium electron concentration, and ρ_0 from relation (11) causes collision integral (10) to vanish. When solving Eq. (9), we will assume that $H_k^{(1)} \ll E_k$ and represent relations (11) and (2) as the sum

$$\hat{\rho} = \frac{1}{2}nf_0(E_k)I + \frac{1}{2}n\frac{\partial f_0}{\partial E_k}H_k^{(1)} + \hat{\rho}^e. \quad (12)$$

Here, $\hat{\rho}^e$ describes variation in the spin density matrix in an electric field. Substituting $\rho_0 = \frac{1}{2}f_0(E_k)I + \frac{1}{2}\frac{\partial f_0}{\partial E_k}H_k^{(1)}$ into relation (8), we obtain $\mathcal{P}_{circ} = 0$, despite the nonzero spin splitting of the states. The absence of circular polarization is associated with the fact that $\hat{\rho}_0$ includes the zero and first circular harmonics, while only the second harmonic can lead to nonzero d_{x_1z} according to relation (8). As a result, $a(k)$ in the denominator of relation (8) linear in $\mathscr{E}$ should be replaced by $f_0(E_k)n$.

To determine $S_i(k)$, ρ_0 should be substituted into the field term, and terms that are linear in H_k' should be retained in the collision integral [5]. Substituting relation (11) into Eq. (9) and, sequentially, calculating $\frac{1}{2}S_p\hat{\sigma}_i$ and $\frac{1}{2}S_p$, we can obtain connected equations for $S_i(k)$ and $a(k)$. Finally, after substituting the expression for $a(k)$ into the equation for $S_i(k)$, we obtain an equation for the carrier spin $S_\alpha(k)$ in the form

$$[\boldsymbol{\Omega}_k\mathbf{S}]_\alpha = \frac{1}{\tau_0}(S_\alpha - \langle S_\alpha\rangle) + \frac{\hbar}{2}(e\mathscr{E}\mathbf{v}\Omega_\alpha - \langle e\mathscr{E}\mathbf{v}\Omega_\alpha(k)\rangle)n\frac{\partial^2 f_0}{\partial E^2}. \quad (13)$$

Here, $[\mathbf{\Omega}_k\mathbf{S}]_\alpha$ denotes the vector product; $\langle\ \rangle$ denotes averaging of the vector k over the angle; and τ_0 is the relaxation time, $\frac{1}{\tau_0} = W_0\sum_{k'}\delta(E - E(k'))$. For the 2D carriers studied here, the relaxation time is energy-independent. In contrast to [5], Eq. (13) is also valid at $\Omega_k^{(1)}\tau_0 \approx 1$. The equations for S_α are easily solved for the arbitrary form of $\Omega_k^{(1)}$; however, the expressions for $S_\alpha(k)$ are very cumbersome. Therefore, as an example, we further consider the cases in which only one of the contributions to the splitting linear in the wave vector is dominant.

The linear splitting is caused by the absence of the center of inversion in a bulk material (the Dresselhaus Hamiltonian) [5]:

$$\Omega_x = \frac{2}{\hbar}\beta_D k_x, \quad \Omega_y = -\frac{2}{\hbar}\beta_D k_y,$$
$$x \parallel (100), \quad y \parallel (010).$$

In this case, solution (12) takes the form

$$S_z = 0, \quad S_y = \kappa\beta_D(\mathscr{E}_x k_x k_y + \mathscr{E}_y k_y^2);$$
$$S_x = -\kappa\beta_D(\mathscr{E}_x k_x^2 + \mathscr{E}_y k_x k_y), \quad \kappa = \frac{e\hbar}{m}\tau_0 n\frac{\partial^2 f_0}{\partial E^2}. \tag{14}$$

We can use solution (14) to obtain an expression for the angle Θ between the average spin and the direction of the electric field [7]:

$$\Theta = \arccos\frac{\mathscr{E}_y^2 - \mathscr{E}_x^2}{\mathscr{E}_x^2 + \mathscr{E}_y^2}. \tag{15}$$

The terms that are linear in k are determined by the asymmetry of the heterointerface (the Rashba effect):

$$\Omega_x = \frac{2}{\hbar}\beta_R k_y; \quad \Omega_y = -\frac{2}{\hbar}\beta_R k_x;$$

as a result, we obtain

$$S_z = 0; \quad S_y = \kappa\beta_D(\mathscr{E}_x k_x^2 + \mathscr{E}_y k_x k_y),$$
$$S_x = -\kappa\beta_R(\mathscr{E}_x k_x k_y + \mathscr{E}_y k_y^2). \tag{16}$$

In this case, the average spin is normal to the direction of the electric field. Relations (14) and (16) are obtained under the assumption that spin relaxation proceeds according to the Dyakonov–Perel kinetic mechanism and τ_0 is independent of the electron energy. It is noteworthy that the average values of $\langle S_i\rangle$ coincide with the corresponding values from [5, 7, 8]. Substituting relations (14) and (16) into the relation for $\mathscr{P}_{circ}$, we obtain

$$\mathscr{P}_{circ}^D = \beta_D(n_x'\mathscr{E}_x - n_y'\mathscr{E}_y)\frac{\sqrt{3}}{4}Q,$$
$$\mathscr{P}_{circ}^R = \beta_R(n_x'\mathscr{E}_y - n_y'\mathscr{E}_x)\frac{5}{4\sqrt{3}}Q, \tag{17}$$
$$Q = \frac{\langle P^2 k^2 V_0 V_2 f^h(k)\kappa\rangle}{\langle P^2 f_0 n f^h(k) V_0^2\rangle}.$$

In relation (17), n' is the unit vector in the direction y_1 of propagation of light. An interesting specific feature of relation (17) consists in its different angular dependences for $\mathscr{P}_{circ}^R$ and $\mathscr{P}_{circ}^D$. For $\mathscr{P}_{circ}^R$, the degree of circular polarization is always highest in the direction normal to the electric field. If the Dresselhaus terms are dominant in the Hamiltonian of the 2D gas, $\mathscr{P}_{circ}^D$ depends not only on the relative orientation of n' and $\mathscr{E}$ but also on their arrangement with respect to the crystallographic axes. If an electric field is applied along the axes [100] $\mathscr{E}_x = \pm\mathscr{E}_y$, then, as follows from [17], the degree of circular polarization is always highest for light propagating normally to the electric field. For $\mathscr{E} \parallel$ [100], $\mathscr{P}_{circ}^D$ is largest for $n' \parallel$ [100], while $\mathscr{P}_{circ}^R = 0$ for this n'. This circumstance makes it possible to determine the relative role of various contributions that are linear in k to the energy spectrum of the 2D gas from the angular dependence of polarization. The magnitudes of $\mathscr{P}_{circ}$ are proportional to the first degree of the parameters β. Strictly speaking, $\beta_R = 0$ for a symmetrical well. However, in this study, a symmetrical rectangular well was used only to calculate the spectrum and wave functions of the ground state of electrons in the case $\hbar\Omega_k^{(1)} \ll E_F$. If the asymmetry of a QW is insignificant, then $\beta_R \neq 0$, and the wave function remains symmetrical relative to the well center. Since the values of S_α are proportional to the first degree of β_R, the above calculation is also valid for asymmetrical electron wells at $\hbar\Omega_k^{(1)} \ll E_F$.

3. Let us estimate the values of $\mathscr{P}_{circ}$ for an infinitely deep potential well for holes. Let us assume that photoexcited holes have a uniform energy distribution in a certain range $(0, E_0)$. $V_2 \approx E_0/\Delta \ll 1$, $V_0 \simeq 1$, and P^2 is independent of the wave vector. The latter condition is satisfied at $E_0/\Delta \ll 1$. Then, $\mathscr{P}_{circ} \approx \langle V_2\rangle\bar{S}/n$, where $\bar{S}$ is the average spin in the electric field according to relation (14) or (16). For a degenerate electron gas, we have $\bar{S}/n \propto e\mathscr{E}\beta\tau_0/E_F$, where E_F is the Fermi energy of the electron gas. For GaAs at $\beta = 10^{-2}$ eV A, $\tau_0 \approx 10^{-11}$ s, $\mathscr{E} = 10$ V/cm, and $n \simeq 10^{12}$ cm^{-2}, we obtain $\bar{S}/n \approx 0.10$. This result means that, at $V_2 \approx 0.2$, the value of $P_{circ} \approx 2\%$.

Although the magnitude of the polarization is not large, it can be detected experimentally. Thus, it has been shown in this study that the spin orientation by a current of majority carriers in a symmetric QW [001] leads to circular polarization of the radiation propagating in the QW plane. For asymmetric QWs, the degree of polarization can be calculated by the method developed in this study. For *n*-type HSs, relations (14) and (16) are conserved. However, the components of the polarization tensor $d_{\alpha\beta}$ will be more cumbersome. Since the expressions for S_α include the zero and second circular harmonics only, the degree of circular polarization for asymmetric heterojunctions is also determined by mixing of the states of heavy and light holes. Therefore, relation (17) can be used to estimate $\mathcal{P}_{circ}$ for asymmetric QWs when spin relaxation of the majority carriers proceeds predominantly according to the Dyakonov–Perel kinetic mechanism.

This study was supported by the Russian Foundation for Basic Research, INTAS, and scientific programs of the Russian Academy of Sciences.

REFERENCES

1. V. I. Belinicher and B. I. Sturman, Usp. Fiz. Nauk **130**, 415 (1980) [Sov. Phys. Usp. **23**, 199 (1980)].
2. E. L. Ivchenko and G. E. Pikus, Pis'ma Zh. Éksp. Teor. Fiz. **27**, 640 (1978) [JETP Lett. **27**, 604 (1978)].
3. L. E. Vorob'ev, E. L. Ivchenko, G. E. Pikus, *et al.*, Pis'ma Zh. Éksp. Teor. Fiz. **29**, 485 (1979) [JETP Lett. **29**, 441 (1979)].
4. M. I. Dyakonov and V. I. Perel, Phys. Lett. A **35A**, 459 (1971).
5. A. G. Aronov, Yu. B. Lyanda-Geller, and E. E. Pikus, Zh. Éksp. Teor. Fiz. **100**, 973 (1991) [Sov. Phys. JETP **73**, 537 (1991)]; A. G. Aronov and Yu. B. Lyanda-Geller, Pis'ma Zh. Éksp. Teor. Fiz. **50**, 398 (1989) [JETP Lett. **50**, 431 (1989)].
6. A. Yu. Silov, P. V. Blajnov, T. H. Wolter, *et al.*, Appl. Phys. Lett. **85**, 5929 (2004).
7. A. V. Chaplik, V. M. Entin, and L. I. Magaril, Physica E (Amsterdam) **13**, 744 (2002).
8. V. M. Edelstein, Solid State Commun. **73**, 233 (1990).
9. M. I. D'yakonov and V. I. Perel', Zh. Éksp. Teor. Fiz. **60**, 1954 (1971) [Sov. Phys. JETP **33**, 1053 (1971)].
10. E. L. Ivchenko and G. Pikus, *Superlattices and Other Heterostructures. Symmetry and Optical Phenomena* (Springer, Berlin, 1995).
11. I. A. Merkulov, V. I. Perel', and M. E. Portnoĭ, Zh. Éksp. Teor. Fiz. **99**, 1202 (1991) [Sov. Phys. JETP **72**, 669 (1991)].

Translated by N. Korovin

Semiconductors, Vol. 39, No. 11, 2005, pp. 1328–1332. Translated from Fizika i Tekhnika Poluprovodnikov, Vol. 39, No. 11, 2005, pp. 1375–1379.

AMORPHOUS, VITREOUS, AND POROUS SEMICONDUCTORS

Opal–ZnO Nanocomposites: Structure and Emission Properties

G. A. Emel'chenko*^, A. N. Gruzintsev, M. N. Koval'chuk**, V. M. Masalov*, É. N. Samarov*, E. E. Yakimov**, C. Barthou***, and I. I. Zver'kova***

**Institute of Solid State Physics, Russian Academy of Sciences, Chernogolovka, Moscow oblast, 142432 Russia*

^e-mail: emelch@issp.ac.ru

***Institute of Microelectronics Technology and High Purity Materials, Russian Academy of Sciences, Chernogolovka, Moscow oblast, 142432 Russia*

****Université P. et M. Curie, Case 80, 4 Place Jussieu, Paris Cedex 05, 75252 France*

Submitted January 13, 2005; accepted for publication January 23, 2005

Abstract—The structure of opal–ZnO composites is studied by transmission electron microscopy and X-ray phase analysis. It is shown that, under thermal treatment of infiltrated samples, a solid-phase reaction proceeds at the opal–ZnO interface. As a result, zinc silicate β-Zn_2SiO_4 and its high-temperature phase, willemite Zn_2SiO_4, are formed. The structure and emission properties of the nanocomposite are studied in relation to the degree of filling. For a sample subjected to 25 cycles of filling, luminescence controlled by the β-Zn_2SiO_4 phase is detected in the blue spectral region (at 430 nm). The angular dependences of the luminescence and reflection spectra of an opal–ZnO composite sample subjected to four cycles of filling show the effect of suppression of a spontaneous emission of zinc oxide in the photonic band gap. © *2005 Pleiades Publishing, Inc.*

1. INTRODUCTION

In the last few years, the development of efficient light emitters based on photonic crystals has attracted increasing interest from researchers [1–3]. In this regard, the greatest potential is exhibited by three-dimensional (3D) photonic structures, e.g., opal matrices [4–7]. A number of studies have dealt with the emitting properties of organic molecules, semiconductor nanocrystals, and rare-earth ions introduced into opal matrices [3–5]. Mo *et al.* [8] reported an enhancement of the green luminescence line in ZnO deposited in the mesovoids of a silicon dioxide aerogel. The luminescence of ZnO oxide quantum dots has been detected in opal–ZnO structures [9] and amorphous silicon dioxide layers deposited on a zinc oxide film on a silicon substrate and subjected to an appropriate thermal treatment [10]. Recently [11], we have developed a technological process consisting in infiltration of zinc oxide into the 3D opal lattice by chemical deposition from a solution and obtained opal–ZnO composite samples that show predominantly ultraviolet (UV) luminescence at room temperature. Fabrication of ZnO-based high-quality nanostructures that emit radiation predominantly in the UV region is required for the development of high-power semiconductor light sources for this spectral region. Zinc oxide is exactly the same as gallium nitride in its optical, electrical, and structural parameters; however, ZnO is much simpler than GaN from a technological standpoint and more stable under operating conditions. Moreover, the free exciton binding energy in ZnO is ~60 meV [12], i.e., is twice higher than that in GaN. As a consequence, excitonic emission is the major channel of recombination in ZnO at room temperature.

In this paper, we report data on the structure of ZnO-infiltrated opal matrices studied by X-ray phase analysis (XPA) and transmission electron microscopy (TEM) in relation to the filling factor. The emission properties of the opal–ZnO composites were also studied. It was found that the excitonic emission of ZnO in the structure features an anisotropy corresponding to dispersion of the first band gap of opal with respect to frequency and angle.

2. EXPERIMENTAL

The pores of the opal matrix were filled by impregnation with a solution of zinc nitrate $Zn(NO_3)_2 \cdot nH_2O$ and subsequent decomposition of the nitrate to oxide by thermal treatment in air for 15 min at 600–800°C. A description of the impregnation procedure can be found in [11]. Samples of about $5 \times 4 \times 3$ mm^3 in size were fabricated. The degree of filling of the pores with zinc oxide was 30, 50, and 100% of the total volume of the pores. The size of the zinc dioxide spheres varied from 220 to 320 nm for different samples. The thin nanocomposite samples needed for the TEM measurements were prepared by mechanical polishing of bulk samples and subsequent thinning by ion etching. The structural studies were performed using a JEOL JEM-2000FX transmission electron microscope. The element composition of the samples was determined by X-ray energy-dispersive spectroscopy. The spectrometer allowed us to detect elements ranging from Na to elements with a higher atomic mass. The X-ray phase analysis was carried out using a Siemens-D500 diffractometer with CuK_α radiation.

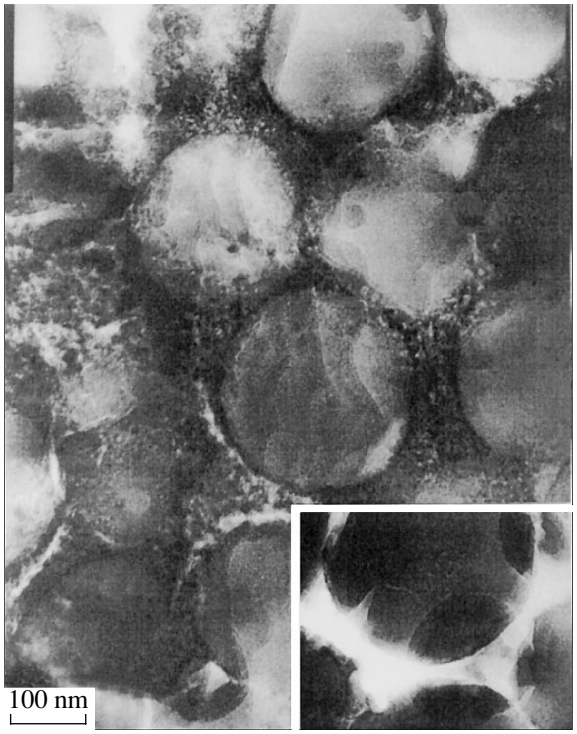

Fig. 1. TEM image of certain areas of the opal–ZnO composite fabricated in four cycles of filling with ZnO.

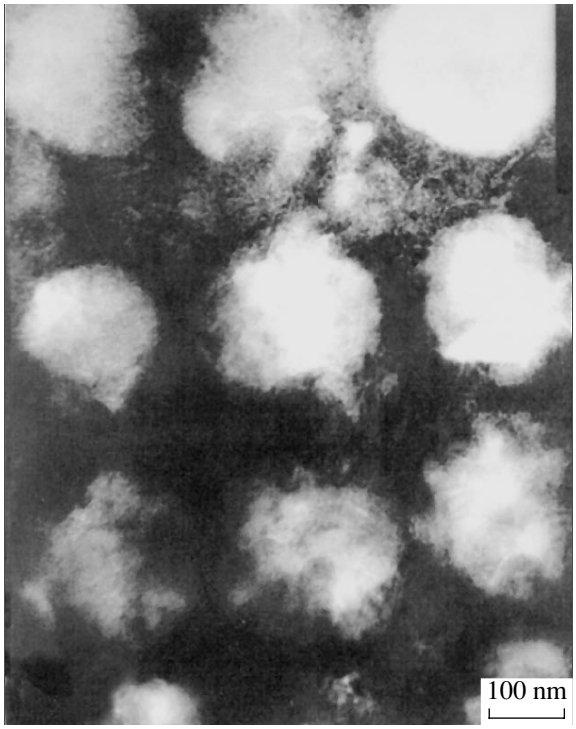

Fig. 2. TEM image of an area of the opal–ZnO composite fabricated in 25 cycles of filling with ZnO.

The spectra of photoluminescence (PL) and reflection of the opal–ZnO nanocomposites were studied. The PL measurements were performed at room temperature with a high angular resolution and at different PL-signal recording angles. The samples were pumped with different intensities of excitation with a pulsed nitrogen laser operating at the wavelength 337.1 nm, a pulse duration of 0.6 ns, and output power of 2.3 MW. The reflection spectra were recorded under irradiation of the samples by a halogen filament lamp with 50 W of power. The radiation of the lamp was transmitted through an MDR-23 monochromator and, then, was incident on the sample surface. The intensity of the reflected signal was measured at different angles of incidence. In the optical experiments, the spectral resolution was no poorer than 0.1 nm.

3. STRUCTURE

We studied opal–ZnO nanocomposite samples differing in relation to the number of cycles used to fill the space between the opal-constituent SiO_2 spheres with zinc oxide. The number of cycles was 4 and 25. For these samples, the fraction of pores filled with ZnO was, correspondingly, 30 and 100%, as calculated from curves for the weight gain. From the TEM images and electron diffraction patterns, it follows that the opal samples have a regular structure of amorphous SiO_2 spheres 240–260 nm in size. The space between the spheres is partially or completely filled with a polycrystalline material. As suggested by the characteristic X-ray emission spectra detected from the space between the spheres, zinc dominates over silicon in the composition of this material. The Si-related signal in the characteristic emission X-ray spectra can be accounted for by the fact that the excitation area was larger than the pore size. The TEM images and the X-ray spectra show that, after four cycles of filling, the empty space between the SiO_2 spheres is not completely filled with zinc oxide. For example, it is evident from the inset in Fig. 1 that, along with domains of nonuniform dark contrast between the spheres, there exist unfilled domains of uniform light contrast. In the dark domains, the fine-grained structure of the filling material is well pronounced (Fig. 1). The electron diffraction patterns show that this material is polycrystalline.

After 25 cycles of filling, the pores between the SiO_2 spheres in opal are completely filled with ZnO, as is clearly shown in Fig. 2.

The constituent SiO_2 spheres of the opal samples subjected to four cycles of filling with ZnO have well-pronounced boundaries; some of the spheres show a border of very dark contrast (Fig. 1). In contrast, the SiO_2 spheres in the samples subjected to 25-fold filling with ZnO essentially have smeared boundaries (Fig. 2). This allows us to suggest that solid-phase reactions proceed at the opal–ZnO interface.

The electron diffraction patterns of both samples show that there is a polycrystalline material between

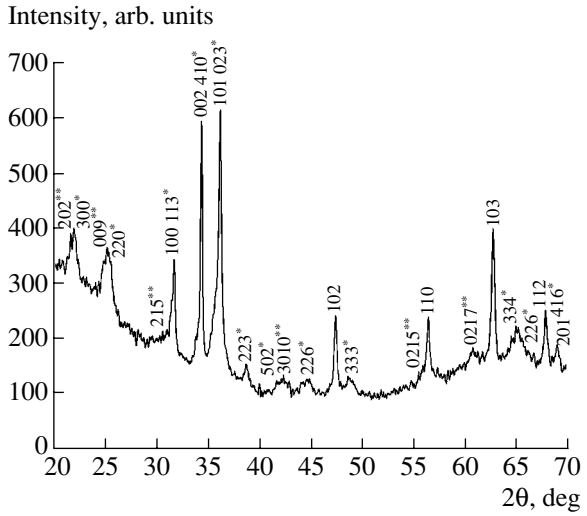

Fig. 3. X-ray diffraction pattern of a lap prepared from the opal–ZnO composite fabricated in four cycles of filling with ZnO. The indices of the reflection peaks not marked by asterisks and marked by one or two asterisks refer to the ZnO, Zn_2SiO_4, and β-Zn_2SiO_4 phases, respectively.

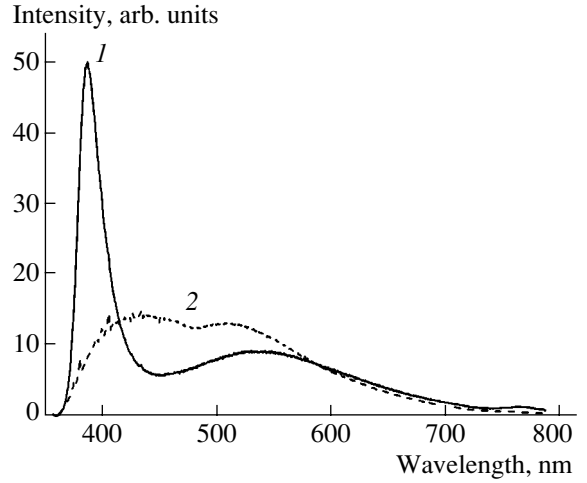

Fig. 4. PL spectra of the opal–ZnO nanocomposite samples differing in the number of cycles used to fill the space between the constituent SiO_2 spheres of opal with ZnO. Curves *1* and *2* refer to samples fabricated in 4 and 25 cycles, respectively. T = 300 K.

the SiO_2 spheres in the opal. Calculation of the diffraction vectors reveals that the electron diffraction patterns contain, along with reflections corresponding to ZnO, a number of reflections belonging to another phase. However, because of the high background level in the patterns due to the amorphous structure of the opal clusters, it is difficult to unambiguously identify what crystalline material is responsible for these additional reflections.

In order to clarify the phase composition of the crystalline phases, X-ray diffraction patterns were obtained for laps prepared from the opal samples subjected to 4 and 25 cycles of filling. Analysis of the diffraction patterns suggests that, in the sample filled in four cycles, the major phase is zinc oxide (Fig. 3). Apart from ZnO, there exist zinc silicate β-Zn_2SiO_4 (ICDD PDF-2, 14–0653) and a small amount of its high-temperature phase, willemite Zn_2SiO_4 (ICDD PDF-2, 37–1485). In the sample filled in 25 cycles, the major phase is zinc silicate β-Zn_2SiO_4; willemite and zinc oxide are also present. These results allow us to conclude that, under thermal treatment of samples impregnated with zinc nitrate, zinc oxide interacts with amorphous silicon dioxide, resulting in the formation of zinc silicates. Since a thermal treatment is performed during each cycle of filling, the higher the number of cycles, the larger the fraction of zinc oxide converted into zinc silicate. The formation of the willemite phase is of particular note. According to the available data (ICDD PDF-2, 14–0653), zinc silicate β-Zn_2SiO_4 transforms into willemite at 960°C. In the experiments carried out during this study, however, the annealing temperature was not higher than 800°C. Such a lowering of the phase transition temperature could be due to the nanometer-scale size of these crystals.

4. LUMINESCENCE AND REFLECTION SPECTRA

Figure 4 shows the room-temperature PL spectra of the opal samples after 4 (curve *1*) and 25 (curve *2*) stages of filling with ZnO. For the samples filled in four stages, a UV excitonic peak and a green peak typical of the ZnO hexagonal phase can clearly be seen at the wavelengths 382 and 530 nm, respectively. The predominance of excitonic emission suggests that the zinc oxide formed in the pores of the opal samples is of high crystal quality and stoichiometric composition. As the number of stages of filling increases, two broad emission bands with peaks at 430 and 515 nm appear in the PL spectra of the opal–ZnO nanocomposites. In this case, the green emission band may be due to oxygen vacancies in zinc oxide [11], while the blue band is controlled by the zinc silicate phase β-Zn_2SiO_4 [13]. The lack of excitonic luminescence from zinc oxide in the spectrum (curve *2*) may be caused by the large amount of silicon admixture remaining in the ZnO phase after 25 stages of filling and thermal treatment of the nanocomposite samples.

Comparison of the PL spectra shown in Fig. 4 suggests that the samples subjected to four stages of filling can be used for the fabrication of UV emitters with a distributed feedback. In this case, the opal matrix controls the allowed modes of the emitter, and the zinc oxide incorporated into the pores of the opal serves as an emitting medium. Due to the opal matrix, the excitonic luminescence of ZnO can be observed only in some specified directions. In this context, we studied the angular dependences of the PL and reflection spectra for the nanocomposites; these spectra featured an

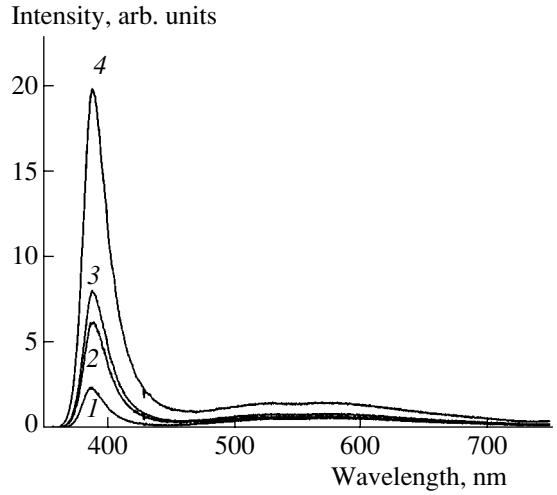

Fig. 5. PL spectra of the opal–ZnO nanocomposite after four cycles of filling with ZnO at different PL-signal recording angles φ: (*1*) 12°, (*2*) 20°, (*3*) 35°, and (*4*) 50°. The PL intensity is divided by sinφ. The excitation power density was 70 MW/cm^2. T = 300 K.

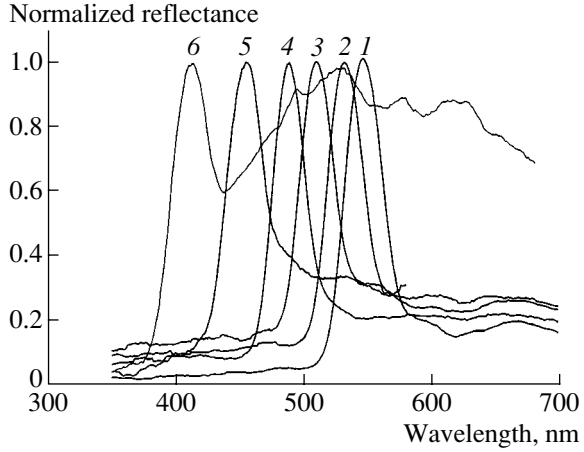

Fig. 6. Reflection spectra of the opal–ZnO nanocomposite samples (four cycles of filling with ZnO) at different angles of incidence with respect to the sample surface: (*1*) 90°, (*2*) 67.5°, (*3*) 52.5°, (*4*) 45°, (*5*) 30°, and (*6*) 22.5°. T = 300 K.

intense UV emission band (there were four stages of filling with ZnO).

Figure 5 shows the PL spectra of the opal–ZnO nanocomposite samples after four stages of filling with ZnO. The spectra were excited in a direction orthogonal to the sample surface and recorded at different angles φ with respect to the surface. The PL intensity was divided by the sine of the angle of recording to compensate for changes corresponding to Lambert's law. Nevertheless, it can clearly be seen that, as the angles φ decrease, the intensity of the excitonic emission of ZnO at 382 nm sharply decreases. This observation can be accounted for by the existence of a stop band for violet light along some directions of the opal structure.

For recording the stop bands of the material, we studied the mirror reflection spectra of the opal–ZnO structures at different angles of incidence of the light beam (Fig. 6). As is evident from Fig. 6, the reflection peak corresponding to the stop-band shifts to shorter wavelengths as the angles of incidence are decreased. It is because of the lack of propagating short-wavelength electromagnetic modes along these directions in the opal matrix that the excitonic emission of zinc oxide is virtually quenched in the PL spectra of the nanocomposite (Fig. 5, curves *1*, *2*). The effect of suppression of spontaneous emission from zinc oxide in the photonic band gap is observed in this case. As a result, the emission of zinc oxide along the other directions of the photonic crystal is enhanced.

5. CONCLUSION

Our TEM and XPA studies of opal–ZnO composites have shown that, under thermal treatment of the infiltrated samples, a solid-state reaction proceeds at the opal–ZnO interface and results in the formation of zinc silicate β-Zn_2SiO_4 and its high-temperature phase, willemite Zn_2SiO_4. It is established that, in these samples, the willemite phase is produced at temperatures below 800°C, which is considerably lower than the phase transition temperature (960°C) reported earlier. For the sample subjected to 25 cycles of filling with ZnO, no luminescence signal in the region of excitonic emission in ZnO was detected. At the same time, a broad emission band controlled by the β-Zn_2SiO_4 phase was observed in the blue spectral region (430 nm). The angular dependence of the PL spectra of the opal–ZnO composite fabricated in four cycles of filling showed a sharp decrease in the intensity of 382-nm excitonic emission at small PL-signal recording angles. This result may be due to the stop band for violet light for certain directions in the opal structure. Such an interpretation is confirmed by measurements of the angular dependence of the mirror reflection spectra. The spectra suggest the effect of suppression of the spontaneous emission in the photonic gap.

ACKNOWLEDGMENTS

This study was supported by Russian Academy of Sciences program "Low-Dimensional Quantum Structures," by the Ministry of Industry and Science of the Russian Federation (contract no. 40.012.1.1.11.54), by the Russian Foundation for Basic Research (project nos. 04-02-97263 and 04-02-16437), and by INTAS (project no. 2002-0796).

REFERENCES

1. T. F. Kraus and R. M. De La Rue, Prog. Quantum Electron. **23**, 51 (1999).
2. J. G. Fleming and S. Y. Lin, Opt. Lett. **24** (1), 49 (1999).

3. S. G. Romanov, T. Maka, C. M. Sotomayor Torres, *et al.*, Appl. Phys. Lett. **79**, 731 (2001).
4. S. V. Gaponenko, V. N. Bogomolov, E. P. Petrov, *et al.*, J. Lightwave Technol. **17**, 2128 (1999).
5. V. N. Astratov, V. N. Bogomolov, A. A. Kaplyanskii, *et al.*, Nuovo Cimento D **17**, 1349 (1995).
6. D. J. Norris and Yu. A. Vlasov, Adv. Mater. **13**, 371 (2001).
7. S. G. Romanov and C. M. Sotomayor Torrers, Phys. Rev. E **69**, 046611 (2004).
8. C. M. Mo, Y. H. Li, Y. S. Liu, *et al.*, J. Appl. Phys. **83**, 4389 (1998).
9. A. N. Gruzintsev, V. T. Volkov, G. A. Emel'chenko, *et al.*, Fiz. Tekh. Poluprovodn. (St. Petersburg) **37**, 330 (2003) [Semiconductors **37**, 314 (2003)].
10. K. K. Kim, N. Koguchi, Y. W. Ok, *et al.*, Appl. Phys. Lett. **84**, 3810 (2004).
11. V. M. Masalov, É. N. Samarov, G. I. Volkodav, *et al.*, Fiz. Tekh. Poluprovodn. (St. Petersburg) **38**, 884 (2004) [Semiconductors **38**, 849 (2004)].
12. *Current Topics on Materials Science*, Ed. by E. Kaldis (North-Holland, Amsterdam, 1981), Vol. 7, p. 244.
13. X. Xu, P. Wang, Z. Qi, *et al.*, J. Phys.: Condens. Matter **15**, L607 (2003).

Translated by É. Smorgonskaya

Semiconductors, Vol. 39, No. 11, 2005, pp. 1333–1337. Translated from Fizika i Tekhnika Poluprovodnikov, Vol. 39, No. 11, 2005, pp. 1380–1384.

AMORPHOUS, VITREOUS, AND POROUS SEMICONDUCTORS

Luminescence and Electrical Conductivity of Polyamide Acid and Its Metal–Polymer Complexes with La and Tb

É. A. Lebedev*^, M. Ya. Goĭkhman, D. M. Zhigunov***, I. V. Podeshvo**, V. V. Kudryavtsev**, and V. Yu. Timoshenko*****

**Ioffe Physicotechnical Institute, Russian Academy of Sciences, Politekhnicheskaya ul. 26, St. Petersburg, 194021 Russia*

^e-mail: Elebedev.ivom@ioffe.rssi.ru

***Institute of Macromolecular Compounds, Russian Academy of Sciences, Bol'shoi proezd 31, St. Petersburg, 119004 Russia*

****Faculty of Physics, Moscow State University, Vorob'evy gory, Moscow, 119899 Russia*

Submitted March 14, 2005; accepted for publication March 16, 2005

Abstract—The photoluminescence and electrical properties of organic semiconductors of polyamide acid (PAA) and its complexes with lanthanides are investigated. On the addition of La and Tb to PAA, the emission intensity increases by 40%. No inherent bands of lanthanides are found in the emission spectrum. The current–voltage characteristics and the temperature dependence of the conductivity of PAA and its complexes are investigated for layers ranging from 40 to 0.1 μm in thickness. A specific feature of its electrical properties is a hysteresis of the temperature dependence of conductivity with an increase or decrease in temperature. A considerable deviation of the current–voltage characteristics from linearity, which is associated with injection currents, is observed for layers 0.1–0.2 μm thick. The breakdown voltage and limiting-current density for these layers are 3–8 V and $(2–1) \times 10^{-2}$ A/cm^2, respectively. The obtained value of the current density is comparable with the current density in layers of electroluminescent conjugate polymers at the same voltages. © *2005 Pleiades Publishing, Inc.*

1. INTRODUCTION

The luminescence and electrical properties of organic polymers are of great interest, since it is possible to fabricate efficient electroluminescent diodes based on them. Promising electroluminescent materials, along with intense luminescence, should have sufficiently high stability and the ability to provide a high current density in the diodes.

The known organic semiconductors with high electroluminescence efficiency are polymers with conjugated bonds, namely, polyphenylvinylene (PPV) and its derivatives [1, 2]. The optical and electrical properties of PPV closely resemble the properties of chalcogenide vitreous semiconductors. For PPV, a relatively broad optical absorption band is observed, the spread of the long-wavelength absorption edge follows the exponential law, and the charge-carrier mobility is ~10^{-5} cm^2/(V s) [3]. Polyamide acid (PAA) and the metal–polymer PAA-based complexes of transition metals exhibit photoluminescence (PL) comparable with that observed for PVV in relation to efficiency and spectral distribution [4]. A metal–polymer complex is a compound with a central metal atom, the so-called complexing agent, which is located in the coordination bond with fragments of a polymer chain, the so-called ligands.

It seems interesting to further study PAA complexes with various elements that can introduce their characteristic bands in the spectrum. Such elements are transition metals, namely, rare-earth metals or lanthanides, which have narrow luminescence bands that are found in a wide wavelength range from visible to IR radiation [2]. In this context, we examined the PL and electrical properties of La-containing PAA complexes (PAA–La^{3+}) and Tb-containing ones (PAA–Tb^{2+}).

2. THE SAMPLES

The polymers of PAA and the PAA-based complexes, specifically, polyamide acids with imide and biquinoline units in their main chain, are soluble hydrolytically stable materials that can form transparent films. These films have high strain–strength properties and thermal stability up to 180°C. Due to the presence of biquinoline units in their main chain, these polymers form stable soluble complexes with transition metals. The La-containing PAA complex was obtained by introduction of $LaCl_3$ into PAA. The general structural formula of the complexes (PAA–La^{3+}) can be represented as

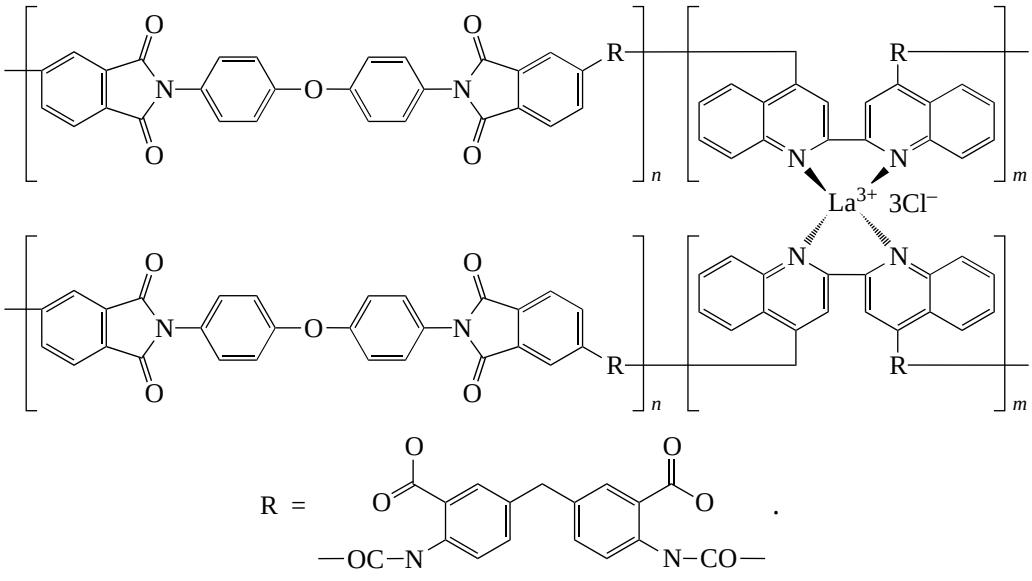

To obtain the Tb^{2+}- and Tb^{3+}-containing metal–polymer complexes, we used $TbCl_2$ and $TbCl_3$ salts, respectively.

On heating to 180–250°C, cyclization sets in the polymers, and they transform to high-strength nonfragile polybenzoxazinonimides [5]. The obtained polymer solution was poured onto glass substrates to form films, which were dried at 100°C to a constant weight. The films were 0.1–40 μm thick.

3. LUMINESCENCE

To excite the PL, we used an N_2 laser with the emission wavelength $\lambda = 337$ nm. When measuring the PL spectra in the visible spectral region 300–900 nm, we used a photomultiplier. To measure the spectra in the IR region 800–1800 nm, we used an InGaAs photodiode.

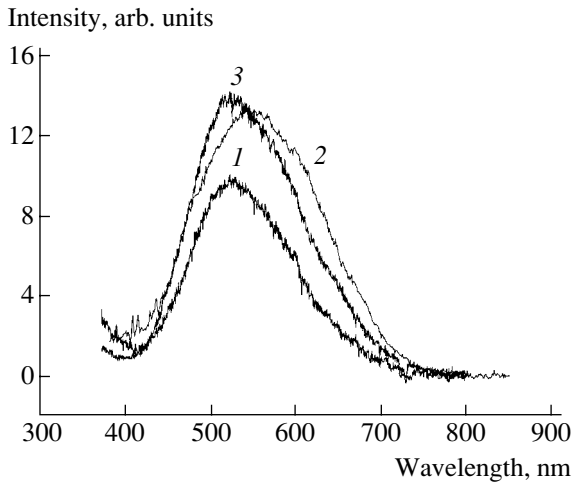

Fig. 1. Spectral distribution of photoluminescence intensity for (*1*) polyamide acid and its (*2*) La^{3+}-containing and (*3*) Tb^{2+}-containing metal–polymer complexes. Curves *1* and *3* are compiled from [4].

The PL spectra are shown in Fig. 1. The spectral dependences of the PL intensity are peaked at 520–540 nm. The peak positions virtually coincide with the wavelength of the PL peak for the conjugate PPV polymer. The PL intensity for PAA and its complexes was of the same order of magnitude as for PPV and its complexes. The similar character of PL for the conjugate PPV polymer and PAA can be accounted for by the existence of sufficiently long sections of conjugated bonds in PAA. After adding La to PAA, we observed a considerable increase in the emission intensity, which attained 40% at the wavelength of light corresponding to the emission peak. No additional bands in the near-IR region were found. It was previously noted that the intensity of the main band increases as Tb is introduced into PAA, although no inherent PL band of Tb was found in this case [4]. It seems likely that the phenomenon observed can be attributed to the effect of introduction of a heavy atom. It is assumed that this effect is associated with the effect of the metal atom on the spin–orbit interaction in the ligand [6–8].

When studying the polymer complexes of lanthanides, it was found that photoexcitation of electrons in the ligands (rather than direct excitation of the metal atom) leads to the emergence of atomic lines of lanthanides [9, 10]. The PL of lanthanides in polymer complexes is usually associated with the electron excitation via energy transfer to the electrons from a triplet level of the ligand and a subsequent electron transition to the lower allowed states. In this case, the ligand serves as an antenna that transfers energy to the excited lanthanide. The absence of the characteristic emission lines of lanthanides in the emission spectrum of the La- and Tb-containing metal–polymer complexes may be caused by the low efficiency of the energy transfer from the ligand to the lanthanide, which is determined by the

distance between the center of the ligand and lanthanide as well as by the ratio between the energies of the triplet state and luminescent state of lanthanide [11, 12].

4. ELECTRICAL PROPERTIES

As the electrical properties, we studied the current–voltage (*I–V*) characteristics and the temperature dependence of the conductivity of the PAA, PAA–La^{3+}, and PAA–Tb^{2+} layers in a wide thickness range from 40 to 0.1 μm. For the layers thinner than 2 μm, one of the electrodes was the ITO layer and the second electrode was made of Al or graphite. Colloidal graphite was used for 20- to 40-μm-thick layers.

The *I–V* characteristics were measured for constant and pulsed voltages. It was found that the shape of the *I–V* characteristics depends strongly on the film thickness. For films 40–5 μm thick, no deviations of the *I–V* characteristics from linearity were observed at voltages as high as 100 V.

A specific feature of the temperature dependence of conductivity for both PAA and its complexes is a hysteresis, which manifests itself in the fact that the conductivity behaves differently as the temperature increases and decreases. Figure 2 shows the variation in the current if the temperature *T* is increased or decreased. In the region *T* = 290–350 K, we observed hysteresis of the temperature dependence. As the temperature increases, the current is considerably higher and depends more weakly on the temperature (curve *1*) than when temperature is decreased (curve *2*). The temperature dependences of the current during the repeated heating–cooling cycle (dependence *3*) are identical to each other and similar to the dependence obtained when temperature is increased in the first cycle. If the temperature is stabilized in the range 320–350 K in the first cycle during the temperature increase, the current decreases with time. For example, as the temperature is stabilized at *T* = 340 K, the current decreases by a factor of approximately 4 in 5 min. This phenomenon shows that the origin of the hysteresis is associated with variation in the composition and structure of the polymer, which leads to a decrease in its electrical conductivity as the temperature increases during the first heating–cooling cycle. During the subsequent cycles, the polymer structure stabilizes. A hysteresis of this type was observed for *trans*-carotene and attributed to a variation in the concentration of oxygen adsorbed in the sample [13].

The temperature dependences of the current, which were recorded during the repeated cycles, are shown in Fig. 3. They show that the conductivity depends on temperature exponentially, and the activation energy for this process is ~1.3 eV for PAA and 1.5 eV for (PAA–La^{3+}).

For layers 20–40 μm thick, the room-temperature conductivity was ~10^{-13} Ω^{-1} cm^{-1}. At such low conductivity of luminescent polymers, a high current density and high emission efficiency in luminescent diodes are

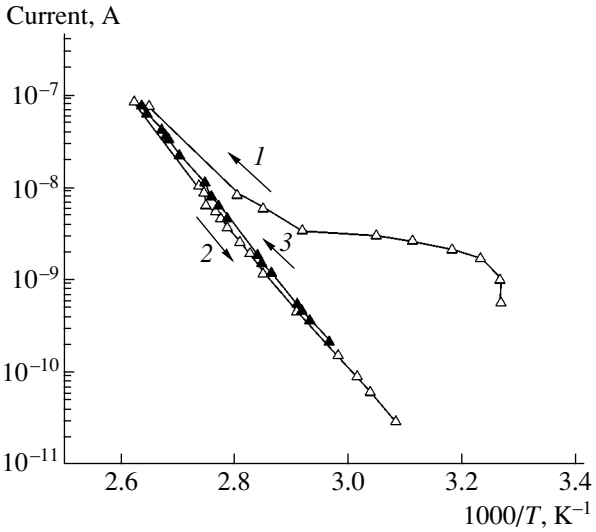

Fig. 2. Temperature dependence of the current in a 40-μm-thick film of the La^{3+}-containing metal–polymer complex of polyamide acid (*1*) for an increase, (*2*) for a decrease, and (*3*) for a repeated increase in temperature. The area of the electrodes is 0.0425 cm^2, and the voltage applied is 9.2 V.

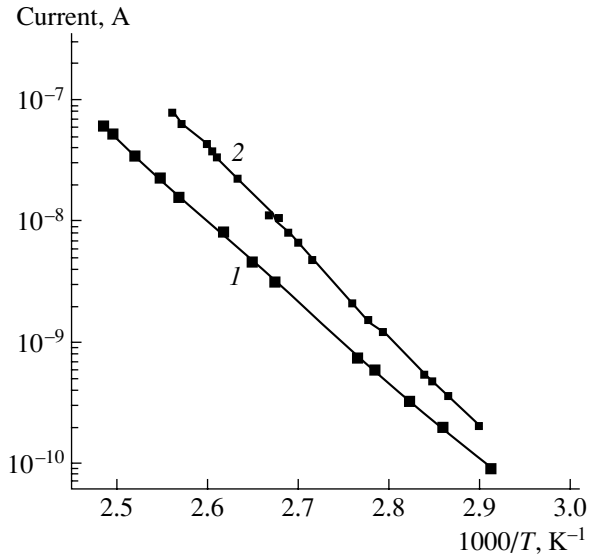

Fig. 3. Temperature dependence of the current in the layers of (*1*) polyamide acid and (*2*) its La^{3+}-containing metal–polymer complex for a repeated increase in temperature. The area of the electrodes is 0.0425 cm^2, and the voltage applied is 9.2 V.

attained due to space-charge-limited injection currents (SCLCs). For the SCLCs to occur, the total charge $q = CU$, which emerges at the electrodes of a sample with the capacitance *C*, should enter a sample when a voltage *U* is applied to the electrodes. The magnitude of the SCLC in the solid state, with or without traps that have a discrete level, is described by the dependence [14]

$$I = 8\varepsilon\mu U^2/9L^3,$$

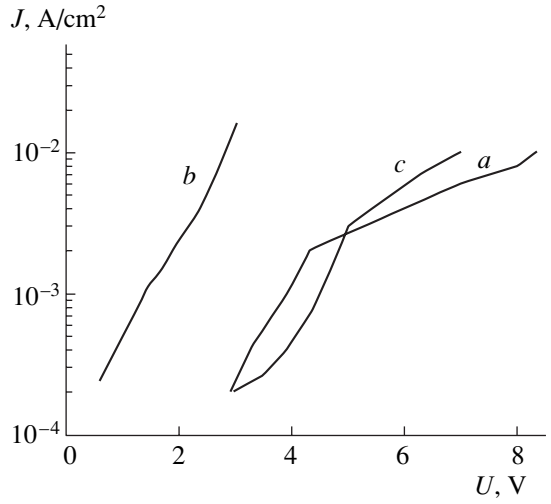

Fig. 4. Current–voltage characteristics of the films of (*a*) polyamide acid and (*b*, *c*) its Tb^{2+}-containing metal–polymer complex at voltages below those corresponding to the threshold. The film thickness was (*a*) 0.2, (*b*) 0.1, and (*c*) 0.16 μm.

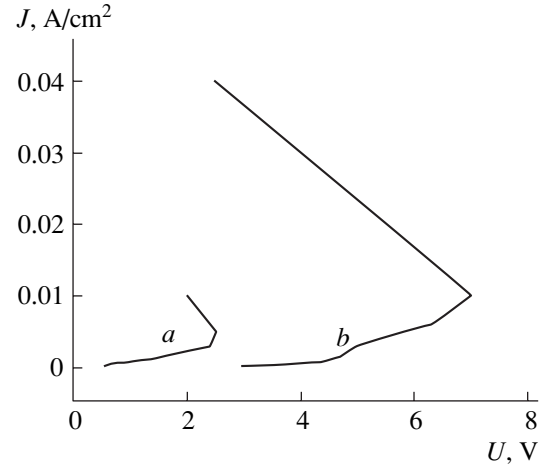

Fig. 5. *S*-shaped current–voltage characteristics of the Tb^{2+}-containing metal–polymer complex of polyamide acid. The film thickness was (*a*) 0.1 and (*b*) 0.16 μm.

where ε is the permittivity, μ is the mobility, and *L* is the sample thickness.

The magnitudes of these currents depend strongly on the thickness. Therefore, the typical thickness of the polymer layer in electroluminescent diodes is only 0.1 μm. A square-law voltage dependence of the current, which is characteristic of an SCLC, is often observed for thin layers of conjugate polymers in the high-field region [15].

Figure 4 shows that nonlinear *I–V* characteristics, which can be represented by an exponential voltage dependence of the current density, are observed for ~0.1-μm-thick layers of PAA and its complexes. The cause of this nonlinearity of the *I–V* characteristics for thin polymer layers can be associated with the presence of an SCLC. In the case of the presence of the SCLC, an exponential dependence is observed for semiconductors if the charge carriers are captured by localized states with a uniform energy distribution [16]. The steeper dependence at lower voltages (Fig 4, curves *a*, *c*) may be caused by the effect of the contacts. An increase in the current was limited by the electrical breakdown or by current instability, which leads to an *S*-shaped *I–V* characteristic. The threshold voltage and the current density for layers 0.1–0.2 μm thick are 3–8 V and $(2–1) \times 10^{-2}$ A/cm^2, respectively. The obtained current density is comparable with that for the layers of conjugate polymers, which equals 10^{-2}–10^{-1} A/cm^2 at the same voltages [15]. However, the films of conjugate polymers withstand considerably higher voltages, which allows one to obtain currents ~10 A/cm^2 in these polymers [17].

The *S*-shaped *I–V* characteristics of thin layers of the Tb-containing metal–polymer complex are shown in Fig. 5. The observed current instability is comparable in its characteristics with the switching effect in chalcogenide vitreous semiconductors [18, 19]. The essence of this effect is a rapid reversible switching of a sample from the high-resistivity state to the low-resistivity one. Current instabilities are of great interest as phenomena that can be used to switch the voltage and current. The origin of this current instability in a metal–polymer complex can be associated with electronic–thermal switching, whose mechanism was considered in detail elsewhere [20, 21].

5. CONCLUSIONS

As a result of our investigations, it is found that, on the introduction of Tb and La into polyamide acid, the PL intensity increases by almost 40%. We found no characteristic PL bands of lanthanides in this case. The PL intensity and injection currents for PAA, metal–polymer PAA-based lanthanide-containing complexes, and the electroluminescent conjugate PPV polymer are quantities that are on the same order of magnitude under comparable voltages. The luminescent and electrical properties of PAA and its complexes, in combination with high thermal stability, allow us to consider them as promising electroluminescent materials. Their disadvantages are their relatively low limiting fields, which makes it necessary to radically improve the technology used to obtain these materials. The observed hysteresis of the temperature dependence of conductivity indicates that the content of absorbed gas and, possibly, the structure of the materials vary as the temperature varies. We know that similar phenomena are also observed for conjugate polymers. These phenomena require extremely thorough further study because they affect the electrical and optical properties of organic semiconductors and can determine the potential for their practical usage.

ACKNOWLEDGMENTS

This study was supported by the St. Petersburg Scientific Center, Russian Academy of Sciences, and the Center of Collective Use, Moscow State University.

REFERENCES

1. J. H. Burroughes, D. D. C. Bradley, A. R. Brown, *et al.*, Nature **347**, 539 (1990).
2. L. H. Slooff, A. Polman, M. P. Oude Wolbers, *et al.*, J. Appl. Phys. **83**, 497 (1998).
3. E. Lebedev, Th. Dittrich, V. Petrova-Koch, *et al.*, Appl. Phys. Lett. **71**, 2686 (1997).
4. É. A. Lebedev, M. Ya. Goĭkhman, M. E. Kompan, *et al.*, Fiz. Tekh. Poluprovodn. (St. Petersburg) **37**, 844 (2003) [Semiconductors **37**, 816 (2003)].
5. I. V. Podeshvo, M. Ya. Goĭkhman, E. L. Aleksandrova, *et al.*, in *Abstracts of 10th International Conference on Synthesis and Study of Properties, Modifications, and Treatment of High-Molecular Compounds* (Kazan, 2001), p. 96.
6. S. Tobita, M. Arakawa, and I. Tanaka, J. Phys. Chem. **88**, 2697 (1984).
7. S. Tobita, M. Arakawa, and I. Tanaka, J. Phys. Chem. **89**, 5649 (1985).
8. S. Klink, L. Grave, D. N. Reinhoudt, *et al.*, J. Phys. Chem. A **104**, 5457 (2000).
9. S. I. Weissman, J. Chem. Phys. **10**, 214 (1942).
10. S. Klink, G. A. Hebbink, L. Grave, *et al.*, J. Appl. Phys. **86**, 1181 (1999).
11. J. Steemers, W. Verboom, D. N. Reinhoudt, *et al.*, J. Am. Chem. Soc. **117**, 9408 (1995).
12. S. Sato and M. Wada, Bull. Chem. Soc. Jpn. **43**, 1955 (1970).
13. B. Rosenberg, J. Chem. Phys. **34**, 812 (1961).
14. M. A. Lampert and P. Mark, *Current Injection in Solids* (Academic, New York, 1970; Mir, Moscow, 1973).
15. S. Karg, M. Meier, and W. Riess, J. Appl. Phys. **82**, 1951 (1997).
16. I. L. Hartke, Phys. Rev. **125**, 1177 (1962).
17. S. Forero, P. H. Nguen, W. Brutting, and M. Schwoerer, Phys. Chem. Chem. Phys. **1**, 1769 (1999).
18. B. T. Kolomiets and É. A. Lebedev, Radiotekh. Élektron. (Moscow) **8**, 2097 (1963).
19. S. R. Ovshinsky, Phys. Rev. Lett. **21**, 1450 (1968).
20. É. A. Lebedev, M. Ya. Goĭkhman, K. D. Tséndin, *et al.*, Fiz. Tekh. Poluprovodn. (St. Petersburg) **38**, 1115 (2004) [Semiconductors **38**, 1078 (2004)].
21. K. D. Tséndin, É. A. Lebedev, and A. B. Shmel'kin, Fiz. Tverd. Tela (St. Petersburg) **47**, 427 (2005) [Phys. Solid State **47**, 439 (2005)].

Translated by N. Korovin

Semiconductors, Vol. 39, No. 11, 2005, pp. 1338–1341. Translated from Fizika i Tekhnika Poluprovodnikov, Vol. 39, No. 11, 2005, pp. 1385–1388.

AMORPHOUS, VITREOUS, AND POROUS SEMICONDUCTORS

Effect of the Initial Doping Level on Changes in the Free-Carrier Concentration in Porous Silicon during Ammonia Adsorption

A. V. Pavlikov^, L. A. Osminkina, I. A. Belogorokhov, E. A. Konstantinova, A. I. Efimova, V. Yu. Timoshenko, and P. K. Kashkarov

Faculty of Physics, Moscow State University, Vorob'evy gory, Moscow, 119992 Russia

^e-mail: pavlikov@vega.phys.msu.ru

Submitted December 1, 2004; accepted for publication March 18, 2005

Abstract—Infrared spectroscopy is used to investigate the effect of ammonia adsorption on the concentration of equilibrium charge carriers in porous-silicon layers with various initial types of dopants at different concentrations. It is found that ammonia adsorption results in an increase in the number of free electrons in *n*-type samples up to a level exceeding 10^{18} cm^{-3}. In *p*-type samples, a nonmonotonic dependence of the charge-carrier concentration on ammonia pressure is observed. The obtained results are accounted for by the appearance of adsorption-induced shallow donor states that, along with the initial-dopant and surface-defect states, specify the charge-carrier type and concentration in the silicon nanocrystals of the porous layer after ammonia adsorption.

1. INTRODUCTION

Porous silicon, obtained by electrochemical etching of silicon single crystals, continues to be an attractive material for investigations of low-dimensional solid systems [1, 2] in physics. The appeal of porous silicon (*por*-Si) is due to its diverse physical properties and the needs of the recently opened fields of optical [3] and biomedical [4] applications. At a reasonably high porosity ($\gtrsim$50%), this material consists of a system of coupled silicon nanocrystals whose surfaces are open for the action of environmental molecules [1]. The *por*-Si specific surface can be as large as ~10^3 m^2/g [2], which leads to the adsorption covering of the nanocrystal surface having a significant effect on their electronic properties. For example, in *por*-Si with an average diameter of pores and silicon nanocrystals exceeding 4–5 nm, i.e., in mesoporous silicon (*mesopor*-Si) [1], depending on the molecular environment and adsorption coverage of the silicon nanocrystals, there can be equilibrium free charge carriers with a concentration of ~10^{16}–10^{18} cm^{-3} [5–7].

Recently, it has been established that the adsorption of molecules with acceptor properties, for example, nitrogen dioxide molecules, results in an increase in the concentration of equilibrium holes in *mesopor*-Si layers up to the doping level of the *p*-type substrates under use [7, 8]. There also exist data on the effect of adsorption of donor molecules, in particular, ammonia molecules, resulting in a change of magnitude and sign of the photovoltage in porous-silicon layers [9]. It has recently been revealed that the adsorption of these molecules on *p*-type samples at low temperatures results in the occurrence of an ESR signal from free electrons [10], which suggests an inversion of the conductivity from *p*- to *n*-type. However, the data reported in the available publications make it impossible to settle the issue of what the role of the initial-dopant type and its concentration is during a change in the concentration of equilibrium charge carriers in *mesopor*-Si when adsorbing ammonia molecules or to deal with the question of how large the absolute changes in the charge-carrier concentration can be after adsorption at room temperature. It should be noted that investigation of ammonia adsorption molecules in porous nanostructured semiconductors is of importance for developing new highly sensitive gas sensors [10, 11].

In this paper, we report the results of studying variations in the charge-carrier concentration in *mesopor*-Si layers caused by ammonia adsorption. We grew *mesopor*-Si layers on both *n*- and *p*-type substrates, which enabled us to establish the role of an initial impurity in the adsorption-induced doping of silicon nanocrystals.

2. EXPERIMENTAL

Mesopor-Si layers were formed by the conventional method of electrochemical etching [1] of *p*-Si:B or *n*-Si:As wafers (see table) in a HF(48%) : C_2H_5OH solution with a ratio of 1 : 1. The anodization-current density j amounted to 50 mA/cm^2 for the *p*-type samples and 80 mA/cm^2 for the *n*-type samples. After accomplishing the pore formation, we separated the layers from the substrates by a short-term increase in j up to 700 mA/cm^2. The porosity of the samples was determined by the gravimetry method and ranged from 50 to 60%.

The optical spectra were detected using a Perkin–Elmer RX I Fourier spectrometer in a range of 400–

Characteristics of the samples and the charge-carrier concentrations determined in them (according to IR-spectroscopy data)

Sample	Substrate-conductivity type	Substrate resistivity ρ, mΩ cm	Charge-carrier concentration in the substrate, cm^{-3}	Charge-carrier concentration N in a sample in vacuum, cm^{-3}	Charge-carrier concentration N in a sample at P_{NH_3} = 20 Torr, cm^{-3}
I	*p*	1–5	10^{20}	4×10^{18}	4.3×10^{17}
II	*p*	10–20	5×10^{18}	3×10^{17}	1.6×10^{18}
III	*n*	3–5	10^{19}	1.6×10^{17}	2.3×10^{18}

6000 cm^{-1} with a spectral resolution of 2 cm^{-1} for the normal incidence of infrared (IR) radiation on a sample. The experiments were carried out at room temperature in vacuum with a pressure of 10^{-5} Torr and at various pressures of ammonia, which was obtained from a 20% aqueous solution. No special purification of ammonia from the water vapor was performed. However, experiments performed to check the water-vapor adsorption showed the water vapors exert a negligible effect on the IR spectra of the *mesopor*-Si layers under investigation.

We determined the absorption spectra from the transmission spectra without taking into account the reflectance and multiple-beam interference using the formula

$$\alpha = -\frac{\ln T}{d},$$

where d is the thickness of a sample under investigation and T is its transmittance. The estimates showed that this simplification does not severely distort the spectral dependence $\alpha(\nu)$ and the free-carrier concentration N in the silicon residuals calculated from this dependence. The value of N was determined using the method described in [8]. In particular, it was assumed that $\alpha(\nu) \propto N$ in the high-frequency range.

3. RESULTS

In Fig. 1, we show the experimental IR absorption spectra (400–3500 cm^{-1}) for sample I. Curve *1* corresponds to the absorption spectrum from a freshly prepared sample in vacuum, while curves *2* and *3* represent the spectra of samples in an ammonia atmosphere at various pressures P_{NH_3}. Similarly, in Figs. 2 and 3, we show the absorption spectra from samples II and III in vacuum and in an ammonia atmosphere at various pressures.

As can be seen from Figs. 1–3, the freshly prepared *mesopor*-Si layers and those in an ammonia atmosphere at low P_{NH_3} are predominantly characterized by hydrogen coverage of the surface. The $\alpha(\nu)$ spectra mainly involve absorption bands caused by Si–H_x (x = 1, 2, 3) stretching vibrations with wave numbers ranging from 2070 to 2170 cm^{-1}, Si–H_x bending vibrations (660 cm^{-1}), and Si–H_2 "scissor" modes (910 cm^{-1}). With an increase in the ammonia pressure (P_{NH_3} > 10 Torr), the

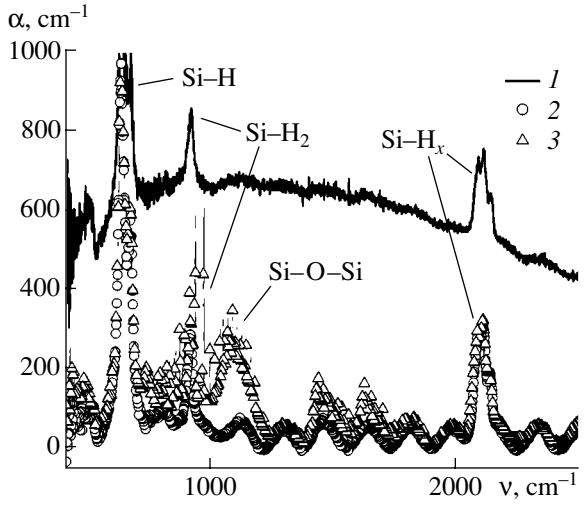

Fig. 1. Absorption spectra for samples I (*1*) in vacuum at a pressure of 10^{-5} Torr and in an ammonia atmosphere at a pressure P_{NH_3} of (*2*) 1 and (*3*) 20 Torr.

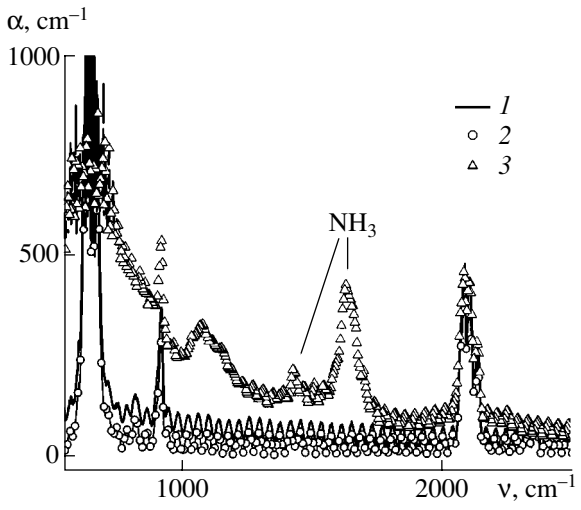

Fig. 2. Absorption spectra of samples II. Designations *1–3* are the same as in Fig. 1.

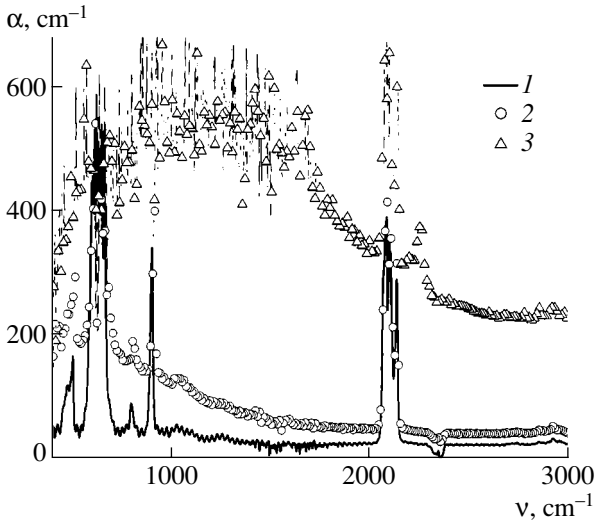

Fig. 3. Absorption spectra of samples III. Designations *1–3* are the same as in Fig. 1.

absorption bands caused by Si–O–Si stretching vibrations (ν = 1050–1100 cm^{-1}) and by stretching vibrations of the bonds of the NH_3 molecules adsorbed on the surface of the silicon nanocrystals (Fig. 2) appear in the spectra.

As follows from the analysis of a monotonic component of the α(ν) spectra shown in Figs. 2 and 3, the freshly prepared samples are characterized by a very weak absorption by free charge carriers. However, significant variations in the value of α are observed (Figs. 1–3, curves *2*, *3*) in the NH_3 vapor. Furthermore, we detected a reduction in the absorption by free charge carriers (Figs. 1, 2, curves *2*) for the *p*-type samples at the pressure P_{NH_3} = 1 Torr and a sharp increase in α (Fig. 2, curve *3*) at P_{NH_3} = 20 Torr. The *n*-type samples are characterized by a monotonic increase in the absorption by free charge carriers in the entire pressure range under study (Fig. 3, curves *2*, *3*).

In Fig. 4, we show the dependence of the concentrations *N* on an ammonia pressure P_{NH_3} calculated using the α(ν) spectra, from which it follows that the free-carrier concentration also depends on the type of substrate used for preparing *mesopor*-Si. We note that the freshly prepared *mesopor*-Si layers are appreciably depleted of free carriers in comparison with a single-crystal substrate (see table) due to an incomplete activation of dopants and a partial trapping of charge carriers by the states of defects on the surface of the silicon nanocrystals [6]. At the same time, the relative dopant concentration (recalculated per number of silicon atoms) in the *mesopor*-Si layers is higher than in the substrate under use [12].

A decrease in *N* with an increase in P_{NH_3} from 0.1 to 1 Torr for *p*-type samples I and II (Fig. 4a) enables us

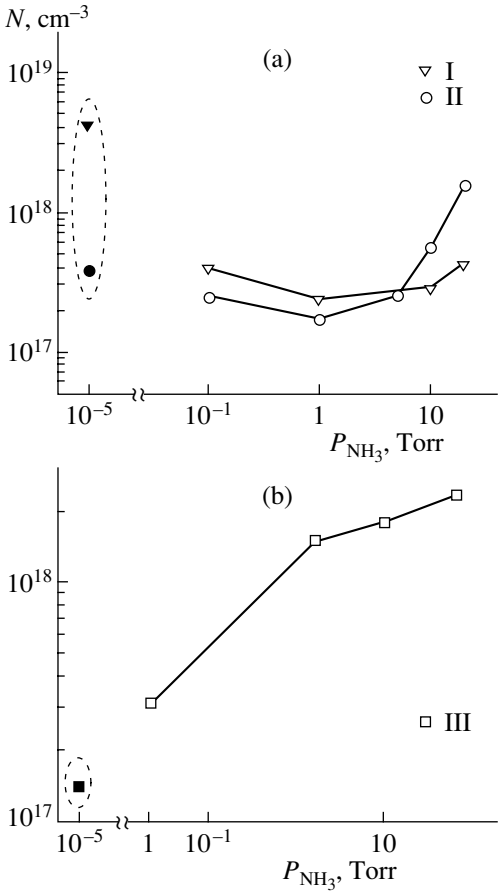

Fig. 4. Dependences of the free-carrier concentration *N* on the ammonia pressure P_{NH_3} for samples (a) I and II and (b) III. The dashed line encloses values of *N* for the freshly prepared samples in vacuum at a pressure of 10^{-5} Torr.

to assume that shallow donor states, which compensate the original acceptor dopants, are formed when the ammonia molecules are adsorbed on the surface of the nanocrystals of porous silicon. With a further increase in P_{NH_3}, the number of adsorbed molecules increases and, therefore, can change the conductivity from *p*- to *n*-type. This phenomenon manifests itself as an increase in *N* for samples I and II at P_{NH_3} > 2 Torr.

For samples III, we detected a monotonic increase in *N* as the ammonia pressure was increased (Fig. 4b), which, obviously, is indicative of an increase in the number of adsorption-induced donor states. The maximum concentration of electrons produced during the adsorption was as high as 2.3×10^{18} cm^{-3} for the *n*-type samples (see table). At the same time, the peak values of *N* were equal to 1.6×10^{18} (sample II) and 4.3×10^{17} cm^{-3} (sample I) for the *p*-type samples. These values agree well with the considered concept of formation of shallow donor states during the ammonia adsorption. At the same time, the absolute maximum

values of N are probably restricted by the formation of defects due to partial oxidation. The latter process is possible at high pressures (see Figs. 1 and 2, curves *3*) owing to the presence of residual water and oxygen impurities in the adsorbate.

Our experiments showed that the absorption by free carriers is virtually completely reversible in the cycles consisting of an inlet of molecules at $P_{NH_3} < 1$ Torr with subsequent evacuation. This observation indicates that the NH_3 molecules and the surface of the silicon nanocrystals do not form a steady chemical bond under adsorption and, consequently, the molecule–surface bonding energy is lower than the thermal energy (~26 meV) at room temperature. Unfortunately, in the performed experiments, it seems to be impossible to determine the parameters (the activation energy and concentration) for adsorption-induced donor states. However, because the silicon-nanocrystal sizes are sufficiently large for the quantum-dimensional effects to become pronounced in the investigated *mesopor*-Si samples, we can assume that the electronic properties of the adsorption states are close to those on the surface of the silicon single crystals. Further investigations are necessary for gaining a deeper insight into the nature and properties of the electronic states arising during ammonia adsorption.

4. CONCLUSIONS

As follows from the performed investigations, shallow donor states are formed as a result of ammonia adsorption on the *mesopor*-Si surface. The resulting concentration and type of charge carriers depend on the adsorbate pressure and the type of single-crystal substrate used for the fabrication of *mesopor*-Si. In *n*-type samples, the ammonia adsorption results in an increase in the free-electron concentration. In boron-doped samples, we observed inversion of the conductivity from *p*- to *n*-type at high ammonia pressures. The obtained results indicate that it is possible to change the type and concentration of equilibrium charge carriers in *mesopor*-Si layers in a controlled manner, which may be of practical interest for developing various electron devices based on this material.

The measurements were performed using instrumentation belonging to the Center of Shared Equipment at Moscow State University.

ACKNOWLEDGMENTS

This study was supported within a program of the Ministry for Industry and Science of the Russian Federation (contract no. 40.012.1.1.1153). E.A. Konstantinova acknowledges the financial support provided by a grant from President of the Russian Federation (project no. MK-2036.2003.02).

REFERENCES

1. A. G. Cullis, L. T. Canham, and P. D. J. Calcott, J. Appl. Phys. **82**, 909 (1997).
2. O. Bisi, S. Ossicini, and L. Pavesi, Surf. Sci. Rep. **38**, 1 (2000).
3. N. Künzner, D. Kovalev, J. Diener, *et al.*, Opt. Lett. **26**, 1265 (2001).
4. D. Kovalev, E. Gross, N. Künzner, *et al.*, Phys. Rev. Lett. **89**, 137401 (2002).
5. V. Yu. Timoshenko, Th. Dittrich, and F. Koch, Phys. Status Solidi B **222**, R1 (2000).
6. L. A. Osminkina, E. V. Kurepina, A. V. Pavlikov, *et al.*, Fiz. Tekh. Poluprovodn. (St. Petersburg) **38**, 603 (2004) [Semiconductors **38**, 581 (2004)].
7. V. Yu. Timoshenko, Th. Dittrich, V. Lysenko, *et al.*, Phys. Rev. B **64**, 085314 (2001).
8. E. A. Konstantinova, L. A. Osminkina, and K. S. Sharov, Zh. Éksp. Teor. Fiz. **126**, 857 (2004) [JETP **99**, 741 (2004)].
9. Yu. V. Vashpanov, Pis'ma Zh. Éksp. Teor. Fiz. **23** (11), 77 (1997) [JETP Lett. **23**, 448 (1997)].
10. M. Chiesa, G. Amato, L. Boarino, *et al.*, Angew. Chem. Int. Ed. Engl. **42**, 5032 (2003).
11. L. Boarino, C. Baratto, F. Geobaldo, *et al.*, Mater. Sci. Eng. B **69–70**, 210 (2000).
12. G. Polisski, D. Kovalev, G. G. Dollinger, *et al.*, Physica B (Amsterdam) **273–274**, 951 (1999).

Translated by V. Bukhanov

Semiconductors, Vol. 39, No. 11, 2005, pp. 1342–1345. Translated from Fizika i Tekhnika Poluprovodnikov, Vol. 39, No. 11, 2005, pp. 1389–1392.

PHYSICS OF SEMICONDUCTOR DEVICES

Removal of Fluoropolimers from the Surface of Silicon Structures by Treatment in an Atomic Hydrogen Flow

E. V. Anishchenko*, V. A. Kagadeĭ*^, E. V. Nefedtsev, D. I. Proskurovskiĭ**, and S. V. Romanenko****

**Research Institute of Semiconductor Devices, ul. Krasnoarmeĭskaya 99a, Tomsk, 634034 Russia*

^e-mail: vak@lve.hcei.tsc.ru

***Institute of High-Current Electronics, Siberian Division, Russian Academy of Sciences, Akademicheskiĭ pr. 4, Tomsk, 634021 Russia*

Submitted January 4, 2005; accepted for publication January 27, 2005

Abstract—The possibility of successful removal of fluoropolimers from the surface of silicon structures by treatment in an atomic hydrogen flow is investigated. It is ascertained that the treatment of samples in a direct atomic hydrogen flow with a density of 2×10^{15} cm^{-2} s^{-1} at temperatures from 20 to 100°C leads to a decrease in the content of fluorocarbon residues (in particular, CF) by 5 orders of magnitude. Fluorocarbon residues are removed from both the planar surface of silicon structures and the lateral walls and the bottom of contact holes with a diameter of 0.3–0.25 μm and larger and a depth of 0.9 μm, opened in a SiO_2 layer by reactive ion etching. A treatment time of 2 min is sufficient for complete removal of the fluoropolimers. This process of dry cleaning can be recommended for use in the fabrication of integrated circuits containing an interlayer of a low-permittivity insulator. © *2005 Pleiades Publishing, Inc.*

1. INTRODUCTION

Materials with a low permittivity ε, for example, carbon-modified silica, are considered to be promising insulators for interlayer isolation in integrated circuits with element sizes of 90 nm and smaller [1–5]. Reactive ion etching in carbon- and fluorine-containing gases is widely used to open contact windows in interlayer isolating films. After opening contact holes, a fluorocarbon polymer film remains on the lateral walls and the bottom of the contact holes [6]. This fluorocarbon residue is a nonvolatile material possessing high chemical and thermal stability. The presence of a fluorocarbon film leads to an increase in the contact resistance between metallization layers and deteriorates the properties of the metal–insulator interface. Therefore, fluorocarbon residues must be completely removed before deposition of metal films. A conventional and effective way to remove fluoropolimers is treatment in an oxygen plasma. However, this process has poor compatibility with technology based on the use of insulators with a low permittivity. Indeed, oxygen-plasma etching leads to losses of carbon and changes in the elemental composition of a material and, as a result, increases the permittivity ε [3–5, 7]. In this context, the search for and development of new processes of removal of fluorocarbon residues that do not lead to the degradation of insulators with a low value of ε is an urgent problem.

A method for removal of a fluoropolimer film in supercritical CO_2 was proposed in [8]. The drawback of this technique is that it is rather difficult to make it compatible with vacuum processes. In [6], the fluoropolimer film was removed by bombarding the contaminated surface with Ar^+ ions. However, high-energy heavy Ar^+ ions generate a large number of radiation defects and cause spurious charging of the surface. The technique of plasma-chemical dry etching is characterized by a much smaller concentration of introduced defects and is more promising for the removal of fluorocarbon residues. In addition, it is known that treatment in a plasma of hydrogen-containing mixtures, in contrast to treatment in oxygen-containing media, is more compatible with technology based on the use of insulators with low ε [3–5, 9]. Therefore, the possibility of removing organic and fluorocarbon residues in plasmas of various hydrogen-containing gases and mixtures (NH_3, H_2–N_2, H_2–He, and H_2) has been considered in a number of studies. Since treatment in a nitrogen-containing plasma of NH_3 or in a H_2–N_2 mixture may lead to photoresist poisoning [5], it should be acknowledged that treatment in a purely hydrogen plasma, which was used in [9] to remove fluorocarbon residues, is a rather promising method for removing fluoropolymers from the surface. However, this method also has a drawback, which consists in the negative effect of charged particles on the semiconductor structure. This effect can be eliminated by treating semiconductor structures in a medium of neutral chemically active particles.

In this study, we demonstrated, for the first time, the possibility of effective removal of fluoropolimers from the surface of semiconductor structures by treating

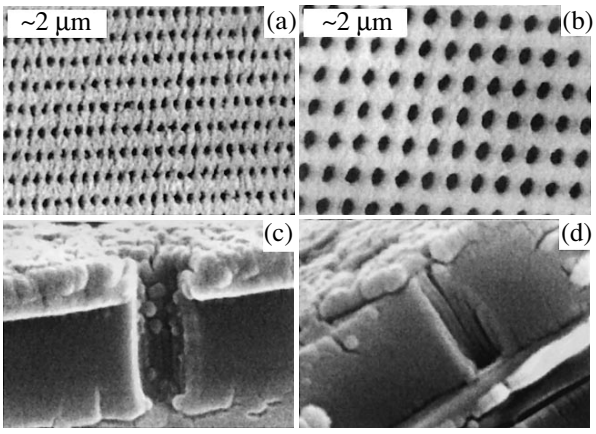

Fig. 1. Images of the (a) surface and (c) cross section of the initial sample before its treatment in an atomic hydrogen flow and after the treatment at a temperature of 22°C for (b) 2 and (d) 20 min.

them in a direct flow of neutral hydrogen atoms. The characteristic features of the removal of fluoropolimers from the surface of the structures, as well as from the walls and bottom of the contact holes, by treatment in an atomic hydrogen flow under different conditions are investigated.

2. EXPERIMENTAL

The experiments were carried out with Si(100) wafers that had a diameter of 150 mm. On the surface of these wafers, a 50-nm-thick layer of thick thermal silicon oxide was first grown, and, then, Al/Ti/TiN films with thicknesses of 500, 15, and 35 nm, respectively, were deposited. Then, a 900-nm-thick SiO_2 film was grown by plasma chemical-vapor deposition. Contact holes 0.25–0.3 μm in diameter were opened in the SiO_2 film through a photoresist mask (UV5) by reactive ion etching in a mixture of Ar, CHF_3, C_4F_8, O_2, CO, and N_2 gases. Next, the wafers were divided into samples 3×4 cm^2 in size and loaded into the vacuum chamber of the experimental setup. The chamber was pumped by a turbomolecular pump. The pressure of the residual gases was $(1–2) \times 10^{-5}$ Pa. The samples were cleaned in a direct flow of hydrogen atoms generated by a low-pressure exposed to source of atomic hydrogen [10]. The flux density of H atoms in the treatment zone was 2×10^{15} cm^{-2} s^{-1}, the average energy of the H atoms was estimated to be no higher than 1–2 eV, and the degree of contamination of the hydrogen flow by spurious metal impurities did not exceed 10^{-6}%. The hydrogen pressure in the vacuum chamber during the treatment was 10^{-2} Pa. The samples were heated by an IR source. The treatment temperature and time were varied in the ranges 20–100°C and 2–40 min, respectively. In some experiments, simultaneously with the treatment in atomic hydrogen, the sample surface was arc-discharge UV light with a wavelength of 172 nm, generated by a xenon lamp [11]. After the treatment, the samples were exposed to air. The composition of the sample surface before and after the treatment in atomic hydrogen was analyzed by time-of-flight secondary-ion mass spectrometry. Images of the surface and cross section of the samples were obtained in a scanning electron microscope.

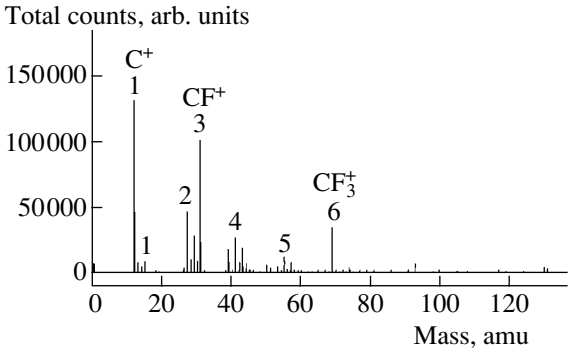

Fig. 2. Mass spectrum of the surface of the initial sample before treatment in an atomic hydrogen flow. The ion-collection time was 2 min.

3. RESULTS AND DISCUSSION

Figures 1a and 1c show images of the surface and cross section of the initial sample before its treatment in an atomic hydrogen flow. It can be seen that the surface and edges of the holes are rough and there is contamination on the walls and bottom of the contact holes, which arose during the opening of the windows in the insulator. Analysis of the chemical composition of the initial-sample surface showed that this contamination is a fluoropolimer film, whose composition is similar to that of polytetrafluoroethylene. The main peaks in the mass spectra are due to C^+ (12 amu), CF^+ (31 amu), and CF_3^+ (69 amu) (Fig. 2). The intensities of these peaks for an ion-collection time of 2 min are, respectively, 140000, 100000, and 50000 total counts. CF_2^+ (50 amu) and $C_3F_3^+$ (93 amu) are also present on the surface, but in smaller amounts.

After the treatment in an atomic hydrogen flow, the situation radically changes. Figures 1b and 1d show images of the surface and cross section of the samples processed in an atomic hydrogen flow for different periods of time. It can be seen that the sample surface becomes smoother, the edges of the holes flatten, and there are no visible fluorocarbon residues either on the walls or the bottom of the contact holes. Analysis of the chemical composition of the sample surface (Fig. 3d) showed that the content of fluorocarbon residues decreased significantly. The content of the main component CF decreased, on average, by 5 orders of magnitude and the intensity of the peaks was lower than 10 total counts (the peak intensity is normalized to an

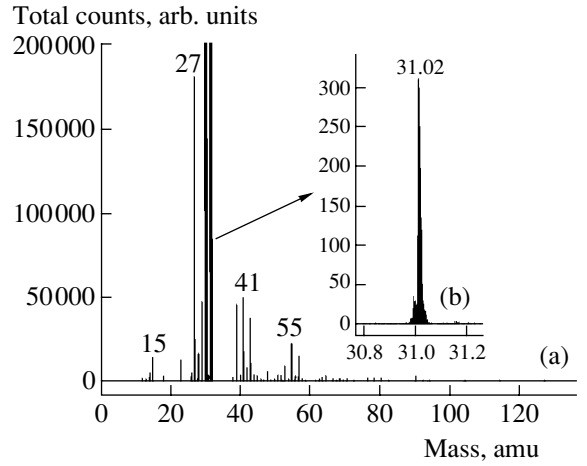

Fig. 3. Mass spectrum of the sample surface after treatment in an atomic hydrogen flow at a temperature of 22°C for 40 min: (a) the entire spectrum and (b) the spectrum in the vicinity of 31 amu. The ion-collection time was 10 min.

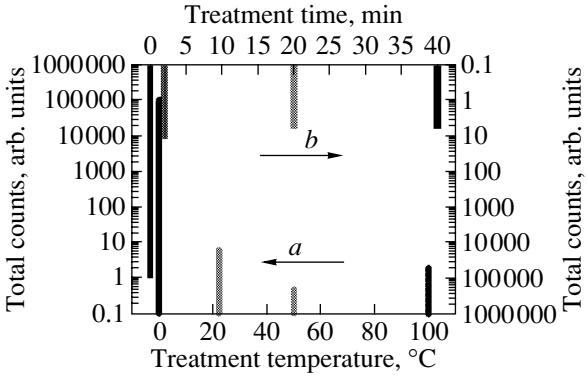

Fig. 4. Intensities of the CF^+ peak for the initial sample and the samples treated in atomic hydrogen as functions of (*a*) the treatment temperature and (*b*) the treatment time.

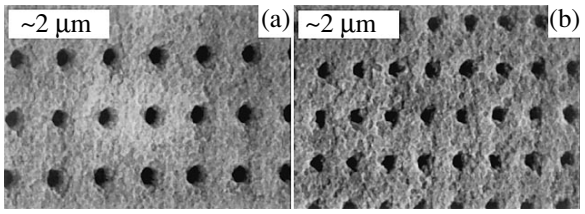

Fig. 5. Images of the sample surfaces after treatment in atomic hydrogen with simultaneous UV irradiation at a temperature of 22°C for (a) 2 and (b) 20 min.

ion-collection time of 2 min). The entire mass spectrum of the cleaned surface corresponds to the spectrum of a surface with a photoresist film exposed to air for some time. Figure 3b shows the detailed mass spectrum of the cleaned sample in the range 30.8–31.2 amu. The peak at 31 amu, corresponding to CF^+ ions, has an intensity of about 4 total counts (the peak intensity is normalized to an ion-collection time of 2 min). The peak with a higher intensity at 31.02 amu is due to CH_3O^+ ions. Thus, the data obtained indicate that, as a result of the treatment in an atomic hydrogen flow, fluorocarbon residues are removed from both the surface of the semiconductor structure and the walls and bottom of the contact holes. As a result of direct motion, neutral H atoms easily penetrate the holes (including those with a high aspect ratio) and effectively remove fluoropolymers from their walls and bottom.

Figure 4 shows the dependences of the content of CF^+ ions on the sample surface on the treatment temperature and time. It can be seen that, when the samples are at room temperature, almost complete removal of the contamination from the surface is obtained even at treatment times of 2 min. An increase in the treatment time to 20 min leads only to a decrease in the intensity of the peak at 31 amu (CF^+) by a factor of 2. A further increase in treatment time does not change the surface content of CF^+: it remains at a level of 4 total counts. The temperature dependence of the CF^+ content is not pronounced. The minimum content of CF^+ on the surface (0.5 total counts) is obtained at a treatment temperature of 50°C. Treatment at room temperature and at 100°C leaves a somewhat larger amount of CF^+ on the surface.

Figure 5 shows images of the surfaces of the samples treated in atomic hydrogen for different time periods with a simultaneous exposure to UV light. At a short treatment time (2 min), the intensity of the peak at 31 amu (CF^+) in the spectrum of the sample subjected to the combined effect of atomic hydrogen and UV light (Fig. 5a) is a factor of 1.6 smaller than for the sample treated only in atomic hydrogen. This result suggests that UV irradiation increases the rate of removal of fluorocarbon residues. At a treatment time of 20 min, the intensities of the CF^+ peaks for the sample subjected to the combined effect (Fig. 5b) and the sample treated only in atomic hydrogen are almost the same and lower than in the case of treatment in atomic hydrogen for 2 min with simultaneous exposure to UV light by a factor of only 1.5. The absolute intensities of these peaks are close to the minimum value obtained in the experiments involving treatment in atomic hydrogen at room temperature (Fig. 4b).

Comparative analysis of the images of the cross sections of the initial sample and the sample cleaned in atomic hydrogen (Figs. 1c, 1d) indicates that the treatment in atomic hydrogen, along with the removal of the fluoropolimer film, also leads to etching of the photoresist layer. A treatment in atomic hydrogen for 2 min makes the photoresist layer thinner by a factor of about 2. Analysis of the images of the surfaces of the samples treated in an atomic hydrogen flow and in atomic hydrogen with a simultaneous exposure to UV light (Figs. 1b, 1d, 5) shows that UV irradiation facilitates not only the removal of fluorocarbon residues but also the etching of the photoresist layer. It can be seen that

the samples subjected to the combined treatment are characterized by a more inhomogeneous surface; the degree of the surface inhomogeneity increases as the treatment time in atomic hydrogen with simultaneous UV irradiation is increased.

In [9], where a fluoropolimer film was removed by treatment in a hydrogen microwave-discharge plasma under the conditions of electron cyclotron resonance, it was suggested that fluorocarbon residues are removed as a result of ion-stimulated chemical reactions, which involve high-energy ions and chemically active H atoms. According to the results of this study, fluorocarbon residues can be effectively removed using only chemically active H atoms with an average kinetic energy no higher than 1–2 eV. In this case, the interaction between fluorocarbons and atomic hydrogen occurs via the mechanism of radical etching (apparently, with the breaking of C–C bonds and subsequent formation of volatile reaction products). The stimulating effect of UV light amounts most likely to the breaking down of the initial fluorocarbon molecules into fragments and radicals and (or) an increase in the desorption rate of the reaction products.

4. CONCLUSIONS

It has been shown that treatment in an atomic hydrogen flow effectively removes fluorocarbon residues from the surface of semiconductor structures. Fluorocarbon residues are removed both from the surface of the semiconductor structure and from the walls and bottom of the contact holes, which is related to the direct motion of H atoms. At a flux density of H atoms equaling 2×10^{15} cm^{-2} s^{-1}, a treatment at room temperature for 2 min is sufficient to clean the surface. The main advantages of treatment in a direct atomic hydrogen flow over the known methods are the compatibility of this process with technology based on the use of low-permittivity insulators; the possibility of cleaning contact holes with a large aspect ratio; and the absence of high-energy and charged particles in the flow, which minimizes the number of introduced charges and defects.

ACKNOWLEDGMENTS

We are grateful to J.C. Voltz for supplying the samples with fluorocarbon residues, V. Diamant and R. Ziskind for their help in organizing the measurements, A. Gladkikh for carrying out the measurements by time-of-flight secondary-ion mass spectrometry, and V.F. Tarasenko and M.I. Lomaev for supplying a xenon flash lamp.

REFERENCES

1. N. H. Hendricks, Solid State Technol. **3**, 31 (2003).
2. M. Uhlig, A. Bertz, M. Rennau, *et al.*, Microelectron. Eng. **50**, 7 (2000).
3. P. T. Liu, T. C. Chang, S. M. Sze, *et al.*, Thin Solid Films **332**, 345 (1998).
4. J. R. Hu, W. Uesato, and P. Schoenborn, in *Proceedings of AVS First International Conference on Microelectronics and Interfaces* (2000); http://www.ulvac.com/pdf/lsilowk.pdf.
5. L. Peters, Semicond. Int. **25** (12), 57 (2002).
6. M. Delfino, S. Salimian, and D. Hodul, J. Appl. Phys. **70**, 1712 (1991).
7. A. E. Braun, Semicond. Int. **22** (11), 44 (1999).
8. D. J. Mount, L. B. Rothman, R. J. Robey, and M. K. Ali, Solid State Technol. **6**, 103 (2002).
9. S.-H. Lim, J.-W. Park, H.-K. Yuh, *et al.*, J. Korean Phys. Soc. **33** (11), S108 (1998).
10. V. A. Kagadei and D. I. Proskurovski, J. Vac. Sci. Technol. A **16**, 2556 (1998).
11. E. Arnold, M. I. Lomaev, V. S. Skakun, *et al.*, Laser Phys. **12** (5), 1 (2002).

Translated by Yu. Sin'kov

Semiconductors, Vol. 39, No. 11, 2005, pp. 1346–1351. Translated from Fizika i Tekhnika Poluprovodnikov, Vol. 39, No. 11, 2005, pp. 1393–1398.

PHYSICS OF SEMICONDUCTOR DEVICES

A New Type of High-Efficiency Bifacial Silicon Solar Cell with External Busbars and a Current-Collecting Wire Grid

G. G. Untila*^, T. N. Kost*, A. B. Chebotareva*, M. B. Zaks, A. M. Sitnikov**, and O. I. Solodukha****

**Nuclear Physics Institute, Moscow State University, Moscow, 119992 Russia*

^e-mail: GUntila@.mics.msu.su

***Kvark Scientific-Production Firm, Krasnodar, 350000 Russia*

Submitted February 28, 2005; accepted for publication March 9, 2005

Abstract—Results regarding bifacial silicon solar cells with external busbars are presented. The cells consist of [$n^+p(n)p^+$] *Cz*-Si structures with a current-collecting system of new design: a laminated grid of wire external busbars (LGWEB). A LGWEB consists of a transparent conducting oxide film deposited onto a Si structure, busbars adjacent to the Si structure, and a contact wire grid attached simultaneously to the oxide and busbars using the low-temperature lamination method. Bifacial LGWEB solar cells demonstrate record high efficiency for similar devices: 17.7%(*n*-Si)/17.3%(*p*-Si) with 74–82% bifaciality for the smooth back surface and 16.3%(*n*-Si)/16.4%(*p*-Si) with 89% bifaciality for the textured back surface. It is shown that the LGWEB technology can provide an efficiency exceeding 21%. © *2005 Pleiades Publishing, Inc.*

1. INTRODUCTION

The development of new techniques for the formation of electric contacts to solar cells is one of the key directions when solving the principal tasks of semiconductor solar photovoltaics.

In order to make solar photovoltaics competitive with present-day energy sources (fossil fuel, nuclear power, other types of renewable energy sources), the cost per peak watt (W_p) of installed power of the solar systems should be lowered by at least by half from its present-day value of \$6/W_p to below \$3/W_p, and the production volume (700 MW_p in 2003) should be raised by approximately a factor of 1000 within 30–50 years [1, 2]. Reasoning from the trend in the development of solar photovoltaics, which steadily demonstrated an annual 25–30% rise in output volume and 5–6% reduction of the W_p cost [1] in the period from 1979 to 2003, these goals seem to be attainable. Accordingly, a historic surmounting of the cost threshold is planned for the year 2013. However, what technical problems are to be resolved in order to achieve this goal?

At present, flat-panel crystalline silicon modules constitute more than 90% of the total manufacture of photovoltaic devices [2]. No alternative to silicon is anticipated in medium-range forecasts [3]. The European Photovoltaics Industrial Association is relying on the flat-panel approach and is planning, among other things [4]:

(i) to raise solar-cell efficiency from the present-day 12–16% to 20%, for which purpose, it is considered necessary, in particular, to develop high-efficiency contacts, preferentially situated on the back surface (back-contact solar cell (BCSC)), in order to reduce the cost of module assembly;

(ii) to reduce the consumption of silicon from 16 g/W_p (now) to 8 g/W_p, because the cost of Si wafers makes up about half of the module cost [5, 6]; therefore, the cell thickness must be reduced from 300 to ~120 μm.

It is necessary to note that the development of bifacial [7] and concentrator [8, 9] cells are also regarded as efficient ways to reduce the W_p cost.

Thus, the need to reduce the W_p cost determines the main lines of research in silicon photovoltaics: solar cells must have a high efficiency, be thin (flat-panel approach), and, desirably, be bifacial with back contacts or of a concentrator type (the concentrator approach is under development now).

Discussing the present-day situation concerning the efficiency of silicon solar cells, it is necessary to note that an efficiency exceeding 20% has already been reached in laboratory devices (the absolute record for silicon cells is 24.7%) [10], but the efficiency of commercially available cells is much lower (12–16%). The main factor limiting the efficiency of commercial cells is the technology of formation of the electric contacts.

Electric contacts define the photocell "face," both in a literal and metaphorical sense. At present, screen-printing (SP) technology involving the baking-in of metal-containing pastes dominates in the industry: it is used in the fabrication of 90% of silicon solar cells. However, the simple and economical SP technology has serious disadvantages, which make it inapplicable for the production of thin solar cells and restrict the efficiency of commercial cells [11]. In turn, all the record-

high values of efficiency have been obtained using the technology of evaporated contacts (ECOs) deposited in vacuum, with the pattern formed by photolithography. However, the ECO technology is not used in wide-scale production because of its high cost.

Therefore, the key long-standing problem in photovoltaics is to reduce the breach between the efficiencies of industrial and laboratory solar cells; thus, new simple and economical technologies must be developed. This problem is particularly important for technologies used in the fabrication of high-efficiency contacts, which should not include photolithographic and masking operations.

Promising designs of solar cells with an efficiency above 20% are being considered, in particular, the HIT structure (heterojunction with an intrinsic thin layer) developed by the Sanyo Electric Co. [12], the point-contact solar cell from Sun Power [13], and the OECO design (oblique evaporated contacts) developed at ISFH [14]. This report presents the results obtained for bifacial silicon solar cells with a wire contact grid and external busbars fabricated by a newly developed low-temperature LGWEB (laminated grid of wire external busbars) technology [15].

2. THE DESIGN OF LGWEB SOLAR CELL

The solar cell (Fig. 1) consists of a $[n^+p(n)p^+]$-Si structure (*1*) and two (facial and back surface) current-collecting systems. Each current-collecting system includes: (i) a transparent conducting oxide (TCO) layer deposited on the surface of a structure, which also serves as an antireflection coating; (ii) electric busbars, facial *2* and back surface *3*, located near structure *1* and a contact grid (facial *4*) produced from a copper wire coated with contact composition and fixed, using the low-temperature lamination method, simultaneously with the facial TCO layer and facial busbars (and similarly on the back surface); (iii) a lamination film (*5*) attached to the TCO surface and fixing the wire contact grid.

3. THE TECHNOLOGY OF LGWEB SOLAR CELL FABRICATION

Solar cells were produced from structures based on *n*- and *p*-type Czochralski-grown silicon (*Cz*-Si). For the *n*-Si structures, the resistivity of silicon was ρ = 4.5 Ω cm and the thickness was 390 μm; for *p*-Si, the corresponding values were 40 Ω cm and 290 μm, respectively. The $[n^+np^+]$-Si and $[n^+pp^+]$-Si structures were produced at Kvark (Krasnodar, Russia) by diffusion of phosphorus and boron from deposited P- and B-containing glass using the standard technological equipment. The used wafers were either textured on both sides or had their back surface smoothed by alkaline etching. After removal of the glass, the structures could be etched in a solution of nitric and hydrofluoric acids [16].

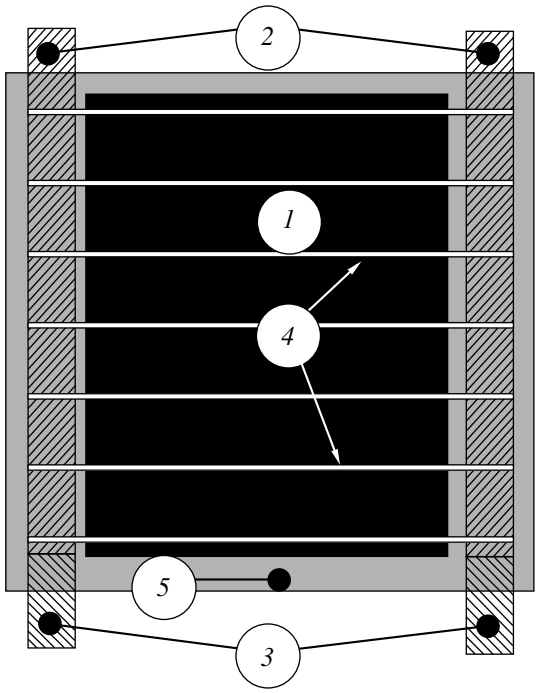

Fig. 1. Design of LGWEB solar cell (the front and back view are identical). (*1*) $[n^+p(n)p^+]$-Si structure with layers of transparent conducting oxide deposited on both sides; (*2*) frontal busbars; (*3*) back-surface busbars; (*4*) wire contact strips; and (*5*) lamination film.

The TCO layers were deposited onto the surfaces of a silicon wafer. For the p^+ layer, this was In_2O_3:Sn (indium tin oxide (ITO)) film, and for the n^+ layer, In_2O_3:F film was used [17]. The films were grown by spraying a solution at the substrate temperature of 400–500°C [18]. The deposition time was ~1 min. The films were ~75 nm thick and dark blue in color. The sheet resistivity of the ITO and In_2O_3:F films was ~50 and ~30 Ω/sq, respectively. After the deposition of the TCO, a sample of the desired area was cut out using a diamond scriber; no additional treatment of edges was performed. The contact grid, made of copper wire 70 μm in diameter and coated with a contact composition, was fixed onto the TCO with a 32-μm-thick lamination film at a temperature of 150°C.

4. THE MERITS OF THE LGWEB DESIGN

(i) The introduction of a TCO makes it possible to use a simple homogeneous (nonselective) emitter with a high sheet resistivity of 100 Ω/sq or higher in an LGWEB.

(ii) The combination of contact grid wire with a TCO in an LGWEB makes it possible to obtain extraordinarily low (3.2%) shadow loss and serial resistance loss [19]. Such losses are no higher than in solar cells with ECO metallization and about three times less than for SP metallization [20–22]. The width of the wire contact finger is only ~80 μm, and it can easily be

Table 1. Parameters of LGWEB solar cells

Parameter	Group 1: n^+–n–p^+				Group 2: n^+–p–p^+			
	#615		#739		#1044-2		#1043-1	
	front	back	front	back	front	back	front	back
Texture	+	+	+	–	+	+	+	–
R_{ini}, Ω cm^2	26		60		52		84	
R_{fin}, Ω cm^2	112		110		85		84	
I_{sc}, mA cm^{-2}	35.0	30.8	36.2	27.3	35.4	31.3	36.6	29.8
V_{oc}, mV	609	607	623	615	617	614	619	615
FF, %	76.5	77.4	78.3	78.5	75.2	76.6	76.2	78.0
Eff, %	16.3	14.5	17.7	13.2	16.4	14.7	17.3	14.3
Eff_{total}, %	30.8		30.9		31.1		31.6	
Bifaciality, %	88.9		74.6		89.6		82.7	
Area, cm^2	32.2		42		42.3		42.3	

Note: R_{ini} denotes the sheet resistivity of the emitter after diffusion; R_{fin}, the sheet resistivity of the emitter after its etching; and Eff_{total}, the total efficiency on the front and back surfaces. Bifaciality refers to the ratio of efficiencies for illumination of the back and front surfaces. Solar cell no. 615 was tested at the Sandia National Laboratories and further used as the reference sample.

reduced. In addition, the copper wire contact fingers have a low longitudinal resistance, ~40 mΩ/cm, which is more than 15 times lower than that obtained by the SP method. These properties are especially important for large-area solar cells and concentrator cells.

(iii) The LGWEB design is preferable to the BCSC variant because it is free of the principal disadvantage of the latter, that is, the production of a high-efficiency BCSC consumes expensive floating-zone *Fz*-Si. For example, calculations carried out by Sun Power have shown that, in order to obtain >20% efficiency in their Point Contact cells, silicon with a carrier lifetime >1 ms is necessary, i.e., *Fz*-Si [13]. Similarly, to obtain high efficiency in an OECO solar cell of 200–300 μm in thickness, the diffusion length must be no less than 500–800 μm [23]. For silicon of inferior quality, the efficiency of a BCSC sharply decreases, and this decrease is even stronger than for cells with contacts on both sides. Thus, the unique advantage of LGWEB solar cells is that their busbars lie clear of the cell but contact strips are present on both surfaces. As a result, not only is the module assembly simplified, even more than in the case of the BCSC version, but the requirements placed on Si quality do not become more stringent.

(iv) The contact fingers can be produced from wire of any cross-sectional shape, e.g., triangular, which is considered to be an efficient method to reduce shading [24].

(v) Wire contact fingers are compatible with virtually any shape of solar cell surface, not only smooth or textured, but also rough, undulated, or curved. This circumstance means that the LGWEB design offers extraordinary advantages over other techniques for ribbon silicon (EFG).

(vi) LGWEB solar cells are bifacial.

(vii) The low (<150°C) temperature of fabrication makes LGWEB technology applicable to solar cells based on amorphous materials, including the HIT structure.

5. PARAMETERS OF AN LGWEB SOLAR CELL

The parameters of the solar cells were determined from light current–voltage (*I*–*V*) characteristics: short-circuit current density J_{sc}, open-circuit voltage V_{oc}, filling factor FF, and efficiency Eff. For sample no. 615, the results were obtained at the Sandia National Laboratories (SNL); these data included spectral response and reflectance. For the other cells, J_{sc} was measured using a Telecom–STV pulse tester, and sample no. 615 was used for current calibration. It was found that, with an adequate current calibration, the Telecom–STV tester provides a correct measurement of J_{sc} with less than ±2% error, but V_{oc}, and especially FF, are underestimated, which is related to the nature of pulse measurements. The extent of underestimation increases as the effective lifetime of minority carriers in the base increases. Therefore, V_{oc}, FF, and Eff were determined from steady-state light *I*–*V* characteristics under illumination with a 1000 W halogen incandescent lamp on a thermostated table, in which case the temperature of the solar cell reached (25 ± 0.1)°C. In these measurements, the short-circuit current of each solar cell was set according to the value measured with the Telecom–STV tester.

The parameters of the LGWEB solar cells made of *n*-Si (group 1) and *p*-Si (group 2), for both a textured and a smooth back surface, are listed in Table 1. As can be seen from Table 1, the LGWEB technology makes it

Table 2. Parameters of LGWEB solar cells and cells produced at ISFH using different contact deposition techniques

Type of solar cell		Si (type)	Area, cm^2	ρ(Si), Ω cm	Eff, % (front)	Eff, % (back)
OECO [14, 23]	Monofacial	*Fz*(*p*)	4	0.5	21.1	–
				1.5	20.4	
			100	0.5	20.0	–
		Cz(*p*)	4	1.3	18.3	–
			100	1.3	17.9	–
	Bifacial	*Fz*(*p*)	4	0.5	19.0	17.0
	Bifacial BCSC				18.1	17.4
					19.2	16.0
ECO (front and back), bifacial [7]		*Fz*(*p*)	4	0.5	20.1	17.2
ECO (front)/SP(back), bifacial [25]		*Fz*(*p*)	4	1.5	17.4	13.4
SP (front and back), bifacial [26]		*Fz*(*p*)	2.6	1.5	14.5	12.7
		Cz(*p*)	4	6.0	13.4	11.5
LGWEB		*Cz*(*p*)	42	40	16.4	14.7*
					17.3	14.3**
		Cz(*n*)	32	4.5	16.3	14.5*
			42		17.7	13.2**

Notes: * Indicates that the front and back surfaces are textured and ** indicates that only front is surface textured.

possible to fabricate bifacial solar cells from *Cz*-Si with a facial and back surface efficiency over 17% and 14%, respectively.

6. COMPARISON OF LGWEB AND OECO SOLAR CELLS

To assess the quality of the obtained results, we compare them with data obtained by R. Hezel, a pioneer and leader in photovoltaics, at ISFH (Germany) using other contact deposition techniques and, in particular, the new high-efficiency OECO technology. The unique specific feature of OECO technology is that, for the first time, high-efficiency MTIS (metal–(tunnel insulator)-semiconductor) contacts were deposited onto a solar cell without photolithography and masking. Table 2 offers a comparison of the parameters of solar cells produced at ISFH by different metallization techniques (OECO, ECO, and SP) and using the LGWEB design developed by our team.

The choice in favor of the ISFH team for the comparison is due exclusively to the wide diversity and record-high level of their results, which make it possible to reveal the influence exerted on solar cell efficiency by such important factors as silicon (*Cz*-Si or *Fz*-Si) quality, silicon resistivity ρ, size of a solar cell, contact deposition technique (ECO or SP), and cell design (monofacial, bifacial, or with all contacts on the back surface (BCSC)).

Analysis of the data in Table 2 shows that the record efficiency for OECO technology (21.1%) was obtained for a monofacial solar cell of 4 cm^2 in area made from *p*-*Fz*-Si with ρ = 0.5 Ω cm. However, the efficiency of OECO cells decreases on passing (i) from *Fz*-Si to *Cz*-Si by 2.1–2.8%, (ii) from monofacial to bifacial design by ~2.1%, (iii) from monofacial to bifacial design with back surface contacts by 1.9–3%, and (iv) from the size of 4 cm^2 to 100 cm^2 by 0.4–1%.

A correct comparison of OECO and LGWEB cells demands data for solar cells with comparable parameters, which are, regretfully, absent. However, the efficiency of a bifacial OECO cell made of *Cz*-Si, with back surface contacts of 4 cm^2 in area, can be estimated as 15.3–16.4% on the front side and 13.2–14.6% on the back surface, which is no higher than the efficiency of an LGWEB solar cell (~1% less on the front side).

7. LGWEB SOLAR CELL AS COMPARED WITH A CELL WITH SCREEN PRINTING METALLIZATION

The data listed in Table 2 can also be used for tracing how the efficiency of a bifacial solar cell based on *Fz*-Si decreases when ECO contacts are replaced by SP ones. For example, when ECO metallization is used on both sides, the front–back efficiencies are fairly high: 20.1 and 17.2%, respectively. When ECO contacts are replaced by SP ones only on the back surface,

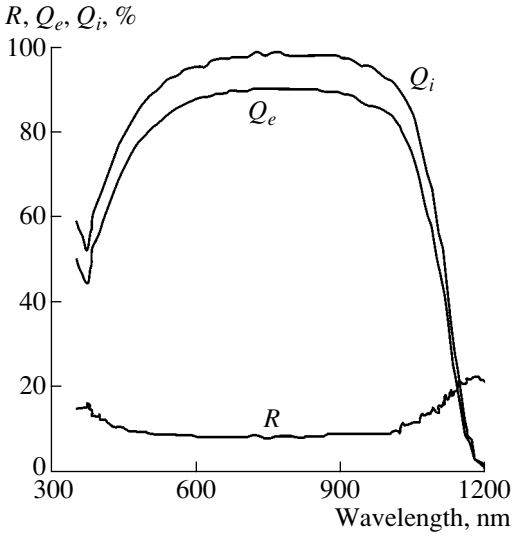

Fig. 2. The reflectance R and internal Q_i and external Q_e quantum yield of charge separation for solar cell no. 615.

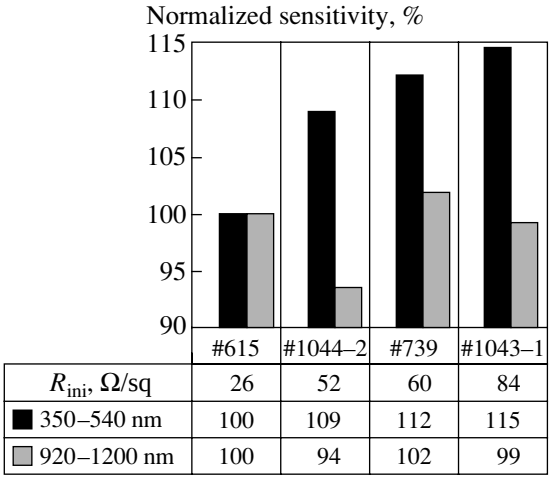

	#615	#1044–2	#739	#1043–1
R_{ini}, Ω/sq	26	52	60	84
■ 350–540 nm	100	109	112	115
■ 920–1200 nm	100	94	102	99

Fig. 3. Comparison of spectral sensitivities of LGWEB solar cells in the blue-green (350–540 nm) and IR (920–1200 nm) spectral ranges under frontal illumination normalized to the sensitivity of solar cell no. 615.

the efficiency falls to 17.4 and 13.4%, and, for a cell with SP contacts on both sides, the efficiency falls to the exceedingly low values of 14.5 and 12.7%. This example clearly demonstrates the drawbacks of SP technology.

8. PROSPECTS FOR RAISING THE EFFICIENCY OF LGWEB SOLAR CELLS

The efficiency of LGWEB solar cells can be raised by more than 4.5% and, correspondingly, exceed 21% by applying the measures considered below.

Reflection. First of all, we stress that our LGWEB solar cell is already laminated, which means that its measured efficiency approaches that in a module. Currently, we use a lamination film with high refractive index ($n \approx 1.56$) which leads to high reflection (~4.8%). Figure 2 shows the reflectance R and external Q_e and internal Q_i quantum yield for solar cell no. 615. It can be seen that, in the range 450–1000 nm, $R \approx 8$–9%, of which ~4.8% and 3.2% are accounted for by the lamination film and wire grid, respectively. Therefore, the efficiency can be raised by ~0.5% by reducing n to 1.3.

Base resistivity. The optimization of the base resistivity ρ offers a significant reserve for increasing LGWEB solar cell efficiency. It is necessary to note that, in the record cells, the base material is usually heavily doped, to $\sim 3 \times 10^{16}$ cm^{-3} ($\rho \approx 0.5$ Ω cm), which improves the efficiency by diminishing the bulk recombination current, series resistance, and negative effect of a high injection level. The influence of ρ in the range ρ = 0.08–1.4 Ω cm on the efficiency of OECO solar cells was studied in detail in [23]. It was shown that, as ρ increases from the optimal value of 0.4 to 1.4 Ω cm, the efficiency decreases from 21.1 to 20.4%, i.e. by 0.7%. At the same time, our LGWEB solar cells are produced from silicon with a nonoptimal doping level, which is 30–100 times lower than that conventionally used in high-efficiency solar cells. Therefore, we believe that optimization of ρ will raise the efficiency of LGWEB cells by more than 1%.

Diffusion layers. The diffusion layers in LGWEB solar cells are not yet optimized. The short-wavelength sensitivity of solar cell no. 615 is low [20], and we attribute this fact to the heavy initial doping of the emitter (26 Ω/sq). It was found, however, that the short-wavelength sensitivity increases as the initial (i.e., immediately after the diffusion) sheet resistivity R_{ini} of the emitter increases (Fig. 3). Moreover, increasing R_{ini} not only makes the short-wavelength sensitivity higher but also improves the other parameters of solar cells (Table 1). It is noteworthy that the long-wavelength sensitivity of the samples with a smooth back surface is higher than that for samples with a textured back surface, which, evidently, is related to enhanced reflection of long-wavelength light from the smooth surface. In addition, the long-wavelength sensitivity of the solar cells based on *n*-Si is, in general, higher than for *p*-Si cells, possibly because their thickness is 100 μm larger.

The edges. The edges of the LGWEB solar cells were not specially treated, so they are a source of losses. The experimental data presented in Fig. 4 show that increasing the area of LGWEB cells results in an increase in their efficiency. This result contrasts strongly with the case of OECO cells, where the opposite effect was observed. Therefore, resolution of the edge problem will allow the efficiency to be increased by ~0.5%.

The quality of silicon. As can be seen from Table 2, the use of high-quality *Fz*-Si can enhance the efficiency of LGWEB solar cells by ~2.5%.

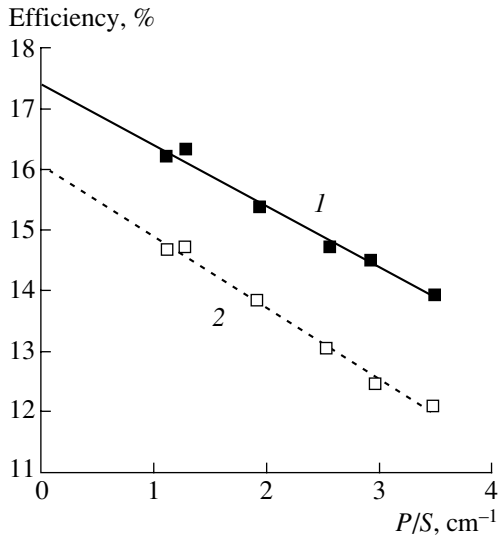

Fig. 4. Efficiency of an LGWEB solar cell vs the ratio between its perimeter and area, *P*/*S*. Curve *1* shows frontal illumination and curve *2*, back surface illumination.

9. CONCLUSION

Thus, solar cells with a new design and technology for the fabrication of the current collecting system, LGWEB, demonstrate record-high efficiency for their class of solar cells (bifacial, back-contact, and *Cz*-Si). The analysis shows that a wide field of action is open for the optimization of LGWEB solar cells and improvement of their efficiency, which can potentially exceed 21%.

ACKNOWLEDGMENTS

The study was supported by the Russian Foundation for Basic Research (project no. 04-02-16691). We are grateful to B.L. Eidel'man and A.F. Yaremchuk for their participation in productive discussions and assistance with measurements.

REFERENCES

1. R. M. Swanson, in *Proceedings of 19th European Photovoltaic Solar Energy Conference* (Paris, 2004), 2CV.2.63.
2. H. A. Aulich and F.-W. Schulze, in *Proceedings of 17th European Photovoltaic Solar Energy Conference* (Munich, Germany, 2001), p. 65.
3. A. Goetzberger, in *Proceedings of 17th European Photovoltaic Solar Energy Conference* (Munich, Germany, 2001), p. 9.
4. G. P. Willeke, in *Proceedings of 19th European Photovoltaic Solar Energy Conference* (Paris, 2004), 2CP.1.1.
5. R. Einhaus, D. Sarti, S. Pleier, *et al.*, in *Proceedings of 16th European Photovoltaic Solar Energy Conference* (Glasgow, UK, 2000), O.D5.5.
6. J. F. Nijs, J. Szlufcik, J. Poortmans, and S. Mertens, in *Proceedings of 16th European Photovoltaic Solar Energy Conference* (Glasgow, UK, 2000), P.D2.1.
7. A. Hubner, A. G. Aberle, and R. Hezel, in *Proceedings of 14th European Photovoltaic Solar Energy Conference* (Montreux, Switzerland, 1992), p. 92.
8. R. Swanson, Prog. Photovoltaics **8**, 93 (2000).
9. Zh. I. Alferov, V. M. Andreev, and V. D. Rumyantsev, Fiz. Tekh. Poluprovodn. (St. Petersburg) **38**, 937 (2004) [Semiconductors **38**, 899 (2004)].
10. J. Zhao, A. Wang, and M. A. Green, Prog. Photovoltaics **7**, 411 (1999).
11. M. A. Green, in *Proceedings of 16th European Photovoltaic Solar Energy Conference* (Glasgow, UK, 2000), OB3.1.
12. H. Sakata, in *Proceedings of 3rd World Conference on Photovoltaic Solar Energy Conversion* (Osaka, Japan, 2003), 4O-D10-01.
13. K. R. McIntosh, M. J. Cudzinovic, D. D. Smith, *et al.*, in *Proceedings of 3rd World Conference on Photovoltaic Solar Energy Conversion* (Osaka, Japan, 2003), 4O-D10-05.
14. R. Hezel, R. Meyer, and J. W. Mueller, in *Proceedings of 19th European Photovoltaic Solar Energy Conference* (Paris, 2004), 2CV.2.40.
15. G. Untila, A. Osipov, T. Kost, *et al.*, in *Proceedings of 16th European Photovoltaic Solar Energy Conference* (Glasgow, UK, 2000), p. 1468.
16. G. Untila, A. Osipov, T. Kost, *et al.*, in *Proceedings of 17th European Photovoltaic Solar Energy Conference* (Munich, Germany, 2001), p. 1796.
17. G. Untila, A. Osipov, T. Kost, *et al.*, in *Proceedings of 17th European Photovoltaic Solar Energy Conference* (Munich, Germany, 2001), p. 1793.
18. G. Untila and A. Osipov, in *Proceedings of 2nd World Conference on Photovoltaic Solar Energy Conversion* (Vienna, 1998), p. 1555.
19. G. Untila, A. Osipov, T. Kost, and A. Chebotareva, in *Proceedings of 17th European Photovoltaic Solar Energy Conference* (Munich, Germany, 2001), p. 265.
20. K. A. Munzer, K. T. Holdermann, R. F. Schlosser, and S. Sterk, in *Proceedings of 16th European Photovoltaic Solar Energy Conference* (Glasgow, UK, 2000), O.B7-2.
21. F. Recart, G. Bueno, J. C. Jimeno, *et al.*, in *Proceedings of 16th European Photovoltaic Solar Energy Conference* (Glasgow, UK, 2000), VA1.50.
22. F. Recart, R. Gutierrez, V. Rodriguez, *et al.*, in *Proceedings of 16th European Photovoltaic Solar Energy Conference* (Glasgow, UK, 2000), p. 1654.
23. R. Hezel and W. Hoffman, in *Proceedings of 3rd World Conference on Photovoltaic Solar Energy Conversion* (Osaka, Japan, 2003), 4P-C4-20.
24. A. W. Blackers, in *Proceedings of 16th European Photovoltaic Solar Energy Conference* (Glasgow, UK, 2000), OB2.2.
25. B. Lenkeit, S. Steckmetz, F. Artuzo, and R. Hezel, Sol. Energy Mater. Sol. Cells **65**, 317 (2001).
26. B. Lenkeit, S. Steckmetz, A. Mucklich, *et al.*, in *Proceedings of 16th European Photovoltaic Solar Energy Conference* (Glasgow, UK, 2000), VA1. 31.

Translated by D. Mashovets

Semiconductors, Vol. 39, No. 11, 2005, pp. 1352–1355. From Fizika i Tekhnika Poluprovodnikov, Vol. 39, No. 11, 2005, pp. 1399–1402.

PHYSICS OF SEMICONDUCTOR DEVICES

Some Aspects of the RHEED Behavior of Low-Temperature GaAs Growth[1]

Á. Nemcsics

Hungarian Academy of Sciences, Research Institute for Technical Physics and Materials Science, P.O. Box 49, H-1525 Budapest, Hungary

Budapest College of Engineering, Institute of Microelectronics and Technology, H-1084 Budapest, Hungary

e-mail: nemcsics@mfa.kfki.hu

Submitted March 3, 2005; accepted for publication March 22, 2005

Abstract—The reflection high-energy electron diffraction (RHEED) behavior manifested during MBE growth on a GaAs(001) surface under low-temperature (LT) growth conditions is examined in this study. RHEED and its intensity oscillations during LT GaAs growth exhibit some particular behavior. The intensity, phase, and decay of the oscillations depend on the beam equivalent pressure (BEP) ratio and substrate temperature, etc. Here, the intensity dependence of RHEED behavior on the BEP ratio, substrate temperature, and excess of As content in the layer are examined. The change in the decay constant of the RHEED oscillations is also discussed. © *2005 Pleiades Publishing, Inc.*

1. INTRODUCTION AND EXPERIMENTAL PRELIMINARIES

Recently, molecular-beam-epitaxial (MBE) growth of GaAs at a low temperature (LT), specifically, around 200°C, has become increasingly important in semiconductor research and technology [1]. LT GaAs growth has become an increasingly important method, since it provides highly insulating films and contributes to the synthesis of magnetic semiconductors. It has been shown that growth at this LT leads to incorporation of excess As in the crystal. The high concentration of excess As in LT GaAs results in a number of novel properties. As-grown and annealed LT GaAs layers exhibit extremely high electrical resistivity and very short lifetimes of photoexcited carriers [2]. Their electrical parameters can be analyzed using a combined band and hopping conduction model [3]. Depending on the growth parameters, these layers may contain up to a 1.5% excess of As [4, 5]. The majority of excess As is in the antisite position, while the remaining atoms are interstitial As or Ga vacancies [6]. The uniqueness of LT GaAs is its high density of midgap states, which are a result of excess As, while the structure of matrix remains perfect [7].

Recently, the use of reflection high-energy electron diffraction (RHEED) to control the growth of LT GaAs has been reported [8–10]. The authors observed RHEED oscillations of the specular spot intensity with a period corresponding to one monolayer of deposition, as is observed during the traditional high-temperature growth process. It is not an unsophisticated event to observe oscillations of RHEED intensity during LT growth. RHEED oscillations are very strongly influenced by the growth parameters, such as deposition temperature, the ratio of beam equivalent pressure (BEP), etc. RHEED oscillations have been found to be fundamental in two regions of the BEP ratio at LTs. One of these regions is near and another is far from unity of the BEP ratio. The strongest oscillations were observed when the BEP ratio was nearly one [8, 9]. Oscillations were also found in the region of 40–100 of the BEP ratio [10].

RHEED and its intensity oscillations during LT GaAs growth exhibit some particular behaviors. In addition, the intensity, phase, and decay of oscillations depend on the BEP ratio, excess As content, and substrate temperature. Here, we investigate the behavior of oscillation decay during the growth of LT GaAs. The investigated deposition temperature and the range of the BEP ratio are 200°C and 0.9–1.3, respectively. This investigation is based on measurements and observed intensity oscillations of RHEED, which are described in [8, 9].

2. RESULTS AND DISCUSSION

Temporal evaluations of RHEED specular intensity during LT GaAs growth, where the BEP ratio is close to unity, are shown in [8] (Fig. 1) and [9] (Fig. 2). It can be seen that, when the BEP ratio moves away from unity, the decay of oscillations becomes stronger. If the ratio is 1.3, then the oscillation intensity is very small, so its evaluation is difficult. The decay of the oscillations was determined as described in [11]. The amplitude decay of the oscillations was investigated peak to peak. The intensity of the oscillation minima is changed. The peak-to-peak series are determined by the

[1]The text was submitted by the author in English.

1063-7826/05/3911-1352$26.00 © 2005 Pleiades Publishing, Inc.

subtraction of the background of the oscillations, which, in turn, is determined by the line of minima of the oscillations. After the subtraction, an exponential function is fitted to determine the decay in intensity with the aid of least-squares method. The exponential approach is performed according to the first part of Eq. (1), where τ_d is a decay time constant. The determined decay constants vs. the BEP ratio are shown in Fig. 1.

It is known that the strain in a grown layer influences the observed RHEED oscillations. If the strain is larger in the grown structure, then the oscillations become faster. If the strain is smaller or absent, then the RHEED intensity oscillates for longer. This effect is demonstrated and described for the case of InGaAs/GaAs heterostructures in [11, 12].

We can observe very strong changes in the oscillation decay depending on the BEP ratio at 20°C (see Fig. 1). Depending on the growth parameters, these LT GaAs layers may contain many excess As atoms. The majority of excess As is in the antisite position. The lattice spacing ($\Delta d/d$) of LT GaAs becomes greater than that of the stoichiometric crystal. The lattice spacing of nonstoichiometric LT GaAs was determined in [7]. The functions of lattice spacing vs. the BEP ratio are also shown in Fig. 1.

We can observe (see Fig. 1) that the decay time constant of oscillations τ_d decreases rapidly during LT GaAs growth as the BEP ratio increases, that is, as the excess As content also increases. The decay of oscillations is due to several factors. The excess As gives rise to a lattice mismatch, and, therefore, also to strain in a grown layer. This strain can influence the decay of intensity oscillations. First, we investigate this effect, as the influence of strain is known and the influence of the growth phenomenon is unknown. The mismatch dependence of the oscillation decay can be determined from the given parameters (see Fig. 1). The variation in decay time constant vs. lattice spacing is shown in Fig. 2. It is clear that not only the mismatch alone is responsible for the decay but also the other growth conditions. Changes in the excess As modify not only the mismatch but also the growth conditions, e.g., growth rate, [13]. Therefore, both the mismatch and the growth parameters influence the behavior of the oscillation decay. We approximate this decay with an exponential function. Furthermore, we assume that the two effects, i.e., the mismatch and the growth influence, can be separated from each other. In this way, the decay phenomenon can be described by two time constants:

$$I(t) = B_0 \exp\left(\frac{-t}{\tau_d}\right) = B_0 \exp\left(\frac{-t}{\tau_G} + \frac{-t}{\tau_M}\right) = B \exp\left(\frac{-t}{\tau_M}\right). \quad (1)$$

Here, τ_G and τ_M are the assumed time constants of the separated influences, i.e., growth and mismatch, respectively, and B and B_0 are the scaling factors, which depend on the excess As and, also, on $\Delta d/d$. The decay originating from the mismatch can be expressed as follows:

$$\frac{1}{\tau_M(\Delta d/d)} = \frac{1}{\tau_d(\Delta d/d)} - \ln\left(\frac{B_0}{B(\Delta d/d)}\right)\frac{1}{t} = \frac{1}{\tau_d(\Delta d/d)} - e(\Delta d/d). \quad (2)$$

Here, the factors are functions of Δ/d and, also, of the BEP ratio. In the case of stoichiometric LT GaAs growth ($\Delta/d = 0$), there is no decay from mismatch. This circumstance means that, for $\Delta/d = 0$, the reciprocal value of the decay time constant originates fully from

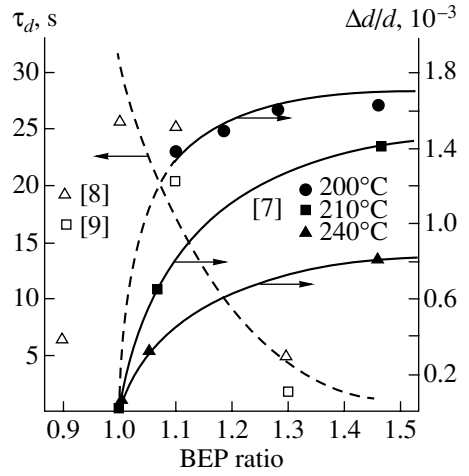

Fig. 1. The decay constant vs. the BEP ratio at 200°C (left) and lattice spacing vs. the BEP ratio at 200, 210, and 240°C (right). The lines are meant to serve as guide to the eye only.

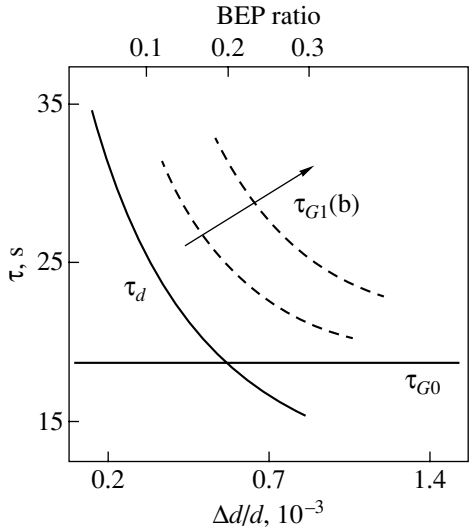

Fig. 2. The decay time constant vs. the lattice spacing derived from Fig. 1.

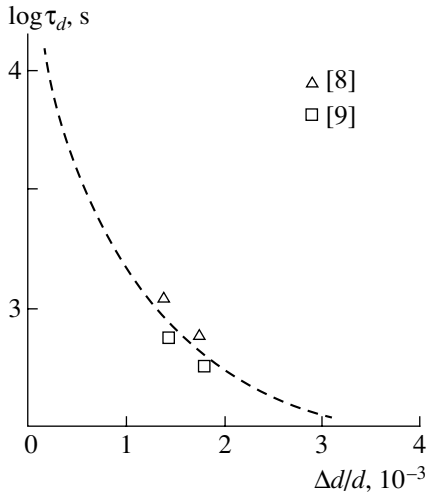

Fig. 3. The function of τ_M vs. $\Delta d/d$, which is derived from high-temperature InGaAs growth. The calculated data originate from LT GaAs growth.

the crystal growth phenomenon ($\tau_d(0) = \tau_G(0) = \tau_{G0}$); that is, the value of $1/\tau_M(0)$ is zero. The value of τ_{G0} remains constant. The other part of τ_G, τ_{G1}, depends on BEP ratio (or Δ/d). The entire $\tau_G = \tau_{G1}(\text{BEP}) + \tau_{G0}$. Therefore, the second term in the $1/\tau_M(\Delta d/d)$ expression $e(\Delta d/d)$ also has an independent and dependent part on the BEP ratio (or Δ/d). The equivalence between the BEP ratio and Δ/d can occur only in the case of a narrow range of growth parameters, where these ratios are proportional with each other.

We have separated the supposed strain effect from the growth phenomenon, which can be responsible for the decay of the oscillations. In the case of InGaAs growth, we have assumed that the influence of the growth remains constant in the low In content region, since one of the most important growth parameters, the deposition temperature, remained the same during the experiment. Under this supposition, we obtained good correspondence between the theoretical critical layer thickness and the threshold thickness, which is derived from the τ_M decay constant [12]. In the case of InGaAs, In replaces Ga in the lattice. Both elements establish similarly strong sp^3-type bonding in the lattice because of their similar valence structure. The situation in the case of LT GaAs is quite different. The excess As that replaces Ga in the lattice has different and weaker bonding than an sp^3 hybrid, because its valence structure is different. This property locally modifies the probability of chemisorption of As atoms and, therefore, the probability of the incorporation of further excess As atoms in the crystal as well [14]. The concentration of excess As can be determined from the rate of chemisorbed As atoms. As atoms that are chemisorbed on an arsenic-terminated GaAs(001) surface serve as precursors of excess As, and, hence, the concentration of excess As depends directly on the steady-state coverage of the chemisorbed As atoms [7]. The excess As perturbs the bonding behavior in the crystal, that is, the energy distribution along the surface. We formulate a simple description for the change in the unperturbed surface layer by layer. At the first step, the unperturbed area A^* can be written as follows: $A_1^* = Ab - Aa$, where A is the whole area of the investigated surface. The factors b and a, which are less than one, give the parts of surface that can be covered by chemisorbed As and that can be incorporated by excess As, respectively. The second step can be described as follows: $A_2^* = (Ab - Aa)b - Aa$. We can obtain the nth layer by following up the former given algorithm. The size of the perturbed area also depends on the number of grown layers. This dependence can be negligible if the number of layers is not large [14]. Among the possible surface reconstructions of a GaAs(001) surface, the $c(4 \times 4)$ reconstruction occurs at low temperatures under high As fluxes [15, 16]. The value of b can be estimated because the maximum coverage of chemisorbed As atoms may be 0.75 monolayers, as in the case of this reconstruction. The value of a can be estimated by the maximum excess As content, which is 0.015 [7]. It can be seen that the factor b is larger than a; therefore, we can obtain, after arranging the expression A^* and disregarding small terms, the following simple power function for the nth step: $A_n^* = Ab^n$. We assume that the intensity of the RHEED is proportional to the size of the unperturbed surface. A continuous description by replacing n with rt yields $I(t) = cA^*(t) = cb^{rt}A$, where r is the growth rate, t is the growth time, and c is a constant characterizing the diffraction power. This description can be written in the following form: $I(t) = cA\exp(-t/\tau_{G1})$. Here, τ_{G1} is the decay time constant originating from the growth phenomena, which depends on the BEP ratio: $\tau_{G1} = -1/r\ln b$. The τ_{G0} and τ_{G1} dependences on b are shown in Fig. 2.

To justify our discussion, we can compare τ_M extracted from the oscillation decay occurring during LT GaAs growth and the material-independent decay constant, which originates from the mismatch. The variation of $\tau_M(\Delta d/d)$ should be determined as follows: $1/\tau_M \propto 1/\tau_d - 1/\tau_{G0} - 1/\tau_{G1}$, similarly to the method described in [12]. The strain-dependent time constant vs. the composition in the case of InGaAs is given in [12]. The composition-independent variation of τ_M vs. Δ/d can be derived from the above-mentioned dependence with the aid of a modified form of Vegard's law [17, 18]. The material-independent variation is shown in Fig. 3, along with the calculated τ_M data from LT GaAs. The fitting parameter of b was determined with the use of the least-squares method [14]. The unity of the BEP ratio serves as a reference point for the calculation of τ_M. In this calculation, we also took into con-

sideration a BEP ratio of 1.3. τ_M as determined from LT growth corresponds to the calculated dependence, but it should be noted that the ratio of 1.3 is very difficult to evaluate. We can establish that separation of the influences of growth and mismatch on the decay of the RHEED oscillations can describe LT growth only in a narrow range. The intensity oscillation at the BEP ratio of 1.3 is very difficult to evaluate because of the very small intensity. This drastic intensity damage can result not only from the mismatch in conjunction with the reduction of the unperturbed area but also from a change in the sticking coefficient of the deposited material.

3. CONCLUSIONS

LT GaAs growth is very complicated process. The observed decay and absence of RHEED intensity oscillations can originate from several effects, e.g., change in the sticking coefficients, change in the unperturbed area, and change in strain. Here, it was found that separation of the influence of growth and strain on the RHEED oscillation decay in the case of LT GaAs is possible in a narrow region of the BEP ratio.

ACKNOWLEDGMENTS

The author is indebted to T. Wosiński for his careful reading of the manuscript. This study was supported by the (Hungarian) National Scientific Research Fund (OTKA) (grant nos. T030426 and T037509).

REFERENCES

1. M. Missous, Mater. Sci. Eng. B **44**, 304 (1997).
2. P. Kordos, A. Foster, J. Betko, *et al.*, Appl. Phys. Lett. **67**, 983 (1995).
3. J. Betko, M. Morvic, J. Novac, *et al.*, J. Appl. Phys. **86**, 6243 (1999).
4. D. C. Look, Thin Solid Films **231**, 61 (1993).
5. G. J. Witt, Mater. Sci. Eng. B **22**, 9 (1993).
6. X. Liu, A. Prasad, J. Nishino, *et al.*, Appl. Phys. Lett. **67**, 279 (1995).
7. A. Shuda and N. Otsuka, Surf. Sci. **458**, 162 (2000).
8. R. P. Mirin, J. P. Ibbetson, U. K. Mishra, and A. Gossard, Appl. Phys. Lett. **65**, 2335 (1994).
9. M. Missous, J. Appl. Phys. **78**, 4467 (1995).
10. A. Shen, H. Ohno, Y. Horikoshi, *et al.*, Appl. Phys. Surf. Sci. **130–132**, 382 (1998).
11. A. Nemcsics, Phys. Status Solidi A **155**, 427 (1996).
12. A. Nemcsics, Thin Solid Films **367**, 302 (2000).
13. A. Nagashima, M. Tazima, A. Nishimura, *et al.*, Surf. Sci. **514**, 350 (2002).
14. A. Nemcsics, in *Quantum Dots: Fundamentals, Applications and Frontiers*, Ed. by B. A. Joyce, P. C. Kelires, A. G. Naumovets, and D. D. Vvedensky (Kluwer, Dordrecht, 2005), p. 221.
15. P. K. Larsen, J. H. Neave, J. F. van der Veen, *et al.*, Phys. Rev. B **27**, 4966 (1983).
16. V. V. Preobrazhenskii, M. A. Putyato, O. P. Pchelyakov, and B. R. Semyagin, J. Cryst. Growth **201–202**, 166 (1999).
17. A. Adachi, J. Appl. Phys. **53**, 8775 (1982).
18. E. Villaggi, C. Bocchi, N. Armani, *et al.*, Jpn. J. Appl. Phys. **41**, 1000 (2002).

Semiconductors, Vol. 39, No. 11, 2005, pp. 1356–1360. Translated from Fizika i Tekhnika Poluprovodnikov, Vol. 39, No. 11, 2005, pp. 1403–1407.

PHYSICS OF SEMICONDUCTOR DEVICES

Enhancement of Spontaneous Erbium Emission near the Photonic Band Edge of Distributed Bragg Reflectors Based on *a*-Si:H/*a*-SiO$_x$:H

A. V. Medvedev^, N. A. Feoktistov, A. B. Pevtsov, and V. G. Golubev

Ioffe Physicotechnical Institute, Russian Academy of Sciences, St. Petersburg, 194021 Russia

^e-mail: Medvedev@gvg.ioffe.ru

Submitted March 24, 2005; accepted for publication April 8, 2005

Abstract—Results obtained in an experimental study of spontaneous emission from erbium ions in a spectral range corresponding to the lower photonic band edge of distributed Bragg reflectors (1D photonic crystals) are presented. The photonic crystals were constituted of alternating quarter-wave *a*-Si:H and *a*-SiO$_x$:H layers grown by PECVD. Erbium was introduced into the *a*-Si:H layers by magnetron sputtering of an erbium target in the course of structure growth. The change observed in the intensity of spontaneous emission is due to the nonmonotonic behavior of the density of optical modes near the photonic band edge. © *2005 Pleiades Publishing, Inc.*

Characteristics of spontaneous emission depend both on the intrinsic properties of an emitting center and on the properties of the ambient medium. Under a weak interaction of an atom with an electromagnetic field, the probability of a spontaneous radiative transition (W_r) is proportional, according to the Fermi golden rule, to the density $\rho(\omega)$ of photonic states in the vicinity of the transition [1]. Thus, modification of the density of modes, compared with the mode distribution in free space, makes it possible to vary W_r and, accordingly, the intensity of spontaneous emission [2]. The most suitable objects for implementing the idea put forward in [2] are photonic crystals (PhCs), which are structures with a periodic spatial modulation of the dielectric constant with a period comparable with the wavelength of light. This periodicity gives rise, by analogy with the electronic band structure of atomic crystals, to a photonic band structure. The existence of photonic bands makes it possible to control the interaction of an emitting center placed within a PhC with an electromagnetic field and, thereby, to suppress or enhance the emission [3, 4]. The possibility of a profound modification of the emission from PhCs indicates prospects for the application of these materials, e.g., in modern information transmission systems [5] and high-efficiency thermophotovoltaic converters [6]. The most interesting objects for studying the influence exerted by PhC properties on the characteristics of spontaneous emission are 3D structures [7–9]. It is in a PhC of this kind that the complete photonic band gap can be obtained and propagation of light in all directions can be prohibited in a certain spectral range. At the same time, it should be noted that specific features of the interaction between radiative centers and the periodic structure of a PhC can also be studied, both experimentally and theoretically, by investigating one-dimensional PhCs [10]. In the case of 1D PhCs, the fabrication technology is considerably simpler and more controllable than in the 3D case.

A change in the emission intensity from a 1D PhC (distributed Bragg reflectors (DBRs)) near the photonic band edge has previously been observed in periodic AlAs/AlGaAs structures with a GaAs emitting layer [11], in liquid-crystal Bragg structures [12], and in Bragg structures based on amorphous nitrides and silicon oxide [13–15]. The present communication reports the experimental results obtained in a study of the modification of spontaneous emission from erbium ions by the nonmonotonic behavior of the density of photon modes at the lower photonic band edge in 1D photonic crystals in the form of DBRs consisting of alternating *a*-Si:H/*a*-SiO$_x$:H layers. The choice of object for study was governed by the following considerations, which are important for technical applications. First, the fabrication technology of *a*-Si:H and *a*-SiO$_x$:H films is comparatively simple, compatible with the standard silicon technology, and widely used in industry for the manufacture of thin-film transistors and solar cells. Second, the radiative transition of an erbium ion from the first excited state to the ground state lies in the 1.5-μm spectral range, coinciding with the transparency window in fiber-optic communication lines [16].

Samples of 1D photonic crystals (Fig. 1a) were grown by RF glow-discharge decomposition of an argon–silane mixture by a technique similar to that described in [17–19]. Erbium ions were chosen as the sources of spontaneous emission and introduced, in contrast to [17–19], by magnetron sputtering of an erbium target into *a*-Si:H layers in the course of growth of a Bragg structure. The target was placed in a technological reactor outside the zone of the RF glow dis-

1063-7826/05/3911-1356$26.00 © 2005 Pleiades Publishing, Inc.

charge and had no effect on the electric field distribution in the discharge gap. The technique developed made it possible to dope any *a*-Si:H layer with erbium in the course of its growth. The central *a*-Si:H layers were doped in the samples (see Fig. 1a), which made it possible to increase the number of emitting centers in the photonic crystal and, thereby, to raise the intensity of the photoluminescence (PL) signal.

The DBR parameters were chosen so that the lower photonic band edge was in the spectral range of the radiative optical transition of an erbium ion from the first excited state to the ground state (λ_{Er} = 1535 nm). For this purpose, the optical thicknesses of separate layers of the structure were preliminarily calculated using ellipsometrically measured refractive indices of *a*-SiO_x:H (n_a = 1.46) and *a*-Si:H (n_b = 3.44) reference films.

In the course of growth of a Bragg structure, the optical thicknesses of the constituent layers were monitored in situ by the interference pattern that appeared in the recording of the signal reflected from the surface of a growing film. It should be noted that, in the course of successive deposition of DBR layers, the reflectance in the spectral range corresponding to the formation of the photonic band gap rapidly approaches 100% and changes only slightly after deposition of the subsequent layers. Therefore, to improve the accuracy of measurement of the optical thicknesses, the signal was recorded in a spectral range in which the reflectance varied widely, outside the photonic band gap.

The growth of the structure was commenced with the *a*-Si:H layer. At the initial instant of time, the reflectance was determined solely by the substrate (glass) and had its smallest value. As the thickness d of the *a*-Si:H film increased, the intensity of reflected light became higher, reached a maximum at $d = \lambda/4n_b$, and then decreased. As the reflection signal passed through a minimum, the gas flows were switched and an *a*-SiO_x:H film with a refractive index n_b started to grow. Then, the deposition cycle was repeated. The resulting DBR samples comprised 13 alternating quarter-wave *a*-Si:H and *a*-SiO_x:H layers. The optical thicknesses of the structures were varied in the course of growth in a prescribed way, which made it possible to shift the edge of the photonic band in a DBR with respect to λ_{Er} both to shorter and to longer wavelengths. The total thickness of the structure (without the substrate) was 1.7 μm.

The PL from the erbium ions was excited by a Kr laser (λ = 647.1 nm). The transmission and PL spectra were recorded in the direction coinciding with the normal to the surface of a Bragg structure using an automated grating monochromator and a lock-in amplifier. An InGaAs photodiode served as a photodetector. All the measurements were made at room temperature.

The experimental transmission spectrum of one of the structures obtained is shown in Fig. 1b. A wide region of low transmission (850–1550 nm) can be seen,

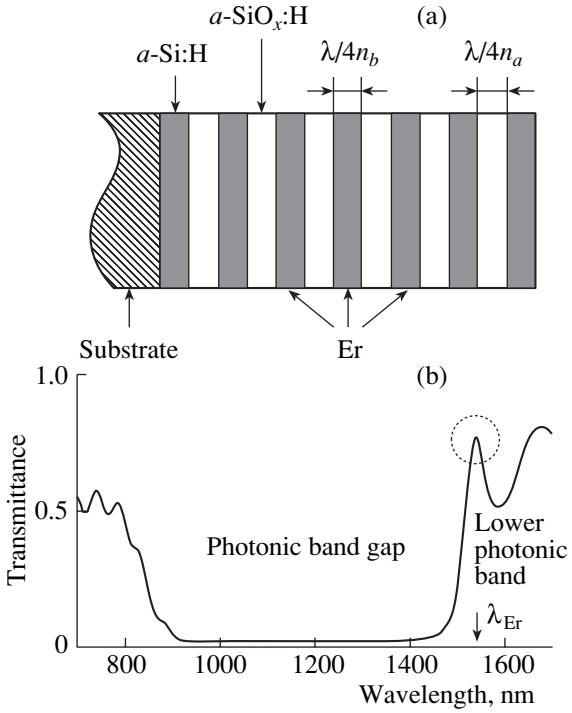

Fig. 1. (a) Schematic diagram of a 13-layered Bragg structure constituted of alternating *a*-Si:H and *a*-SiO_x:H layers. The three central *a*-Si:H layers of the structure are erbium-doped. (b) Transmission spectrum of the structure shown in Fig. 1a. The arrow indicates the wavelength λ_{Er} = 1535 nm, which corresponds to radiative transition of erbium ions from the first excited state to the ground state. The closed circle denotes the edge interference peak.

which corresponds to the 1D photonic band gap, within which the density of photon modes is close to zero and the propagation of electromagnetic waves in the direction perpendicular to the surface of the Bragg structure is suppressed. Outside this region (in bands of allowed states), photons propagate freely and a complex interference pattern, determined by the finite thickness of the Bragg structure, is observed in the spectrum.

In the ideal case of an infinite photonic crystal and absence of dissipation, the frequency dependence of the density of photon modes should exhibit a singularity at the photonic band edge $\rho(\omega) \propto dk/d\omega \longrightarrow \infty$, where k is the wave vector) [20]. In real structures of finite dimensions, the density of photon modes grows as the frequency increases in the spectral range corresponding to the lower photonic band and reaches a maximum that exceeds the corresponding value of $\rho(\omega)$ in free space [7, 11, 21]. However, in the region of the photonic band gap, $\rho(\omega)$ falls steeply. According to an inference from the electromagnetic variational theorem [22], the energy density of the electromagnetic field in photonic crystals at frequencies corresponding to the lower photonic band is concentrated in regions with a high refractive index, i.e., in the *a*-Si:H layers for the samples

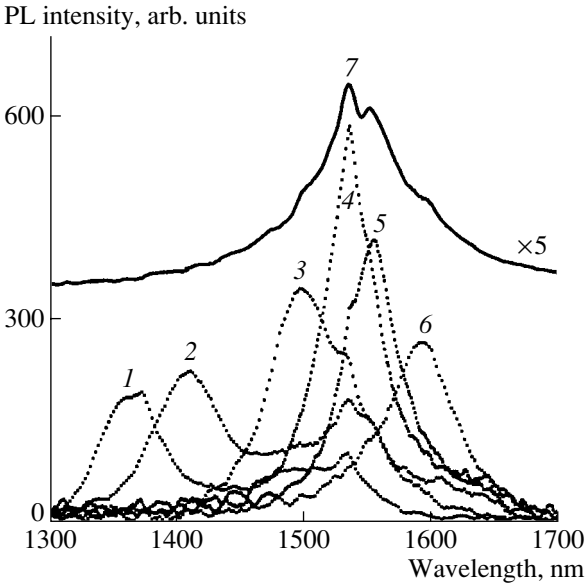

Fig. 2. PL spectra of 13-layered Bragg structures constituted of alternating *a*-Si:H and *a*-SiO_x:H layers with three erbium-doped central *a*-Si:H layers. The plots differ in relation to the positions of the edge interference peak in the transmission spectrum (see Fig. 1b) ((*1*) 1365, (*2*) 1410, (*3*) 1495, (*4*) 1535, (*5*) 1555, and (*6*) 1595 nm). The emission spectrum of erbium ions in a single *a*-Si:H film (curve *7*) is shifted along the ordinate axis for clarity.

examined in this study. It follows from the aforesaid that the influence exerted by the periodic structure of a photonic crystal on the interaction of the emitting erbium centers with a electromagnetic field in the structures under study should be more strongly pronounced in the spectral range corresponding to the lower photonic band edge.

All the subsequent measurements (Figs. 2–4) were made in the spectral range corresponding to the lower photonic band edge. As has already been mentioned, the samples studied had somewhat different layer thicknesses, which led to a spectral shift of the "edge" interference peak (denoted by a circle in Fig. 1b). Figure 2 shows the luminescence spectra of six DBRs (curves *1–6*) exhibiting different positions of the edge interference peak, measured under identical conditions of PL excitation and recording of the PL signal. Curve *7* corresponds to an inhomogeneously broadened emission band of erbium ions in a single *a*-Si:H film. It can be seen from the figure that the distribution of the main (with the highest intensities) peaks in the emission spectra of the Bragg structures reproduces the profile of the Er PL line in a single *a*-Si:H film.

Now, the influence exerted by the nonmonotonic behavior of the density of photon modes near the photonic band edge on the intensity of emission from erbium ions will be considered. Figure 3 shows the transmission (Fig. 3a) and luminescence (Fig. 3b) spectra of three Bragg structures with specially selected

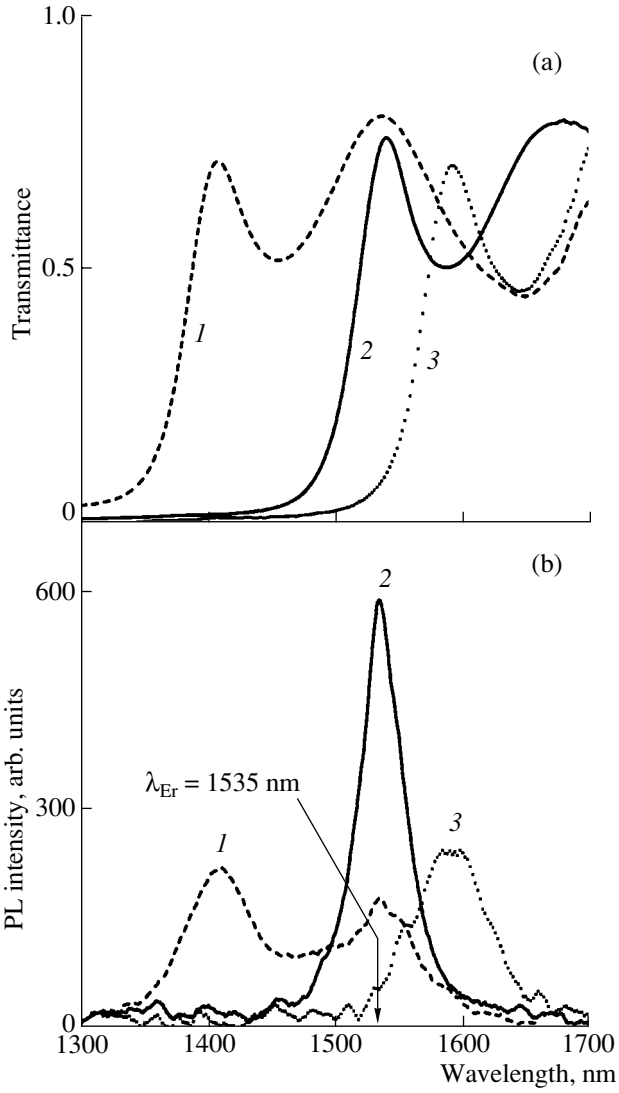

Fig. 3. Comparison of (a) transmission and (b) PL spectra of three Bragg structures with different spectral positions of the edge interference peak with respect to a wavelength (λ_{Er} = 1535 nm) corresponding to the radiative transition of erbium ions from the first excited state to the ground state. The energy of the radiative transition (*1*) falls within the range of allowed states of the lower photonic band far from its edge, (*2*) lies near the edge of this band, and (*3*) falls within the photonic band gap.

spectral positions of the edge interference peak in the transmission spectrum with respect to the position of the λ_{Er} peak in a single *a*-Si:H film. In structure no. 1, the edge interference peak in the transmission spectrum is shifted to shorter wavelengths with respect to λ_{Er}, and the energy of the radiative transition falls within the region of photon states of the lower photonic band, where the mode density is markedly lower than that at the edge of this band [21]. In this case, λ_{Er} lies near the second interference peak, which is characterized by a higher transmittance than the edge interference peak in the transmission spectrum. In structure no. 2, the edge

interference peak coincides with λ_{Er}, and the energy of the radiative transition lies near the photonic band edge, where the density of the photon modes is at its highest. In structure no. 3, the edge interference peak lies at a wavelength longer than λ_{Er}, and the radiative transition energy falls within the photonic band gap, in which the density of photon states is low.

Comparison of the transmission and PL spectra in Fig. 3 shows that the emission intensity is at its highest when λ_{Er} (curve *2*, Fig. 3b) lies near the edge interference peak in the transmission spectrum and markedly decreases as this peak is shifted both to shorter (curve *1*) and to longer (curve *3*) wavelengths with respect to λ_{Er}. It should be emphasized that the fall in PL intensity is observed for Bragg structure no. 1 at the wavelength λ_{Er} (curve *1*, Fig. 3b) despite the fact that the transmittance in this region (curve *1*, Fig. 3a) exceeds that in the vicinity of the edge interference peak. This result indicates that the experimentally observed increase (decrease) in the PL intensity does not correlate with periodic modulation of the transparency of the Bragg structure [17, 23] but is a consequence of the nonmonotonic variation of the density of optical modes in the 1D photonic crystal.

In order to evaluate the increase in the intensity of the spontaneous emission from erbium ions near the photonic band edge in DBRs, a reference sample was grown. After the seventh (central) erbium-doped *a*-Si:H layer was deposited, the surface of the structure was partly screened (right-hand part of the structure shown in Fig. 4). Then, the growth process was continued until 13 layers had been grown (left-hand part of the structure in Fig. 4). The emission spectra of erbium ions from the surface *a*-Si:H layer in a 7-layered structure and from the central *a*-Si:H layer within the 13-layered structure are shown in Fig. 4. Comparison of the spectra suggests that the intensity of spontaneous emission from erbium ions placed within a 1D photonic crystal increases by nearly an order of magnitude in the spectral range corresponding to the lower photonic band edge.

Thus, 1D photonic crystals were grown in the form of Bragg structures constituted of alternating *a*-Si:H and *a*-SiO_x:H layers. Erbium ions, serving as a source of spontaneous emission, were introduced into the central *a*-Si:H layers in the course of their growth. The transmission and PL spectra of the structures synthesized were studied. It was experimentally shown that the frequency shift of the photonic band edge with respect to the spectral position of the radiative transition of an erbium ion makes it possible to strongly modify the intensity of spontaneous emission from erbium ions through a pronounced change in the density of optical modes in a 1D photonic crystal. The spectral range in which the emission enhancement was observed corresponds to the standard spectral range (1.5 μm) of modern telecommunication technologies, which gives grounds to believe that the Bragg structures obtained can be used in, e.g., planar optical amplifiers for information transmission systems.

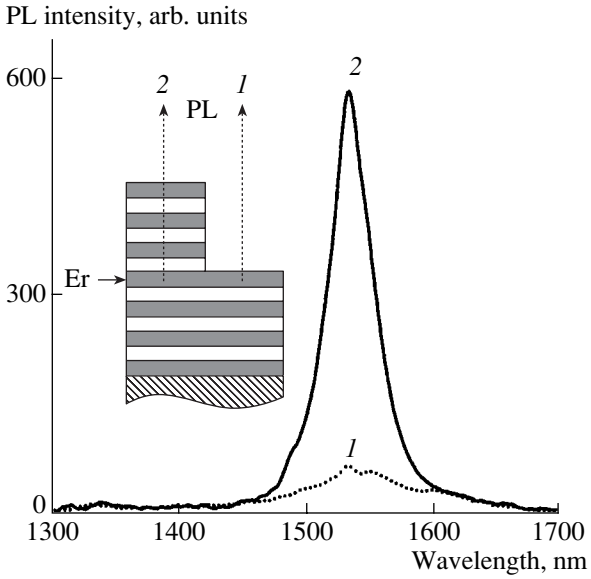

Fig. 4. Emission spectrum of erbium ions from (*1*) a quarter-wave film on the surface of a 7-layered Bragg structure (right-hand part of the structure shown in the figure) constituted of alternating *a*-Si:H and *a*-SiO_x:H layers and (*2*) from the central quarter-wave layer of a 13-layered Bragg structure (left-hand part of the structure shown in the figure). Spectrum *2* was measured under conditions in which the energy of the radiative transitions of erbium ions from the first excited state to the ground state is close to the lower photonic band edge.

The authors are grateful to A.V. Sel'kin and A.A. Dukin for their participation in helpful discussions.

The study was supported by the Russian Foundation for Basic Research (project no. 05-02-17803), NATO (grant PST.CLG 980399), and PHOREMOST (Nanophotonics for Realizing Molecular-Scale Technologies) (contract FP6/2003/IST-2-511616).

REFERENCES

1. R. Loudon, *The Quantum Theory of Light* (Clarendon, Oxford, 1973; Mir, Moscow, 1976).
2. E. M. Purcell, Phys. Rev. **69**, 681 (1946).
3. E. Yablonovitch, Phys. Rev. Lett. **58**, 2059 (1987).
4. S. John, Phys. Rev. Lett. **58**, 2486 (1987).
5. A. Polman and P. Wiltzius, MRS Bull. **26**, 608 (2001).
6. S. Y. Lin, J. G. Fleming, and I. El-Kady, Appl. Phys. Lett. **83**, 593 (2003).
7. M. Woldeyohannes and S. John, J. Opt. B: Quantum Semiclassic. Opt. **5**, R43 (2003).
8. P. Lodahl, A. F. van Driel, I. S. Nikolaev, *et al.*, Nature **430**, 654 (2003).
9. M. J. A. de Dood, A. Polman, and J. G. Fleming, Phys. Rev. B **67**, 115106 (2003).
10. C. Weisbuch, H. Benisty, and R. Houdre, J. Lumin. **85**, 271 (2000).

11. M. D. Tocci, M. Scalora, M. J. Bloemer, *et al.*, Phys. Rev. A **53**, 2799 (1996).
12. V. I. Kopp, B. Fan, H. K. M. Vithana, and A. Z. Genack, Opt. Lett. **23**, 1707 (1998).
13. F. Giorgis, Appl. Phys. Lett. **77**, 522 (2000).
14. A. Serpenguzel and S. Tanriseven, Appl. Phys. Lett. **78**, 1388 (2001).
15. E. Ozbay, I. Bulu, K. Aydin, *et al.*, Photonics Nanostruct. Fundam. Appl. **2**, 87 (2004).
16. A. Polman, J. Appl. Phys. **82**, 1 (1997).
17. A. A. Dukin, N. A. Feoktistov, V. G. Golubev, *et al.*, Appl. Phys. Lett. **77**, 3009 (2000).
18. V. G. Golubev, A. A. Dukin, A. V. Medvedev, *et al.*, Fiz. Tekh. Poluprovodn. (St. Petersburg) **35**, 1266 (2001) [Semiconductors **35**, 1213 (2001)].
19. A. A. Dukin, N. A. Feoktistov, V. G. Golubev, *et al.*, Phys. Rev. E **67**, 046602 (2003).
20. A. Yariv and P. Yeh, *Optical Waves in Crystals* (Wiley, New York, 1984; Mir, Moscow, 1987).
21. J. M. Bendickson, J. Dowling, and M. Scalora, Phys. Rev. E **53**, 4107 (1996).
22. J. D. Joannopoulos, R. D. Meade, and R. D. Winn, *Photonic Crystals. Molding the Flow of Light* (Princeton Univ. Press, Princeton, N.J., 1995).
23. V. G. Golubev, A. V. Medvedev, A. B. Pevtsov, *et al.*, Fiz. Tverd. Tela (St. Petersburg) **41**, 153 (1999) [Phys. Solid State **41**, 137 (1999)].

Translated by M. Tagirdzhanov